The Globular Cluster System of M31

Keys to its Formation History

by

Kathryn Perrett, M.Sc.

A thesis submitted to the Department of Physics
in conformity with the requirements
for the degree of Doctor of Philosophy

Queen's University
Kingston, Ontario, Canada
September, 2001

ABSTRACT

Various models have been proposed to describe the formation of galaxy halos, including monolithic or multiphase collapse, mergers and accretion. With the aim of probing the dynamical and chemical enrichment history of the nearby spiral galaxy M31, a spectroscopic study has been conducted of its globular cluster system. Observations were obtained using the Wide Field Fibre Optic Spectrograph (WYFFOS) at the William Herschel Telescope, and using the MOS/ARGUS integral field spectrograph at the Canada-France-Hawaii Telescope. This work has yielded precise radial velocities (good to ± 12 km s^{-1}) and metallicities (good to ± 0.26 dex) for over 200 M31 globular clusters, many of which have no prior spectroscopic data.

Analyses of the spatial, kinematic and metal abundance properties of the M31 clusters are made and discussed in the context of the proposed galaxy formation models. The M31 globular cluster metallicity distribution is found to be bimodal, with peaks at [Fe/H] $\simeq -1.4$ and -0.5. M31's metal-rich globular clusters appear to constitute a distinct kinematic subsystem which is centrally-concentrated, consistent with membership in a bulge population. There is a measurable metallicity gradient within the inner metal-poor cluster system, and both metallicity populations demonstrate significant rotation.

In addition, the best current sample of M31 globular cluster data is used to search for the presence of substructure in the three-parameter space of position, velocity, and metallicity. Convincing evidence of at least four groups is found. These globular cluster groups may represent the remnants of recent satellite mergers, an observation which would favour a hierarchical formation scenario for M31.

STATEMENT OF CO-AUTHORSHIP

This study was performed under the supervision of Dr. Dave Hanes at Queen's University. It is based on observations obtained at the Canada-France-Hawaii telescope (K. Perrett and D. Hanes, observers) and at the William Herschel Telescope (T. Bridges, observer).

All of the work described herein was done by the author (K. Perrett) except where explicitly stated otherwise.

ACKNOWLEDGEMENTS

It is with great pleasure that I thank my supervisor, Dave Hanes, for his guidance and for sharing his obvious enthusiasm for astronomy. I sincerely appreciate the many opportunities I have been given throughout my years with the QUARG.

I am also deeply indebted to both Terry Bridges and Dave Stiff for their invaluable assistance, wise council, patience and encouragement. I really can't thank you guys enough! I would also like to acknowledge Steve Butterworth, JJ Kavelaars, Siow Wang Lee, Doug McNeil and the rest of the QUARG for the useful (and even the not-so-useful) discussions. I am grateful to the following people for making their code available: Josh Barnes, Christine Bird, Karl Gebhardt, Jim Lewis, Steve Zepf, and the IRAF group at NOAO. I also thank Pauline Barmby for sharing unpublished reddenings.

I appreciate the support I have received from Mom, Al, Raymonde, and the rest of my family. I would like to thank Annie Hsu, Scott Young, Judith Irwin, Margaret Morris and Edith Engelberg for their kind encouragement. Thanks also go out to the telescope support staff at CFHT and WHT, to the Free Software Foundation for their commitment to the liberation of humankind, to the Queen's fencing team for the contusions, to Blizzard Entertainment and ID Software for the RSI, to Pisco for the distraction, to the QUARG grad students for all the frags and to the Adopt a Star Campaign for making the fun last so much longer than it had to.

This work was supported by the Natural Sciences and Engineering Research Council of Canada and the National Research Council in the form of operating grants to Dave Hanes.

CONTENTS

LIST OF FIGURES

LIST OF TABLES

1. INTRODUCTION: GALAXY STRUCTURE AND FORMATION

Today we recognize the Milky Way as a spiral galaxy, an enormous system composed of hundreds of billions of stars and copious amounts of gas, dust and dark (unseen) matter. Most of the luminous matter of the Galaxy is found within a flattened disk-like component which extends out many tens of thousands of light years in radius. Within the disk, spiral arms wind outwards from the central regions of the Galaxy and mark regions of ongoing star formation. At the centre lies the Galactic bulge, a triaxial spheroid of older stars which juts out above and below the luminous disk. Within the bulge is found the nucleus, an active region at the heart of the Galaxy whose mysteries are gradually being unveiled thanks to observations in the radio, infrared, x-ray and γ-ray regions of the electromagnetic spectrum.

The Earth orbits the Sun, an average star in many respects, which itself is hardly a speck in the vast wash of starlight of the Galactic disk. Our humble position is roughly two-thirds of the way out from the Galactic centre, slightly above the disk at the outer edge of the Sagittarius spiral arm of the Milky Way. The luminescent band we call the Milky Way represents the collective appearance of the stars, glowing gaseous nebulae and silhouetted clouds of obscuring dust which constitute the disk of our Galaxy. The stars visible to the naked eye typically lie only a few hundred light years distant, although the stellar disk of the Milky Way extends considerably further. Surrounding the disk is a relatively sparsely-populated halo of older stars and dark matter which is not readily observable by the backyard astronomer. Indeed, very little visible evidence can be seen of this expansive Galactic halo, although the ancient

stars of the halo provide us with an important key to unlocking the history of the Galaxy. Direct observations within our local environment (the solar neighbourhood) have provided us with a significant amount of first-hand data about the structural components of our Galaxy. Considerable information has also been gleaned from observations of other nearby galaxies.

Our current vision of the Galaxy has been established thanks to the momentous efforts of a myriad of astronomers throughout human history. But what can we infer about the Galaxy's formation and evolutionary history? These compelling questions form the basis of the upcoming chapters. This introductory chapter provides a look at what we know of galactic structure and the processes that shape it. Chapter 2 introduces the particular interest of this study — the Andromeda Galaxy and its globular clusters — and puts this work in the broader context of related studies. Chapters 3, 4 and 5 present a description of the astronomical data sets obtained and the analytical procedure used to address the question of galaxy formation. A kinematic and metal abundance analysis of the best available spectroscopic sample to-date of the dynamical and chemical enrichment probes of the Andromeda Galaxy is provided in Chapter 6. Chapter 7 incorporates an examination of the possibility that the Andromeda Galaxy formed at least in part from the merger and accretion of dwarf satellites. A summary of the results and the conclusions of this study are presented in Chapter 8. A glossary of terms and units is provided at the end of this document.

1.1 A Brief History of Galactic Astronomy

In the year 1610, Galileo first turned his telescope towards the Milky Way and discovered that it contained an astonishing number of stars. The shape and nature of the Galaxy (which was then thought to be the Universe) remained a great mystery at that time. Centuries later, with the development of powerful instruments and the

refinement of astronomical techniques, we have now established the basic structure and composition of our Galaxy and others. This section provides a very brief synopsis of the history of the human endeavour to understand the galaxy in which we live[1].

Until the 18th century, a majority of the galactic theories were based primarily on religious or philosophical speculation. Some of these theories (generally unsuccessfully) attempted to explain the observed concentration of stars in the band of the Milky Way. Towards the year 1775, Immanuel Kant expressed his vision of a universe consisting of a multitude of stars orbiting a common centre, an idea which was surprisingly not far off the mark! Almost prophetically, he reasoned that if the Milky Way was a flattened disk of stars, other similar stellar aggregations might also occur.

During the late 18th century, astronomer William Herschel had access to the largest and most powerful telescopes of that time. His careful study of the distribution of stars revealed that the Milky Way was indeed a flattened system, as Kant had speculated. Herschel also discovered many nebulous objects, some of which could be resolved into stars themselves; he hypothesized that these curious objects formed distant stellar systems, possibly ones of even greater size than the Milky Way. These stellar nebulae were later identified as star clusters within our Galaxy, but Herschel's work represents one of the first *systematic* scientific studies of galactic astronomy. As an interesting note, in 1845 William Parsons (Earl of Rosse) was the first to identify spiral structure in some of Herschel's unresolved nebulae.

By 1901, the refinement of the techniques of astrometry — the measurement of stellar positions and motions — permitted J. C. Kapteyn to infer that the Milky Way was a flattened stellar system roughly 2 kpc thick and 10 kpc in diameter...the so-called "Kapteyn Universe" (Kapteyn & van Rhijn 1920). Kapteyn astutely recognized that absorption by interstellar dust would dim the light from stars, making them

[1] For a more detailed description of the fascinating history of galactic astronomy, the reader is referred to the works of Berendzen, Hart & Seeley (1976) and Binney & Merrifield (1998).

appear more distant than they actually were. Unfortunately, Kapteyn could neither confirm the presence of nor compensate for the effects of absorption (Kapteyn 1909).

The general thinking at that time was that the Sun was centrally located in the Galaxy. Harlow Shapley, an American astronomer, studied the distances and positions of globular star clusters and discovered that the clusters formed a distribution centred on a point in the direction of the constellation of Sagittarius, at a distance of 20 kpc from the Earth (Shapley 1918). His conclusion was that these stellar systems were associated with the Milky Way and reflected its geometry: the Sun and Earth were located towards the edge of the Milky Way, the true centre of which was revealed by the centroid of the globular cluster distribution. Shapley's assertion that the Galaxy was ten times larger than commonly believed met with intense criticism. However, a direct result of this rescaling of the Milky Way also led Shapley to conclude that the spiral nebulae first observed by Lord Rosse could not be external systems.

During that same period, Herber D. Curtis was studying these spiral nebulae. From his investigation of Galactic novae, Curtis believed these spiral nebulae to be distant stellar systems or "island universes" (Curtis 1917). He also supported Kapteyn's idea of a smaller Milky Way. Shapley and Curtis presented their views on the size of the Milky Way and the nature of the spiral nebulae at the so-called "Great Debate" of 1920 (Curtis 1921; Shapley 1921). Shapley, as it turns out, was essentially correct in his distance estimates to the globular clusters (fortuitously, various errors in his method of distance determination canceled out). Curtis, on the other hand, was correct in his conclusion that the spiral nebulae were distant systems, although his distance estimates were somewhat too low. The obscuring effects of interstellar absorption were still confounding the astronomers of that day.

It has therefore been less than a century since galaxies were first identified as systems of comparable structure, scale and composition to our own Milky Way system. In 1924, Edwin Hubble's observations of variable stars in a spiral nebula in the

constellation of Andromeda using the 2.5 m telescope at Mount Wilson conclusively showed that this was a distant object outside the Milky Way which was itself composed of stars, gas and dust. The Andromeda Nebula was thereby identified as a spiral galaxy, conceivably of similar size, shape and composition to the Milky Way (Hubble 1929). Hubble's early concept of galaxies as isolated island universes has since been replaced by the recognition that they are dynamic, evolving structures which are strongly influenced by their environments.

1.2 Spiral Galaxies and the Milky Way

Since the days of Herschel, the use of star count data has been of great value in the study of Galactic structure. This technique involves counting the number of stars of a given type or colour per unit area of the sky in magnitude bins. Determinations of stellar composition and kinematics based on spectroscopic measurements have also played a valuable role in forming our current picture of the Milky Way galaxy (see Gilmore, King & van der Kruit 1989). Increasingly precise photometry and proper motion measurements of stars in the solar neighbourhood from ground- and space-based astrometry missions like the Hipparcos satellite have already helped to provide a better understanding of local stellar dynamics and ages (e.g. Binney et al. 2000), and to establish a firmer basis for the Galactic and extragalactic distance scale (e.g. Reid 1997). Many of the difficulties associated with investigating the structure of the Milky Way stem from our location within its murky disk. Self-discovery has also largely been accomplished through surface photometry from orbiting infrared satellites. In particular, at near-infrared wavelengths ($\lambda \sim 2-4\ \mu$m), the effects of obscuring dust in the plane of the Galaxy are minimized and stars stand out most clearly against the background. All of these techniques (and others) have been instrumental in providing us with our current concept of Galaxy structure.

In many respects, the Milky Way is a typical spiral galaxy of Hubble morpholog-

ical type Sbc. It has a pronounced disk with conspicuous spiral arms and a fairly prominent central bulge. The globular star clusters found in its bulge, disk and halo constitute the best-studied sample of old stellar aggregations.

1.2.1 The Galactic Disks: Thick and Thin

The Galaxy's thin disk component has a roughly exponential density distribution in both height (z) and radius (R), with scales of a few hundred parsecs (pc) and several kiloparsecs, respectively. Metal abundances[2] are typically solar, with arguable signs of a gradient in the radial direction towards lower values at large R (see Chiappini, Matteucci & Romano (2001) and references therein).

Regions of high-density gas and star formation delineate the spiral arms of the Galaxy (see example in Figure 1.1). The Sun and Solar System are at a Galactocentric radius of $R_\odot \sim 8.5$ kpc within the thin disk, on the edge of one of spiral arms roughly 14 ± 4 pc above the plane of the Galaxy, (Binney et al. 1997). Although the overall system is rotating, it is not doing so as a solid body: the angular velocity of the disk stars decreases with increasing Galactocentric distance. The period of revolution for the Sun about the Galactic centre is $\sim$ 250 Myr. Studies of the kinematics of the disks in other galaxies reveal that stars in these components follow roughly circular orbits with low velocity dispersion (i.e. small random motion).

Burstein (1979) noted the presence of a second disk component in certain lenticular galaxies. This so-called "thick disk" is a flattened distribution of stars with an exponential luminosity profile which is more extended than the thin disk component. Similar thick disk features have since been found in many disk galaxies, including the Milky Way (Gilmore & Reid 1983). Based on star count data, the scale heights of the thin and thick disks in the solar neighbourhood are 330 ± 3 pc and $\sim$ 750 kpc, respectively (Chen et al. 2001). The mean metal abundance of the stars in the thick disk is

[2] In astronomy, a metal generally refers to any element heavier than helium. The terms *metallicity* and *abundance* will be used to refer to metal abundance.

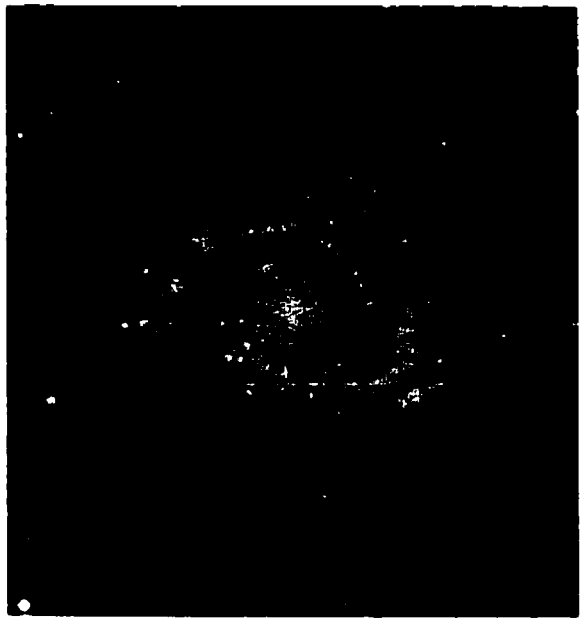

Figure 1.1: The Milky Way Galaxy might resemble the general form of this spiral galaxy, NGC 2997, if we were able to view it face-on from the outside. The central bulge and spiral arms of this galaxy are evident in this photograph (from the Digitized Sky Survey).

found to be distinct from that of the stars in the thin disk. Thick disk members tend to have relatively low metal abundances, with chemical abundance patterns comparable to the inner (metal-richer) halo and to the metal-poor bulge stars (Prochaska et al. 2000). Liu & Chaboyer (2000) reported a gap in the ages of the nearby thin and thick disks, such that the thick disk appears to have formed $\gtrsim 1$ Gyr earlier.

The origin of the thick disk is still in question. This component could have formed from processes such as the dissipational collapse of the halo (Jones & Wyse 1983), or a gradual heating of an early thin disk resulting from a merger event (Quinn, Hernquist & Fullagar 1993; Sellwood, Nelson & Tremaine 1998). Gilmore, Wyse & Jones (1995) probed the chemical abundance distribution in the stars found 500 to 3000 pc above the Galactic plane at the solar radius $R_{\odot}$. Based on their findings, they argued that the thick disk could not have formed due to dissipational settling on account of its lack of any notable gradient in metal abundance.

1.2.2 The Bulge and Nucleus

The detailed structure of the innermost regions ($\lesssim 3$ kpc) of the Milky Way is ostensibly complex and remains poorly understood. At the middle of the Galaxy lies the nucleus, currently quiescent although it is believed that nuclear activity is episodic (Binney & Merrifield 1998). There is a compact, variable radio source Sgr A* at the very centre of the Milky Way which is thought to betray the presence of a supermassive black hole (Genzel & Townes 1987; Blitz et al. 1993; Ghez et al. 1998).

The bulge itself is triaxial with axis ratios 1.0 : 0.6 : 0.4 and a semi-major-axis length of roughly 2 kpc (Binney et al. 1997). It is surrounded by an elliptical nuclear disk which extends out to roughly 3.5 kpc on the major axis. Early 2.4 μm measurements (Hayakawa et al. 1979) and near-infrared COBE/DIRBE images (Weiland et al. 1994) revealed a Milky Way bulge that is markedly "boxy" or "peanut-shaped", a shape often explained in terms of perturbations on the orbits of bulge stars due to the presence of a bar at the Galactic centre (Combes et al. 1990; Binney et al. 1991). A COBE/DIRBE image showing the plane and bulge of the Milky Way is provided in Figure 1.2.

The stars in the inner region of the Milky Way demonstrate a sizeable range of metal abundances and are predominantly old (although see Feltzing & Gilmore 2000). A kinematic study of giant stars within the inner Galaxy by Minniti (1996) revealed that the metal-poor stars have a high velocity dispersion (~ 120 km s^{-1}) and no significant rotation, and hence may represent an extension of the halo. The bulge itself is a rotating system (Minniti et al. 1992) which demonstrates a gradient towards decreasing metal abundance at larger radii (Minniti et al. 1995).

It has been suggested that most of the gas in the young Galaxy ended up sinking to the centre of the potential well, forming the bulge via dissipational collapse (Minniti

[4] The COBE datasets were developed by the NASA Goddard Space Flight Center under the guidance of the COBE Science Working Group and were provided by the National Space Science Data Center.

Figure 1.2: Infrared image of the Milky Way Galaxy obtained by the COBE satellite and DIRBE at 1.25, 2.2, and 3.5 μm wavelengths[4]. The plane of the Galaxy is horizontal across the middle. The thin disk and central bulge stars are apparent, with the plane of the Galaxy cutting horizontally across this image.

1995, 1996; Sommer-Larsen et al. 1997). A striking similarity between the metal abundances of the thick disk and bulge seems to point towards a coeval origin of these two galactic components (Prochaska et al. 2000). For further details about the structure and dynamics of the Galactic bulge, the reader is referred to the work of Beaulieu et al. (2000) and references therein.

1.2.3 The Galactic Halo

The Galactic disk is surrounded by an expansive ($\sim$ 100 kpc radius) spherical halo of stars, globular clusters and dark matter. Spiral galaxies rotate about an axis through the centre of the bulge and perpendicular to the disk. A balance between the centripetal and gravitational forces prevents the galaxy from collapsing in upon itself. Away from the plane of the disk, however, the stellar population is "pressure-supported", with a large velocity dispersion. Outwards from the axis of rotation, the light from the stars in the galaxy is found to decrease, whereas the rotation velocity

does not drop off substantially (Rubin et al. 1985; Kent 1986). This is one indication of the presence of large quantities of dark matter in galactic halos, the exact nature of which remains a current topic of hot debate. From dynamical observations, it appears that dark matter may account for $\sim 90\%$ of the total mass of the Universe (see review by Trimble 1987).

The halo is metal-poor, on average, and is believed to be the oldest component of the Galaxy. The inner region of the halo has an age similar to that of the thick disk, an indication that *if* the thick disk formed from the gravitational collapse of the halo, the collapse of the protogalactic cloud took place on a timescale of less than 1 Gyr (Liu & Chaboyer 2000; Chiappini, Matteucci & Romano 2001).

The kinematics of the halo are dominated by random motions. Although the stellar halo represents a mere 1% of the total luminous mass of the Milky Way, its residents can be used as dynamical tracers of the mass of the Galaxy's dark matter halo. The most prominent objects found in galactic halos are the globular clusters.

1.3 The Galaxy's Globular Cluster System

When William Herschel first resolved some of the Milky Way's globular clusters into individual stars, it led him to consider the possibility that the more distant, unresolved nebulae might themselves be distinct stellar systems. Globular cluster systems (GCSs) are now known to be associated with galaxies of all types and sizes. The Milky Way's GCS includes nearly 150 known members which are located at positions ranging from the Galactic centre to the outer halo (Harris 1996). Globular clusters (GCs) are gravitationally bound spherical aggregations of several tens of thousands to a few million stars. Their high intrinsic brightness makes globular clusters prime targets for observation, even at great distances. For some excellent reviews on the subject of globular clusters, the reader is referred to the works of Harris (1991, 1998) and Ashman & Zepf (1998).

1.3.1 Age and Metallicity

In general, globular clusters are old. Chaboyer et al. (1996) calculated a mean age of the oldest Galactic globular clusters of 11.5 ± 1.3 Gyr. There is no discernible age gradient in the globular clusters between galactocentric radii of $\sim 4 - 100$ kpc, implying that the bulk of the cluster system formation occurred roughly simultaneously throughout the Galactic halo (Richer et al. 1996; Harris et al. 1997; Rosenberg et al. 1999). Age determinations are normally performed from the comparison of theoretical stellar-evolutionary models with the observed properties of the globular cluster colour-magnitude diagram (e.g. Sarajedini & King 1989).

A model of GC formation has been devised by Harris & Pudritz (1994) and McLaughlin & Pudritz (1996) in which globular clusters formed within the cores of self-gravitating supergiant molecular clouds (SGMCs) in the forming protogalaxies. These SGMCs represent larger (10^9 $M_\odot$, 1 kpc diameter) versions of the giant molecular clouds observed in spiral galaxies in the current epoch.

Globular clusters ages and metallicities are known to span a relatively broad range, although their metallicities do not generally exceed solar. There are signs of a weak metallicity gradient within the inner Milky Way globular cluster system towards decreasing values at large radii (Harris & Canterna 1979; Pilachowski 1984; Zinn 1985; although see also Alfaro, Cabrera-Caño & Delgado 1993).

The Milky Way GCS has a distinctly bimodal metallicity distribution, revealing the presence of a metal-rich and a metal-poor component in the population (Zinn 1985; Armandroff 1989). The metallicity distribution of the metal-poor Milky Way GC population peaks at roughly the same value as that for the halo field stars, but has less extended tails (Laird et al. 1988). The metal-poor GCs are thought to have formed on a relatively short timescale, roughly that of the free-fall collapse time of the proto-Galaxy (Richer et al. 1996; Chiappini, Matteucci & Romano 2001). The metal-rich GCs of the Milky Way are a few Gyr younger than the low-metallicity clusters;

they have ages of $9 - 10$ Gyr, comparable with that of the old stellar residents of the disk (Salaris & Weiss 1998).

1.3.2 Spatial Distribution

It was Shapley (1918) who first recognized that "the globular clusters outline the extent and arrangement of the total galactic organization". The spatial distribution of the Milky Way globular cluster system is roughly spherically symmetric about the Galactic centre as shown in Figure 1.3. The spatial density distribution of the GCS is well-matched by a $\rho \sim R^{-3.5}$ radial profile over most of the Galactic halo (Harris 1998). This is comparable to the distribution of halo RR Lyrae stars, which follow a $\rho \sim R^{-3.2}$ profile (Preston, Shectman & Beers 1991). The metal-rich globular clusters of the Milky Way are noticeably more centrally concentrated than the metal-poor GCs, a property which is also demonstrated in Figure 1.3.

1.3.3 Kinematics

The spatial distribution and kinematics of old stellar systems are determined by the properties of the parent protogalaxy and the physics of galaxy formation. That is, the position, orbital energy and angular momentum of a given globular cluster will depend on factors such as the shape and depth of the potential well in which it is formed, its maximum distance from the centre of the protogalaxy, its initial angular momentum and the evolution of its orbital path. The properties of globular cluster systems in the current epoch can thus betray the nature of galaxy formation and evolutionary processes.

Within the Milky Way GCS, the metal-poor clusters form a dynamically hot system with low systematic rotation and a high velocity dispersion. These objects are typically associated with the halo due to their kinematic properties and less concentrated spherical spatial distribution. The metal-rich clusters, on the other

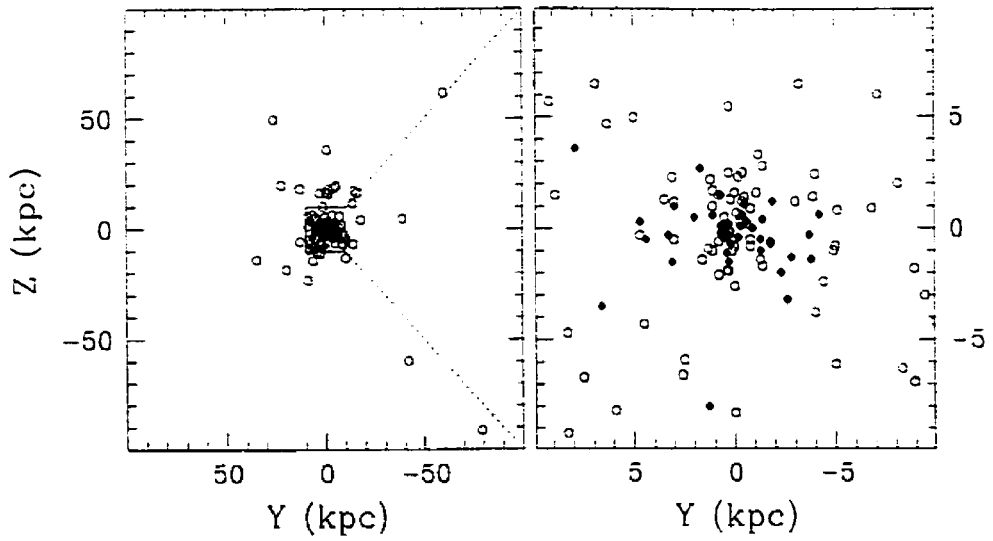

Figure 1.3: The spatial distribution of the outer (left) and inner (right) globular clusters of the Milky Way. Their positions have been projected onto the YZ plane, and our perspective is that of looking along a line of sight directed towards the Galactic centre (from a long way out). Filled symbols represent metal-rich clusters and open symbols are the metal-poor GCs.

hand, form a centrally-concentrated, flattened distribution with a mean net rotation about the Galactic centre. These higher metallicity clusters are typically associated with either the thick disk (Zinn 1985; Armandroff 1989) or the bulge/bar (Minniti 1995; Côté 1999; Forbes, Brodie & Larsen 2001).

1.4 Galaxy Formation

The mechanisms involved in galaxy formation remain one of the major unsolved problems in astronomy. Over the past several decades, various groups have proposed models which endeavor to explain the observed properties of galaxies and their globular cluster systems. One early formation model from Eggen, Lynden-Bell & Sandage (1962) argued for a single, large-scale collapse of material to form galactic systems like the Milky Way. A principal competing model proposed by Searle & Zinn

(1978) maintained that formation occurred through random mergers of fragmented gas clouds over the course of billions of years, implying a hierarchical origin. Additional scenarios such as multiphase *in situ* formation (Forbes et al. 1997), major mergers (Schweizer 1987; Ashman & Zepf 1992) and tidal stripping/capture (Côté, Marzke & West 1998) have also been put forth to interpret the bimodality seen in the globular cluster metallicity and colour distributions of many galaxies (e.g. Larsen et al. 2001; Forbes & Forte 2001).

1.4.1 *Monolithic Collapse*

In their landmark paper of 1962, Eggen, Lynden-Bell & Sandage (henceforth ELS) interpreted a correlation between the eccentricity of stellar orbits with ultraviolet excess (hence metallicity) of halo stars as evidence for an early, rapid, homogeneous dissipative collapse of proto-Galactic material from the halo onto the galactic plane. ELS observed that stars with the lowest metal abundance move on the most radial orbits, with high eccentricities and low angular momenta. For a particular star, the values of orbital eccentricity and angular momentum are not significantly changed if the potential in which the star is moving varies gradually (Binney & Tremaine 1987 §3.6). Therefore, either stars of low metallicity formed on highly eccentric orbits in the first place, or the Milky Way experienced a rapid, violent change in its potential during its formation history.

Based on their observations, ELS illustrated a formation scenario for the Milky Way as follows. The proto-Galaxy was born of a spinning, spherical cloud of metal-poor gas in approximate free-fall. The first generations of stars in the Galaxy formed of this metal-poor gas on the most plunging of halo orbits with high eccentricities. This explained their observed lack of metal-poor stars with low-eccentricity orbits. As the system cooled and collapsed due to gravitational forces, its spin increased to conserve angular momentum. The mean metal abundance in the proto-Galactic

cloud increased as supernovae and stellar winds enriched the environment with heavy elements fused within stellar interiors. After the proto-Galaxy had shrunk in radius by a factor of 10 or so, its collapse was halted by rotation as the metal-rich cloud flattened out into a rotationally-supported thin disk. Later generations of more metal enriched stars formed on circular orbits within this disk. The first generation of stars and globular clusters continued on their radial orbits initiated during the primeval collapse, forming the extended component known as the halo. The ELS scenario therefore suggests a stellar formation sequence with increasing systematic rotation, decreasing random velocities and increasing metal abundance as the proto-Galactic material became enriched by supernovae-driven winds.

Fragmentation into distinct regions of star formation could have resulted from gravitational and thermal instabilities in a collapsing proto-Galactic gas cloud (Fall & Rees 1985). The more diffuse sub-systems which may have been created during the early stages of Galaxy formation would have been preferentially disturbed or destroyed by the effects of dynamical friction, tidal interaction, disk shocking and star formation feedback processes. The gas originally tied up in these sub-systems may have settled into the massive differentially-rotating disk (Sommer-Larson et al. 1997). The more compact globular clusters had a better chance for survival in the early Galaxy.

Subsequent determinations of the angular momentum distributions within the structural subsystems of the Galaxy have shown that there exist distinct similarities between the thick and the thin disk components (angular-momentum-supported systems), and between the bulge and halo (pressure-supported systems). These two angular momentum distributions differ from each other considerably, however. An excessively large collapse factor would have been required in order to form a centrifugally-supported disk (Gilmore 1996). The halo's half-mass radius is smaller than that of the disk, and hence the halo could not have collapsed enough to form

the present-day disk. Therefore, an alternative interpretation to the ELS model later suggested that the metal-poor halo underwent an early, rapid, monolithic collapse to form the bulge, not the disk, and that the thin/thick disk and halo/bulge components are essentially independent (Ibata & Gilmore 1995; Chiappini, Matteucci & Romano 2001).

Further problems with the monolithic collapse scenario soon emerged. ELS provided a timescale for collapse and halo formation of $\sim 10^8$ years, on the order of the free-fall time. At that time, the age spread among halo globular clusters was believed to be significantly longer (e.g. Rood & Iben 1968), at odds with the ELS view. Also, as observational data for halo objects became more readily available, there was little evidence for a correlation between stellar chemical and kinematical properties.

The apparent correlation between the orbital eccentricity and metallicity of halo stars found by ELS was confirmed by Twarog & Anthony-Twarog (1994, see their Figure 10). However, a recent study of the kinematics of metal-poor stars in the Galaxy by Chiba & Beers (2000) maintained that the correlation found by ELS was principally the result of a sample selection bias. Nonetheless, Chiba & Beers did identify a small concentration of lower metallicity halo stars on high-ellipticity orbits which may have originated in the gaseous infall within the proto-Galaxy.

1.4.2 Random Mergers

The galaxy formation picture evolved during the 1970s. In a quote from a 1977 conference, Toomre effectively summarized the emerging view at that time:

> It seems almost inconceivable that there wasn't a great deal of merging of sizeable bits and pieces (including quite a few lesser galaxies) early in the career of every major galaxy, no matter what it now looks like. The process would obviously have yielded halos from the stars already born, whereas any leftover gas would have settled quickly into new disks

> embedded within such piles of stars. More or less simultaneously though, any compact and presumably more metal-rich partners or galaxy cores should have sunk quite deep into this brew before losing their separate identities, thereby contributing to what we call central bulges. In short, vague though it all seems, I really do suspect that the few mergers we are still privileged to witness are just the statistical dregs of a once very common process.

Current theories for the formation of the Universe suggest that early structure formed and grew through the amplification of small density fluctuations brought about by gravitational forces. In this hierarchical formation scheme, over-dense regions in the early Universe amalgamated to form larger structures. It might then follow that our Galaxy and others formed, at least in part, in a similar hierarchical fashion (e.g. Cole et al. 2000). In this "building block" scenario, small objects would form first and merge to form progressively larger structures. Galaxies could thus be assembled by the accretion of many satellites of varying mass and size.

In 1978, Searle & Zinn (henceforth SZ) proposed an alternative to the ELS picture wherein the Galaxy halo formed largely by the protracted accretion of smaller, independently-formed fragments. These fragments were gas-rich and metal-poor, with sizes comparable to dwarf galaxies and masses of $\sim 10^8 M_\odot$. Interactions of the infalling gas clouds dissipated their kinetic energy and produced transient high-density regions appropriate for star formation. The stars which formed in this manner dispersed and fell into dynamical equilibrium within the Galaxy, producing the outer halo. The enriched gas expelled from these clumps could have been swept into the flattened Galactic disk and then recycled to produce the metal-rich, younger stellar population.

At that time, it had been noted that the metallicities of the halo cluster population varied considerably and showed no correlation with galactocentric radius. The SZ

picture seemed to account for this perceived lack of a radial abundance gradient in the halo globular clusters as well for the large (several Gyr) spread in the inferred ages of Galactic globular clusters. Since the mean metal abundance of each accreting clump should be regulated by the internal enrichment history of the fragment itself, it would stand to reason that GC chemical and dynamical properties in an accreted halo would be largely independent. Chiba & Beers (2000) have confirmed a lack of correlation between the kinematics and metallicity within their large sample of halo stars, in agreement with the expected results of a formation driven by random mergers.

Improvements in sample size and in measurements of the metal abundances of Galactic globular clusters have shown that there is, in fact, a weak but measurable gradient towards decreasing metallicity at large radii in all but the outermost halo (Harris & Canterna 1979; Pilachowski 1984; Zinn 1985). There are also signs of a metallicity gradient in the halo field stars (Yoss, Neese & Hartkopf 1997). However, the discovery of a metallicity gradient, in and of itself, is not sufficient to confirm an early dissipational collapse. Such a gradient could be mimicked by a hierarchical halo formation if the metallicity of the accreting fragments correlates with their mass and mean density (Freeman 1996). In such a case, the material from disrupted fragments may become segregated as the more metal-rich debris from the denser fragments preferentially settles towards the inner halo, leaving the more metal-poor fragments within the outer halo. Detailed chemical and kinematical information is thus required to distinguish between formation models.

Some studies of the stellar halo have uncovered a component which is in retrograde motion with respect to the Sun's motion in the disk (Majewski 1992; Carney et al. 1996). Such kinematics imply that the bulk of the stars in this region of the halo may have formed as a result of the accretion of fragments either during or following a dissipative settling of the disk component. The ELS collapse scenario could not

account for the contrast in the mean angular momenta of the galactic disk and halo.

The metal-poor thick disk may have originated by the heating/disruption of early thin disk stars by accretion events. Alternatively, it may be the debris remaining from cannibalized low-metallicity satellite galaxies, whose orbits have become circularized due to the effects of dynamical friction (Freeman 1996).

The mere existence of the thin disk in the Milky Way has previously been cited as evidence against a large contribution of material to the Galaxy by satellite accretion (Quinn, Hernquist & Fullagar 1993). However, Johnston, Spergel & Hernquist (1995) argued that the contribution of halo shocking of dwarfs with large orbital pericentres could effectively destroy the satellites with negligible effects on the Milky Way disk. The disruption of dwarf galaxies with $M \lesssim 0.01 M_{disk}$ could thus occur within the Galactic halo without dynamically heating the disk (Mateo 1996).

The model of globular cluster formation in SGMCs fits in well with the SZ view (Harris & Pudritz 1994; McLaughlin & Pudritz 1996). These molecular clouds are found to be of the correct range in mass and density to resemble the primordial fragments postulated by Searle & Zinn. The apparent age range in the outermost halo could be explained as a consequence of this model: the timescale for growth of SGMCs should increase in the low-density outer regions of the Galaxy.

Côté et al. (2000b) proposed that the Galactic bulge may have formed as the dominant building block of the proto-Galaxy with its own original complement of metal-rich globular clusters[5]. Their Galaxy formation picture incorporates a halo constructed by numerous ($\sim 10^3$) disrupted proto-Galactic fragments, the more massive fragments having spawned the metal-poor globular clusters.

In addition to the globular star clusters, the most notable inhabitants of the outer Galactic halo are the dwarf galaxies. In particular, there are observed signs of disruption of the Sagittarius dwarf galaxy within the bounds of the Milky Way, implying

[5] There is an observed relationship between galaxy luminosity and the mean metallicity of its GCS (e.g. Brodie & Huchra 1991).

that satellite accretion may be an important and ongoing process (Ibata et al. 1994, 1997). There are four globular clusters which are believed to be associated with the Sagittarius dwarf galaxy based on their spatial position and kinematic properties. These clusters have a large spread in ages (van den Bergh 1998), a fact which seems to link the formation of the Sagittarius dwarf to the outer halo of the Milky Way.

1.4.3 Other Scenarios

Is it possible that the Galaxy formed entirely from either a rapid radial collapse or random accretion? There is considerable evidence that supports the idea that the Milky Way halo formed at least in part in a hierarchical or episodic manner. To summarize, this evidence includes the lack of a significant abundance gradient throughout the *entire* Galactic halo (Parmentier et al. 2000), a notable decrease in the radial component of the velocity ellipsoid of the stellar halo beyond the solar circle (Sommer-Larsen et al. 1997), the detection of a possible spread in cluster and stellar ages within the outer halo (Sarajedini et al. 1997; Rosenberg et al. 1999; Stetson et al. 1999), the detection of stellar and globular cluster streams (e.g. Mathewson, Schwarz & Murray 1977; Majewski 1994; Lynden-Bell & Lynden-Bell 1995; Bullock, Kravtsov & Weinberg 2001) and the apparent disruption of the Sagittarius dwarf galaxy in the halo of the Milky Way (Ibata, Gilmore & Irwin 1994; Dohm-Palmer et al. 2001).

Mateo (1996) discussed the possibility that the Galactic halo was formed in its entirety from the accretion of dwarf satellites. Mateo compared the stellar populations, variable stars, globular clusters and dark matter content of the present-day dwarf galaxies and the Galactic halo, and was unable to rule out such a formation scenario based on the available data. It is possible that a significant portion of the Milky Way halo could have formed from galaxies similar to the current complement of local dwarf galaxies (Unavane, Wyse & Gilmore 1996; although see also van den Bergh 1994).

A hybrid of the ELS infall and SZ merger models for galaxy formation is certainly plausible. The Galactic stellar halo is radially anisotropic within the solar circle, but changes to tangential anisotropy at large radii (Sommer-Larsen et al. 1997). The inner halo is flattened with a prograde rotation of 30 to 50 $\mathrm{km\,s^{-1}}$(Sommer-Larsen et al. 1997; Chiba & Beers 2000). If the Milky Way formed solely from a radial infall, one would expect the entire halo to demonstrate radial anisotropy. The kinematics of the outer halo are therefore consistent with a random merger scenario, while the radial anisotropy of the inner halo hints at a dissipational collapse. This line of evidence suggests that a complete picture of the formation of the Galaxy requires a possible merger of both the collapse and accretion scenarios. The inner halo may have formed from a rapid, dissipative collapse of gas, while the outer halo may have been largely built from the random accretion of fragments.

In an effort to explain the observed properties of massive early-type galaxy GCSs such as their multimodal metallicity distributions, GC population sizes and spatial densities, Forbes, Brodie & Grillmair (1997) proposed that the majority of globular clusters formed *in situ* in two phases. In this scenario, the metal-poor clusters formed within the early collapse of the protogalaxy, while a second (and possibly third) episode of star formation yielded later generations of clusters from enriched gas. The detailed mechanism by which these later episodes of star formation could have been sparked remains unclear.

Galaxies do not generally form and evolve in splendid isolation; interactions and mergers can seriously complicate the evolutionary history of many systems. There is evidence for the formation of young globular clusters in merger remnants (e.g. Schweizer & Seitzer 1993; Whitmore & Schweizer 1995). HST observations have lent further credibility to the theory of hierarchical formation through galaxy mergers in the early Universe. Pascharelle et al. (1996) detected a group of high-redshift galaxies which are apparently in the process of merging to form a larger galaxy.

Ashman & Zepf (1992) suggest that at least some fraction of a globular cluster system is formed during spiral-spiral mergers or interactions. They use this mechanism to explain the overly-populous GCSs of some large galaxies in the centres of galaxy clusters, as well as the larger GC populations of elliptical galaxies compared to spiral (the thinking being that at least some elliptical galaxies are the result of mergers between gas-rich spiral galaxies). A number of interesting counter-arguments to the Ashman & Zepf galaxy merger model are discussed by Forbes, Brodie & Grillmair (1997).

It may also be possible to explain the bimodality detected in GC metallicity distributions without relying on GC formation in mergers or additional bursts of star formation. Côté, Marzke & West (1998) argued that the capture of globular clusters by giant elliptical galaxies either through mergers or tidal stripping provides a good match to the observed properties of their GCSs. In this scenario, the metal-rich GCs represent the original population of the luminous host galaxy, whereas the metal-poor component is captured during the natural evolution of cluster galaxies.

Persuasive evidence which would allow us to distinguish between the various formation models — or indeed to suggest a clear hybrid of (or alternative to) the classical formation scenarios (e.g. van den Bergh 1996) — is unfortunately lacking. It is clear that an extensive database of high-precision data for the kinematic and chemical tracers of a large number of host galaxies would provide useful ammunition in our efforts to solve this currently intractable problem of galaxy formation.

From an observational perspective, our position in the disk of the Milky Way is both an advantage and a disadvantage. It permits a close-up look at the stars of the solar neighbourhood, a stellar component which might otherwise be too faint or obscured from view in distant galaxies. However, our location prevents us from obtaining a full portrait of the overall structure of the Galaxy. Interstellar absorption adds to our troubles, hindering observations in the disk at optical wavelengths.

Nearby galaxies often provide us with a much better look at the overall structure of galactic systems, but the finer details of their stellar systems are rarely discernible. Globular clusters are among the most luminous, ancient galactic residents. As the relic survivors of galaxy formation, globular clusters therefore allow us to probe the early processes which shaped their host galaxies. In this respect, the globular cluster system of the nearby Andromeda Galaxy provides us with an ideal target of study.

2. TARGET AND METHOD: PROBING THE M31 GLOBULAR CLUSTER SYSTEM

2.1 The Andromeda Galaxy (M31)

The Andromeda Galaxy — also known as M31 and NGC 224 — has long provided astronomers with an excellent target for the investigation of the structure, dynamics, and stellar content of external galaxies. Its proximity and size make the components of this galaxy readily accessible for observation. M31 provides a nearby look at a spiral galaxy from which much can be learned of other spirals, such as our own Milky Way.

M31's rich history of study has generated a considerable amount of data. Below, a few key aspects of this galaxy's structure are presented, with a particular emphasis on its globular cluster system. For a more comprehensive description of the extensive research which has been done on M31, the reader is directed to the book *The Andromeda Galaxy* by Hodge (1992).

2.1.1 General Attributes

The Milky Way and M31 are the two dominant galaxies located in a loose collection of galaxies known as the Local Group. Each of these massive galaxies has its own complement of dwarf galaxies; M31's dwarf satellites in particular will be discussed in Chapter 7. The Andromeda Galaxy is approaching the Milky Way at a rate of roughly 60 $\mathrm{km\,s^{-1}}$, and these two large systems may eventually merge (Dubinski, Mihos & Hernquist 1996; Forbes et al. 2000).

Table 2.1: Andromeda Galaxy general properties

Parameter	Value
Right Ascension (α_{B1950})	$00^h40^m00^s.1$
Declination (δ_{B1950})	$+40°59'43''$
Morphological type	SAb
Distance[a]	770 kpc
Apparent V magnitude[b]	4.16 ± 0.19
Total $(B-V)$ colour	0.92 ± 0.02
Angular diameter	$190' \times 60'$
Position angle[c]	$38°$
Inclination angle[c]	$77.7°$
Heliocentric Radial Velocity (v_r)	-300 ± 4 km s^{-1}

a) Freedman & Madore 1990; b) Hodge 1992 and references therein; c) Kent 1989.

The basic components of M31 are very similar to those of the Milky Way: it has a bulge, disk, halo and a relatively large population of globular clusters. Table 2.1 provides a list of M31's general parameters (with data from de Vaucouleurs et al. 1991 (henceforth RC3) and NED[1], except where specified otherwise). The orientation and tilt of the disk of the galaxy respect to our line of sight are demonstrated schematically in Figure 2.1.

2.1.2 The Disk of M31

M31 has an exponential disk $\sim$ 0.8 kpc thick which accounts for most of the galaxy light (de Vaucouleurs 1958). The luminosity distribution and colour-magnitude diagrams for the field stars in the disk of M31 are similar to those of the solar neighbourhood within the Milky Way (Hodge & Lee 1988). Hydrogen gas is concentrated in a thin disk which extends out to a radius of roughly 40 kpc from the galaxy centre (Hodge 1992). A number of studies have probed the neutral hydrogen (HI) content

[1] The NASA/IPAC Extragalactic Database, operated by the Jet Propulsion Laboratory, California Institute of Technology, under contract with the National Aeronautics and Space Administration.

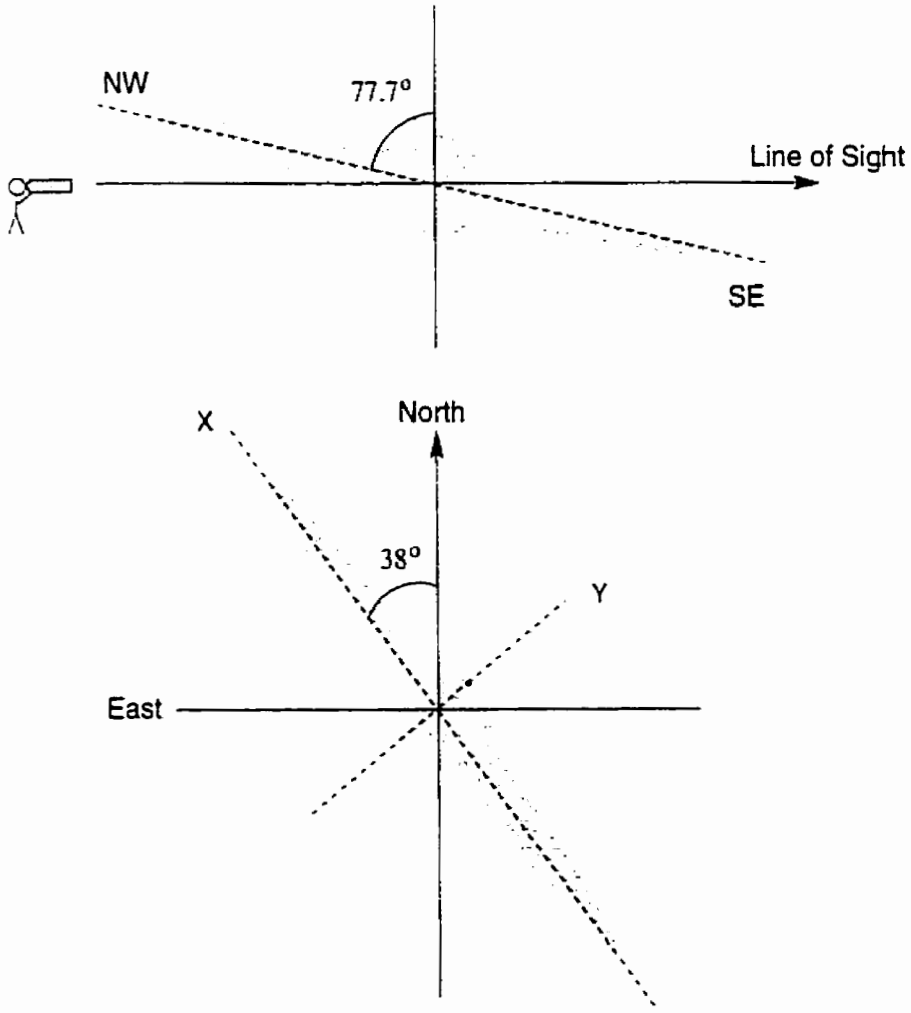

Figure 2.1: Sketches showing the orientation of the disk of M31. The drawing at the top demonstrates the inclination of the galaxy with respect to the line of sight. The hatched area represents positions at which objects will suffer greater obscuration and reddening due to the disk of the galaxy. The lower drawing shows M31's position angle on the sky, with the line of sight directed into the page.

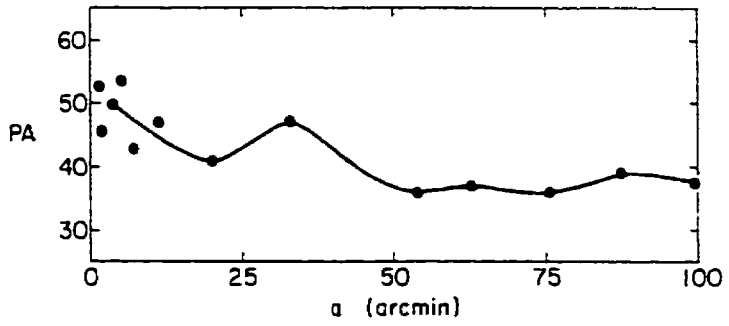

Figure 2.2: The observed variation in position angle of ellipses fit to the isophotes of M31 (reproduced from Hodge & Kennicutt 1982).

of M31 and have led to the recognition of the galaxy's spiral arm structure (Cram, Roberts & Whitehurst 1980; Sofue & Kato 1981; Braun 1990). It has been suggested that the spiral pattern in M31 may have been both created *and* distorted by an interaction with its nearby satellite, M32 (Braun 1991).

The interstellar medium within the disk of M31 incorporates a substantial amount of dust. A study of the differential reddening in M31's GCS by Iye & Richter (1985) revealed that the clusters on the northwest side of the galaxy are more severely reddened than those on its southeast side, an indication that the northwest side of the disk is closer to us along the line of sight (see upper diagram in Figure 2.1).

A plot of the variation in the position angle of elliptical isophotes fitted to the surface brightness of M31 as a function of galactocentric distance is shown in Figure 2.2. Position angle (PA) refers to the angle measured eastward of north to the major axis of the ellipse (see lower sketch in Figure 2.1). HI studies and optical surface photometry have both revealed a warp in the disk of M31, resulting in a change in the position angle of the light distribution beyond $\sim$ 100 arcminutes (Walterbos & Kennicutt 1988).

Rotation curves for M31 have been measured using velocities from HI (21 cm) emission and optical spectroscopy. Rubin & Ford (1970, 1971) compiled detailed rotation curves for the bulge and disk of M31 and found a maximum disk rotational

velocity of 270 ± 10 km s^{-1} at a galactocentric radius of roughly 10 kpc. The rotation curve remains flat out to large radii, a discovery which marked one of the early indications of the presence of massive dark halos in galaxies (see review in Rubin 1995). Based on fits of mass models to velocity measurements, Kent (1989) obtained a disk mass-to-light ratio of $M/L \sim 10$.

Josey & Arimoto (1992) described the formation of M31's disk in terms of a biased infall scenario (Larson 1976), proposing that its timescale of formation varied from 0.7 Gyr at the centre to 5 Gyr at a radius of 10 kpc. This model might account for the observed radial colour/metallicity gradients within the disk (Hoessel & Melnick 1980; Brewer, Richer & Crabtree 1995).

2.1.3 The Bulge of M31

The nuclear bulge of M31 contributes $30-40\%$ of the visual light of the galaxy. The effective radius of the bulge is 2.0 kpc, and its surface brightness profile is reasonably well represented by an $r^{1/4}$ law (Walterbos & Kennicutt 1988). The bulge is thought to be triaxial in shape due to the apparent position angle of its major axis of PA = 50°, significantly larger than PA = 38° found for the disk (Figure 2.2). This component may have been formed from gas which was ejected from stellar winds and supernovae based on its relatively high metal abundance (Walterbos & Kennicutt 1988; van den Bergh 1999).

HST observations of M31 by Lauer et al. (1993) revealed the presence of a double nucleus in the innermost regions of the galaxy. They suggested that the second component represents the remains of a galactic nucleus in the final stages of cannibalization by the M31 nucleus. There are strong indications of the presence of a massive ($\sim 3 \times 10^7 M_\odot$) black hole at the centre of M31 (Kormendy 1988; Tremaine 1995; Kormendy & Bender 1999). Spectroscopy of M31's double nucleus reveals a steep rise in the rotation curve and velocity dispersion, consistent with an eccentric disk of

stars orbiting a concentrated central mass. Numerical simulations by Bekki (2000) demonstrated that the present M31 nucleus could have been formed by a merger between a central black hole and a compact stellar system.

There is a steep initial rise in the rotation curve of the galaxy to a velocity of 270 $\mathrm{km\,s^{-1}}$ due to the rotation of the bulge (Kent 1989). The M31 bulge also has a relatively high velocity dispersion, measured at $\sigma_v = 156 \pm 23$ $\mathrm{km\,s^{-1}}$ (Lawrie 1983; see also Whitmore 1980 and references therein). Kent (1989) modeled the M31 bulge as an isotropic, oblate, rotating spheroid and estimated its mass to be $4.0 \times 10^{10}\,M_{\odot}$. This yields a mass-to-light ratio of $M/L \sim 5$, an indication that there is very little dark matter within the bulge of M31. Unlike the Milky Way, there does not appear to be a bar at the centre of M31 (Morrison 1996; although see Loinard et al. 1999).

2.1.4 The Halo of M31

M31 is surrounded by an extended halo of globular clusters and field stars. The M31 halo, like the bulge, is composed of predominantly old stars, indicating that star formation occurred early and rapidly within the protogalaxy. There are signs that the inner halo of M31 may be somewhat flattened, although the difficulty in distinguishing the separate components of the galaxy may complicate these results (Pritchet & van den Bergh 1994). Additional information on the stellar populations of M31 is available in a summary by van den Bergh (1991).

A recent publication by Durrell, Harris & Pritchet (2001) outlined a scenario wherein M31 formed via the gaseous amalgamation of dwarf-sized fragments which themselves underwent early star formation. The metal-poor halo stars and globular clusters could have originated from the early accretion of these fragments. The halo of the galaxy may have then proceeded to form stars and some of the more metal-rich GCs. They proposed that the inner metal-rich population formed from the infall of enriched gas towards the bulge.

2.1.5 M31 Mass Estimates

It is possible to infer the mass of a system based on the dynamics of its components. A number of studies have provided dynamical mass estimates for M31 out to various radii (see Table 8.1 of Hodge 1992, and Table 6 of Evans & Wilkinson 2000).

In a recent study, Evans & Wilkinson (2000) calculated the mass of the Andromeda Galaxy using the positions and radial velocities of its satellite galaxy companions, outer globular clusters and planetary nebulae to probe the gravity field at large radii. Approximating the halo by an isotropic velocity distribution, their model yielded a galaxy mass of $M_{M31} \simeq 12.3^{+18}_{-6} \times 10^{11}\, M_{\odot}$ and an extent of $\sim$ 90 kpc for the halo based on an adopted distance of 770 kpc to M31. Despite the large uncertainties, this value is almost certainly smaller than their mass estimate for the Milky Way of $M_{MW} \simeq 19^{+36}_{-17} \times 10^{11}\, M_{\odot}$, which itself has a total expanse of $\sim$ 170 kpc.

Côté et al. (2000) presented a mass determination of M31 based on the dynamics of its dwarf satellites at de-projected galactocentric distances of $100 \lesssim R_{gc} \lesssim 500$ kpc. They found a mass of $M_{M31} \simeq (7.9 \pm 0.5) \times 10^{11}\, M_{\odot}$ under the assumption of isotropic orbits, in reasonable agreement with the Evans & Wilkinson result.

2.2 The Particular Interest: M31's Globular Cluster System (GCS)

The particular interest of the current study is the globular cluster system of M31. An analysis of the kinematics and abundances of a large sample of the M31 GCS will be performed within the context of the galaxy formation scenarios discussed in Chapter 1. A brief summary of the significant works which have contributed to the identification and study of the M31 GCS will now be presented. Following that, a justification of the target selection and an outline of the methodology will be given.

2.2.1 Previous Investigations

In a pioneering study in 1932, Hubble was the first to identify globular clusters in M31 based on their photometry and structure. Hubble found 140 objects which had the appearance of "nebulous stars" resembling the most condensed of the Milky Way globular clusters known at that time. On the basis of their number and spatial distribution, Hubble proposed that these globular nebulae were associated with M31 itself. To serve as further evidence of this association, Hubble cited the observation[2] that a "typical example" of one of these objects (his No. 62) had a radial velocity of $-210\ \mathrm{km\,s^{-1}}$. The uncertainty on this result was of order $100\ \mathrm{km\,s^{-1}}$, making it consistent with M31's systemic velocity of $-300\ \mathrm{km\,s^{-1}}$.

Early investigations of the globular clusters of M31 were performed by Seyfert & Nassau (1945), Mayall & Eggen (1953), Hiltner (1960), Kron & Mayall (1960) and van den Bergh (1969). Significant attempts to catalogue the positions and magnitudes of a growing number of M31 cluster candidates were made by Vetešnik (1962) and Sargent et al. (1977). Sargent et al. listed 355 globular cluster candidates based on photographic observations from the 4-m telescope at the Kitt Peak National Observatory.

Subsequent searches have added more GCs to this list, revealing an M31 cluster population roughly three times the size of the Milky Way GCS. As part of a major photographic survey in search of more M31 globular cluster candidates, Battistini et al. (1980, 1987, see also Buonanno et al. 1982) published a catalogue of 353 "probable" clusters found within a $3^\circ \times 3^\circ$ area centred on the galaxy (the *Bologna Catalogue*, see review by Fusi Pecci et al. 1993). Their list also included positions for more than 150 additional "plausible" candidates. The Bologna group later identified several more GC candidates within the inner regions of M31 (Battistini et al. 1993).

[2] Based on a spectrum obtained by M. L. Humason using a small-scale spectrograph and the 100-inch reflector at Mount Wilson.

A photographic and spectroscopic study by Crampton et al. (1985) added 109 new GC candidates around M31, and provided intrinsic colour estimates for a large sample of the Bologna Catalogue objects. A lengthy series of papers by Sharov & Lyutyi (1983 compilation) and Sharov, Lyutyi & Esipov (1983, 1984, 1987, 1995, 1996) have provided photoelectric photometry for various samples of M31 globular clusters. CCD (charge-coupled device) photometry published by Racine (1991), Racine & Harris (1992), and Reed, Harris & Harris (1992, 1994) has further improved upon the sample of candidate magnitudes and colours, also permitting a better culling of non-clusters from the database. Other studies have discovered dozens of additional candidates (Aurière, Coupinot, & Hecquet 1992; Mochejska et al. 1998), and further M31 globular cluster searches are ongoing (Lee et al. 2001).

A relatively small sample of the M31 globular cluster system has also been observed in the near-infrared (Frogel, Persson & Cohen 1980; Sitko 1984; Bònoli et al. 1987, 1992; Cohen & Matthews 1994). A recent publication by Barmby et al. (2000) presented a compilation of the current best list of photometry for the M31 GCS, bringing the tally to 435 clusters and cluster candidates. Barmby et al. have also added to or improved upon the existing photometry of several hundred of these objects in both the optical and near-infrared.

The M31 GCS has also been well-studied spectroscopically, yielding cluster line-of-sight velocities and abundance estimates to varying degrees of precision. Measurements and analyses of the heliocentric radial velocities and absorption line strengths of $\sim$ 150 M31 globular clusters have been published based on the substantial works of Huchra, Stauffer & Van Speybroeck (1982), Brodie & Huchra (1990, 1991), Huchra, Brodie & Kent (1991), and Huchra et al. (1996). Radial velocities for 65 clusters have also been provided by Federici et al. (1990, 1993), with roughly 40% of their targets overlapping with the Huchra et al. samples. Two high-resolution spectroscopic studies have provided precise velocities for a handful of M31 globular clusters: Peterson

(1989: 14 GCs) and Dubath & Grillmair (1997; 9 GCs).

Considering the now-sizeable database of globular cluster candidates, however, the M31 GCS has suffered a surprising lack of spectroscopic observations.

2.2.2 *Method: Spectroscopy of the M31 GCS*

Spectroscopy can provide us with critical insights into the properties of stars and stellar systems[3]. It allows us to investigate the chemical composition of objects as well as measure their radial velocities. Changes in chemical composition of globular clusters in particular are closely tied with galaxy formation and evolution. To a large extent, the kinematics of these ancient stellar systems reflect the initial conditions and the physical processes which occurred within the forming protogalaxy. The dynamical state of a GCS also permits a glimpse at the underlying mass distribution of its parent galaxy. It has been noted often that globular clusters make ideal probes of galaxy structure and formation mechanisms, and that they hold the key to uncovering the fossil record of their parent galaxy.

The radial velocity of a target can be measured by cross-correlating its spectrum with that of a template object of known velocity, and determining the Doppler shift (Tonry & Davis 1979). The metal abundance of a target is obtained from the strengths of absorption or emission features in its spectrum. *Metallicity* generally refers to the logarithmic abundance of iron relative to hydrogen as expressed in term of solar abundance:

$$[\mathrm{Fe/H}] = \log \frac{N_{\mathrm{Fe}}}{N_{\mathrm{H}}} - \log \left(\frac{N_{\mathrm{Fe}}}{N_{\mathrm{H}}} \right)_{\odot} \tag{2.1}$$

The primary difference between globular cluster integrated spectral types lies with metal abundance, yet there is some age dependence. Metal-poor GCs can have metallicities as low as $[\mathrm{Fe/H}] \simeq -2.5$, while the most metal-rich GCs have values approaching solar ($[\mathrm{Fe/H}] = 0$). There are metal-rich stars in the bulge with metallicities as

[3] Information on the history of spectroscopy can be obtained in the delightful summary by Rubin (1995) and the work of Hearnshaw (1986).

high as [Fe/H] = +1. Younger stars tend to be somewhat more metal-rich on average, yet there is a sizeable spread in [Fe/H] for any given age. Stars with ages $\gtrsim$ 10 Gyr are relatively metal-poor, with [Fe/H] ≤ -0.5. Stars younger than $\sim$ 5 Gyr generally have [Fe/H] $\gtrsim -0.5$, having been formed from the material enriched by nucleosynthesis within previous generations of stars.

Difficulties arise in defining a mean metallicity of composite systems such as globular clusters. It becomes necessary to define a class of features present in the integrated spectra of late-type (old) stellar systems which provide sensitive gauges of mean chemical abundance. The relative strengths of these line indices will be used to intercompare and rank the members of the M31 GCS in this study. Since most of the spectral features studied will not directly measure the abundance of iron (N_{Fe}) or hydrogen (N_H), an estimate of [Fe/H] is made based on calibrations with local objects.

The Milky Way's globular cluster system has so far been the only one for which we have been able to obtain detailed kinematic, chemical, and age information. Unfortunately, our Galaxy is home to a mere 150 or so globular clusters, many of which suffer from line-of-sight problems and significant distance uncertainties. The M31 GCS, however, provides us with an obvious and desirable sample:

1. M31's proximity (770 kpc) makes it the most accessible large system outside of the Milky Way.

2. With roughly 435 confirmed candidate members (Barmby et al. 2000), the M31 GCS is sufficiently populous that it provides a more statistically significant sample size.

3. Unlike the Milky Way GCS, the M31 population can be observed over essentially the full extent of the galaxy, with less severe effects of contamination along the line of sight.

4. All of the M31 clusters lie at roughly the same distance, and are thus not subject to such large individual distance uncertainties as are the Galactic globulars.

Previous studies have uncovered both similarities and differences between the M31 and Milky Way globular cluster systems. Djorgovski et al. (1997) explored the correlations of various internal parameters for 21 M31 GCs with those of Milky Way clusters. Apparent correlations between projected central velocity dispersion and absolute cluster magnitude, central and half-light averaged surface brightness (in V and K bands) were found to be similar between the Milky Way and M31 globular cluster systems (see Figure 2 of Djorgovski et al. 1997). This would seem to indicate a common physical origin, and hence similar formation mechanisms in both galaxies. Djorgovski et al. claim that the observed correlations are more likely to have arisen from the conditions and physical processes at the time the clusters were formed rather than from dynamical evolution.

Frogel, Persson & Cohen (1980) verified that the broad-band optical and infrared colours of the Galactic and M31 globular cluster populations are indistinguishable. A later investigation by Elson & Walterbos (1988) also found no significant difference in the intrinsic UBV colours within the Milky Way and M31 cluster systems. A recent compilation of the available M31 globular cluster photometry by Barmby et al. (2000, 2001) revealed that the (projected) inner GCS of M31 is on average $V \sim 0.5$ mag brighter than its outer clusters. They also found a difference in the luminosity distribution of the M31 metal-rich and metal-poor clusters, such that the low-metallicity population is fainter by ~ 0.4 mag in V. Barmby, Huchra & Brodie (2001) attributed these differences to the effects of dynamical destruction within the inner galaxy, as well as to a younger mean age for their metal-rich cluster sample. The mean estimated age of a small sample of 12 M31 globular clusters studied by de Freitas Pacheco (1997) is 15 ± 2.8 Gyr, comparable to ages determined for Galactic globular clusters.

Existing spectroscopic results for the M31 GCS have also revealed some remarkable similarities with the Galactic population. Zinn (1985) found that the Galactic GCS demonstrated clear evidence for bimodality in its metallicity distribution, and proposed that it could be considered as two distinct subsystems: a flattened, metal-rich, rapidly-rotating, kinematically cold disk system, and a spherical, metal-poor halo with lower net rotation and higher velocity dispersion. Signs of bimodality have also been found in the M31 cluster metallicity distribution (Ashman & Bird 1993) and in metallicity-sensitive colour distributions (Barmby et al. 2000). Separating their sample of $\sim$ 150 M31 clusters into metallicity sub-systems along the same lines as the Milky Way GCS, Huchra, Brodie & Kent (1991) found that the metal-rich clusters within $R \sim 7'$ of the galaxy centre form a rapidly-rotating ($100-200$ km s^{-1}) disk-like system, whereas the metal-poor clusters within this radius exhibit no net rotation. Beyond this radius, they were unable to distinguish the metal-rich from metal-poor populations on the basis of kinematics.

In 1989, Armandroff confirmed the presence of a modest metallicity gradient within the disk clusters of the Milky Way. The first extensive spectroscopic survey of the M31 GCS was performed by van den Bergh (1969); van den Bergh found no significant metallicity gradient with position, but did report a wide range of abundances at any given radius (see also Spinrad and Schweizer 1972). More recently, Huchra et al. (1982, 1991) and Sharov (1988) have shown evidence for a weak but measurable metallicity gradient with projected radius within the M31 GCS. A similar finding was reported by Barmby et al. (2000) based on their large sample of metal-sensitive colours. Huchra, Brodie & Kent (1991) discovered a mean M31 GC metallicity of [Fe/H] $= -1.2$, slightly higher than that for the Milky Way.

Interestingly, the metallicity distribution of the globular cluster system in M31 also differs from that of its halo stars in the sense that the GCs are found to be systematically more metal-poor (van den Bergh 1969; Durrell et al. 1994, 2001). This

resembles the case in many giant elliptical galaxies but is dissimilar to the situation in the Milky Way, a fact which may point to a disparate origin for the halos of these neighbouring galaxies. The apparent deficiency in the luminosity distribution of metal-poor halo stars may indicate that significantly more chemical enrichment occurred in M31 prior to the formation of the bulk of the halo. Were these halo stars formed *in situ* or were they incorporated later à la Searle-Zinn?

2.2.3 Substructure in the M31 GCS?

In the hierarchical model of galaxy formation, one might reasonably expect to see some residual evidence of past formation activity, such as in star counts, kinematics, and metal abundances. Helmi & White (2001) performed simulations of satellite galaxy disruptions within a potential similar to that of the Milky Way. They found that after $\sim$ 10 Gyr, the maximum density of satellite debris was significantly lower than that of the progenitor and was comparable to the local density of the stellar halo. Little or no evidence remained of the spatial distribution of particles, although strong correlations did persist in velocity space. Stellar debris resulting from the disintegration of a dwarf galaxy with a low initial velocity dispersion ($\sim$ 10 km s^{-1}) can remain coherent along the satellite's orbital path over timescales of 10^9 yr (Johnston et al. 1995).

Not only have stellar streams been discovered within the Milky Way and, more recently, within M31 (Ibata et al. 2001b), but streams of *globular clusters* have also been found within the Milky Way halo GCS (Majewski 1994; Lynden-Bell and Lynden-Bell 1995). These could represent the remains of a galaxy formation era dominated by satellite accretion.

Two studies have uncovered tentative evidence for kinematic and chemical subclustering within the globular cluster population of the Andromeda Galaxy. A formidable effort by Ashman & Bird (1993) suggested the presence of significant substructure within the M31 GCS. Their analysis grouped globular clusters based on the

deviations from global mean velocities and velocity dispersions between each cluster and its N nearest neighbours. Ashman & Bird proposed that some fraction of the M31 halo GCS is clustered into small groups of half-a-dozen or so globulars each. They interpreted these cluster groups as being the surviving remnants of a hierarchical halo formation.

Saito & Iye (2000) reported the discovery of an inner subsystem of M31 globular clusters which distinguish themselves from the remainder of the GCS based on their kinematics, metal abundances (from Barmby et al. 2000), and spatial location. They postulated that this subsystem may have experienced a separate formation history, and perhaps resulted from the merger of a dwarf galaxy after the formation of the bulk of the M31 GCS.

Regrettably, we currently only have projected positions and line-of-sight velocities for a modest sample of clusters. Furthermore, the uncertainties associated with existing GC velocities and metallicities are, in many cases, prohibitively large. In light of these limitations, we must approach such grouping analyses with trepidation. Are these *bona fide* GC groups that are physically associated? Do they represent the relic globular cluster systems of accreted dwarfs? Is it even reasonable to be searching for residual evidence of cannibalized fragments within the globular cluster systems of massive galaxies like M31? These are all valid questions.

The M31 globular clusters provide us with ideal targets for a statistically meaningful study of galaxy formation and evolution scenarios. Clearly, an expanded and improved database of cluster velocities and abundances is required in order to provide a more comprehensive examination of the kinematics and abundance properties of the M31 globular cluster system. Two large sets of spectroscopic observations of M31 GCs have been obtained with this objective: 288 targets were observed using the WYFFOS spectrograph at the William Herschel Telescope, and 198 clusters were observed at the Canada-France-Hawaii Telescope using the MOS/ARGUS integral

field spectrograph. These data sets and the analysis thereof are described in the upcoming chapters. The final sample of M31 GCS data will be examined for signs of distinct metallicity populations, gradients, kinematic anomalies and substructure which, if present, may point to the formation and enrichment processes which have occurred in M31.

3. THE WHT SPECTRA: DATA ACQUISITION AND ANALYSIS

3.1 The WYFFOS Observations

A large sample of M31 globular clusters were observed at the William Herschel 4.2 m telescope[1] (WHT) in La Palma, Canary Islands, during the four nights of November 3 to 6, 1996 (observer: Terry Bridges). The WYFFOS Wide Field Fibre Optic Spectrograph (Bridges 1998) was used with two gratings to provide a total spectral coverage of $\sim$ 3700 – 5600 Å. The H2400B 2400-line grating yielded a dispersion of 0.8 Å/pixel and a spectral resolution of 2.5 Å over the range 3700 – 4500 Å. This wavelength range was selected to investigate the CN feature at 3883 Å, the H & K lines of calcium, Hδ, the CH G-band and the 4000 Å continuum break. The numerous lines in this spectral range facilitated the velocity determinations via cross-correlation (Section 4.1.1). The R1200R 1200-line grating observations had a dispersion of 1.5 Å/pixel and a resolution of 5.1 Å over the spectral range 4400–5600 Å to add absorption features such as Hβ, the Mgb triplet and two iron lines near 5300 Å. Magnesium and iron lines typically serve as good indicators of metallicity, while the Hβ line is a known age discriminator (e.g. Brodie & Huchra 1990; Worthey 1994).

[1] Operated by the Isaac Newton Group in the Spanish Observatorio del Roque de los Muchachos of the Instituto de Astrofisica de Canarias.

3.1.1 Target Selection and APM Coordinates

Targets were selected from the Battistini et al. (1980, 1987, 1993) sample of M31 globular cluster candidates, with some additional central targets from unpublished CCD photometry by John Huchra (private communication). The Battistini et al. best sample includes 341 globular cluster candidates down to a limiting magnitude of $V = 18$ and out to a galactocentric radius of about 25 kpc: of these, 257 are *confirmed* clusters as determined from high-resolution spectroscopy, image structure, and/or photometric colours.

Cluster positions accurate to 0.2 arcsec were determined from automatic plate-measuring machine (APM) scans of deep photographic plates of a $6° \times 6°$ area around M31. The plates were obtained by Mike Irwin and were analyzed by Terry Bridges. The APM facility is run by the Institute of Astronomy in Cambridge and uses a fast laser microdensitometer to obtain accurate astrometry. The accuracy of these APM cluster coordinates represents a significant improvement over preexisting M31 GCS positions, which have typically been measured to the nearest arcsecond.

Galactocentric coordinates for the GCs were derived from standard spherical trigonometry, using an adopted M31 central position of $\alpha_0 = 00^h40^m00^s.1$, $\delta_0 = +40°59'43''$ (B1950):

$$\begin{aligned} X &= C_1 \sin(PA) + C_2 \cos(PA) \\ Y &= -C_1 \cos(PA) + C_2 \sin(PA) \\ C_1 &= [\sin(\alpha - \alpha_0)\cos\delta] \\ C_2 &= [\sin\delta\cos\delta_0 - \cos(\alpha - \alpha_0)\cos\delta\sin\delta_0] \end{aligned} \tag{3.1}$$

The X coordinate represents the position along the major axis of the galaxy, increasing towards the northeast along the major axis. The Y coordinate is the distance from the major axis above and below the galactic plane, with positive values towards the northwest. Target right ascensions (α) and declinations (δ) were converted into

Table 3.1: Target catalogue references

Code	Reference
B	Battistini et al. 1980, 1987
S	Sargent et al. 1977
BA	Baade & Arp 1964
BoD	Battistini et al. 1987 (Table VI)
DAO	Crampton et al. 1985
NB	Battistini et al. 1993
V	Vetešnik 1962

degrees, and the position angle (PA) of the major axis was taken to be 38° (Kent 1989).

Numerous groups have contributed to the identification of the globular cluster members of M31 (e.g. Hubble 1932; Vetešnik 1962; Baade and Arp 1964; Sargent et al. 1977; Crampton et al. 1985; Battistini et al. 1980, 1987, 1993). The ultimate result of this combined effort is that most of the clusters are known by more than one name, a fact which has the potential to cause confusion. The letters preceding the identification number in the M31 target names given hereafter indicate the relevant catalogue reference provided in Table 3.1.

3.1.2 WYFFOS Fields

At the WHT, six different WYFFOS fibre configurations were selected in order to target a total of 288 globular cluster candidates over the full extent of the major axis of M31. There are 114 active fibres within the 1° WYFFOS field, each of which subtend an angle of 2.7 arcsec. For comparison, the M31 globulars subtend angles of $2-3$ arcsec, an excellent match for this instrument. An overlay of the WYFFOS target fields is shown on a Digitized Sky Survey[2] optical image of the galaxy in

[2] The Digitized Sky Survey was produced at the Space Telescope Science Institute under U.S. Government grant NAG W-2166. The images of these surveys are based on photographic data obtained using the Oschin Schmidt Telescope on Palomar Mountain and the UK Schmidt Telescope.

Table 3.2: WHT observing log

Field ID	α_{B1950}	δ_{B1950}	Night	UT	Exp (sec)	Grating
Central 1	00:40:00.18	+40:59:59.9	Nov. 3/4	21:00	6 × 1800	H2400B
Central 1	00:40:00.43	+41:00:00.5	Nov. 3/4	00:43	3 × 1200	R1200R
Northeast 1	00:42:29.88	+41:36:02.0	Nov. 4/5	21:52	6 × 1800	H2400B
Northeast 1	00:42:29.88	+41:36:01.1	Nov. 4/5	01:22	3 × 1200	R1200R
Southwest 1	00:37:30.15	+40:24:01.7	Nov. 5/6	19:32	3 × 1200	R1200R
Southwest 1	00:37:30.51	+40:24:00.0	Nov. 5/6	20:42	4 × 1800	H2400B
Northeast 2	00:44:59.97	+42:11:53.4	Nov. 5/6	23:43	5 × 1800	H2400B
Northeast 2	00:45:00.70	+42:11:56.3	Nov. 5/6	02:40	3 × 1200	R1200R
Central 2	00:39:59.20	+41:00:05.2	Nov. 6/7	19:26	3 × 1200	R1200R
Central 2	00:39:59.34	+41:00:03.7	Nov. 6/7	20:38	4 × 1800	H2400B
Southwest 2	00:34:59.80	+39:47:54.6	Nov. 6/7	23:33	5 × 1800	H2400B
Southwest 2	00:35:00.56	+39:47:54.6	Nov. 6/7	02:25	4 × 1200	R1200R

Figure 3.1. Spectra of twilight flats, argon emission lamps, and velocity template stars were also obtained during the same nights in each fibre configuration for the purposes of calibration. A log of the field observations is provided in Table 3.2, and a full target list is given in Table A.1.

The output from each WYFFOS fibre is individually routed to the CCD via the collimator, grating and correctors (see Pollacco et al. (2000) for more information on the WYFFOS system). In the output image, the dispersed fibre light is stacked horizontally, with lower fibre numbers to the right of the image. A sample frame is shown in Figure 3.2. The dispersion axis lies vertically with blue wavelengths at the top and red wavelengths towards the bottom of the frame.

3.2 Data Reduction

This section details the image processing steps which were necessary to produce the final target spectra. The raw frame constitutes an array of data values or "counts" which are themselves proportional to the number of photons detected at each CCD

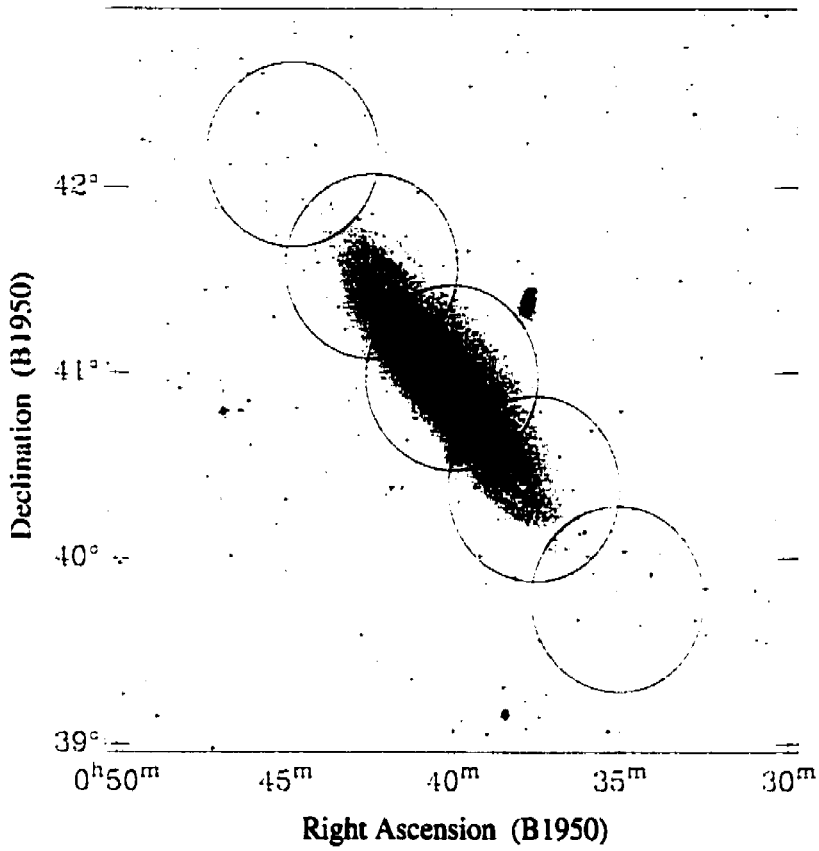

Figure 3.1: Five 1° WYFFOS fields shown superimposed over an optical image of M31 from the Digitized Sky Survey. Two central fibre configurations were used to yield spectral observations for a total of 288 cluster candidates in six fields. North is to the top, east is towards the left.

pixel position during the image exposure.

The data reduction included frame preprocessing, fibre throughput corrections, spectral extraction, sky subtraction and wavelength calibration. These steps were accomplished using the standard Solaris and Linux implementations of IRAF[3], as well as the **wyf_red** WYFFOS Multi-fiber IRAF package written by Jim Lewis (see Lewis 1996 for more information).

[3] Image Reduction and Analysis Facility, distributed by the National Optical Astronomical Observatories, which is operated by AURA under contract with the NSF.

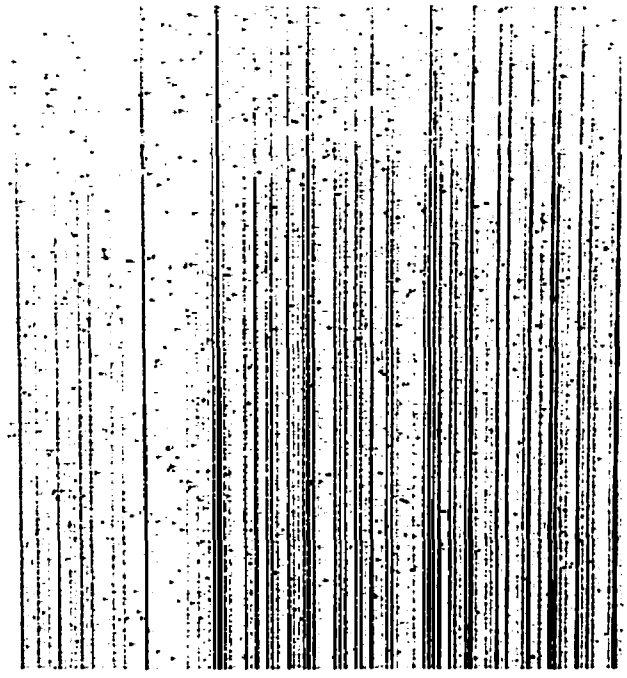

Figure 3.2: A sample exposure of M31's central field obtained with the WYFFOS system at WHT. The dispersion axis is vertical, with blue wavelengths at the top and red at the bottom. Fibre numbers increase to the left of the CCD image.

3.2.1 Frame Preprocessing

Preprocessing of the raw frames included bias subtraction and division by a scaled dome flatfield exposure. After the preprocessing stage, zero counts on the data frame should correspond to zero light on the CCD, and the pixels should be uniformly sensitive.

Bias Subtraction

The bias level includes a constant additive offset which may vary from frame to frame, as well as a fixed-signal pattern which can normally be considered to be constant along one of the image dimensions (i.e. varying only along the columns of the chip). The bias offset is imposed to ensure that the CCD chip is operating in a linear regime, and to preclude the readout of statistically feasible negative data values in regions

of low photon counts. The bias pattern is a result of the readout noise associated with the CCD electronics. The bias subtraction step is aimed at removing any signal registered by the detector in the absence of exposure to light.

Traditionally, there are two ways to determine the bias level of a raw CCD frame. One is to obtain a series of zero-length exposures (typically 10 to 20) and average these to reduce the statistical (readout) noise introduced by this step to a negligible value. The mean frame thus created is then subtracted from every image, pixel by pixel. This is the method to use if there is structure in the bias level across the chip. The second method is to determine the mean bias level from the overscan region of each image and subtract this as a constant from the rest of the frame. Full bias frames were unnecessary using the WYFFOS configuration at WHT (Terry Bridges, WYFFOS Project Scientist, private communication) and were not obtained. The mean bias level for each WYFFOS frame was determined from the overscan strip and was subtracted from each of the image frames.

A Note on Flatfielding

In general, a flatfield image is used to correct for pixel-to-pixel sensitivity variations in the detector, as well as to compensate for the effects of vignetting and other large-scale response variations. For broadband observations, a flatfield image can be obtained by taking an exposure of a uniform continuum light source such as the illumination of the interior of the observatory dome by an incandescent lamp. The variation in the image of a uniform light source maps out the changes in sensitivity across the chip, which can then be divided out of the frame.

No conventional flatfield images were obtained during the WYFFOS run. Instead, the removal of sensitivity variations was performed using the throughput correction images in the following manner. Offset frames were obtained during the night by slewing the telescope off of the field and integrating for a few hundred seconds, ideally

capturing no bright objects in any of the fibres. Several such offset exposures were obtained of the dispersed light at slightly different pointings, well away from the variable background of the galaxy. These offset images were used to scale the fibres to the same level by taking into account the relative throughputs of each fibre as well as any vignetting across the field. It was therefore essential that the fibres in the offset image be in the same configuration as in the science frames so as to fall on the same area of the CCD. The relative fibre response is independent of wavelength, and thus did not depend on the grating used. Note that this method of flattening does not remove the broad instrumental signature in the images, something which is generally accomplished with flux calibration when required.

3.2.2 Aperture Extraction

A critical step in the reduction of multi-fibre data is the aperture definition: locating the position of each spectrum in the image frame, determining the spread along the spatial axis and the distortion along the dispersion axis. At this stage of the reduction, it should be noted that spatial and wavelength information in the preprocessed image are only approximately constant along image rows and columns. Curvature and distortions are evident in the frames; these can be due to imperfections or slight misalignments in the optics of the spectrograph or CCD and differential refraction in the Earth's atmosphere. These effects are most pronounced near the edges of the frame.

To resolve this problem, aperture reference images were used to identify and trace the shape of the spectra on the CCD. These reference frames consisted of twilight sky images that were recorded at the beginning of each night of observation to provide high signal-to-noise spectra with all usable fibres uniformly illuminated.

The geometry of the WYFFOS images is such that the dispersion direction lies (roughly) along the vertical axis with blue wavelengths at the top of the image and

red at the bottom. The spatial axis is horizontal, and the centre of each individual spectrum can be located by determining the row of peak intensity in the aperture reference image. This aperture definition was performed interactively with the `apfind` IRAF task which is embedded in the `wyf_red` reduction script. The software interactively identified a specified number of apertures as roughly evenly-spaced peaks in a horizontal cut across the middle of the dispersion axis. A sample portion of an aperture reference frame cross-section is shown in Figure 3.3. The aperture identifications were cross-referenced with the image header information for record-keeping in order to keep track of fibre placement (target allocation) and status information.

The size of the extraction aperture was set by the width at which the spatial profile decays to 10% of the peak value. Similarly, a background window several pixels wide was specified on either side of the central row of the profile. The median of three adjacent points were taken within each background sample to determine the value of the background to fit with a first order Chebyshev function; this was done in an effort to weed out cosmic ray features. Both the extraction and background regions were examined with the aperture editor, a graphic display showing a cut through the data frame along the spatial axis (Figure 3.3). The aperture designations were altered interactively to recentre or resize them, as required.

In practice, the spectra are never perfectly aligned with the CCD columns. The location of the peak row of the spatial profile gets shifted slightly along the columns. Such distortions are especially apparent in the apertures on either edge of the example frame shown in Figure 3.2. This effect can be due to field distortions resulting from the optics of the instrument or if the grating was not sitting perfectly squarely in the light path. The deviation will thus depend on wavelength, wavelength coverage, airmass and orientation of the fibre bundle. The principal effect of such a misalignment along the dispersion axis is a broadening of the spectral lines due to the shift in wavelength on either side of the aperture centre. To compensate for this effect, the centre of the

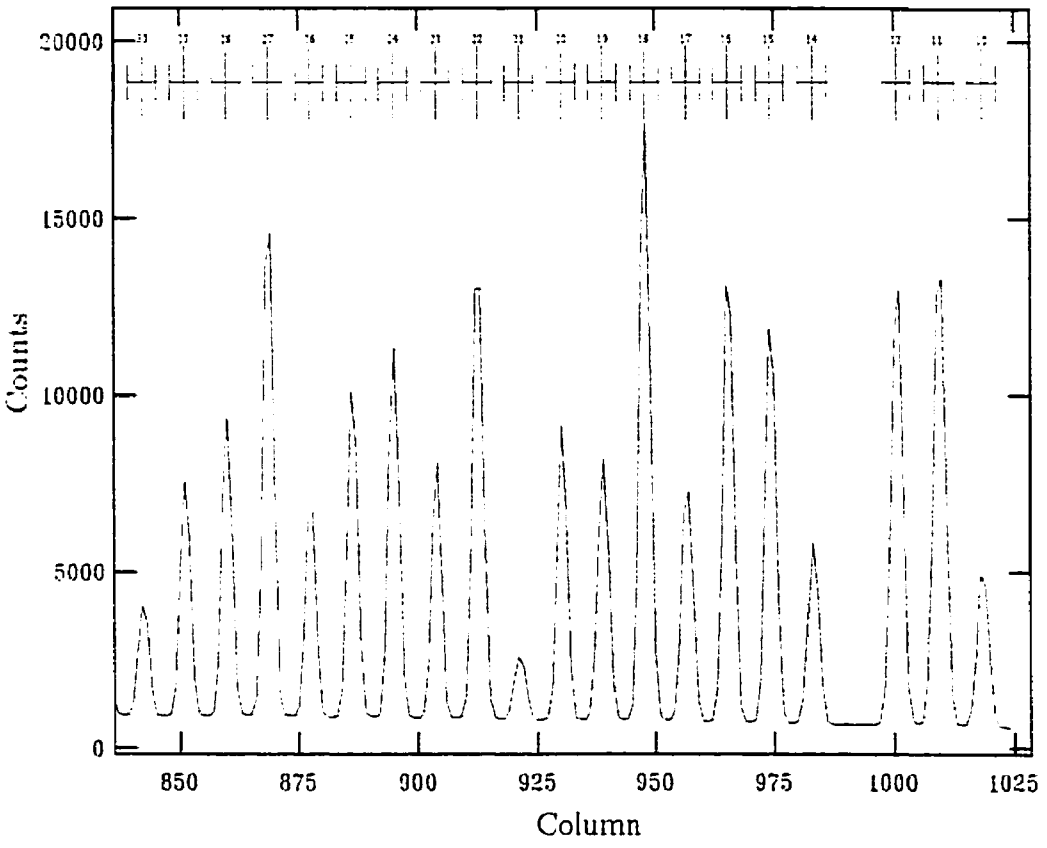

Figure 3.3: A section of an aperture reference image showing (at the top) the centres and widths of some of the apertures identified for extraction.

spatial profile was traced along the dispersion direction using the aptrace task in IRAF. A smooth function (a Legendre polynomial) was interactively fit to the set of peak positions along the dispersion axis in the aperture reference image. This fit was used to determine the shift in aperture position as a function of dispersion for each spectrum to be extracted from the image.

It was then necessary to remove the scattered light component from the WYFFOS spectrograph output. The wyf_red task fit a cubic spline to the excess (scattered) light between the fibres along a cut in the spatial direction between the pre-defined aperture ranges. The fitting was verified manually, and a fourth order cubic spline function was found to provide an adequate fit with the lowest RMS residuals. Broad-scale fits were then performed by the task to determine the scattered light components along each of the spatial and spectral axes between the fibre outputs using higher-order cubic splines. The scattered light components were subtracted from each of the frames.

The fibre throughput and vignetting corrections for the offset image were then determined and applied. The mean number of counts per fibre was calculated, and the total flux obtained for a given fibre compared to the mean flux of all the fibres yielded its relative transmission or throughput. The results were normalized to a mean response of unity to preserve the total number of counts in the frame. Due to the large variation in background galaxy light and the concentration of objects towards the centre of M31, offset frames were selected which were well away from the galaxy. Two or more off-field images were obtained in case starlight coincided with one or more fibres in any of the frames.

The flux within the apertures was then extracted into a set of one-dimensional spectra. In this step, the signal was summed within the selected aperture along a given point on the dispersion axis, centred by the trace at that location. The background at each point was subtracted based on the window defined above.

A technique known as "optimal extraction" was employed to produce a final one-dimensional spectrum with the maximum signal-to-noise. This method assigns appropriate weights based on signal-to-noise (S/N) across the spatial profile (see Marsh 1989). Cosmic ray events were identified based on their anomalously high pixel values, and most were removed along with many spurious pixel detections during this procedure. A sawtooth correction was also performed to adjust for the set staggering of the WYFFOS fibres in a sawtooth pattern on the slit end.

3.2.3 *Wavelength Calibration*

Argon emission lamps were observed to determine the wavelength scale for each spectrum. It was necessary to obtain these comparison spectra for recalibration each time the grating was switched or the fibre configuration was altered. The WYFFOS instrument is bench-mounted and is unaffected by flexure (variable gravitational deformation), therefore the dispersion did not change during the observations due to telescope motion alone.

In each frame, a dozen or so of the more prominent argon lines were identified interactively using a list of standard argon spectral line wavelengths in air at standard temperature and pressure. A cubic spline function was fit to the data to yield the dispersion solution — the equation relating pixel value along the dispersion axis with the true wavelength — for each aperture within the image. An example of an argon emission spectrum is shown in Figure 3.4. The dispersion solutions were saved to the image header to set the wavelength scale for each individual fibre spectrum. The ensemble median RMS values for these fits were typically $\sim 0.02 - 0.08$ Å in the H2400B grating images and $0.08 - 0.13$ Å for the R1200R grating.

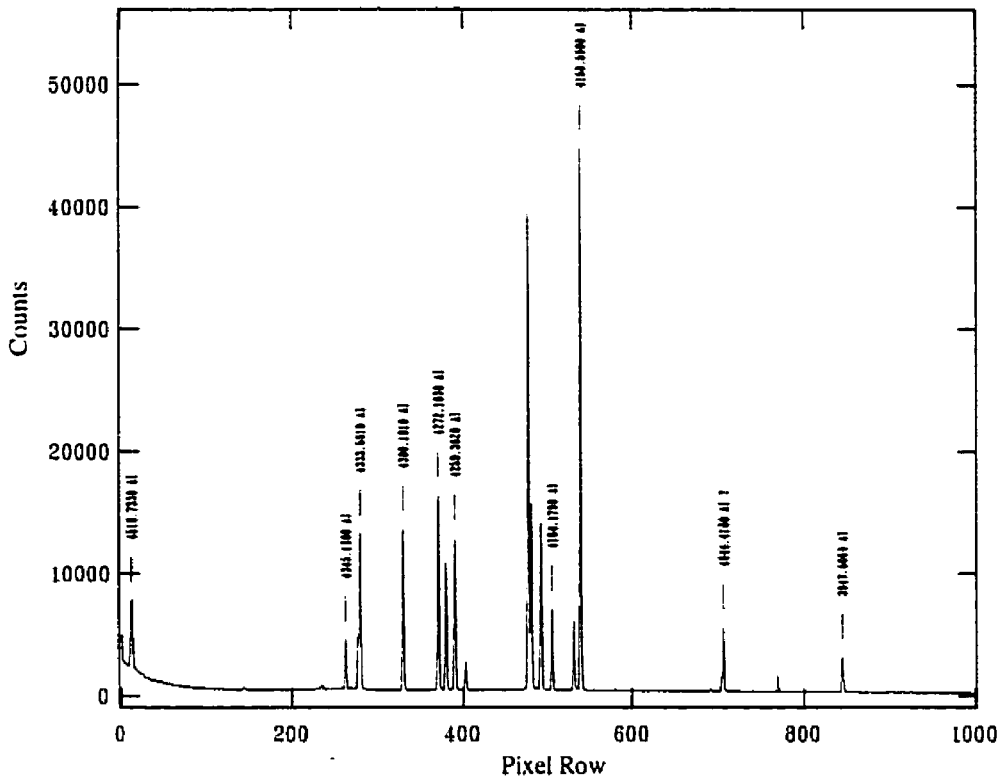

Figure 3.4: An argon emission lamp spectrum obtained using the H2400B grating, used to set the wavelength scale of the observations. Several of the prominent lines are identified with their wavelengths in Angstroms.

3.2.4 Sky Subtraction

The brightness of the night sky is due to the contribution of the following components (Binney & Merrifield 1998):

1. Air glow from photochemical processes occurring in Earth's upper atmosphere in addition to mercury and sodium emission from city lights. The resulting spectrum of this component is highly variable from observatory to observatory and fluctuates in brightness over time and with pointing direction.

2. Zodiacal light from the scattering of sunlight from particles within the Solar System.

3. Faint, unresolved stars in our Galaxy.

4. Diffuse light from background galaxies.

The cluster spectra in the M31 fields are also invariably superimposed on a non-uniform background of galaxy light. For the central WYFFOS fibre configurations, about 20 blank-sky fibres were arranged in a regular pattern across the 1° field to help characterize the background intensity. The outer fields contained more dedicated sky fibres thanks to a lower density of targets in the area. Spectra obtained through the dedicated background sky fibres were averaged to form a composite sky spectrum which was then subtracted from each target. Attempting to match one or a few nearby sky fibres to each target spectrum (i.e. to associate the local sky level with each cluster) did not prove advantageous, since the resulting losses in signal-to-noise were found to largely outweigh any gains made by compensating for background variability.

Examples of a WYFFOS spectrum before and after sky subtraction are provided in Figures 3.5 and 3.6, respectively. In many cases, noticeable residuals remained after the subtraction of a particularly prominent sky line such as the bright night sky

(O I auroral) emission feature at 5577 Å. These wavelength regions were flagged and omitted from the analysis procedure.

Examples of reduced spectra obtained using both gratings are shown in Figures 3.7 and 3.8, with the absorption features of interest labelled.

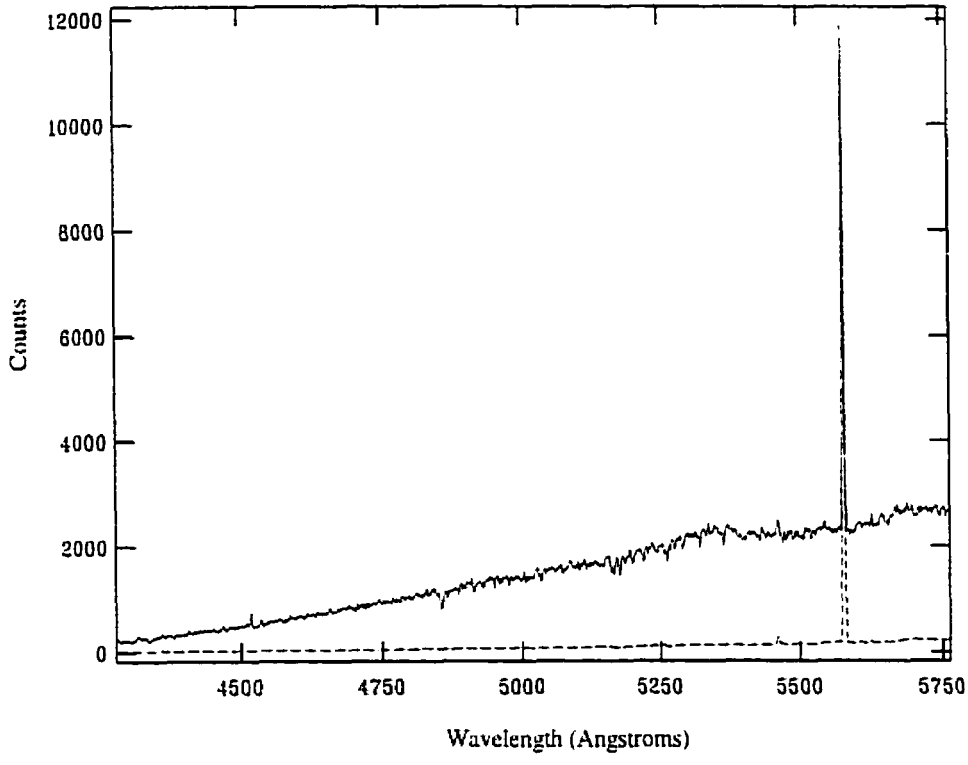

Figure 3.5: A spectrum of M31 cluster B386 obtained in one of the northeast fields using the R1200R grating. The solid line shows the spectrum prior to mean sky subtraction, and the dashed line is the mean sky spectrum obtained in that field. Note the prominent sky emission line at 5577 Å. The difference between these two spectra is shown in Figure 3.6.

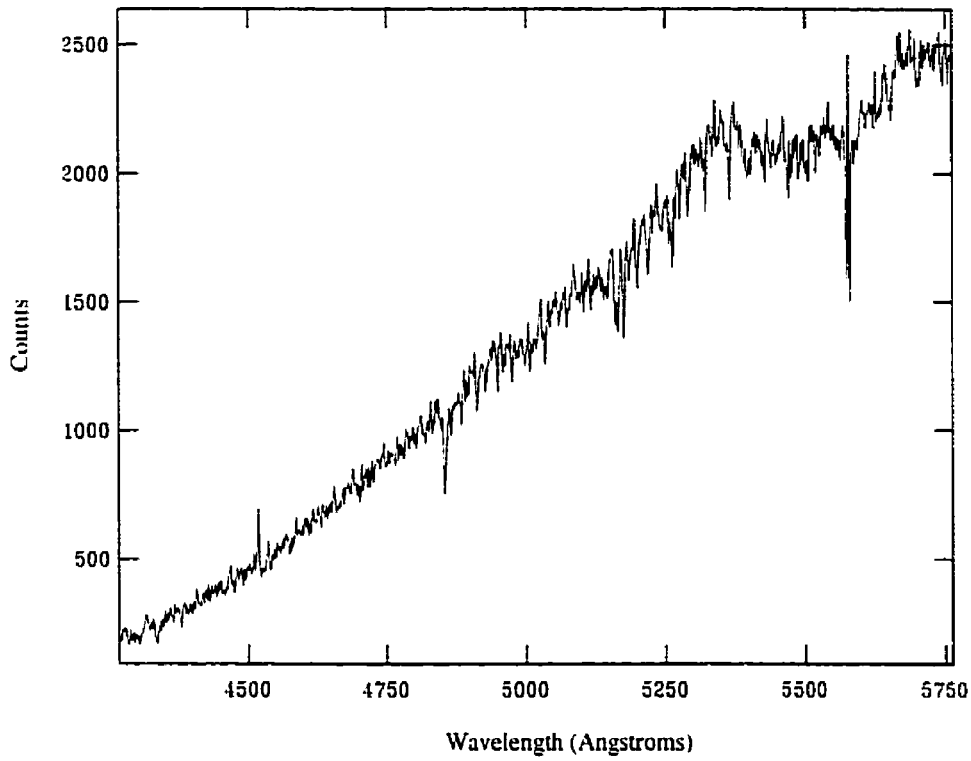

Figure 3.6: A spectrum of M31 cluster B386, as in Figure 3.5, but with the mean sky spectrum subtracted. Note the sky line residual around 5577 Å.

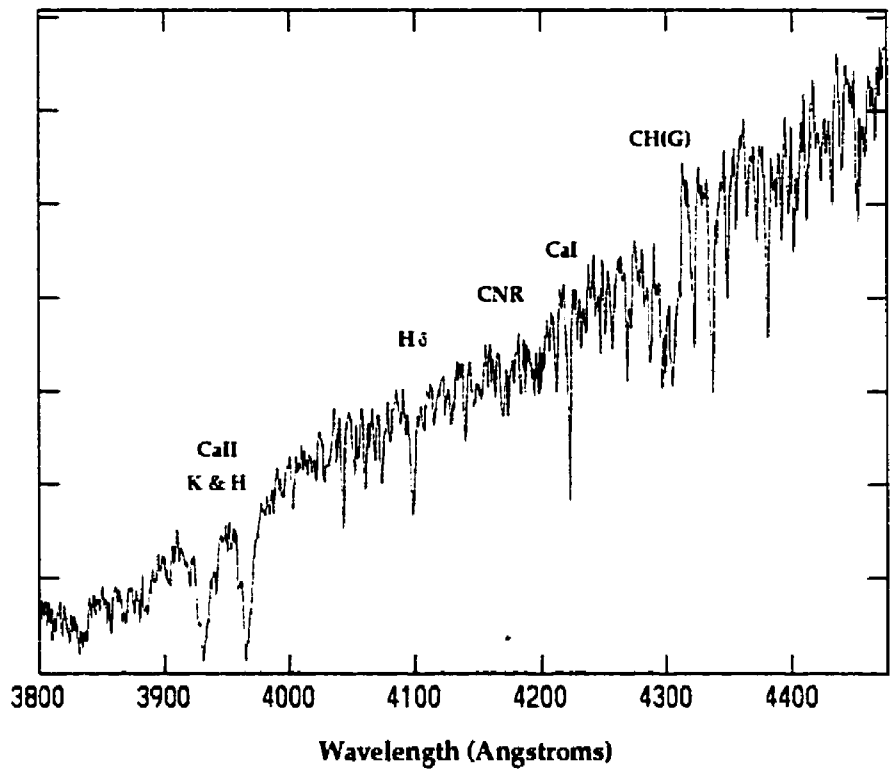

Figure 3.7: A sample reduced spectrum for M31 globular cluster B19, obtained using the WYFFOS system and the H2400B grating. The ordinate axis is linear in arbitrary units (zero is at the bottom).

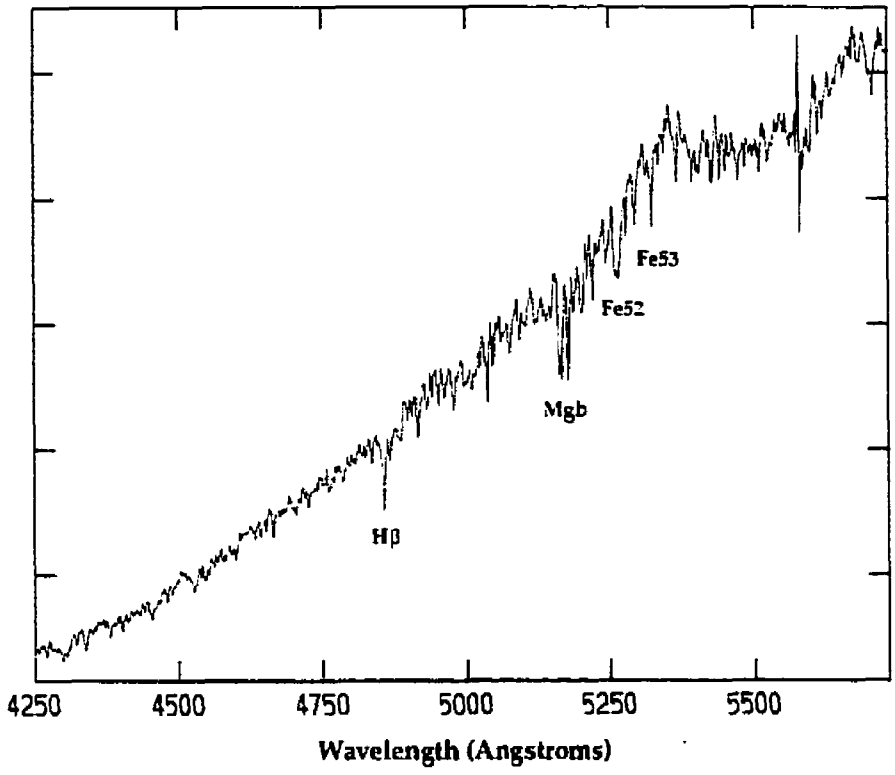

Figure 3.8: A sample reduced spectrum for M31 globular cluster B19 obtained using the WYFFOS system and the R1200R grating. The ordinate axis is linear in arbitrary units (zero is at the bottom).

4. WHT RESULTS: VELOCITIES AND METALLICITIES

The final set of WYFFOS spectra was used to measure the radial velocities and absorption feature strengths for this large sample of M31 globular clusters. A description of the analysis procedure and a comparison with published data are provided in this chapter. These WYFFOS results are later combined with other samples from the literature, and the "best sample" of M31 globular cluster velocities and metallicities will be examined and discussed in Chapter 6.

4.1 Radial Velocity Determinations

A globular cluster's spectrum is a composite of the spectra of its individual stellar members. Two bright, standard radial velocity stars were observed to provide template spectra for the calculation of the M31 globular cluster velocities. Data for the template stars is provided in Table 4.1, including coordinates, apparent V magnitude, spectral type (SpT) and heliocentric radial velocity v_r. These data were obtained through one fibre in each configuration by slewing the telescope to the appropriate position without altering the field configuration. Template spectra were extracted in the same fashion as the target spectra; this procedure was described in the previous chapter.

Table 4.1: Radial velocity standards (Astronomical Almanac 1998)

Stellar Template	RA (B1950)	Dec (B1950)	V mag	SpT	v_r (km s^{-1})
HD12029	01:55:49.8	+29:08:13	7.80	K2 III	$+38.6 \pm 0.5$
HD23169	03:40:52.8	+25:34:06	8.75	G2 V	$+13.3 \pm 0.2$

4.1.1 Cross-Correlations

Radial velocities can be calculated from the Doppler Shift of the absorption or emission features in their spectra:

$$v = c\frac{(\lambda - \lambda_0)}{\lambda_0}, \tag{4.1}$$

where c is the speed of light, λ is the wavelength of a spectral line as measured by the observer and λ_0 is the wavelength of the line in the rest frame of the emitter. When the distance between source and observer is increasing, the radial velocity has a positive sign.

Spectral line wavelengths are affected by pressure changes and blending, and tend to vary between stellar spectral types. The conventional method for calculating the radial velocity of a source is to cross-correlate its spectrum with that of a standard template star of known velocity and comparable spectral type. The spectra of individual globular clusters are generally similar to those of stars with spectral type F2 to G5 (Harris 1996).

Cross-correlations of the target object spectra with spectra of the template stars in Table 4.1 were performed using the IRAF task `rv.fxcor`. This task also fit a cubic spline to each spectrum, then subtracted the fit to remove the continuum background prior to the cross-correlation procedure.

A rigorous mathematical justification of cross-correlation analysis theory is presented in Tonry & Davis (1979). In brief, the Fourier transforms of the spectra are computed and the globular cluster spectra are individually correlated against the

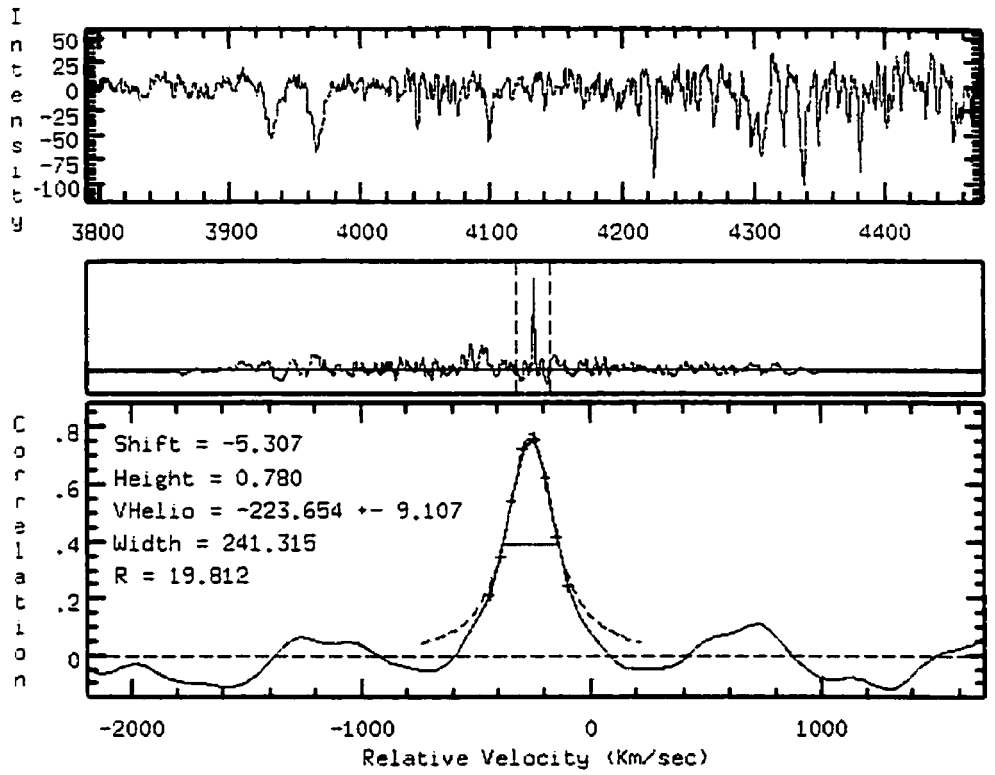

Figure 4.1: A cross-correlation result for the M31 globular cluster B19 (H2400B grating) obtained using the IRAF task `rv.fxcor`. The correlation was performed against the template star HD12029. The top panel shows the continuum-subtracted object spectrum in counts as a function of wavelength. The middle panel shows the full range of the correlation function and the bottom frame presents a zoomed-in view of the peak (the range of the lower plot is shown by the dashed lines in the middle panel).

available template spectra. The resulting normalized cross-correlation function peak is fit with a smooth function — here a normalized Gaussian or Lorentzian — to determine the position and height of the central peak of the power spectrum. The height of the peak is called the correlation coefficient (CC). A good cross-correlation result typical of the M31 globular cluster WYFFOS spectra is presented in Figure 4.1. Note that the parameters of interest are the position and the height of the correlation peak, while the overall quality of the fit to the function is not important.

Two spectra were associated with each target, obtained using each of the R1200R

and H2400B gratings. With the two template stars (HD12029 and HD23169), this yielded four cross-correlation combinations for the derivation of velocities for each cluster target. In general, a correlation was deemed successful if the CC exceeded a value of 0.3. For faint clusters with poor spectral signal-to-noise, there was occasionally some difficulty in recognizing the true correlation function peak in the midst of other peaks of comparable height. In such cases, the largest peak within reasonable velocity limits which appeared in more than one of the four correlation combinations for each object was selected.

Heliocentric corrections were automatically applied to the radial velocity determinations to convert from geocentric to Solar-centred values (see Walker 1987, pp. 64-65). Final target velocities were determined by calculating the mean of the cross-correlation results obtained in each grating with each template used. Each constituent velocity was weighted by its Tonry & Davis R value, the ratio of the correlation peak height to the amplitude of the antisymmetric noise.

About 70% of the targets yielded adequate cross-correlation velocities. The remainder represent:

1. Confirmed non-clusters (foreground stars, background galaxies, HII regions, open clusters etc.) identified by spectral features grossly atypical of globular clusters or radial velocities which were significantly beyond reasonable limits for the M31 GC population ($|v_{\rm obs} - v_{\rm sys}| > 3\sigma_v$ where $\sigma_v \sim 150$ km s^{-1}). These objects are noted in the final column of Table 4.7 presented at the end of this chapter.

2. Target spectra with insufficient signal-to-noise to generate reliable velocities.

3. Seven objects with inaccurate coordinates due to misidentifications or saturation on the APM scans.

4.1.2 Internal Velocity Uncertainties

Comparisons between the radial velocities obtained from both gratings and using each of the velocity standard stars, HD12029 and HD23169, are shown in Figure 4.2. Robust fits were made to the data, a method selected to minimize the influence of extreme outlying points (c.f. Hoaglin, Mosteller & Tukey 2000). These fits revealed no significant differences between the velocities determined using either template object using the same grating. A comparison of the velocities calculated from the two gratings showed only slightly larger systematic differences; the derived velocities found using the R1200R grating data, for example, were $\lesssim 6$ km s^{-1} larger than those determined from the spectra obtained using the H2400B grating.

Several dozen objects were observed in multiple (two or three) fibre configurations in order to establish the internal uncertainty on the cluster velocities. A total of 28 targets yielded cross-correlation results in more than one field. The median value of the differences between these multiple observations in the various pointings was found to be quite small, only 6.1 km s^{-1}. The root-mean-square (RMS) of these differences was found to be 12 km s^{-1}. Therefore, an uncertainty of ± 12 km s^{-1} is adopted here as the formal error on the individual M31 GC velocities from the WYFFOS sample. On average, this may represent an overestimate of the true uncertainty since it incorporates certain internal systematic errors (e.g. frame-to-frame shifts, grating differences) as well as statistical errors. For GCs observed in more than one fibre configuration, a mean value of the results is adopted as the cluster velocity.

4.1.3 Comparisons with Published Data

The small internal uncertainty associated with the WYFFOS velocities represents a significant improvement over many existing M31 velocities in the literature. Radial velocities for various samples of M31 globular clusters have been previously determined in studies by Huchra, Stauffer & Van Speybroeck (1982), Peterson (1989),

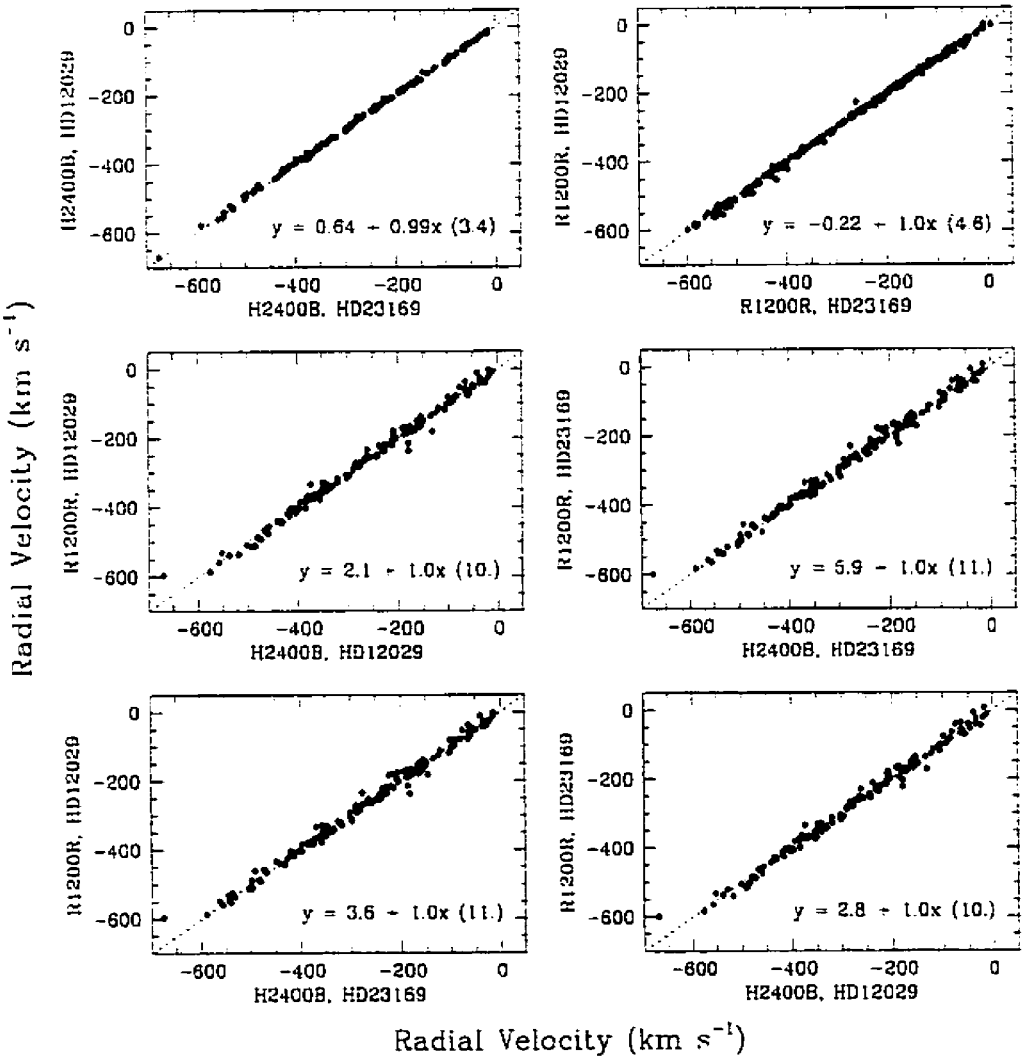

Figure 4.2: Correlations between the radial velocities determined for a given target in each grating (H2400B and R1200R) and cross-correlated with each template star (HD12029 and HD23169). For reference, the dashed lines show the unity relation. The results of robust fits to the data are provided in each panel, and the numbers in parentheses refer to the mean absolute deviations of the points from each fit in units of km s^{-1}.

Huchra, Brodie & Kent (1991), Federici et al. (1993), Dubath & Grillmair (1997), and Barmby et al. (2000). Note that the sample of Huchra, Brodie & Kent (1991) incorporates and expands the sample of velocities presented in Kent, Huchra & Stauffer (1989), which itself incorporates and expands on the results of Huchra, Stauffer & Van Speybroeck (1982).

Figure 4.3 shows a plot of the major and minor axis positions of the 202 M31 clusters for which high-precision (± 12 km s^{-1}) velocities have been obtained from the WYFFOS sample. Over half (109) of these M31 GCs with velocity determinations had no previously published spectroscopic data. The majority of the remaining clusters (72) had published velocities with uncertainties ≥ 20 km s^{-1}, and the remainder (21) had modest- to high-precision velocities with errors < 20 km s^{-1}. The positions of the WYFFOS targets in each of these three categories are shown schematically in Figure 4.3.

Figure 4.4 shows a comparison of those radial velocities in the present study which overlap with other samples from the literature. A linear fit, weighted by the inverse square of the published velocity uncertainties, yields the relation

$$v_{\rm publ} = 0.43 + 1.02\, v_{\rm WHT} \ {\rm km\,s^{-1}}. \qquad (4.2)$$

Overall, there is good agreement between the WYFFOS velocities derived herein and those of other studies within the adopted errors. Encouragingly, the RMS residuals of independent fits to the separate velocity samples were particularly low for the clusters which overlap with the high-precision studies of Peterson (1989: RMS $= 5.7$ km s^{-1} for 8 objects) and Dubath & Grillmair (1997: RMS $= 8.2$ km s^{-1} for 5 objects). Note that the only high-precision result which deviates significantly from the fit is that for B29, a cluster for which Peterson (1989) notes her velocity may be incorrect. This GC was not used in the calculation of the weighted fit or RMS, and it is circled in Figure 4.4.

There are two other points in Figure 4.4 which deviate significantly from the fit

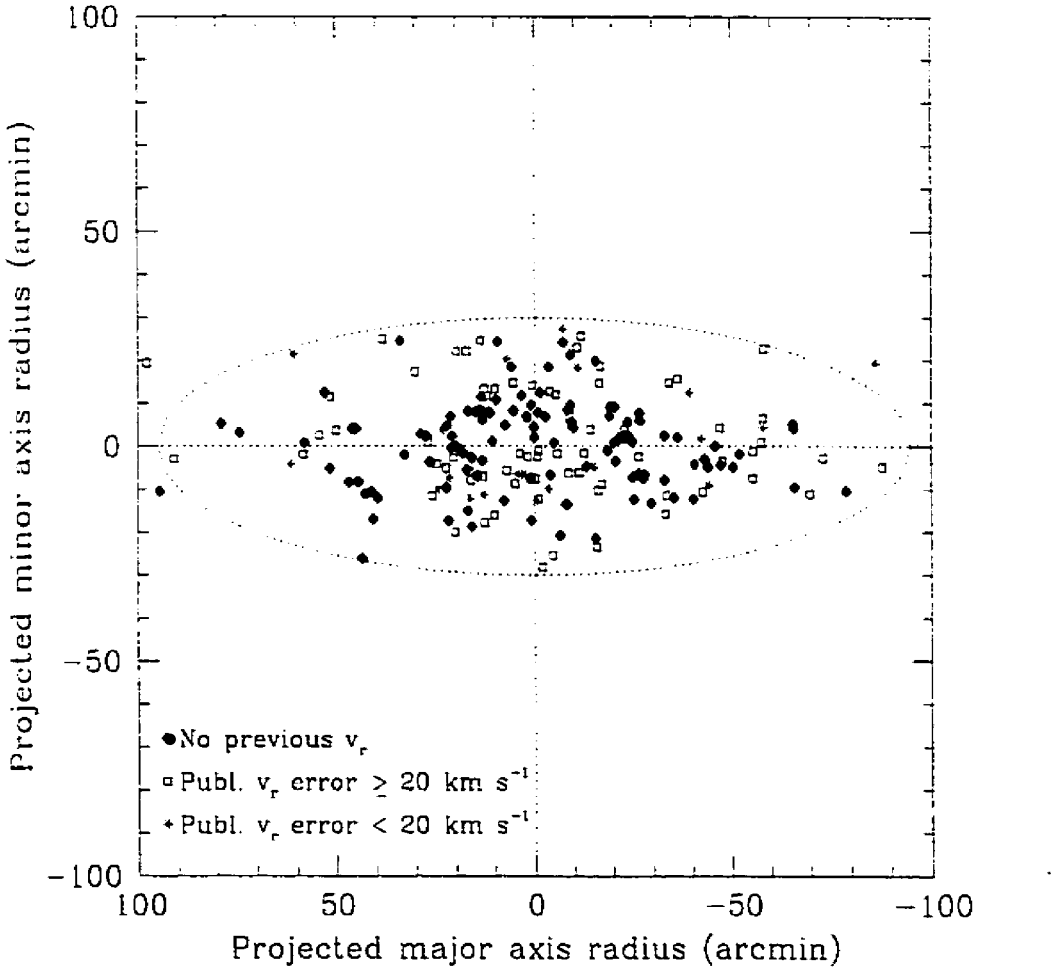

Figure 4.3: The positions of the 202 M31 GCs for which radial velocities were obtained from the WYFFOS spectra. Over half of this sample had no previously published spectroscopic data. Of those that had, the WYFFOS velocities (with adopted uncertainties of ± 12 km s^{-1}) represent significant improvements over most of the preexisting spectroscopic data.

and thus deserve mention. The open diamond above the best fit line represents the M31 globular cluster B301-S22: Barmby et al. (2000) obtained $v_r = -30 \pm 20$ km s^{-1}, in poor agreement with the value of -374 ± 12 km s^{-1} measured in the current study. The Barmby et al. coordinates match well with the APM coordinates for this object as provided in Table 4.7, so the velocity deviation does not appear to be due to a target misidentification in either study. This cluster was also measured by Federici et al. (1993), who obtained a velocity of -419 ± 30 km s^{-1}, in agreement with the WYFFOS result. The Barmby et al. sample also had the largest RMS residuals in the comparison fits: RMS = 110 km s^{-1} for 16 objects, not including B301-S22. The reasons for this large discrepancy are not known. The open upright triangle which deviates from the fit in Figure 4.4 represents B109-S170, for which Huchra, Brodie & Kent (1991) measured a velocity of -613 ± 24 km s^{-1} (compared to -372 ± 12 km s^{-1} from the WYFFOS results). Again, the coordinates for this object match well between both studies and the deviation does not appear to be due to a misidentification.

4.2 Feature Strengths: Definition and Measurement

The WYFFOS data were of sufficiently high dispersion and S/N to permit an accurate determination of the M31 GC feature strengths and metallicities.

4.2.1 Atmospheric Extinction Corrections

Before calculating the strength of the absorption features in the M31 globular cluster spectra, it was necessary to correct for the effects of scattering and absorption of light caused by the Earth's atmosphere (atmospheric extinction) and by intervening dust grains in space (interstellar extinction). Extinction refers to the difference between the observed magnitude and the intrinsic magnitude of the object resulting from the intervening medium; it increases with the path-length of the radiation and density of the medium and decreases with wavelength.

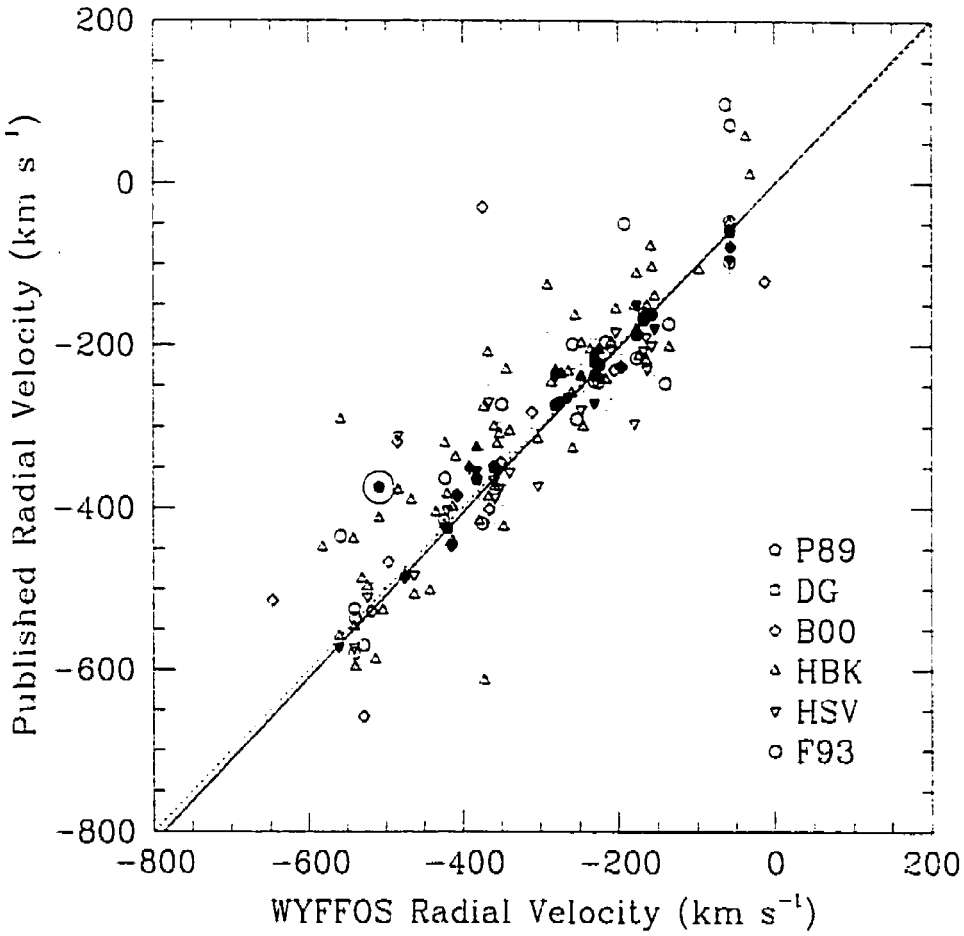

Figure 4.4: A comparison between radial velocity results obtained from this study and those of other publications: P89 = Peterson 1989; DG = Dubath & Grillmair 1997; B00 = Barmby et al. 2000; HBK = Huchra, Brodie & Kent 1991; HSV = Huchra, Stauffer & Van Speybroeck 1982; F93 = Federici et al. 1993). Filled symbols represent high-precision velocity determinations with quoted errors less than 20 km s^{-1}. The unity relation is represented by the dotted line, and the results of a linear fit with a $1/\sigma^2$ weighting is shown by the solid line. The circled (filled) point is M31 globular cluster B29 (see text for details).

All of the spectra were corrected for atmospheric extinction using the IRAF task `calibrate`. This applies a correction factor $\varepsilon(\lambda)$ based on the effective airmass $\mathcal{X}$ of the observation and the tabulated value of extinction as a function of wavelength (see Figure 4.5):

$$\varepsilon(\lambda) = 10^{0.4\,\mathcal{X}\,\mathrm{Extinction}(\lambda)}. \tag{4.3}$$

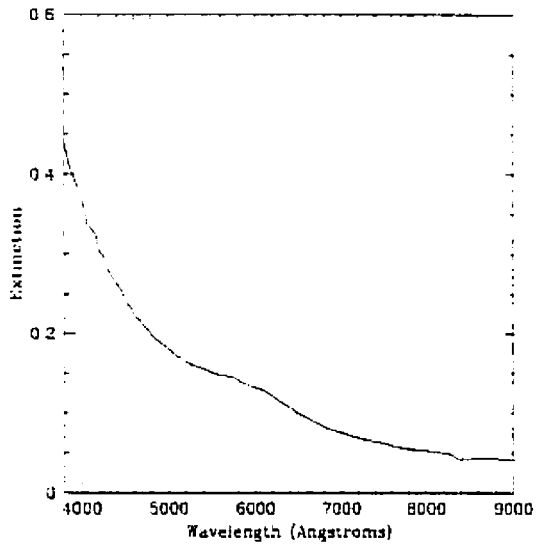

Figure 4.5: Tabulated extinction values as a function of wavelength from standard calibration data from Kitt Peak National Observatory.

4.2.2 *Interstellar Reddening Corrections*

The amount of reddening is expressed in terms of a colour excess,

$$E_{B-V} \equiv (B-V) - (B-V)_0 \tag{4.4}$$

where $(B-V)$ is the observed colour index and $(B-V)_0$ is the intrinsic colour index of the object. In the standard (Johnson-Morgan) photometric system, B and V correspond to the object magnitude at wavelengths of 4400 Å and 5500 Å, respectively. Observations of the M31 globular cluster system are affected by obscuration due to

dust within our own Galaxy, as well as by the variable reddening from dust within M31 itself. Clusters within or behind the disk of M31 will be more significantly reddened than those in the halo. The northwestern side of the galactic disk is nearer to us along the line of sight (Iye & Richter 1985), hence clusters on the lower side of the major axis will suffer greater reddening effects (see Figure 2.1). Since only projected positions in the galaxy can be measured, this makes the severity of reddening and absorption within M31 quite variable and difficult to pinpoint for any given cluster.

Colour excess values upon which the absorption calculations are based were determined using the slope (S) of the continuum between $\sim 4000-5000$ Å as tabulated in Crampton et al. (1985), where available:

$$E_{B-V} = -0.066\,S + 1.17\,(B-V) - 0.32. \tag{4.5}$$

The Crampton S parameter has been shown to be a good estimator of reddening and is not very sensitive to cluster metallicity (Elson & Walterbos 1988), although the method itself is subject to systematic errors (see discussion in Crampton et al. 1985).

The targets with published $(B-V)$ colours but with no slope parameters or intrinsic colours have been de-reddened to a typical colour of $(B-V)_0 = 0.76$ for M31 globular clusters at large galactocentric radii (Crampton et al. 1985). Observed $(B-V)$ colours are from the catalogue of CCD photometry of Reed et al. (1992, 1994) or the photoelectric photometry of Sharov & Lyutyi (1983), where available. Otherwise, the PDS microdensitometer magnitudes from the Schmidt plates of Battistini et al. (1987) or the less reliable photographic estimates from Crampton et al. (1985) have been used.

Clusters with no available S values or colours, or for which the calculated excess values were lower than a minimum foreground colour excess of $E_{B-V} = 0.10$ due to errors in the slope parameter or in the photometry, were assigned this minimum value (c.f. Frogel et al. 1980; Elson & Walterbos 1988).

The reddening correction procedure was facilitated by the IRAF task **deredden**,

which applies the empirical extinction function of Cardelli, Clayton & Mathis (1989, see their Figure 3). The quantity R_V is defined as the ratio of total absorption in the visual band (A_V) to the colour excess (E_{B-V}) between the V and B bands. A standard Galactic value of $R_V = 3.1$ for the diffuse interstellar medium was adopted for this procedure. The absorption at wavelength λ can thus be determined from the empirical extinction function and the derived A_V based on the known R_V and the colour excess of the target in question, via

$$A_V = R_V \times E_{B-V}. \tag{4.6}$$

All of the spectra were corrected for interstellar absorption/reddening in this manner. In general, the feature strengths were measured over a small wavelength range and errors in the reddening corrections had negligible effects on the line index calculations.

4.2.3 *Absorption Line Indices*

The strengths of various absorption features in the integrated spectra of the M31 clusters in the WYFFOS sample are used to rank them by metallicity. Line indices were calculated to measure the signal in a wavelength-delineated region centred on each spectral feature relative to the signal in the blue and red continuum zones flanking the feature (e.g. Brodie & Hanes 1986; Brodie & Huchra 1990). In light of the fact that no flux standard star spectra were obtained during the WYFFOS observing run, it was not possible to convert photon counts directly into flux for these targets. Our motivation, however, was to obtain a metallicity ranking of the globular clusters in M31; relative flux calibration was not essential as its absence will not significantly affect narrow features. Mean count ratios were used instead.

The generalized feature index is defined as

$$I = -2.5 \log \left[\frac{2\bar{\mathcal{F}}_I}{\bar{\mathcal{F}}_{C1} + \bar{\mathcal{F}}_{C2}} \right] \tag{4.7}$$

where $\bar{\mathcal{F}}_I$, $\bar{\mathcal{F}}_{C1}$ and $\bar{\mathcal{F}}_{C2}$ represent the mean count levels in the feature bandpass and associated continuum bandpasses $C1$ and $C2$ as given by $\bar{\mathcal{F}} = (\lambda_2 - \lambda_1)^{-1} \int_{\lambda_1}^{\lambda_2} \mathcal{F} d\lambda$ (Brodie & Hanes 1986; Brodie & Huchra 1990).

The continuum break feature,

$$\Delta = 2.5 \log \left[\frac{\bar{\mathcal{F}}_{C2}}{\bar{\mathcal{F}}_{C1}} \right] \tag{4.8}$$

is a measure of the discontinuity in the continuum due to Fraunhofer line-blanketing shortward of 4000 Å. This feature is somewhat more vulnerable to errors in the reddening and absorption corrections, as it spans a broad range in wavelength and is asymmetric. Uncertainties arising from the stability of atmospheric extinction may also have a more significant effect on the calculation of the continuum break. Moreover, many of the spectra do not extend the full range of wavelengths required to fully sample this colour feature (i.e. down to 3800 Å).

The line index and continuum bandpasses used in this study are defined in Table 4.2 (Burstein et al. 1984; Brodie & Hanes 1986; Brodie & Huchra 1990). The index designation is provided in column 1, the continuum bandpasses C1 and C2 are listed in columns 2 and 4 respectively, and the feature index bandpass (I) is given in column 3.

Prior to the line index determinations, each spectrum was shifted to zero radial velocity based on its cross-correlation results from Section 4.1.1 to define consistent line index wavelengths in the rest frame. The velocity dispersion of the M31 globular cluster system is roughly 150 km s^{-1}, a spread which translates into a nominal range of $4\sigma_v \gtrsim 600$ km s^{-1} in velocity. This would correspond to a wavelength shift of ~ 9 Å at $\lambda = 4500$ Å, a significant fraction of the width of most of the bandpasses selected for measurement. Therefore, metallicity determinations were not pursued for target spectra which had yielded no cross-correlation velocities.

Each final GC spectrum was examined for the presence of cosmic ray remnants or large residual sky lines within the spectral bands of interest. Line index results which

Table 4.2: Line indices and colours (Angstroms)

Index	C1	I	C2	Source
HK	3910.00 - 3925.00	3925.00 - 3995.00	3995.00 - 4015.00	BH86
CNR	4082.00 - 4118.50	4144.00 - 4177.50	4246.00 - 4284.75	BFGK
CaI	4200.00 - 4215.00	4215.00 - 4245.00	4245.00 - 4260.00	BH86
CHG	4268.25 - 4283.25	4283.25 - 4317.00	4320.75 - 4335.75	BFGK
Δ	3800.00 - 4000.00	—	4000.00 - 4200.00	BH86
Hβ	4829.50 - 4848.25	4849.50 - 4877.00	4878.25 - 4892.00	BFGK
MgH	4897.00 - 4958.25	5071.00 - 5134.75	5303.00 - 5366.75	BFGK
Mg2	4897.00 - 4958.25	5156.00 - 5197.25	5303.00 - 5366.75	BFGK
MgG	5125.00 - 5150.00	5150.00 - 5195.00	5195.00 - 5220.00	BH86
Mgb	5144.50 - 5162.00	5162.00 - 5193.25	5193.25 - 5207.00	BFGK
Fe52	5235.50 - 5249.25	5248.00 - 5286.75	5288.00 - 5319.25	BFGK
Fe53	5307.25 - 5317.25	5314.75 - 5353.50	5356.00 - 5364.75	BFGK

were clearly affected by such features were removed from further analysis. Tables A.2 and A.3 contain the line index values for the WYFFOS targets. Objects are listed according to the common name of the target (see Table 3.1 for source references).

4.2.4 *Line Index Uncertainties*

Feature strengths determined from the spectra of the 28 targets observed in multiple fibre configurations were compared in order to provide an estimate of the internal line index errors. The RMS differences between line indices calculated for these multiple observations are presented graphically in Figure 4.6 (H2400B) and Figure 4.7 (R1200R), and are listed in Table 4.3. Once again, such estimates incorporate statistical uncertainty and some internal systematic errors. For clusters measured more than once, the mean value of the line index determinations was adopted.

As mentioned previously in Section 4.2.3, inaccurate reddening corrections will not make a significant contribution to the line index uncertainties over their small wavelength ranges. The effects of varying the reddening correction were examined for several cases, including extremely red objects and those for which the adopted colour

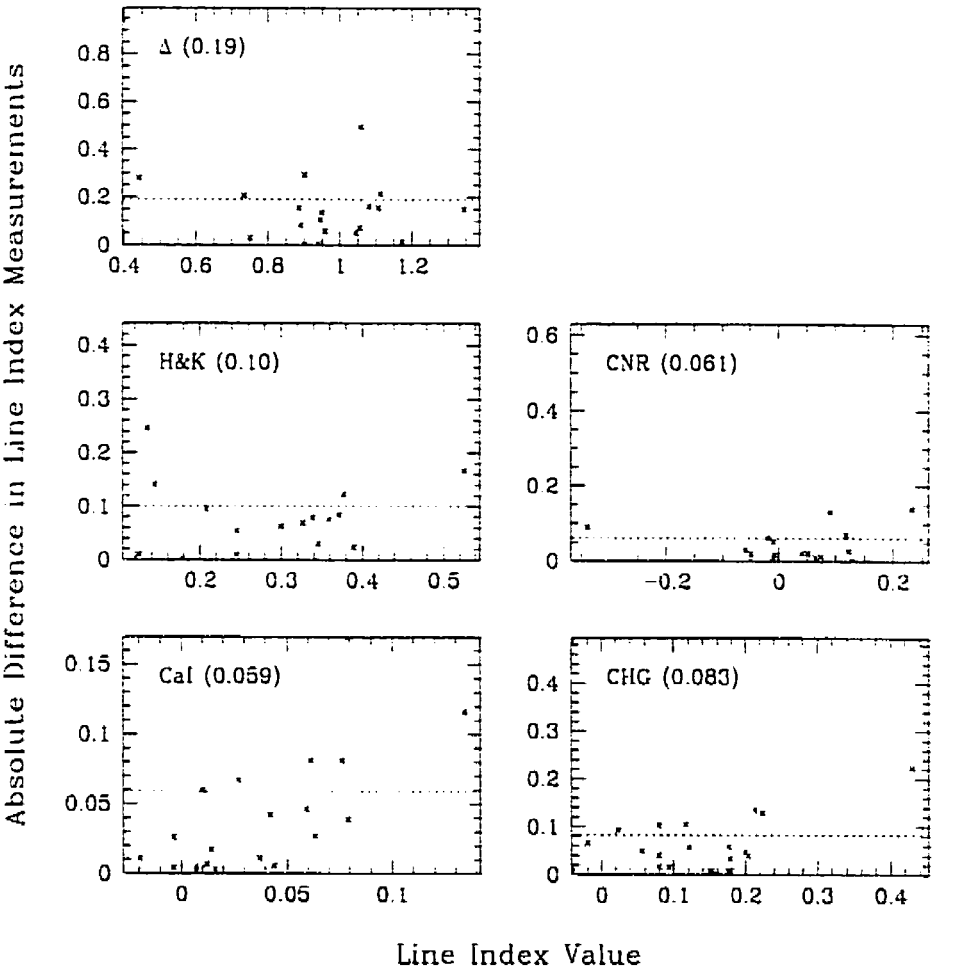

Figure 4.6: The absolute value of the difference between calculated line indices for the H2400B grating spectra for targets observed in multiple WYFFOS fibre configurations. The RMS values of the overlap differences are shown in parentheses and by the dotted line in each panel.

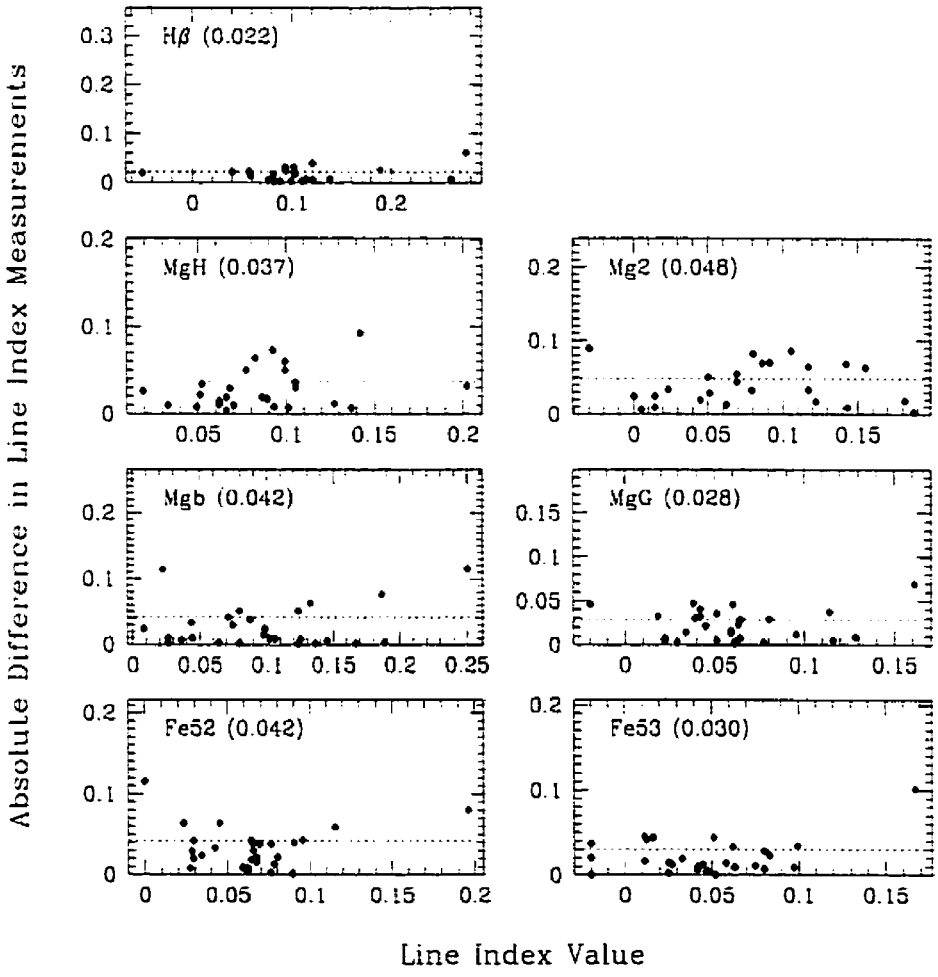

Figure 4.7: The absolute value of the difference between calculated line indices for the R1200R grating spectra for targets observed in multiple WYFFOS fibre configurations. The RMS values of the overlap differences are shown in parentheses and by the dotted line in each panel.

Table 4.3: Internal uncertainties on the features

Feature	σ	Feature	σ
H&K	0.10	MgH	0.04
CNR	0.06	Mg2	0.05
CaI	0.06	MgG	0.03
CHG	0.08	Mgb	0.04
Δ	0.20	Fe52	0.04
Hβ	0.02	Fe53	0.03

excess differed most significantly from that determined by Barmby et al. (2000)[1]. The only feature which suffered any significant variation due to a change in adopted colour excess was the continuum break at 4000 Å. This feature is asymmetric and is determined over the broadest wavelength range. The CNR and MgH line indices suffered less significant but still noticeable changes in value in the presence of large ($\gtrsim 0.2$) differences in the adopted reddening. The CNR line spans the largest wavelength range of all the indices in the blue, as does MgH in the red. Even for extreme selections of E_{B-V}, the resulting changes in all line index values remained within the RMS uncertainties quoted in Table 4.3.

Errors in the velocity shifts corresponding to the quoted internal uncertainty of 12 $\mathrm{km\,s^{-1}}$ would result in a wavelength shift of only a fraction of an Angstrom, and will not significantly affect the measured feature strengths.

4.2.5 *Comparisons with Previous Studies*

Studies of M31 globular cluster metallicities by Burstein et al. (1984) and Huchra et al. (1996) include tables of their derived line indices, several of which overlap with those determined for the WYFFOS sample.

Burstein et al. (1984) obtained integrated spectra with 9 Å resolution for Galactic and M31 globular clusters in a spectral range of 4000 – 6300 Å. A comparison of

[1] Unpublished reddening values from this study were kindly provided by P. Barmby.

the Burstein et al. line indices for targets in common with the WYFFOS sample is presented in Figure 4.8. Linear fits to the results weighted by the inverse square of their published uncertainties are also shown in Figure 4.8. There is a fairly tight linear correlation between the Burstein et al. line index results and those from WYFFOS sample: the RMS residuals for all of the fits lie between $0.01 - 0.03$.

Huchra et al. (1996) derived absorption line strengths for a large number of targets including 151 M31 globular clusters. Comparisons of the line index results for targets in common with the WYFFOS sample are shown in Figures 4.9 and 4.10. Again, there is a good correlation between the WYFFOS results and this other study. Observational errors can account for the relatively large scatter about the best-fit lines in each case.

4.3 Hβ and Young Clusters

The presence of strong Balmer absorption is characteristic of A type stars. These early-type stars have typical masses of $2-3M_{\odot}$ and short ($\lesssim 1$ Gyr) lifetimes (Binney & Merrifield 1998). Therefore, the presence of particularly strong Hβ absorption in the integrated spectra of globular cluster candidates may be indicative of a young stellar system. Burstein et al. (1984) reported an excess of Hβ in many of the M31 globular clusters in their sample relative to Milky Way GCs, suggestive of a population of younger clusters. This anomaly is demonstrated in Figure 4.11.

A number of targets in the WYFFOS sample were found to have strong Hβ absorption and may represent young clusters or clusters with a second population of intermediate age; these candidates are listed in Table 4.4. Figure 4.12 (upper panel) shows a plot of the line index measurements for Hβ versus the abundance indicator Mg2 (Table A.3 in Appendix A).

For comparison, the lower panel of Figure 4.12 shows a similar plot of the results from Brodie & Huchra (1990) and Huchra et al. (1996). The Huchra et al. objects

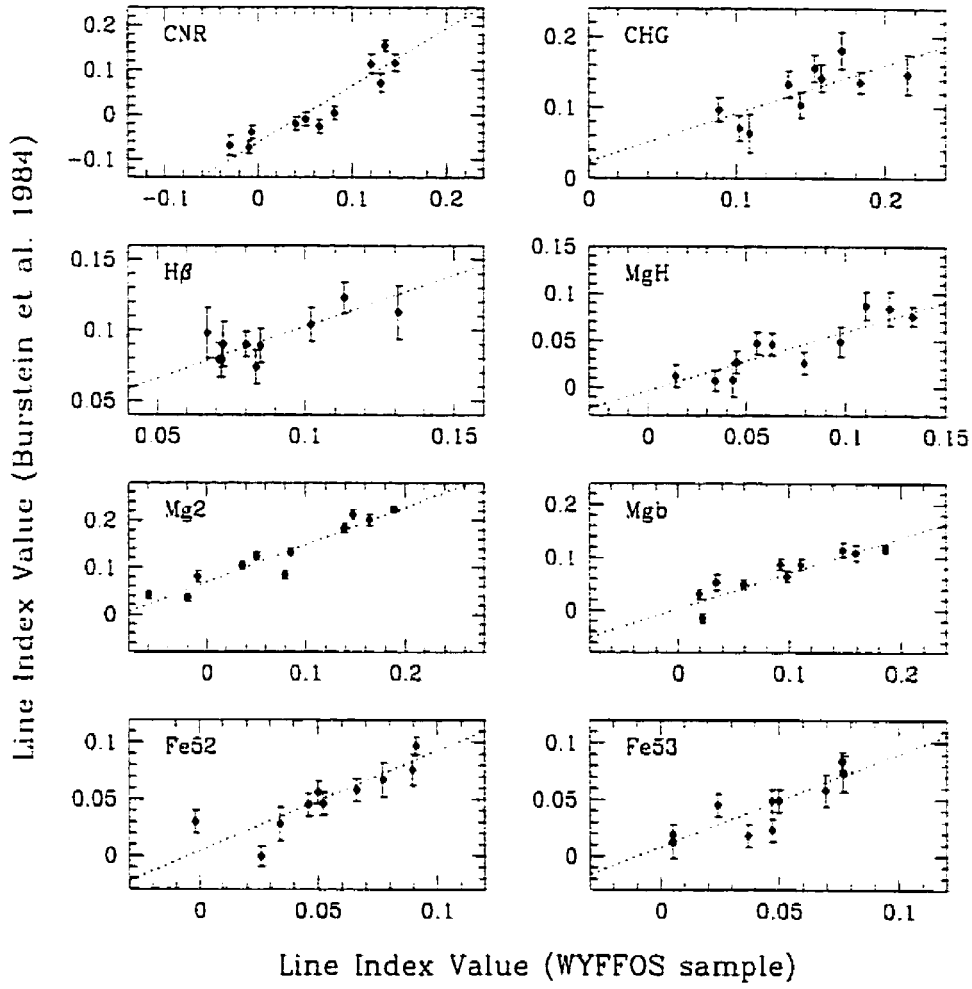

Figure 4.8: A comparison between published line index values from Burstein et al. (1984) and those determined in this study. Each panel shows a linear fit to the data, weighted by the inverse square of the error bars.

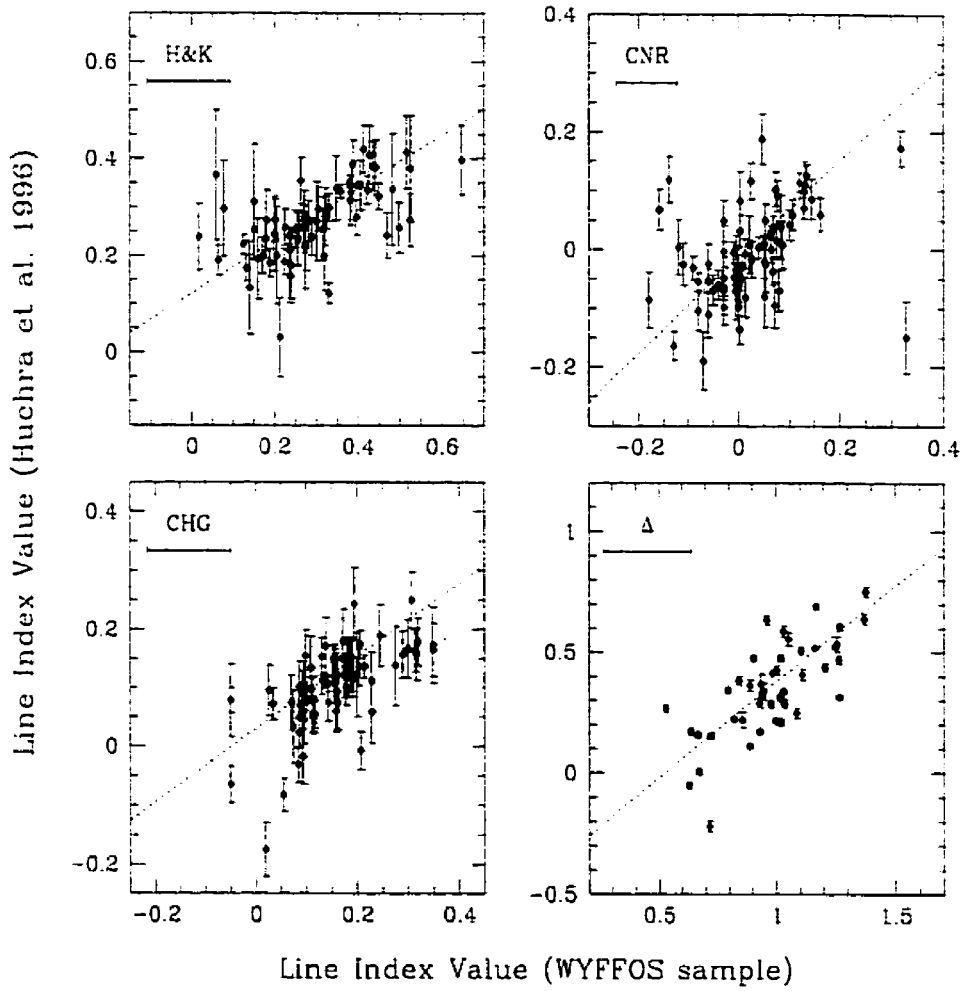

Figure 4.9: A comparison between published line index values from Huchra et al. (1996) and those determined from the H2400B grating data in the current study. The dotted lines show linear fits weighted by the inverse square of the error bars. Note that the data point at the lower-right of the CNR plot was not used in the fit.

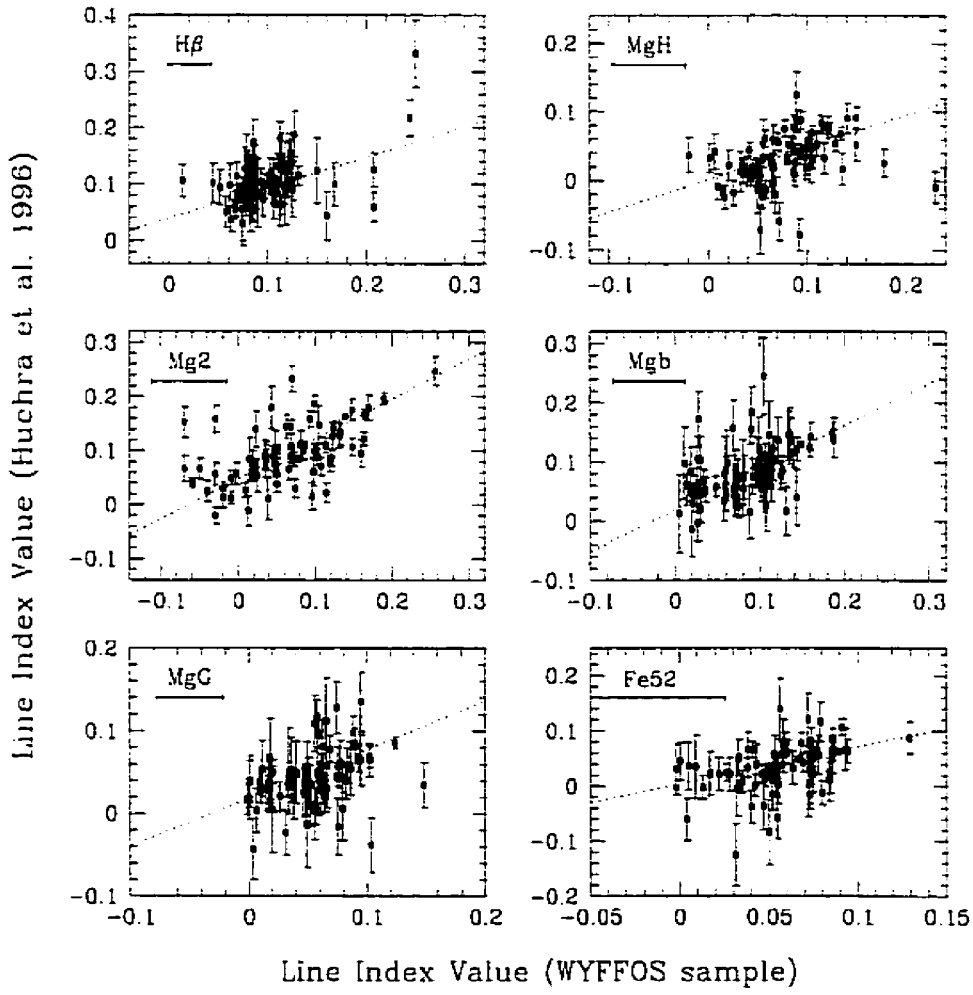

Figure 4.10: A comparison between published line index values from Huchra et al. (1996) and those determined from the R1200R grating data in the current study. The dotted lines show linear fits weighted by the inverse square of the error bars.

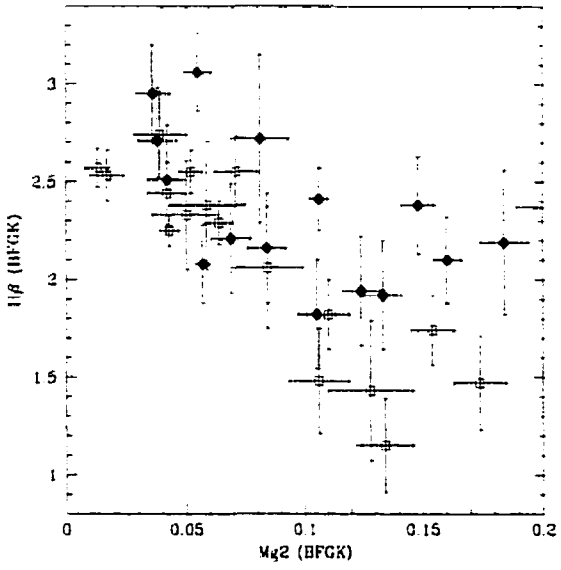

Figure 4.11: Hβ line indices for Galactic GCs (open squares) and M31 GCs (filled diamonds) plotted against the abundance indicator Mg2 from Burstein et al. (1984, their Figure 5k). Burstein et al. found an enhancement in the Hβ of several M31 globulars in comparison to their Milky Way counterparts.

which coincide with the WYFFOS sample *and* which fall more than 2σ above linear fits to their data are circled in the upper panel of Figure 4.12. Barmby et al. (2000) identified some additional potentially young objects based on the strengths of their Hβ absorption; these candidates are boxed in Figure 4.12. Except for cluster B327-S53 from the Barmby et al. sample, all of these objects also fall $\gtrsim 1\sigma$ above the best-fit shown for the current study. The strong Balmer absorption of cluster B380-S313 found by Barmby et al. (2000) is confirmed by the present study. Unfortunately, none of the WYFFOS targets with anomalously strong Hβ were present in the Huchra et al. sample, and thus could not be confirmed using the lower plot of Figure 4.12.

4.4 Globular Cluster Metallicities

The absorption feature strengths obtained from the WYFFOS spectra can be used to determine the cluster metallicities. A comparison with metallicity-sensitive infra-

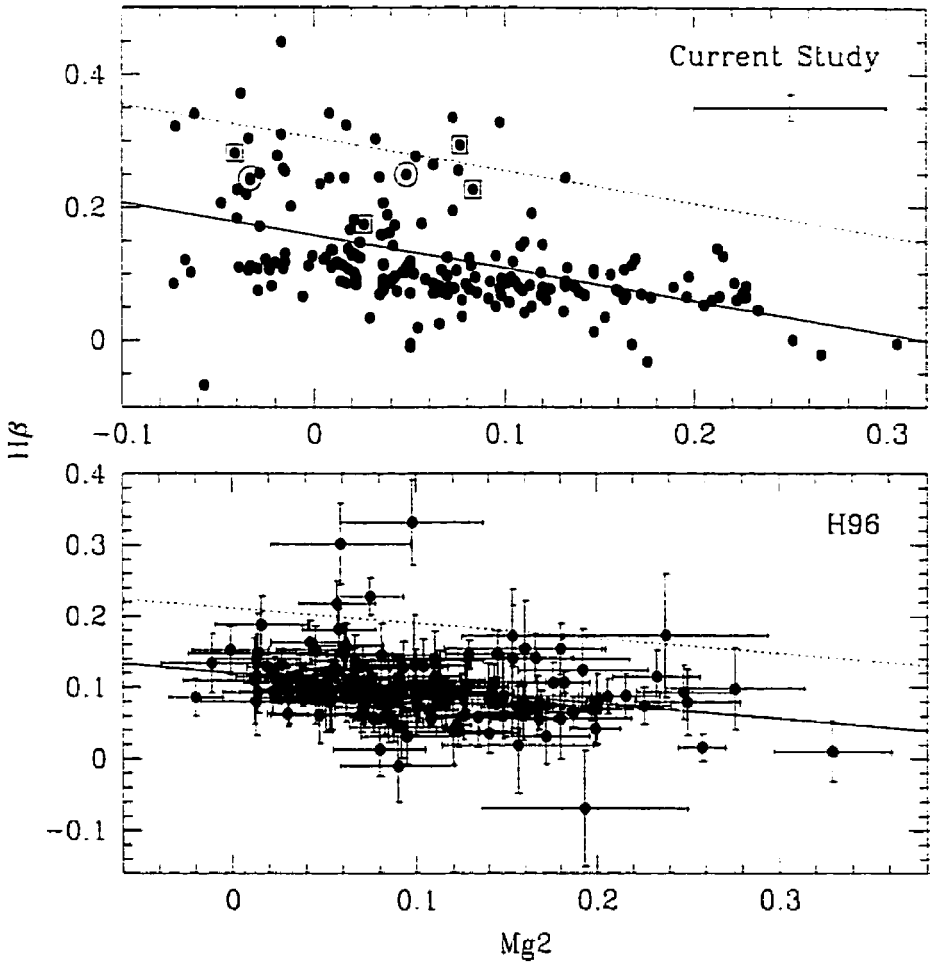

Figure 4.12: Hβ feature strengths versus the Mg2 abundance indicator. Solid lines show linear fits to the data, while the dotted lines represent a threshold of twice the RMS of the fit. The lower panel shows M31 globular cluster line index data from Table 2 of Huchra et al. (1996). The upper panel shows line indices from the current study, with a sample error bar given in the top-right corner. The large open circles in the upper panel show targets which were found to have strong Hβ lines in the Huchra et al. (1996) sample (B43-S106, B216-S267). Large open squares are the targets flagged as potentially young objects by Barmby et al. (2000) based on the strength of their Balmer lines (B314-S37, B321-S46, B327-S53, B380-S313). Note that a simple linear fit to the Hβ versus Mg2 plots may be inappropriate.

Table 4.4: Clusters with strong Hβ

Name	Hβ
B40-S102	0.341
B49-S112	0.449
B69-S132	0.328
B81-S142	0.372
B91-S151	0.335
B237-S299	0.342
B281-S288	0.245
B380-S313	0.294
B448	0.303
DAO39	0.324

red colours and published values of [Fe/H] will be used to establish the metallicity calibration.

4.4.1 *Infrared Colours*

The integrated colours of star clusters depend on stellar content, age and metallicity. In particular, broadband infrared colours are primarily sensitive to the bolometric luminosity of the cluster and the mean effective temperature of the composite red giant branch within the colour-magnitude diagram (e.g. Cohen et al. 1978; Frogel, Persson & Cohen 1980). This correlation is due to a redward shift in the giant branch with increasing cluster metallicity. As a result, infrared colours such as $(V-K)$ provide effective measures of the abundances of old stellar systems (Aaronson et al. 1978). An age difference of 5 Gyr between two GCs in the same cluster system would produce a deviation of only 0.1 mag in reddening-corrected $(V-K)_0$ (Frogel, Persson & Cohen 1980).

Frogel, Persson & Cohen (1980, henceforth FPC) presented infrared photometry for a total of 40 M31 globular clusters, of which there are 20 objects in common with the WYFFOS sample. FPC found that the $(V-K)_0$ colours of M31 globular clus-

ters correlated well with reddening-free metallicity parameters obtained from optical spectro-photometry (unpublished data from Searle 1980; see FPC's Figure 5). FPC quoted nominal 1σ uncertainties of ± 0.10 on their $(V-K)_0$ colours, and obtained 1σ residuals of 0.28 in [Fe/H], comparable to the error expected from observational uncertainties alone. Bònoli et al. (1987) obtained infrared photometry for 18 globular clusters in M31 on a similar photometric system to that used by FPC. Bònoli et al. quoted a mean error of ± 0.20 mag on their $(V-K)_0$ colours, a value which incorporated errors in the photometry as well as the uncertainty in the individual reddening corrections.

Brodie & Huchra (1990) used these known infrared colours in combination with Zinn & West's (1984) metallicities for Galactic globular clusters to derive a calibrating relationship:

$$[\mathrm{Fe/H}] = 1.574\,(V-K)_0 - 5.110 \tag{4.9}$$

They employed this calibration to determine [Fe/H] values for M31 GCs with published IR photometry (from FPC and Bònoli et al. 1987). Brodie & Huchra (1990) then derived metallicities for the remaining clusters in their sample based on the results of linear least-squares fits of their measured line indices versus calculated [Fe/H].

Cohen & Matthews (1994) observed 23 M31 GCs in optical and infrared, and compared these data with the metallicities of low-reddening calibrating clusters from Zinn & West (1984, updated by Armandroff & Zinn 1988). They obtained the relationship:

$$[\mathrm{Fe/H}] = 1.487\,(\pm 0.192)\,(V-K)_0 - 4.886\,(\pm 0.434) \tag{4.10}$$

There is a negligible ($\lesssim 0.06$ dex) difference in the [Fe/H] values predicted by the $(V-K)_0$ relationship derived by Cohen & Matthews and those from the calibration of Brodie & Huchra (1990, Equation 4.9 above).

Correlations between measured line indices and the known $(V-K)_0$ colours for the WYFFOS targets in common with the samples of Frogel, Persson & Cohen (1980),

Bònoli et al. (1987), and Cohen & Matthews (1994) are shown in Figure 4.13. Despite some scatter, there is a clear trend of increasing line index value with infrared colour for most of the feature strengths, an indication that these will provide good measures of metal abundance.

Table 4.5 lists the results of robust fits to the plots of line index versus infrared colour (Figure 4.13) of the form

$$LI = a + b(V - K)_0. \tag{4.11}$$

Column 4 of Table 4.5 provides the "range-normalized" deviation (Δ_{RN}) of the data from the fit, calculated by dividing the mean absolute deviation of the data by the y-axis range of the fit:

$$\Delta_{\rm RN} = \frac{\frac{1}{N}\sum_i |(V-K)_0/b - LI|}{b\left[(V-K)_0^{\rm max} - (V-K)_0^{\rm min}\right]} \tag{4.12}$$

where LI is the measured value of the line index. Linear correlation coefficients (r) are provided in column 5 of Table 4.5.

The CaI index is obviously not a good indicator of metallicity for the M31 globular clusters. Hβ is weakly anti-correlated with $(V-K)_0$ and metallicity, in agreement with the findings of Brodie & Huchra (1990). Instead, Hβ can be used as an age indicator, as discussed in Section 4.3. The metallicity calibration used to convert the WYFFOS line indices into [Fe/H] values is discussed in the upcoming section (4.4.2).

Metallicity determinations based on $(V-K)_0$ are sensitive to the assumed reddening for the calibrating clusters. Furthermore, the infrared colour-metallicity calibrations used in the samples above rely on the assumption that globular clusters in the Andromeda Galaxy exhibit the same general properties as those of the Milky Way. A given variation in infrared colour must correspond to metallicity changes in a similar manner as observed in Galactic clusters. Burstein et al. (1984) compared the line index strengths of M31 globular clusters with those of Galactic GCs and the nuclei of elliptical galaxies. They found that most of their indices (CHG, Mgb, MgH,

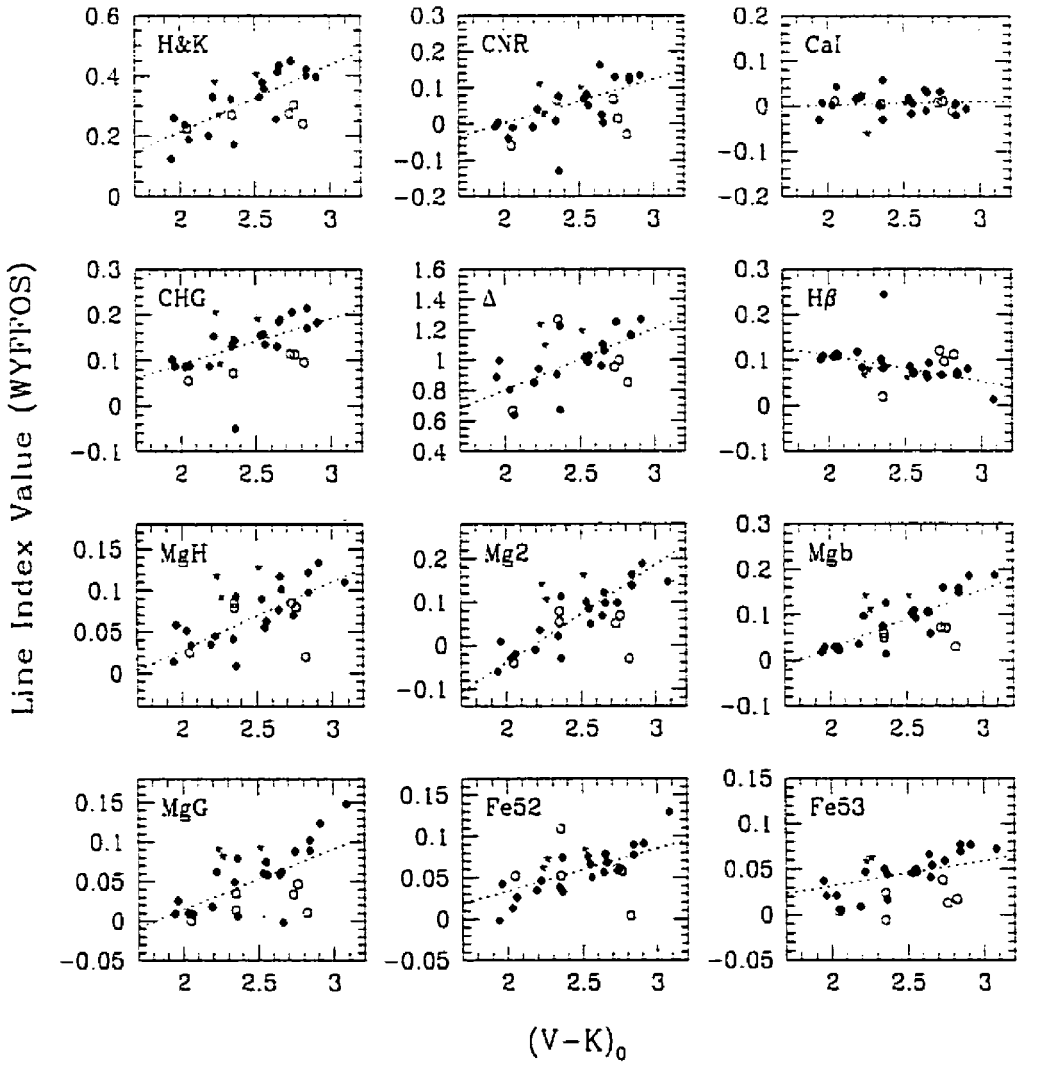

Figure 4.13: The quality of the abundance indicators as determined from the WYFFOS data based on a comparison with infrared colour $(V-K)_0$. Colours are from Frogel et al. (1980: *filled diamonds*), Bònoli et al. (1987: *open circles*), and Cohen & Matthews (1994: *asterisks*).

Table 4.5: Correlations between line indices and $(V-K)_0$

Line Index	a	b	Δ_{RN}	r
H&K	-0.23	0.22	0.22	0.64
CNR	-0.24	0.12	0.31	0.53
CaI	0.02	0.01	1.87	-0.09
CHG	-0.11	0.10	0.30	0.49
Δ	0.00	0.40	0.27	0.48
Hβ	0.22	-0.06	-0.33	-0.34
MgH	-0.14	0.08	0.25	0.55
Mg2	-0.49	0.22	0.16	0.64
Mgb	-0.23	0.13	0.20	0.65
MgG	-0.14	0.08	0.28	0.59
Fe52	-0.07	0.05	0.30	0.57
Fe53	-0.02	0.03	0.51	0.55

Fe) followed a smooth sequence with no offsets. However, they did find anomalously strong values of CNR and Hβ in M31 GCs compared to those of the Milky Way. Brodie & Huchra (1990) also found offsets in CNR abundance as well as in H&K for Galactic and M31 clusters, in the sense that the Andromeda GCs tended to have greater line strengths.

4.4.2 The Metallicity Calibration

The metallicity calibration is often performed using observations of Galactic globular clusters for which metallicities are reasonably well-known. No Milky Way globular clusters were observed during this WYFFOS run at WHT, so the metallicity calibration was derived based on published spectroscopic metallicities of M31 globular clusters from the literature.

Figure 4.14 shows a comparison of the WYFFOS line index results with published M31 globular cluster [Fe/H] values from various sources (Bònoli et al. 1987; Huchra, Brodie & Kent 1991; Barmby et al. 2000). The results of linear fits of the form $LI = a + b$[Fe/H] weighted by $1/\sigma^2_{\rm [Fe/H]}$ are provided in columns 2 and 3 of Table 4.6.

Table 4.6: Metallicity calibration

Line	a	b	σ	RMS	r
H&K	0.51	0.16	0.10	0.12	0.37
CNR	0.18	0.11	0.06	0.08	0.51
CaI	0.00	-0.01	0.06	0.06	-0.05
CHG*	0.25	0.09	0.08	0.06	0.68
Δ	1.31	0.24	0.20	0.14	0.70
Hβ	0.03	-0.05	0.02	0.05	-0.34
MgH	0.13	0.02	0.04	0.04	0.52
Mg2	0.20	0.11	0.05	0.05	0.72
MgG	0.13	0.06	0.03	0.02	0.75
Mgb*	0.20	0.09	0.04	0.03	0.80
Fe52	0.11	0.05	0.04	0.02	0.61
Fe53*	0.09	0.04	0.03	0.02	0.66

Note: Features marked with an asterisk were used in the final [Fe/H] calibration.

Note that only spectroscopically-determined metallicities for overlapping targets were considered in the calibration, and hence the Bònoli et al. (1987) near infrared photometric metallicities were not used in the fits. The internal errors of each feature are reproduced in column 4 of Table 4.6, with the RMS residuals of the fit and its linear correlation coefficient given in columns 5 and 6, respectively.

To best represent the metal abundances of the WYFFOS targets, a line index was selected to contribute to the calibration if it met the following four criteria:

1. The uncertainties associated with the line index did not exceed $\sim$ 20% of the full range of observed values. The Fe52 index did not satisfy this condition and was thus rejected from the calibration.

2. The linear correlation coefficient r exceeded a minimum value of $r = 0.65$.

3. Numerical experimentation demonstrated that the feature strength was stable in the presence of variation in the adopted value of cluster reddening. The

continuum break was found to be susceptible to reddening uncertainties and was thus rejected.

4. Only one line index which characterizes a given spectral feature was incorporated into the estimate. In the case of the magnesium triplet, the indices MgG, Mg2 and Mgb all provided an acceptable measure of essentially the same absorption feature. Of these, the Mgb index demonstrated the highest correlation coefficient and a relatively low RMS uncertainty, and was thus selected for use over the others.

Line indices which met the above criteria included the CH G-band feature, Mgb to characterize the strength of the magnesium *b* triplet, and the Fe53 iron line. Final cluster metallicities and the associated uncertainties have been determined from the unweighted mean of the [Fe/H] values calculated from each of the CHG, Mgb and Fe53 line strengths for 202 of the WYFFOS targets. A plot of the correlation between [Fe/H] values in the current sample which overlap with samples from the literature is presented in Figure 4.15. The median value of the formal errors on the WYFFOS sample metallicities is ±0.26 dex.

The final results derived from the WYFFOS spectra are provided in Table 4.7, including target name, right ascension and declination, X and Y positions in arcminutes from the centre of M31, cluster velocity and metallicity. Objects which have been identified as non-clusters and targets with higher-precision velocities or metallicities from the literature are noted in the final column of Table 4.7. In Chapter 6, these data are incorporated into the "best current sample" of spectroscopic results for M31 globular clusters for subsequent analysis.

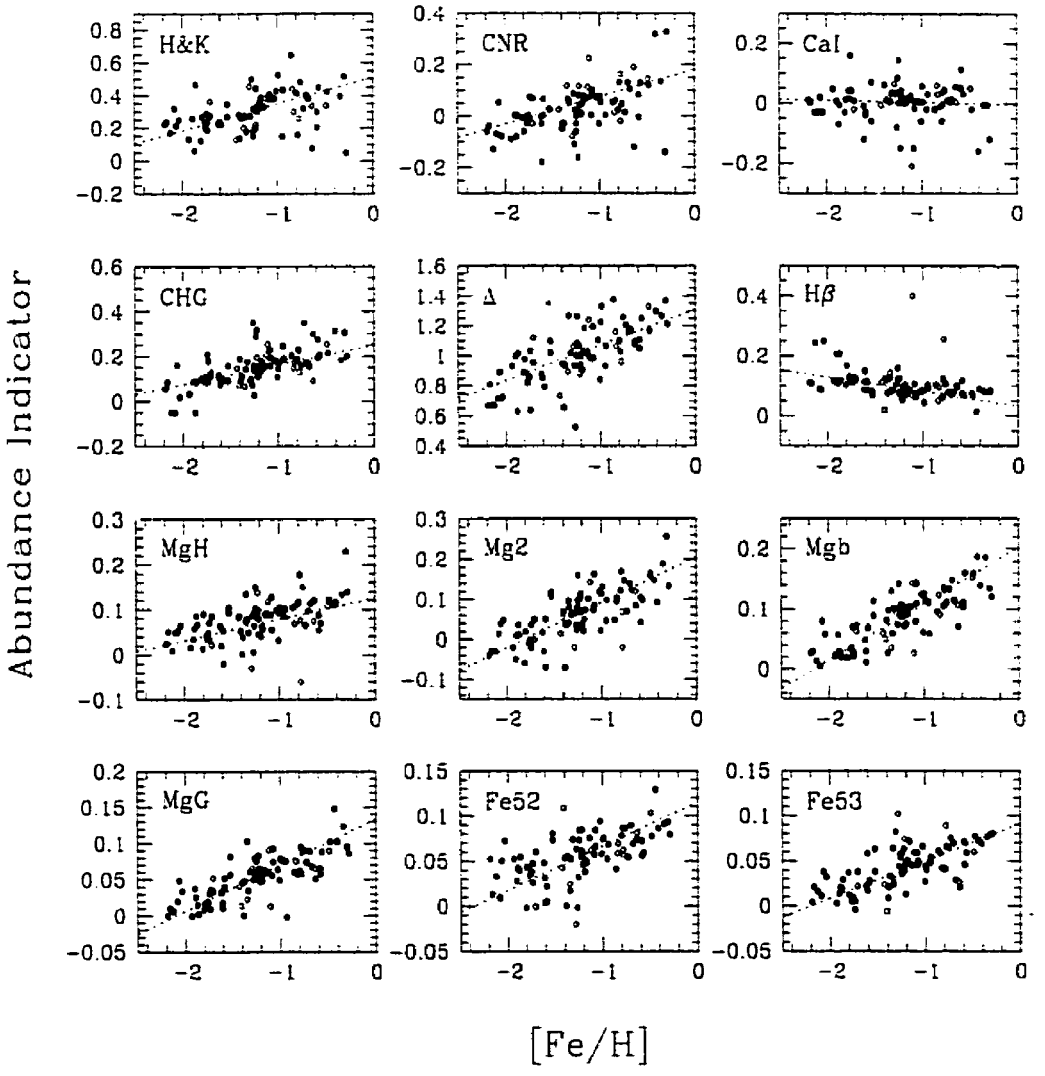

Figure 4.14: The relationship between published line [Fe/H] values and the line indices in this study. Metallicity sources are as follows: • Huchra, Brodie & Kent 1991, ◇ Barmby et al. 2000 and □ Bònoli et al. 1987. The dotted lines represent linear fits to the data, weighted by $1/\sigma^2_{[Fe/H]}$.

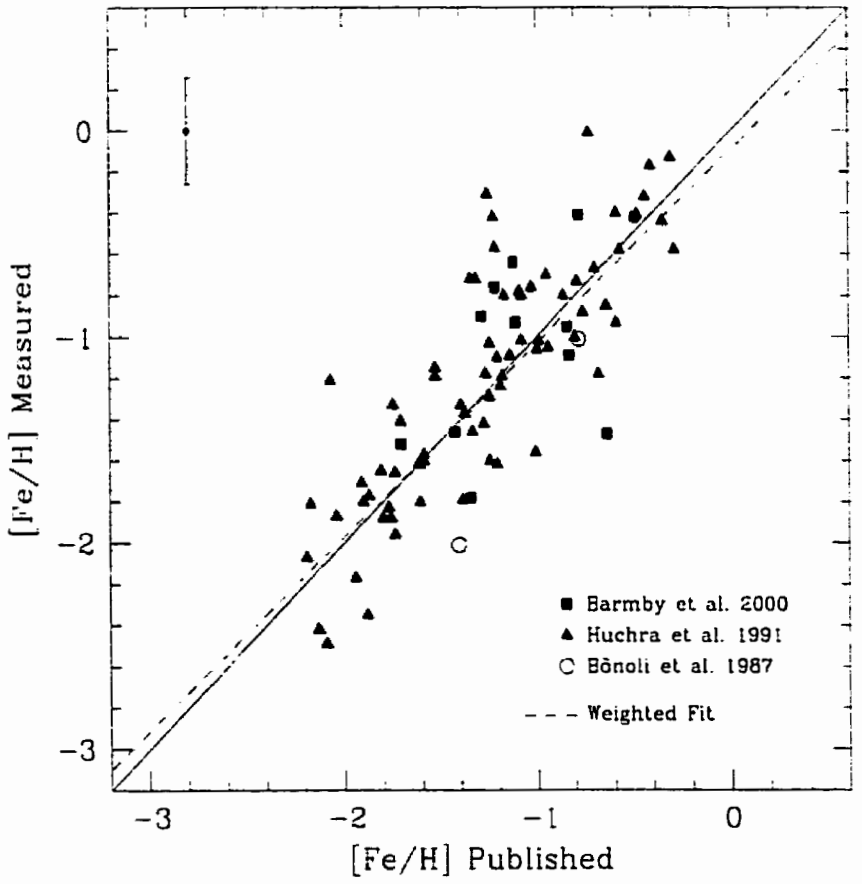

Figure 4.15: The relationship between published [Fe/H] values and the calibrated WYFFOS metallicities. The error bar in the upper left represents the median formal error quoted on the WYFFOS values. A linear fit, weighted by the inverse-square of the individual uncertainties, is shown by the dashed line for comparison to the unity relation (solid line). The RMS on the fit is 0.24 dex and its slope is 0.94 ± 0.02.

Table 4.7: WYFFOS results

GC	α_{B1950}	δ_{B1950}	X (′)	Y (′)	v_r	[Fe/H]	Notes
DAO1	00:32:36.85	39:52:40.6	-104.46	26.28	—	—	galaxy
DAO3	00:33:09.83	40:04:29.1	-91.22	28.31	—	—	galaxy
B294-S12	00:33:50.55	40:08:23.7	-83.42	24.44	—	—	galaxy
DAO5	00:33:53.24	40:11:45.2	-80.43	26.05	—	—	galaxy
B295-S14	00:34:04.29	40:03:12.6	-85.98	19.22	-423	-1.71 ± 0.15	
DAO6	00:34:13.62	39:52:22.7	-93.55	11.26	—	—	
DAO8	00:34:19.30	39:31:36.6	-109.45	-2.13	—	—	stellar
S18	00:34:35.90	40:04:50.3	-81.04	15.37	—	—	stellar
DAO9	00:34:43.31	39:48:25.1	-93.27	4.33	—	—	galaxy
B419	00:34:44.85	39:26:39.7	-110.42	-9.05	—	—	galaxy?
DAO11	00:34:46.70	39:40:32.3	-99.15	-0.95	—	—	
DAO12	00:34:57.00	39:30:01.8	-106.32	-8.88	—	—	galaxy
DAO13	00:35:03.45	39:48:43.3	-90.69	1.43	—	—	galaxy
DAO14	00:35:07.97	39:54:10.8	-85.82	4.04	—	—	galaxy
B298-S21	00:35:17.40	40:27:26.8	-58.24	22.73	-542	-2.07 ± 0.11	
B424	00:35:20.52	39:28:54.3	-104.48	-13.17	—	—	galaxy?
B301-S22	00:35:38.86	39:47:08.4	-87.83	-4.94	-374	-0.76 ± 0.25	B00 [Fe/H]
B427	00:35:39.98	39:41:41.9	-92.03	-8.41	—	—	galaxy?
DAO20	00:35:42.42	39:24:22.6	-105.52	-19.28	—	—	
DAO21	00:35:45.50	39:27:37.5	-102.57	-17.78	—	—	
B303-S26	00:36:07.55	40:11:02.8	-65.50	5.19	-464	-2.09 ± 0.41	
DAO22	00:36:10.99	39:35:02.3	-93.70	-17.20	—	—	galaxy
DAO23	00:36:11.34	40:10:18.4	-65.65	4.16	-75	-0.43 ± 0.13	
B305	00:36:15.91	40:00:04.0	-73.25	-2.75	-497	-0.90 ± 0.61	B00 [Fe/H]
B306-S29	00:36:25.62	40:17:52.5	-57.98	6.59	-424	-0.85 ± 0.71	HBK [Fe/H]
DAO25	00:36:30.37	39:51:03.8	-78.71	-10.42	-188	-1.96 ± 0.97	
DAO27	00:36:33.28	40:24:36.5	-51.75	9.53	—	—	HII region
B435	00:36:35.20	40:31:57.4	-45.69	13.71	—	—	galaxy?
B307-S30	00:36:35.34	40:16:29.9	-57.95	4.29	-407	-0.41 ± 0.36	
B308	00:36:35.80	40:13:04.9	-60.60	2.14	—	—	galaxy
B311-S33	00:36:50.55	40:14:46.7	-57.55	0.94	-463	-1.96 ± 0.07	
B439	00:36:56.78	40:45:46.0	-32.24	18.86	—	—	galaxy?
B312-S35	00:36:56.82	40:40:34.3	-36.36	15.69	-164	-1.41 ± 0.08	
B314-S37	00:37:01.17	39:57:40.2	-69.88	-11.09	-485	-1.61 ± 0.32	
B313-S36	00:37:01.29	40:36:26.9	-39.11	12.51	-415	-1.09 ± 0.10	
B315-S38	00:37:05.29	40:15:02.5	-55.62	-1.13	-559	-2.35 ± 0.54	HBK [Fe/H]
B1-S39	00:37:07.61	40:41:42.7	-34.21	14.76	-174	-0.58 ± 0.18	
DAO30	00:37:07.65	40:01:47.4	-65.86	-9.56	-535	-0.65 ± 0.34	
B316-S40	00:37:10.26	40:25:11.1	-47.00	4.29	-350	-1.47 ± 0.23	

CONTINUED ON NEXT PAGE

Table 4.7 (CONTINUED FROM PREVIOUS PAGE)

GC	α_{B1950}	δ_{B1950}	X (′)	Y (′)	v_r	[Fe/H]	Notes
B319-S44	00:37:19.72	40:17:30.7	-51.99	-1.81	-535	-2.27 ± 0.47	
B321-S46	00:37:32.05	40:11:18.6	-55.47	-7.46	-518	-2.39 ± 0.41	
S47	00:37:32.09	40:23:32.0	-45.78	-0.01	-584	-1.19 ± 0.29	
B4-S50	00:37:34.27	41:06:12.6	-11.72	25.70	-373	-0.31 ± 0.74	HBK [Fe/H]
B5-S52	00:37:36.71	40:27:30.1	-42.10	1.72	-273	-1.18 ± 0.17	
B443	00:37:37.38	40:16:54.8	-50.41	-4.85	-532	-2.37 ± 0.46	
B327-S53	00:37:40.69	40:19:55.0	-47.65	-3.51	-528	-2.33 ± 0.49	
B6-S58	00:37:42.76	41:10:59.1	-6.96	27.35	-230	-0.58 ± 0.10	DG v_r
BoD195	00:37:45.92	40:19:47.4	-47.14	-4.38	-552	-1.64 ± 0.19	
B8-S60	00:37:46.61	40:59:41.3	-15.46	19.88	-319	-0.41 ± 0.38	
B10-S62	00:37:47.90	40:57:55.1	-16.72	18.61	-159	-1.77 ± 0.14	
B12-S64	00:37:48.75	41:05:16.7	-10.79	22.98	-358	-1.65 ± 0.19	
B245	00:37:52.46	40:51:06.0	-21.59	13.76	—	—	
B448	00:37:53.06	40:23:47.9	-43.13	-3.01	-552	-2.16 ± 0.19	
DAO36	00:37:53.77	40:32:17.5	-36.33	2.07	-522	-2.16 ± 0.32	
B13-S65	00:37:54.70	41:08:56.4	-7.21	24.32	-409	-1.01 ± 0.49	
B14	00:37:54.93	40:56:18.4	-17.18	16.57	—	—	
B335	00:37:58.18	40:22:01.1	-43.95	-4.87	-514	-1.05 ± 0.26	
B15	00:38:01.36	40:43:30.0	-26.57	7.78	-460	-0.35 ± 0.96	
B16-S66	00:38:01.40	41:05:42.7	-8.99	21.35	-406	-0.78 ± 0.19	
B451	00:38:02.83	40:35:13.5	-32.95	2.50	-514	-2.13 ± 0.43	
B17-S70	00:38:05.00	40:55:39.8	-16.53	14.67	-524	-0.42 ± 0.45	
B18-S71	00:38:05.85	40:25:05.1	-40.63	-4.15	-585	-1.63 ± 0.77	
DAO39	00:38:08.62	40:42:14.4	-26.73	5.92	-478	-1.22 ± 0.41	
B19-S72	00:38:08.75	41:02:26.2	-10.73	18.25	-224	-1.09 ± 0.02	P89 v_r
B22-S74	00:38:15.24	41:08:15.0	-5.39	20.84	—	—	
B21-S75	00:38:15.30	40:49:12.3	-20.45	9.18	-403	-0.90 ± 0.06	
B338-S76	00:38:15.44	40:19:22.3	-44.03	-9.09	-248	-1.46 ± 0.12	HBK [Fe/H]
DAO41	00:38:18.97	40:50:09.1	-19.27	9.21	-445	-1.14 ± 0.30	
B453	00:38:19.63	40:44:28.6	-23.69	5.64	-446	-2.09 ± 0.53	
B341-S81	00:38:25.62	40:19:26.3	-42.79	-10.58	-349	-1.17 ± 0.05	
V31	00:38:28.45	40:49:02.1	-19.06	7.11	-433	-1.59 ± 0.06	
B25-S84	00:38:28.81	40:44:01.3	-22.98	3.99	-204	-1.46 ± 0.13	
B26-S86	00:38:30.63	41:08:13.2	-3.64	18.53	-243	0.01 ± 0.38	
B28-S88	00:38:32.72	40:42:36.5	-23.64	2.54	-434	-1.87 ± 0.29	
B29-S90	00:38:34.06	40:43:56.3	-22.44	3.15	-509	-0.32 ± 0.14	
B30-S91	00:38:34.98	40:40:48.9	-24.80	1.10	-380	-0.39 ± 0.36	
B31-S92	00:38:37.15	40:42:37.4	-23.12	1.88	-400	-1.22 ± 0.40	
B32-S93	00:38:37.64	41:01:03.4	-8.49	13.10	—	—	
B456	00:38:37.90	39:58:42.0	-57.75	-25.14	—	—	

CONTINUED ON NEXT PAGE

Table 4.7 (CONTINUED FROM PREVIOUS PAGE)

GC	α_{B1950}	δ_{B1950}	X (′)	Y (′)	v_r	[Fe/H]	Notes
B342-S94	00:38:40.46	40:20:20.1	-40.35	-12.27	-479	-1.62 ± 0.02	
B33-S95	00:38:42.58	40:43:46.9	-21.57	1.78	-439	-1.33 ± 0.24	
B34-S96	00:38:44.32	40:37:23.0	-26.43	-2.40	-540	-1.01 ± 0.22	
DAO47	00:38:45.74	40:28:50.5	-33.01	-7.85	-490	-1.13 ± 0.57	
B35	00:38:48.50	41:22:06.0	9.39	24.38	-49	-0.20 ± 0.54	
B36	00:38:48.84	41:09:38.0	-0.42	16.69	—	—	B00 v_r, [Fe/H]
V216	00:38:50.52	40:44:23.2	-20.17	0.96	-465	-1.15 ± 0.26	
B37	00:38:51.04	40:58:28.1	-8.99	9.52	-338	-1.07 ± 0.20	
B38-S98	00:38:52.00	41:02:48.0	-5.45	12.03	-177	-1.66 ± 0.44	
B39-S101	00:38:53.89	41:04:23.0	-3.99	12.72	-248	-0.70 ± 0.32	
B40-S102	00:38:55.10	40:24:27.6	-35.38	-11.94	-463	-0.98 ± 0.48	
DAO48	00:38:56.78	40:33:40.3	-27.91	-6.55	-490	-2.01 ± 0.99	
B41-S103	00:38:56.85	40:58:18.8	-8.44	8.56	-372	-1.22 ± 0.23	
B42-S104	00:38:57.76	40:50:59.6	-14.11	3.93	-352	-0.78 ± 0.31	
B43-S106	00:38:58.56	40:26:13.4	-33.58	-11.38	-414	-2.42 ± 0.51	
B45-S108	00:38:59.03	41:17:53.4	7.28	20.24	-420	-1.05 ± 0.25	DG v_r
B458	00:39:00.80	40:34:56.4	-26.44	-6.37	-521	-1.18 ± 0.67	
B47-S111	00:39:01.41	41:25:37.2	13.66	24.63	-291	-1.62 ± 0.41	
B48-S110	00:39:01.55	40:57:04.1	-8.88	7.09	-255	-0.40 ± 0.37	
B49-S112	00:39:01.73	40:33:28.3	-27.49	-7.41	-481	-2.14 ± 0.55	
B50-S113	00:39:02.19	41:15:51.7	6.04	18.52	-114	-1.42 ± 0.37	
B51-S114	00:39:02.64	41:08:52.5	0.57	14.17	-259	-1.00 ± 0.13	
B52	00:39:02.83	41:21:43.2	10.74	22.02	—	—	
B53	00:39:03.19	41:06:18.7	-1.39	12.52	-13	-0.33 ± 0.26	
B54-S115	00:39:03.77	40:44:28.8	-18.56	-0.96	-412	-0.45 ± 0.17	
B55-S116	00:39:06.42	40:55:45.8	-9.34	5.56	-338	-0.23 ± 0.07	
B56-S117	00:39:07.27	40:41:13.9	-20.72	-3.48	-382	-0.06 ± 0.10	
B57-S118	00:39:08.93	40:35:38.7	-24.94	-7.16	-437	-2.12 ± 0.32	
B59-S120	00:39:10.06	40:54:34.7	-9.86	4.29	-332	-1.36 ± 0.52	
B61-S122	00:39:15.96	41:13:09.2	5.49	14.82	-286	-0.73 ± 0.28	
B62-S123	00:39:16.09	41:22:05.8	12.56	20.29	—	—	
B65-S126	00:39:18.06	40:23:46.7	-33.24	-15.81	-378	-1.56 ± 0.03	
B66-S128	00:39:19.19	40:28:20.9	-29.50	-13.18	-389	-2.10 ± 0.35	
B69-S132	00:39:21.40	41:09:42.8	3.40	11.90	-295	-1.35 ± 0.43	
V246	00:39:22.49	41:01:40.3	-2.82	6.80	-344	-1.35 ± 0.29	
V228	00:39:23.12	40:43:49.6	-16.83	-4.26	—	—	
B72	00:39:23.27	41:06:21.3	0.97	9.56	-89	-0.38 ± 0.25	
B74-S135	00:39:23.80	41:26:55.4	17.26	22.11	-435	-1.88 ± 0.06	
B75-S136	00:39:24.69	41:03:54.9	-0.79	7.85	-212	-1.03 ± 0.33	
DAO52	00:39:24.88	40:34:26.5	-24.03	-10.29	—	—	

CONTINUED ON NEXT PAGE

Table 4.7 (CONTINUED FROM PREVIOUS PAGE)

GC	α_{B1950}	δ_{B1950}	X (′)	Y (′)	v_r	[Fe/H]	Notes
DAO53	00:39:26.04	40:21:37.9	-34.00	-18.33	—	—	
B76-S138	00:39:26.21	40:48:55.8	-12.44	-1.58	-514	-0.72 ± 0.06	
B79	00:39:27.97	41:13:01.1	6.77	12.95	—	—	
B81-S142	00:39:29.65	40:32:13.5	-25.22	-12.36	-430	-1.74 ± 0.40	
B82-S144	00:39:31.80	40:44:48.5	-15.04	-4.95	-381	-0.80 ± 0.18	P89 v_r
B83-S146	00:39:32.14	41:28:54.4	19.78	22.10	-367	-1.18 ± 0.44	HBK [Fe/H]
B346-S149	00:39:36.30	40:14:04.9	-38.75	-24.51	—	—	
B88-S150	00:39:36.82	41:15:48.2	9.99	13.35	-484	-1.81 ± 0.06	
B90	00:39:37.04	40:46:31.7	-13.07	-4.68	-428	-1.39 ± 0.80	
B91-S151	00:39:37.51	41:05:38.8	2.06	7.01	-290	-1.80 ± 0.61	
B93-S155	00:39:38.94	41:05:17.3	1.94	6.57	-442	-1.03 ± 0.12	
NB20	00:39:40.46	40:56:16.3	-4.99	0.80	-402	-0.80 ± 0.23	
B94-S156	00:39:41.01	40:40:51.8	-17.08	-8.75	-561	-0.17 ± 0.45	HBK [Fe/H]
NB33	00:39:41.89	41:02:39.5	0.21	4.52	-183	0.04 ± 0.38	(stellar?)
B97-S159	00:39:43.21	41:09:06.2	5.44	8.29	-282	-1.21 ± 0.13	
B102	00:39:45.51	41:17:52.5	12.63	13.34	-236	-1.57 ± 0.10	
V234	00:39:45.74	40:49:25.4	-9.78	-4.20	—	—	
B105-S166	00:39:46.46	41:14:01.8	9.71	10.83	-238	-1.13 ± 0.32	
B109-S170	00:39:48.05	40:54:02.0	-5.88	-1.70	-372	-0.13 ± 0.41	
B110-S172	00:39:48.99	40:47:02.4	-11.28	-6.15	-264	-1.06 ± 0.12	
B113	00:39:49.33	41:05:12.9	3.09	4.99	—	—	stellar
B116-S178	00:39:50.25	41:16:25.5	12.03	11.75	-339	-0.88 ± 0.12	
B117-S176	00:39:50.31	40:40:43.6	-16.10	-10.23	-531	-1.33 ± 0.45	
B119	00:39:51.89	41:01:09.8	0.19	2.11	-310	-0.49 ± 0.18	
B122-S181	00:39:55.74	41:17:21.1	13.40	11.50	-437	-1.69 ± 0.34	
B125-S183	00:39:58.10	40:49:05.4	-8.60	-6.24	-647	-1.52 ± 0.08	
B127-S185	00:40:00.28	40:58:15.7	-1.12	-0.92	-475	-0.80 ± 0.14	
B354-S186	00:40:03.08	41:44:00.0	35.24	26.83	—	—	B00 v_r, [Fe/H]
B129	00:40:04.01	41:08:41.3	7.53	4.94	-75	-1.21 ± 0.32	
B130-S188	00:40:04.51	41:13:26.9	11.34	7.80	-22	-1.28 ± 0.19	
B134-S190	00:40:07.41	40:57:37.9	-0.79	-2.37	-365	-0.64 ± 0.08	
B135-S192	00:40:07.56	41:14:42.2	12.68	8.12	-366	-1.62 ± 0.04	
B355-S193	00:40:08.33	41:41:34.1	33.93	24.56	-114	-1.62 ± 0.43	
B137-S195	00:40:09.60	41:15:48.7	13.79	8.50	-215	-1.21 ± 0.29	
B140	00:40:14.47	40:52:27.3	-4.04	-6.61	-413	-0.88 ± 0.77	
B141-S197	00:40:14.88	41:16:21.9	14.83	8.06	-180	-1.59 ± 0.21	
B144	00:40:15.55	40:59:40.1	1.76	-2.33	-140	-0.64 ± 0.21	
DAO58	00:40:17.12	41:13:52.0	13.13	6.19	-125	-0.87 ± 0.07	
B148-S200	00:40:19.51	41:01:39.1	3.78	-1.69	-303	-1.15 ± 0.34	
B149-S201	00:40:21.03	41:18:01.7	16.86	8.18	-60	-1.35 ± 0.25	

CONTINUED ON NEXT PAGE

Table 4.7 (CONTINUED FROM PREVIOUS PAGE)

GC	α_{B1950}	δ_{B1950}	X (′)	Y (′)	v_r	[Fe/H]	Notes
B467-S202	00:40:21.81	41:45:23.7	38.49	24.93	-344	-2.49 ± 0.47	
B356-S206	00:40:25.80	41:34:05.8	30.06	17.38	-192	-1.46 ± 0.28	
B156-S211	00:40:29.45	40:44:52.5	-8.27	-13.51	-417	-1.51 ± 0.38	
B158-S213	00:40:30.05	40:50:55.1	-3.44	-9.88	-177	-1.02 ± 0.02	DG v_r
B159	00:40:30.20	41:08:48.1	10.66	1.13	-175	-1.58 ± 0.41	
B160-S214	00:40:30.64	40:45:10.2	-7.89	-13.51	-354	-1.17 ± 1.25	
B161-S215	00:40:31.06	40:54:59.6	-0.11	-7.51	-413	-1.60 ± 0.48	HBK [Fe/H]
B164	00:40:33.77	40:56:03.9	1.05	-7.26	-294	-0.09 ± 0.40	
B469-S220	00:40:34.64	41:53:52.1	46.64	28.28	—	—	
B166	00:40:36.09	40:56:08.2	1.37	-7.56	-23	-1.33 ± 0.37	
B167	00:40:36.73	40:57:42.9	2.69	-6.68	-229	-0.42 ± 0.23	
B168	00:40:37.87	41:27:39.6	26.39	11.63	—	—	
B170-S221	00:40:39.24	40:34:16.5	-15.46	-21.52	-295	-0.54 ± 0.24	
DAO60	00:40:39.76	41:29:29.7	28.05	12.49	—	—	stellar
B272-V294	00:40:40.94	41:20:46.4	21 32	6.93	-120	-1.25 ± 0.16	
B171-S222	00:40:41.17	40:59:11.8	4.37	-6.42	-280	-0.41 ± 0.04	P89 v_r
B176-S227	00:40:46.17	40:32:45.6	-15.84	-23.49	-525	-1.60 ± 0.10	
B179-S230	00:40:46.67	41:01:49.5	7.08	-5.62	-153	-1.10 ± 0.02	
B180-S231	00:40:47.36	40:51:21.8	-1.07	-12.18	-203	-1.19 ± 0.07	
B182-S233	00:40:52.24	40:51:47.1	-0.17	-12.64	-359	-1.24 ± 0.12	P89 v_r
B470	00:40:52.74	41:53:22.0	48.32	25.32	—	—	
B185-S235	00:40:52.82	40:58:17.3	5.02	-8.71	-163	-0.76 ± 0.08	
B184-S236	00:40:52.91	41:20:09.6	22.23	4.78	-152	-0.37 ± 0.40	
B471-S238	00:40:56.86	41:51:31.7	47.35	23.58	—	—	
B188-S239	00:40:56.99	41:08:00.6	13.15	-3.33	-184	-1.51 ± 0.17	
B190-S241	00:40:58.79	41:17:40.5	20.95	2.38	-86	-1.03 ± 0.09	
B193-S244	00:41:00.91	41:20:32.4	23.45	3.84	-59	-0.44 ± 0.17	P89 v_r
S245	00:41:02.94	41:10:42.7	15.96	-2.54	-148	-0.31 ± 0.16	
B472	00:41:03.85	41:10:27.8	15.87	-2.83	-117	-1.45 ± 0.02	
B197-S247	00:41:05.13	41:13:45.2	18.61	-0.98	-9	-0.43 ± 0.36	
B199-S248	00:41:05.43	40:41:49.7	-6.45	-20.76	-396	-1.59 ± 0.11	
B198-S249	00:41:05.45	41:15:27.3	19.98	0.02	-105	-1.13 ± 0.30	
B200	00:41:05.82	41:12:57.7	18.07	-1.57	-153	-0.91 ± 0.61	
B203-S252	00:41:11.05	41:16:10.0	21.19	-0.36	-199	-0.90 ± 0.32	
B204-S254	00:41:11.84	41:05:37.8	13.00	-7.00	-355	-0.80 ± 0.17	
B207-S258	00:41:14.96	40:49:45.7	0.90	-17.27	-173	-0.81 ± 0.59	
B208-S259	00:41:15.48	41:06:46.5	14.33	-6.83	-222	-0.84 ± 0.04	
B209-S261	00:41:18.01	41:09:01.5	16.39	-5.81	-467	-1.37 ± 0.13	
B210	00:41:18.22	40:57:59.4	7.74	-12.67	-265	-1.90 ± 0.32	
B213-S264	00:41:18.85	41:14:13.8	20.58	-2.71	-539	-1.02 ± 0.11	

CONTINUED ON NEXT PAGE

Table 4.7 (CONTINUED FROM PREVIOUS PAGE)

GC	α_{B1950}	δ_{B1950}	X (′)	Y (′)	v_r	[Fe/H]	Notes
B214-S265	00:41:19.32	41:09:53.5	17.22	-5.47	-258	-1.00 ± 0.61	
DAO65	00:41:20.19	41:22:40.7	27.37	2.32	-130	-1.80 ± 0.36	
DAO66	00:41:22.14	41:24:03.4	28.68	2.88	-148	-1.82 ± 0.26	
B216-S267	00:41:24.07	41:21:30.2	26.90	1.02	-84	-1.87 ± 0.39	
DAO67	00:41:25.41	41:42:25.6	43.49	13.77	—	—	HII region
B217-S269	00:41:25.96	41:07:26.2	16.07	-7.97	-38	-0.93 ± 0.14	
B218-S272	00:41:29.69	41:02:54.7	12.95	-11.32	-231	-1.19 ± 0.07	DG v_r
B219-S271	00:41:30.54	40:40:22.5	-4.65	-25.40	-504	-0.01 ± 0.57	HBK [Fe/H]
B220-S275	00:41:34.73	41:14:10.2	22.38	-5.10	-245	-1.21 ± 0.09	
B221-S276	00:41:38.30	41:16:41.7	24.78	-4.06	-410	-1.29 ± 0.04	
B222-S277	00:41:40.72	40:57:47.7	10.22	-16.12	-311	-0.93 ± 0.95	B00 [Fe/H]
B223-S278	00:41:42.27	41:18:14.7	26.45	-3.68	-101	-1.13 ± 0.51	
B224-S279	00:41:42.34	41:12:25.0	21.89	-7.30	-157	-1.80 ± 0.05	P89 v_r
B225-S280	00:41:44.85	41:05:11.1	16.50	-12.16	-167	-0.67 ± 0.12	DG v_r
B226	00:41:45.86	40:54:34.8	8.30	-18.88	—	—	
DAO69	00:41:49.85	41:37:02.9	42.09	6.85	—	—	
B230-S283	00:41:50.60	40:40:48.0	-1.96	-28.12	-583	-2.17 ± 0.16	HBK
B365-S284	00:41:51.34	42:00:56.3	61.01	21.44	-58	-1.78 ± 0.19	B00 [Fe/H]
B231-S285	00:41:53.81	41:11:22.3	22.40	-9.65	-266	-1.49 ± 0.41	
B232-S286	00:41:55.52	40:58:36.1	12.58	-17.82	-179	-1.83 ± 0.14	
DAO70	00:41:55.70	41:24:19.0	32.78	-1.90	-66	0.33 ± 0.36	
B281-S288	00:41:58.08	41:03:44.2	16.91	-15.01	-203	-0.87 ± 0.52	
B234-S290	00:42:01.58	41:12:53.7	24.51	-9.85	-196	-0.95 ± 0.13	
B366-S291	00:42:01.61	41:47:26.1	51.60	11.57	-135	-1.79 ± 0.05	
B367-S292	00:42:02.08	41:49:07.7	52.98	12.55	-152	-2.32 ± 0.53	
B368-S293	00:42:02.77	41:34:45.0	41.79	3.53	—	—	
B283-S296	00:42:10.56	41:00:36.3	15.92	-18.80	-83	-0.06 ± 0.20	
B475	00:42:11.00	41:37:36.3	44.98	4.10	-120	-2.00 ± 0.14	
B235-S297	00:42:13.09	41:13:00.0	25.93	-11.48	-98	-0.72 ± 0.26	
DAO73	00:42:14.40	41:38:22.9	45.98	4.08	-114	-1.99 ± 0.19	
B477	00:42:23.35	41:23:13.9	35.15	-6.64	—	—	HII region?
B237-S299	00:42:24.34	41:06:10.4	21.89	-17.38	-86	-2.09 ± 0.28	
B478	00:42:27.44	42:07:44.1	70.49	20.41	—	—	galaxy?
B370-S300	00:42:29.27	41:41:16.9	49.98	3.71	-347	-1.80 ± 0.02	
B238-S301	00:42:29.81	41:03:13.0	20.22	-20.02	-32	-0.57 ± 0.66	
DAO78	00:42:36.87	42:04:33.0	69.09	17.06	—	—	galaxy?
B479	00:42:42.67	41:50:39.4	58.88	7.58	—	—	
DAO81	00:42:44.89	41:57:56.3	64.83	11.78	—	—	galaxy
B372-S304	00:42:48.14	41:44:00.7	54.31	2.64	-216	-1.42 ± 0.17	
V129	00:42:58.98	41:35:43.9	49.09	-4.09	—	—	HII region

CONTINUED ON NEXT PAGE

Table 4.7 (CONTINUED FROM PREVIOUS PAGE)

GC	α_{B1950}	δ_{B1950}	X (′)	Y (′)	v_r	[Fe/H]	Notes
B374-S306	00:42:59.36	41:25:31.5	41.14	-10.50	-96	-1.90 ± 0.67	
B480	00:43:00.36	41:29:29.2	44.36	-8.18	-135	-1.86 ± 0.66	
B375-S307	00:43:00.42	41:23:18.8	39.53	-12.03	-209	—	HBK [Fe/H]
DAO84	00:43:07.14	41:26:25.6	42.76	-11.08	-192	-1.79 ± 0.72	
B483	00:43:08.60	41:45:54.6	58.17	0.84	-53	-2.96 ± 0.35	
B484-S310	00:43:08.66	41:31:13.8	46.69	-8.31	-104	-1.95 ± 0.59	
B378-S311	00:43:11.94	41:37:07.4	51.68	-5.12	-205	-1.64 ± 0.26	
DAO86	00:43:20.02	42:13:15.6	80.88	16.22	—	—	galaxy
B380-S313	00:43:20.76	41:44:29.3	58.47	-1.82	-13	-2.31 ± 0.45	
B382-S317	00:43:25.09	41:21:17.3	40.83	-16.92	-302	-1.52 ± 0.27	
DAO87	00:43:36.01	42:17:56.7	86.38	16.83	—	—	galaxy
B385-S321	00:43:39.62	41:18:46.3	40.57	-20.62	—	—	
B386-S322	00:43:41.55	41:45:29.0	61.66	-4.23	-391	-1.62 ± 0.14	
BoD289	00:43:53.07	42:00:02.1	74.37	3.18	-78	-1.71 ± 0.63	
DAO88	00:43:56.26	41:59:16.8	74.15	2.24	—	—	
B389-S326	00:43:58.33	41:32:47.4	53.71	-14.60	—	—	
BoD292	00:43:59.97	42:04:53.1	78.96	5.21	-70	-0.47 ± 0.54	
DAO89	00:44:00.44	42:32:08.2	100.28	22.16	—	—	
S327	00:44:03.60	42:28:24.3	97.73	19.38	-259	-1.88 ± 0.06	
B391-S328	00:44:12.68	41:17:34.4	43.51	-26.21	-325	-0.55 ± 0.59	
B392-S329	00:44:15.32	41:38:22.0	60.04	-13.60	—	—	stellar
B493	00:44:28.69	42:00:43.3	79.04	-1.56	—	—	
DAO91	00:44:38.86	42:23:22.2	97.87	11.15	—	—	
S337	00:44:44.04	41:26:59.1	54.53	-24.91	—	—	galaxy
DAO92	00:44:51.51	42:31:32.5	105.70	14.45	—	—	
DAO93	00:45:00.04	42:28:34.1	104.37	11.36	—	—	
DAO94	00:45:08.19	42:27:39.7	104.61	9.62	—	—	
DAO95	00:45:11.35	41:50:35.7	76.12	-14.09	—	—	galaxy
B400-S343	00:45:15.36	42:09:11.1	91.06	-3.00	-253	-2.01 ± 0.21	
DAO97	00:45:22.74	42:38:57.8	115.08	14.63	—	—	galaxy
DAO98	00:45:43.02	42:02:20.4	88.96	-11.29	—	—	
B402-S346	00:45:50.00	41:45:13.5	76.47	-23.07	—	—	F93 v_r
BA11	00:45:59.35	42:07:16.9	94.70	-10.54	-97	-1.14 ± 0.61	
DAO99	00:46:02.00	42:16:24.1	102.09	-5.18	—	—	
DAO100	00:46:14.98	41:59:18.6	90.33	-17.81	—	—	galaxy
DAO101	00:46:20.09	42:14:12.4	102.50	-9.17	—	—	
B505	00:46:28.99	42:02:43.5	94.62	-17.68	—	—	
DAO104	00:46:34.96	41:59:56.0	93.16	-20.30	—	—	
DAO106	00:46:49.57	41:59:59.2	94.91	-22.38	—	—	galaxy
DAO107	00:46:54.67	42:29:11.2	118.14	-4.68	—	—	galaxy
B406	00:47:12.80	41:59:36.0	97.33	-25.97	—	—	galaxy
S353	00:47:31.42	42:19:24.6	114.86	-16.11	—	—	F93 v_r

Column 6: Radial velocities in $\mathrm{km\,s^{-1}}$, with associated uncertainty of $\pm 12\ \mathrm{km\,s^{-1}}$.
Column 8: P89 = Peterson 1989; HBK = Huchra, Brodie & Kent 1991; F93 = Federici et al. 1993; DG = Dubath & Grillmair 1997; B00 = Barmby et al. 2000.

5. THE CFHT MOS/ARGUS SPECTRA: DATA AND ANALYSIS

In addition to the WYFFOS data presented in the previous chapter, moderate- to low-resolution spectra for $\sim$ 200 of the brightest M31 globular clusters were obtained from the Canada-France-Hawaii 3.6 m telescope[1] (CFHT) using the MOS/ARGUS system. The targets of this study extended out into the halo of the galaxy and the primary intention was to improve upon and extend the kinematic database of M31's GCS. Although the image processing procedure followed the same general principles presented for the WYFFOS spectra, it was necessary to adapt the reduction algorithms to the unique format of the ARGUS data. The ARGUS instrument, data, image processing method and results are described in this chapter.

5.1 The MOS/ARGUS Instrument and Data Acquisition

5.1.1 Instrument Description

The ARGUS multi-fibre system is an Integral Field Spectroscopy (IFS) device wherein three-dimensional data (two spatial dimensions and one spectral) can be obtained for the purpose of studying small, extended astronomical objects. ARGUS rearranges the light from a $12.8'' \times 7.8''$ area of the sky into a long "pseudo-slit", the light from which gets dispersed in wavelength using the CFHT Multi-Object Imaging Spectrograph (MOS) system.

[1] CFHT run by the National Research Council of Canada, le Centre National de la Recherche Scientifique de France, and the University of Hawaii.

A schematic of the complete MOS/ARGUS system at CFHT is provided in Figure 5.1 (adapted from Figure 3 of Vanderriest 1995). At the entrance side of the fibre-optics system, the fibres are arranged in a lozenge-shaped array: 25 rows with a middle row consisting of 30 fibres and edges of 18. This fibre arrangement is shown in Figure 5.2. The fibre bundle collects the light at the Cassegrain focus (with the MOS mirror out), then redirects it into the collimator of the multi-object spectrometer. At the exit, successive rows of the lozenge are aligned vertically with the internal order maintained within each row. One-fibre-diameter "dead fibre" spacers have been inserted between each row in order to facilitate image reconstruction and geometrical distortion corrections. In all, there are 622 fibres: 594 active fibres plus dead fibre spacers. The total length of the pseudo-slit is 77.75 mm with some vignetting occurring at the edges. The ARGUS image layout is described in more detail in Section 5.2.1.

The fibres themselves are 80 cm long and have a 100 μm diameter silica core, with cladding which brings the total diameter up to 125 μm. The outer fibre cladding has been removed at the entrance so that the distance between adjacent fibre centres is 110 μm. Each 100 μm fibre samples a 0.40″ field, thanks to an enlarger mounted at Cassegrain focus which transforms the beam from F/8 to F/14.5 to account for focal ratio degradation within the fibres. At the exit, the MOS collimator (F/8) collects the beam. For a technical description of the Multi-Object Imaging Spectrograph, the reader is referred to the MOS User's Manual (Vanderriest & Bohlender, 1996).

By virtue of its two-dimensional collecting area of packed fibres, the key advantage of the ARGUS system is that it permits a greater light throughput than would be feasible using conventional slit spectroscopy, while providing the spectral resolution one would enjoy with a very thin slit. With a grism in place, the spectral resolution is similar to what could be obtained using a slit 100 μm wide, which would itself subtend an angle of 0.7″ on the sky. This instrument is ideal for obtaining spectra of extended

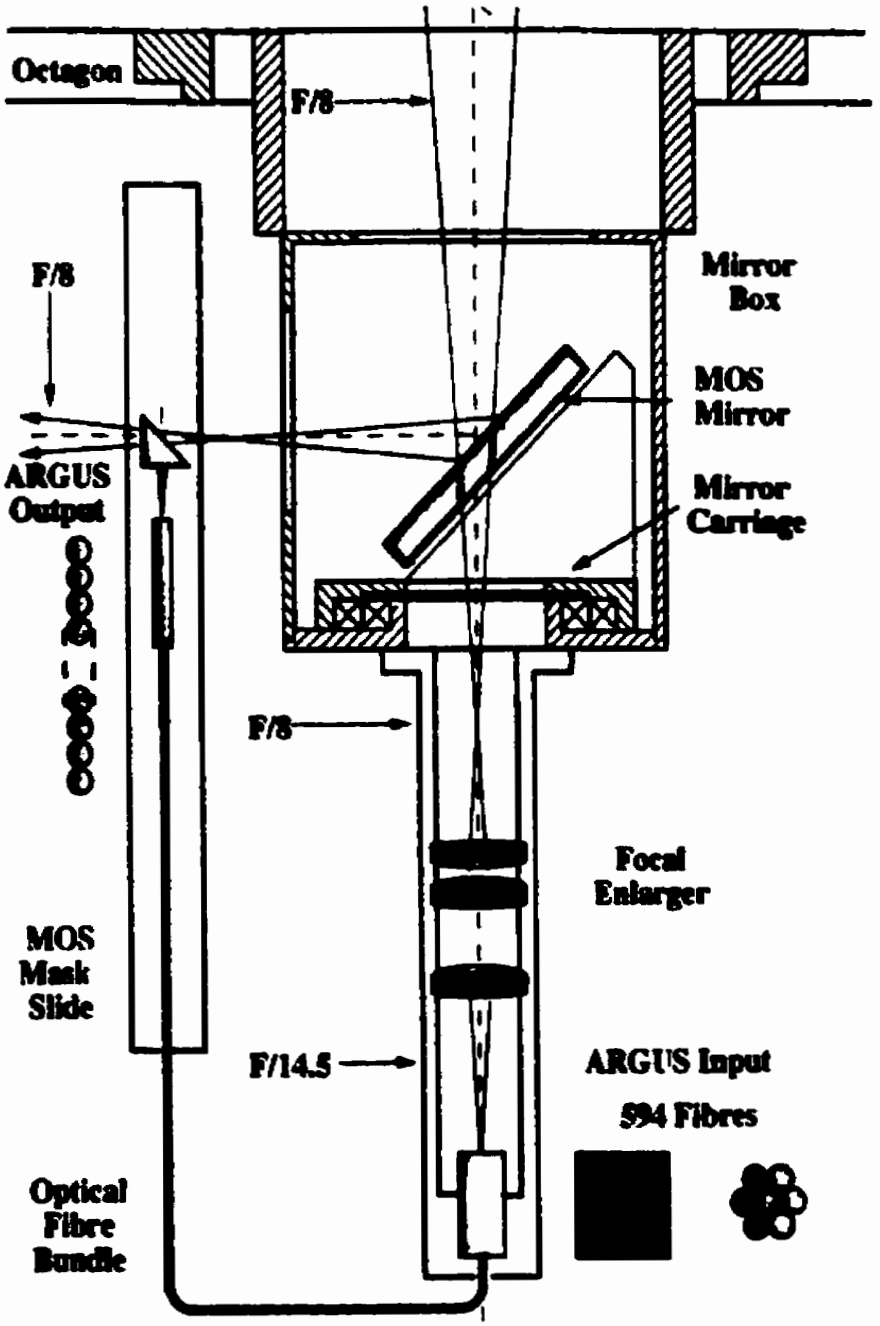

Figure 5.1: A schematic showing the MOS/ARGUS system (see Section 5.1 for details). This figure has been duplicated from Figure 3 of Vanderriest (1995).

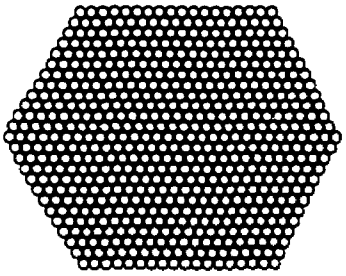

Figure 5.2: A schematic the ARGUS fibre arrangement. There are 25 rows of fibres with 30 fibres in the middle row.

resolved objects such as the M31 globular clusters, which themselves subtend effective diameters of a couple of arcseconds on the sky. Since the transmission of the fibres is $\sim$ 80% down to 2800 Å, the overall system throughput is quite high.

In addition to its greater throughput of light for a slit of comparable resolution, this instrument provides spectroscopic information while preserving some degree of spatial information over the extent of the target. With the large field of view obtained with MOS/ARGUS, one can collect most of the cluster light (minus the usual fibre losses) along with good simultaneous local sky sampling for the M31 globular clusters.

5.1.2 The Observations

The MOS/ARGUS observations of the M31 GCS were made by D. Hanes and K. Perrett at the CFHT 3.6 m telescope over the course of four nights from August 18 to 21, 1995, during which excellent (sub-arcsecond) seeing conditions were enjoyed. Individual integration times were set in the range of 100 to 300 seconds, depending on the brightness of the target.

The original intention for the MOS/ARGUS observations was to obtain data in the blue region of the spectrum (e.g. shortwards of $\sim$ 5500 Å) using the blue-sensitive Orbit CCD chip and an appropriate grism. As has been demonstrated in the preceding chapters, this spectral range is rich in absorption features and provides some favourable metallicity indicators. At the time of the observations, however, it was

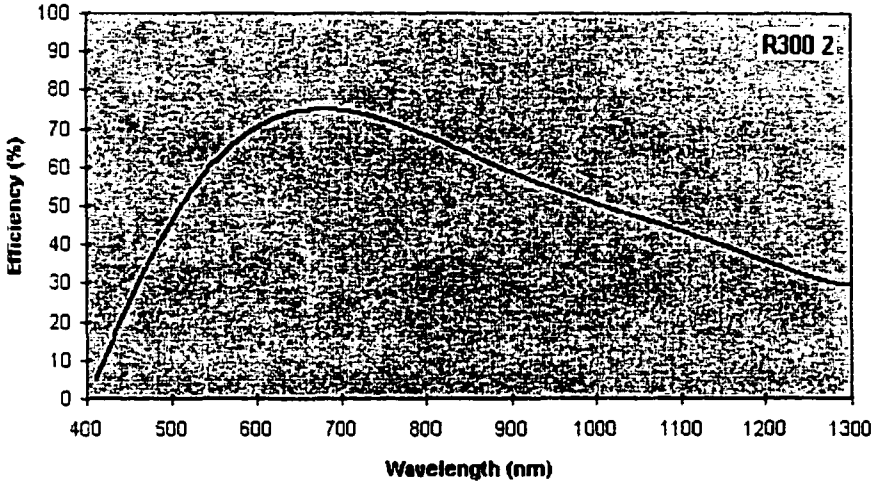

Figure 5.3: The response curve for the R300-2 grism used to obtain the ARGUS images at CFHT (obtained from the CFHT web site *www.cfht.hawaii.edu*).

learned that the blue-sensitive Orbit chip was not available for use due to unexpected delays in testing. The observing program was modified on-site to accommodate an available detector. The Loral3 detector (2048×2048 pix^2) was used with a nominal gain set to 2.37 electrons/ADU and with a readout noise of 5.3 electrons/pixel.

Unfortunately, the Loral3 detector had poor sensitivity below $\sim$ 6000 Å and, as a result, we opted to obtain lower dispersion spectra towards red and near-infrared wavelengths. At the time of the observations, no 600-line R grism was available. Therefore, the R300-2 grism was used, yielding a spectral resolution of around 7.5 Å. The spectral coverage with this grism was 4800 to 10 000 Å with a null deviation of $\lambda = 7307$ Å. The prominent absorption features in this range of the spectrum include NaD, H_α, and the CaII triplet. The response curve of the R300-2 grism used at CFHT is shown in Figure 5.3. The detector, mounted behind the re-imaging optics of the MOS instrument, yielded an image scale of 0.31″/pix for 15 μm pixels. Spectra were obtained with the MOS mirror out and grism in place (see Figure 5.1).

Centring of the target objects was achieved by taking a direct image of a bright guide star at the start of each night and at intervals thereafter. The centre of the

ARGUS fibre bundle was known to be located at pixels X = 111.5, Y = 110.0 for a 200×200 pix^2 sub-raster centred on pixel coordinate (1024, 1024). Targeting was facilitated by the fact that M31 globular clusters appear distinctly non-stellar on the display: the clusters were easily distinguishable from foreground stars. The focus was periodically adjusted during the night using a bright star in order to concentrate the light into a minimum number of fibres.

The target objects for this run were selected from the clusters in the Battistini et al. (1987) catalogue for which there existed no accurate radial velocity determinations from the literature. In particular, these included clusters for which no velocities had previously been determined, as well as those for which the uncertainties exceeded $\sim \pm 50$ km s^{-1}. The observations were obtained during the relatively short nights of August, yet we were able to obtain a total of 198 cluster spectra down to a limiting magnitude of $V \sim 17$. A log of the observations is provided in Table B.1. Figure 5.4 shows a plot of the major and minor axis positions of the M31 clusters observed at CFHT. There were 102 ARGUS targets which overlapped with the WYFFOS sample.

Comparison exposures of helium and neon/argon emission lamps were interspersed with the program object observations for the purpose of wavelength calibration. Spectral calibrations were obtained every hour or less during the night in order to compensate for internal flexure in the MOS/ARGUS instrument system as the telescope tracked M31 across the sky. According to the MOS manual (Vanderriest & Bohlender 1996), internal flexures of MOS and the CCD used for testing amounted to roughly 15μm at the focal plane of the detector over a motion of 4 hr across the sky.

Spectra of the halogen lamp and of the twilight sky were obtained for the purposes of flatfielding (see Section 5.2.1). Several Galactic globular clusters with well-determined velocities and [Fe/H] values were also observed, along with G and K giants with high-precision velocities for use as stellar templates. Spectra for several flux standard stars were also obtained in order to calibrate the absolute throughput of

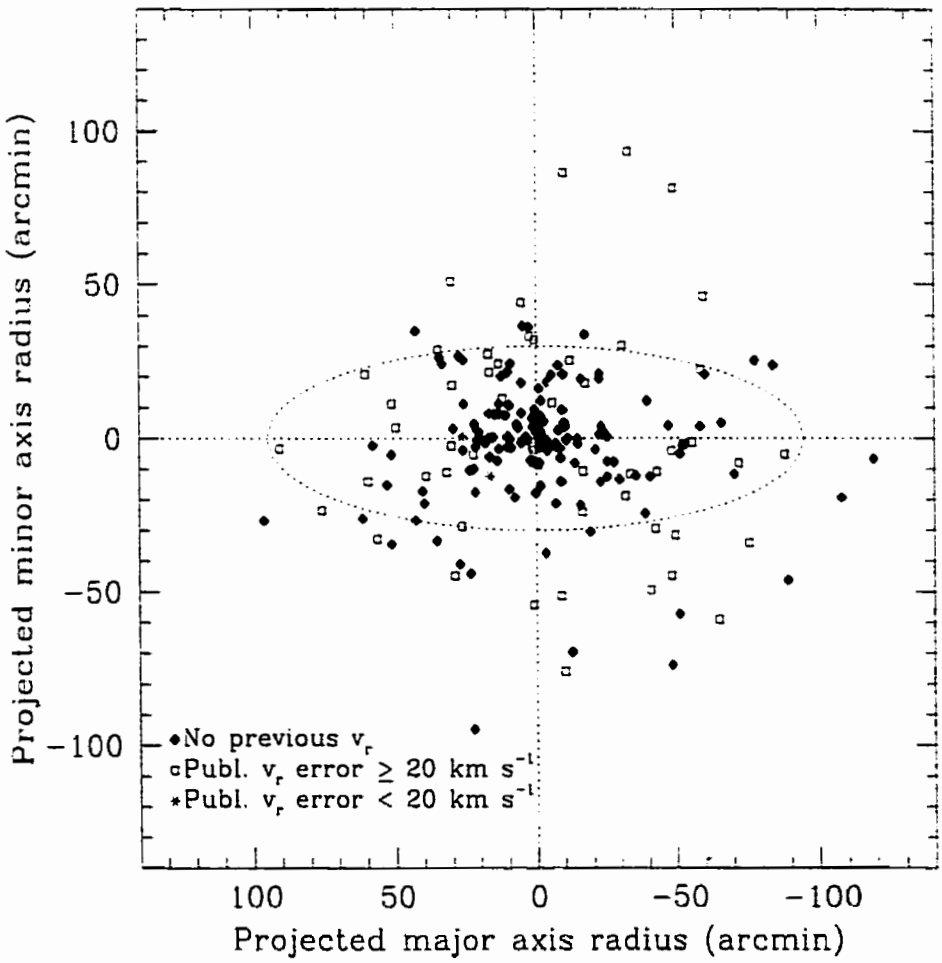

Figure 5.4: Major and minor axis positions for the 198 MOS/ARGUS targets observed at CFHT. Objects for which there exist no prior published velocity results are shown by the solid diamonds. M31 targets with low-precision previously-published results are represented by open squares, and those with high-precision velocities are shown by asterisks.

the fibres and to compensate for the wavelength-dependent sensitivity of the optical system (discussed later in Section 5.4.1).

5.2 ARGUS Data Reduction

The data reduction of the ARGUS images followed the same general procedure as outlined for the WYFFOS data in Chapter 3. Due to the unique image format of the data obtained, the reduction software was tailored specifically for dealing with the ARGUS fibre bundle output.

Image preprocessing, spectral extraction and direct image reconstruction of the ARGUS frames were facilitated by a set of IRAF procedures and FORTRAN code designed and written by D. Hanes. These tools were converted and combined into an IRAF task (named `ARGUS.cl`) by K. Perrett, incorporating minor modifications in technique and procedure. The particulars of this data reduction procedure are described in this section.

5.2.1 Image Layout and Preprocessing

A schematic of the fibre geometry and image layout obtained through the ARGUS/MOS system is shown in Figure 5.5. The dispersion axis is horizontal, following along the pixel rows of the CCD frame with wavelength increasing to the left. The spatial axis lies vertically along the image columns. Adjacent pixels along the pseudo-slit (i.e. along a column in the detector) correspond to successive fibres along a row in the focal image (i.e. same wavelength λ), and accordingly there is some degree of mixing in the spectra from different spatial points on the target object. Adjacent rows of fibres are separated by dead fibres intended for use as spacers in the data.

Preprocessing of the raw ARGUS frames included bias subtraction and distortion correction. Bias images were generated from the mean of 12 zero-duration exposures for the necessary raster sizes which were obtained over the course of the observing

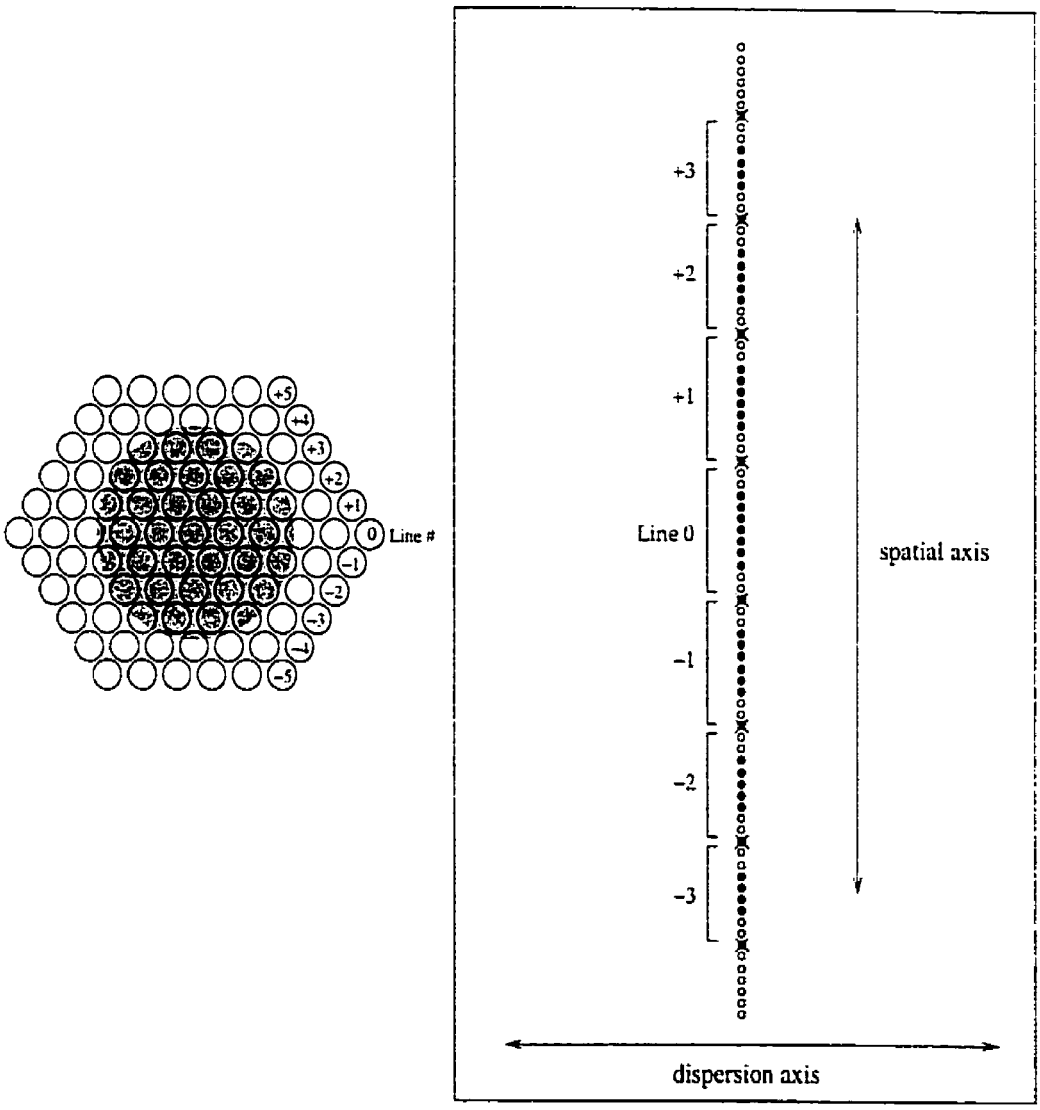

Figure 5.5: A simplified schematic of the image layout obtained using the MOS/ARGUS setup at CFHT. On the left is a stylized diagram of the ARGUS fibre bundle, showing the hexagonal packing of the fibres (small circles) overlying the light profile of the target object (large filled circle). The lines of fibres are reorganized onto the image as shown on the right, separated by "dead" fibres (shown with crosses). The light emerging from the fibres is dispersed along the horizontal axis.

run to provide a model of the bias levels of the CCD (bias subtraction is discussed in Section 3.2.1). Any deviations in the bias structure from night to night were found to be insignificant, thus a single mean bias frame was created by averaging all of biases obtained for a given raster. The overscan strip level from each image and the mean bias frame were each subtracted from the program images in order to remove the bias offsets and pixel-to-pixel structure in the chip, respectively. A sample bias-subtracted frame of an M31 globular cluster is shown in Figure 5.6.

Optical distortions within the instrument cause curvature which is typically most evident in the outer regions of the image. This curvature was removed prior to spectral extraction by mapping the dead fibre positions across the chip into straight rows using the IRAF task `geomap`, which computed the spatial transformation functions using a polynomial surface fit. The frames were then reconfigured into undistorted images using the geometrical transformation task `geotran`. The dead row positions were determined from the halogen spectral images, in which the entire fibre bundle was illuminated quite brightly. The distortion itself was discovered to be remarkably consistent from frame to frame, hence it was possible to apply the same spatial correction to each ARGUS image. Towards the top and bottom of each ARGUS frame, the variation in the vertical position of the dead fibre row was of the order of 6 pixels from the edge of the image to the centre. Towards the middle rows of the image, this variation was much less severe. In the straightened images, the null spectra corresponding to dead spacers were redistributed linearly along the CCD rows. Typical RMS uncertainties in the distortion corrected (row-straightened) images were of order 0.3 pixels across the frame.

Cosmic ray events appear as bright pixels within the data frame, and such features should generally be removed from the image during preprocessing. The ARGUS image format intrinsically yielded some large variations in brightness between adjacent rows of sky light, cluster light and dead fibre rows. As a result, a straightforward

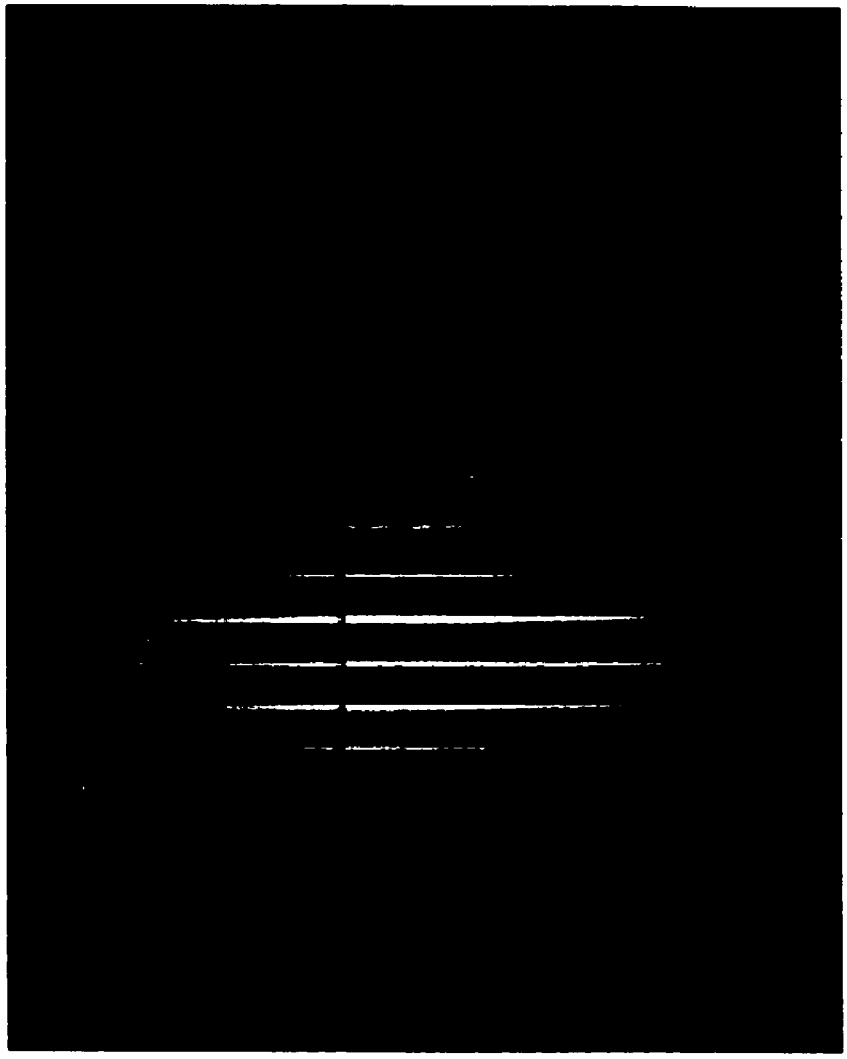

Figure 5.6: A sample preprocessed frame of M31 globular cluster B124 obtained with the MOS/ARGUS setup at CFHT. The dispersion axis is horizontal. Refer to Figure 5.5 for a frame layout schematic. Cosmic ray events are evident as small bright specks in the image.

sigma-clipping algorithm was inadequate for cosmic ray identification since this technique erroneously identified some of the feature lines as spurious counts. Instead, an algorithm was used whereby large positive deviations in brightness were identified initially only along (straightened) image rows. This stage flagged cosmic rays and hot pixels in addition to the nearly-vertical sky emission lines. The second stage of the algorithm then distinguished large sigma deviations along image columns, to remove the misidentified sky lines from the cosmic ray list. Cosmic ray hits were then removed by replacing each affected pixel with the median count value in the 15 pixels flanking the offending pixel. Several glancing cosmic ray events which fell by chance along image columns were unavoidably missed due to their orientation, but these few "hot pixels" were later flagged and disregarded in the final spectra.

The 618 fibre positions (including the 24 dead fibre spacers) were mapped to their exact output locations on the straightened frame using the known positions of the dead fibres in the ARGUS bundle, their measured output frame locations (dead rows), as well as the exact sizes and spacing of the individual optical fibres. A linear least-squares fit was used to determine the scaling of the frame: the fibre-to-pixel correspondence. The fraction of light from each fibre which got projected into a given row was found from the known physical extent of each fibre image output on the CCD.

More specifically, the coordinate system along the pseudo-slit was defined such that the centre of the first active fibre lies at $\mathcal{Y}_{ps} = 0.00$ along the pseudo-slit. Each fibre has an internal radius of 0.05 mm and a total outer diameter of 0.125 mm, including the cladding. The centre of the second fibre in the slit is therefore known to lie at $\mathcal{Y}_{ps} = 0.125$ mm, and so on. A least-squares fit was used to determine the correlation between the known dead fibre positions in millimeters ($\mathcal{Y}_{ps}$) and the measured pixel coordinate position $\mathcal{Y}_{CCD}$ for each of the dead fibre minima; these dead fibre positions were specified during using `geotran` during the image straightening

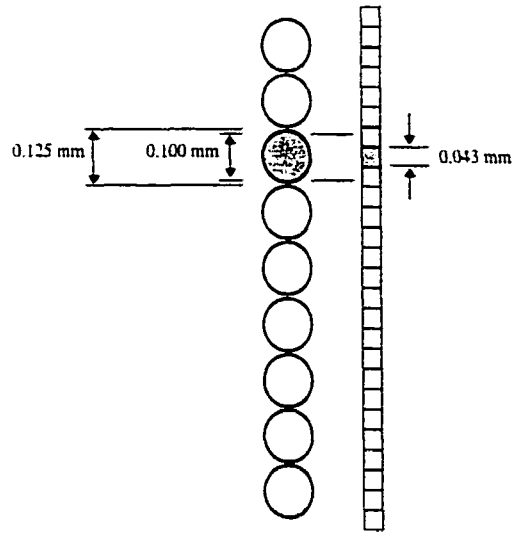

Figure 5.7: This schematic demonstrates the relative size of the ARGUS fibres (circles) and the CCD pixels (squares) in the plane of the pseudo-slit. Note that the individual fibres do not project into an integral number of rows, and some flux redistribution is required.

step discussed previously. The least-squares solution for images which used the full raster was

$$\mathcal{Y}_{\rm CCD} = 23.5\,\mathcal{Y}_{\rm ps} + 94.4 \tag{5.1}$$

where $\mathcal{Y}_{\rm CCD}$ is expressed in pixels and $\mathcal{Y}_{\rm ps}$ is in units of mm. The size of one pixel translates into $\mathcal{Y}_{\rm ps} = 0.043$ mm in the plane of the pseudo-slit. The "back-projected" limits of each CCD pixel were determined in this manner, thus defining the extent to which the light from a given fibre falls into any particular pixel. This understanding of how light from each fibre is divided among the pixels into which the fibre gets projected allowed for the integration of signal over the appropriate CCD area. Figure 5.7 shows a graphical representation of the fibre-pixel correlation as projected onto the pseudo-slit.

The flux was then redistributed into an output image such that each row on the image frame was set to correspond to the light from a single fibre. The dead fibres

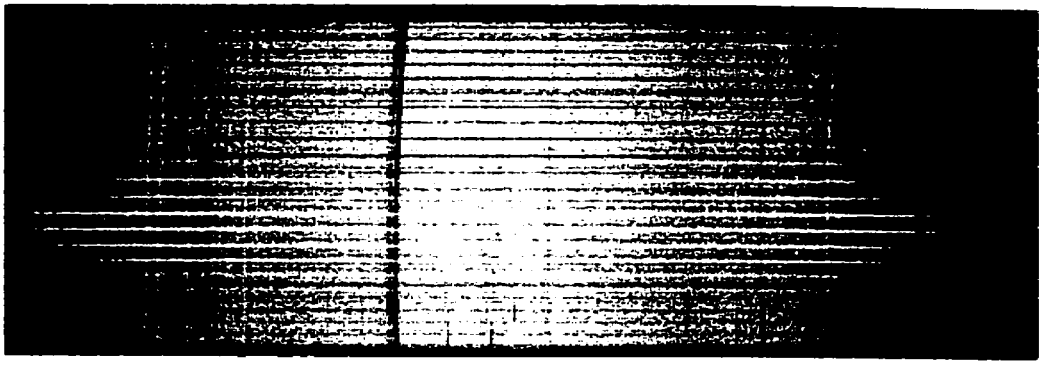

Figure 5.8: A sample ARGUS image of the M31 globular cluster B124 which has been straightened and flux-redistributed. The size of the original image was 1400 × 2048 pix^2, while the refluxed image shown here is 1400 × 594 pix^2. Note the remaining curvature along the vertical axis; it was not necessary to remove this curvature since each row was treated independently.

were discarded, leaving images consisting of 594 rows, one per fibre (most of the original target frames were initially 2048 rows). The effects of scattered light in the image were found to be negligible, and it was not necessary to pursue this form of correction for the ARGUS data. These straightened, flux-redistributed images served as the input frames to the spectral extraction software described below. A sample image is shown in Figure 5.8.

5.2.2 Reconstruction of the Direct Image

The bias-subtracted, straightened and refluxed images were used as input to the ARGUS task. First, it is useful to reconstruct the direct image of the target as it was incident on the fibre bundle, based on the output pattern received at the CCD from the pseudo-slit. This allowed for a visual inspection of the target field to identify and flag areas containing light from peripheral stars in the field as well as fibres which were flawed.

To reconstruct the direct image of the target on the CCD, the pixel data were collapsed along the dispersion axis into a single summed column. In this manner, each pixel value down the column represented the total light from one fibre over

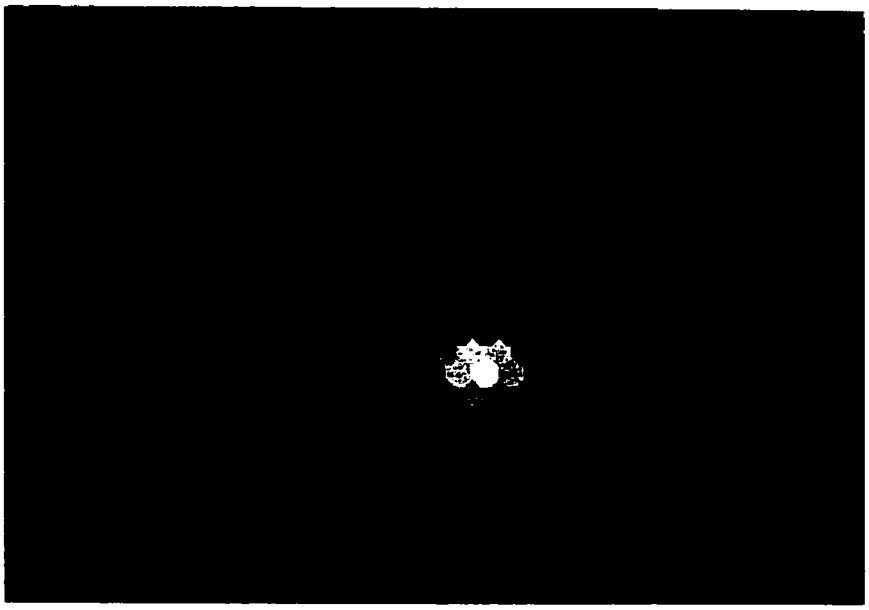

Figure 5.9: A sample reconstructed ARGUS image of M31 globular cluster B124. The hexagonal shape of the ARGUS fibre bundle is apparent. The bright area to the lower-right of the image centre indicates the region of the fibre bundle which was illuminated by cluster light. Note the fading (to the right) in the top row and a similar effect (to the left) in the bottom row. This is due to vignetting at the ends of the pseudo-slit.

a defined wavelength range. Each pixel's light was mapped onto the fibre's known coordinates in the hexagonal bundle, and the direct image of the target was recreated in a 400×300 pix^2 grid. An example of such a reconstructed ARGUS image is shown in Figure 5.9, and the full M31 GCS catalogue of direct images is given in Appendix C.

This image reconstruction was used to interactively define the extent of the target light in the fibre bundle, permitting the designation of sky fibres for later use in the sky subtraction procedure. The reconstructed frames were also useful for defining unwanted regions in the frame in order to omit them from the spectral extraction, these bad regions being due to image bleeding, companion objects, or defective fibres. At the completion of this step, the allocated target and sky fibre positions were marked on the direct image for verification.

5.2.3 Spectral Extraction

The light transmission efficiencies of the fibres were ascertained and tabulated by D. Hanes using twilight sky flatfield images with uniform illumination across the fibre bundle. The flux in each fibre was divided by the fibre's relative throughput to boost the less sensitive fibres and to decrease the response of those with greater light transmission, in essence creating the equivalent of a flatfielded image.

With the throughput correction complete, the mean sky brightness per fibre was determined from the average of the sky fibre intensities. The data were then summed over each target fibre to determine the signal-to-noise ratio (S/N) in each fibre. The S/N values for the cluster fibres were used to assign the fibre's weighting factor for the purpose of spectral extraction. This form of optimal extraction was used to construct the output spectrum from each fibre: pixels containing the lowest flux and largest uncertainties were duly assigned the lowest weights and vice versa.

The next stage was to set the dispersion (wavelength) scale for each spectrum. Composite "arc" frames were constructed by combining the nearest available helium and neon/argon emission lamp images which flanked the target observation in time of exposure. The input arc spectral images were preprocessed, straightened and refluxed in a manner identical to that for the program frames. As such, each fibre row in the composite arc images corresponded to the very same fibre row in the associated target spectrum. This made it a very straightforward task to assign an appropriate wavelength scale to the dispersed light collected by each fibre. The dispersion solution was computed in the same manner as the WYFFOS data, using the IRAF task `identify` in the central fibre row of the composite arc frame to semi-manually identify and compare bright spectral features from a table of accurately known He–Ne–Ar line wavelengths. A total of 35 to 40 lines were identified in the arcs spectra. The observed positions and wavelengths of these lines were fit with a 4th order cubic spline, yielding the dispersion solution. This reference dispersion solution and the feature database

with a 3 pixel tolerance were used to compute the wavelength scale of each fibre row individually.

The RMS of the dispersion fits were typically $\lesssim 0.1 - 0.15$ Å for roughly 38 lines over the wavelength range of interest. This value is satisfactory considering that, with the R300-2 grism's dispersion of 3.55 Å/pixel, this yields RMS errors on the wavelength scale which amount to less than ~ 0.04 pixels over the usable width of the chip. The IRAF task `dispcor` was used to assign the appropriate dispersion solution to each program spectrum fibre row.

Mean sky spectra were determined using the average of the dispersed light from the fibres beyond the radius of the M31 globular cluster target, as specified interactively by visual inspection of the reconstructed direct image. The vignetted ends of the pseudo-slit were omitted. In the case of the Galactic globular cluster calibration frames, where the cluster light spans the entire image and beyond, separate frames were obtained in a region of blank sky near the target. The mean sky spectrum was subtracted from each target, scaling the sky image by the ratio of the exposure times where necessary.

A high-S/N example of an extracted, sky-subtracted ARGUS spectrum for M31 globular cluster B225 is shown in Figure 5.10.

5.3 Radial Velocities from the ARGUS Data

The final one-dimensional extracted, dispersion-corrected and sky-subtracted ARGUS spectra were used to measure cluster radial velocities by cross-correlating them with template object spectra. This is the same procedure used for the WYFFOS data (Section 4.1.1).

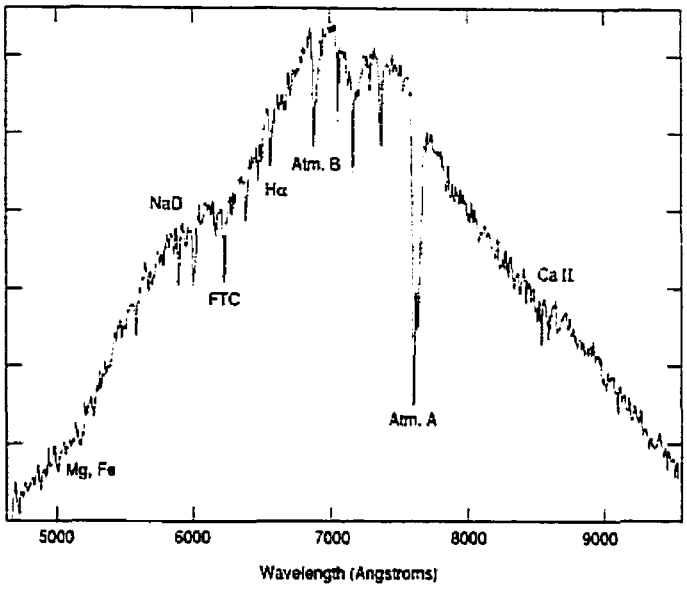

Figure 5.10: A sample extracted, sky-subtracted ARGUS spectrum of M31 globular cluster B225, with some of the absorption features labelled. The ordinate axis is linear in arbitrary units, with zero at the bottom.

5.3.1 Cross-correlations

A total of 12 radial velocity standards were observed in the hopes of securing the best radial velocity estimates possible. These calibrating templates are listed in Tables 5.1 and 5.2. Stellar template data given in Table 5.1 are from the Astronomical Almanac (1998): B1950 target right ascension (RA) and declination (Dec), visual magnitude V, stellar spectral type SpT and heliocentric radial velocity v_r of the stellar template and its associated uncertainty are provided. Galactic globular cluster data listed in Table 5.2 are from Harris (1996) and references therein: cluster coordinates (B1950), integrated V magnitude (V_t), integrated $(B-V)$ colour index (not corrected for reddening), colour excess E_{B-V}, integrated spectral type SpT, heliocentric radial velocity v_r, and metallicity [Fe/H].

Due to time constraints and equipment problems during the final night of observation, spectral calibration arcs were not obtained for every single one of the templates

Table 5.1: ARGUS stellar templates

Template	RA	Dec	V	SpT	v_r (km s^{-1})
HD12029	01:55:49.8	29:08:13	7.80	K2 III	-38.6 ± 0.5
HD22484	03:34:18.4	00:14:16	4.28	F9 IV-V	$+27.9 \pm 0.1$
HD149803	16:33:56.2	29:50:46	8.40	F7 V	-7.6 ± 0.4
HD171232	18:30:33.9	25:27:03	7.73	G8 III	-35.9 ± 0.5
HD194071	20:20:33.0	28:05:07	8.13	G8 III	-9.8 ± 0.1
HD213947	22:32:15.0	26:20:21	7.53	K4 III	$+16.7 \pm 0.3$

Table 5.2: ARGUS Galactic globular cluster templates

Template Name	RA	Dec	SpT V_t	$(B-V)$ E_{B-V}	v_r (km s^{-1})	[Fe/H]
NGC 5272	13:39:53.0	+28:37:38	F6	0.69	-148.5 ± 0.4	-1.66 ± 0.06
(M3)			6.19	0.01		
NGC 6171	16:29:43.0	-12:56:54	G0	1.10	-33.6 ± 0.3	-0.99 ± 0.06
(M107)			7.93	0.33		
NGC 6341	17:15:35.1	+43:11:21	F2	0.63	-122.2 ± 1.3	-2.24 ± 0.08
(M92)			6.44	0.02		
NGC 6356	17:20:40.1	-17:46:02	G3	1.13	$+27.0 \pm 4.3$	-0.62 ± 0.20
			8.25	0.28		
NGC 7078	21:27:33.3	+11:56:49	F3/F4	0.68	-107.5 ± 0.2	-2.15 ± 0.08
(M1)			6.20	0.10		
NGC 7089	21:30:54.9	-01:02:44	F4	0.66	-5.3 ± 2.0	-1.62 ± 0.07
(M2)			6.47	0.06		

at their corresponding telescope pointing positions. As a result, the wavelength calibrations for several of the targets (NGC 6171, NGC 6356, NGC 7078 and NGC 7089) were calculated using the nearest arcs possible in time and pointing position (hour angle), and were adjusted in zero point accordingly.

Comparisons between the velocities obtained when the final template spectra were correlated against each other are shown in Figures 5.11 (Galactic GCs) and 5.12 (stellar templates). These plots demonstrate a tight correlation between measured and true velocity for the ARGUS cross-correlation templates. The slopes of linear fits to the template velocities were consistent with the unity relation, and the RMS residuals of the fits were all lower than 9 $\mathrm{km\,s^{-1}}$.

5.3.2 Comparisons with Published Velocities

The M31 globular cluster spectra obtained with ARGUS were clearly of lower S/N than the velocity template spectra of Galactic globular clusters and stellar standards, and suffered more from the effects of high sky background. Therefore, specific wavelength ranges were selected to target the more distinct GC absorption features in these spectra. This allowed for the exclusion of atmospheric absorption lines, residual sky emission or cosmic rays, as well as any low-S/N regions which would substantially degrade the correlation results. The wavelength ranges selected for use in the cross-correlation procedure were: 4800 – 5400 Å (Hβ, Mgb triplet, Fe52 and Fe53), 6100 – 6600 Å (FTC, Hα), and 8400 – 8800 Å (CaII triplet). It should be noted that each spectrum was inspected and tested on a case-by-case basis, and that the cross-correlation ranges were modified appropriately in the presence of high sky background or spurious features. Unfortunately, the CaII triplet was often lost in strong residual sky lines and in second-order blue light, as no order-sorting filter was used to block second-order light at $\lambda \gtrsim 8000$ Å.

Each M31 globular cluster spectrum was cross-correlated with the velocity tem-

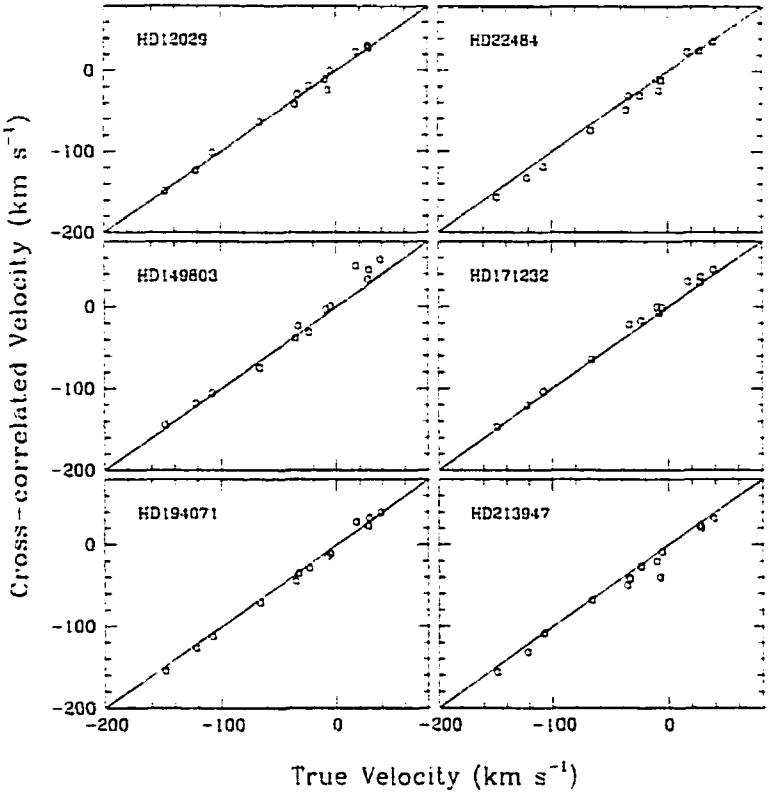

Figure 5.11: The results of cross-correlations between the stellar templates and the Milky Way GCs and the other stellar templates. The unity relation is shown by the solid lines.

plates independently to obtain up to 12 measures of its heliocentric radial velocity. A cross-correlation was deemed successful if the correlation function had a peak with $CC \gtrsim 0.3$ and the resulting heliocentric radial velocity fell within $2.5\sigma_v$ or roughly ± 375 km s^{-1} of the systemic velocity of M31 ($v_{\rm sys} = -300$ km s^{-1}). The accepted range of velocities is slightly more restrictive than that adopted for the WYFFOS correlations ($3\sigma_v$), since the ARGUS correlation peaks were considerably less prominent due to lower dispersion, lower S/N, residual sky lines, and the general lack of sharp metallic absorption features in the spectral range of these observations. Final M31 GC velocities and their associated uncertainties were determined from the mean

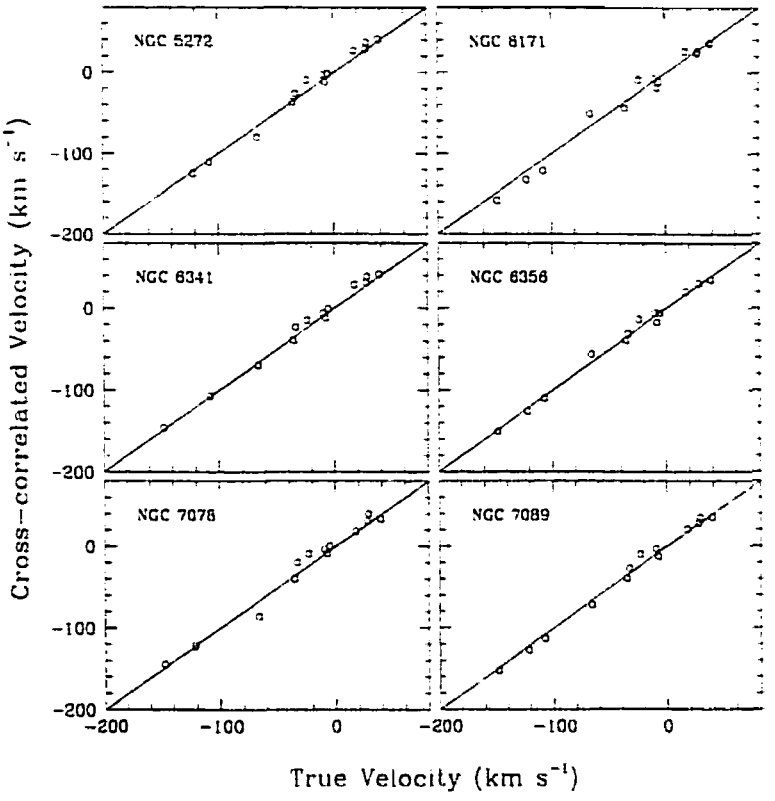

Figure 5.12: The results of cross-correlations between Milky Way globular clusters and the other cluster and stellar templates. The unity relation is shown by the solid lines.

of the cross-correlation results, weighted by the Tonry & Davis (1979) R-value.

Comparisons with published velocities are presented in Figures 5.13 and 5.14 to gauge the quality of the velocity results obtained from the various templates and to estimate their external uncertainties. Published velocities include those from Peterson (1989), Huchra, Brodie & Kent (1991), Federici et al. (1993), Dubath & Grillmair (1997), Barmby et al. (2000), and the WYFFOS results presented in Table 4.7 which overlap with the ARGUS sample. Robust fits were performed on the results using both the measured and published velocities as the independent variable, in turn. The bisectors of the resulting linear fits are shown in Figures 5.13 and 5.14, and the

Table 5.3: Correlation with published velocities

Template	intercept ($km\,s^{-1}$)	slope	RMS ($km\,s^{-1}$)
NGC 5272	-32.6	0.952	133
NGC 6171	-19.5	0.906	142
NGC 6341	-26.6	0.962	134
NGC 6356	-7.9	0.946	133
NGC 7078	-40.3	0.888	141
NGC 7089	-11.8	0.972	127
HD12029	28.5	1.068	120
HD22484	-38.3	0.927	134
HD149803	-61.0	0.943	103
HD171232	-11.9	0.996	122
HD194071	-5.3	1.010	118
HD213947	43.6	1.089	118

coefficients of the fits are provided in Table 5.3.

The RMS deviations in the measured velocities in the final column of Table 5.3 are $\sim 100 - 135\ km\,s^{-1}$. Unfortunately, this scatter and thus the external uncertainty in the ARGUS velocities are disappointingly high. In each panel of Figures 5.13 and 5.14, there is a smattering of points around zero measured velocity (i.e. at $x = 0$) which may be attributable to the effects of sky contamination on the cross-correlation results. Even the removal of these points did not bring the RMS deviations below about 80 $km\,s^{-1}$.

As mentioned previously, arc lamp spectra were obtained frequently during the observations (every 5 to 10 integrations), and a dispersion solution for each globular cluster spectrum was determined by interpolating between the solutions for the set of arcs preceding and following the target in question. The M31 globular clusters are at essentially the same pointing locations, and thus the only large variation in pointing occurs gradually over time as M31 makes its way across the sky. Subsequent arcs were found to yield dispersion solutions which were similar to within $\sim 0.001 - 0.0015$ Å

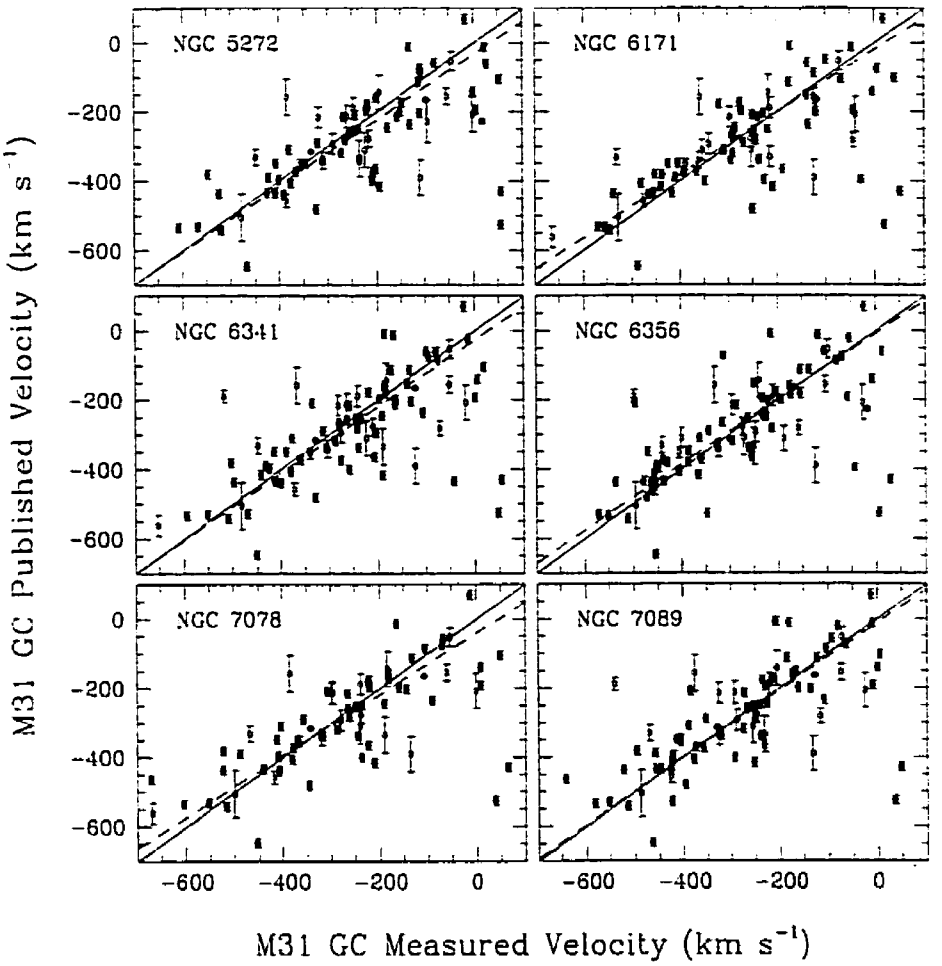

Figure 5.13: A comparison between measured and published radial velocities for the M31 GCs using each of the Galactic globular cluster velocity templates. Filled symbols represent high-precision published data with uncertainties lower than ± 15 km s^{-1}. Bisector robust linear fits to the data are represented by the dashed lines, and the unity relation is shown by the solid lines.

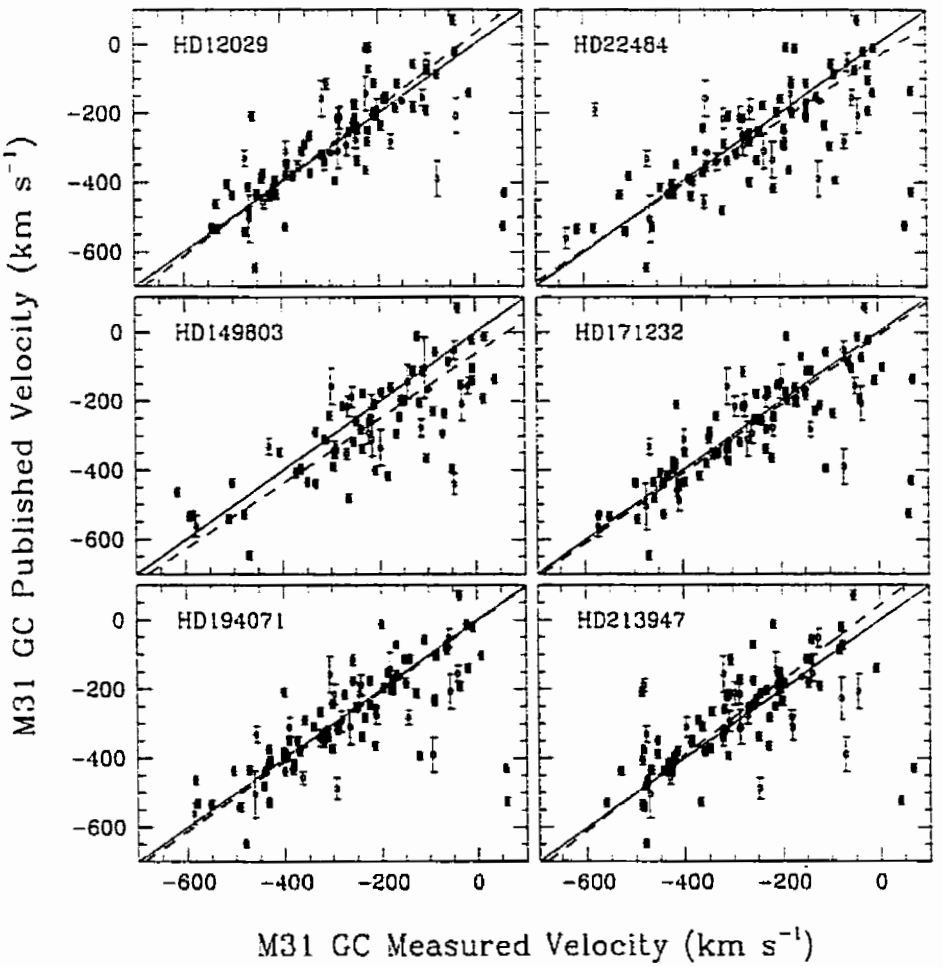

Figure 5.14: A comparison between measured and published radial velocities for the M31 GCs using each of the stellar velocity templates. Filled symbols represent high-precision published data with uncertainties lower than ± 15 km s^{-1}. Robust bisector linear fits to the data are represented by the dashed lines, and the unity relation is shown by the solid lines.

per pixel. It is unlikely that such small differences in the dispersion solution made a significant contribution to the variation in the cross-correlation results. As noted earlier, the desired blue-sensitive CCD was unavailable at the time of observation and we elected to work at lower dispersion and in the red and near-infrared spectral regime: at these wavelengths, the effects of ambient sky brightness can become prohibitive. This was found to be especially problematic at the CaII triplet above 8000 Å, and made it difficult to distinguish the correct correlation peak for some of the ARGUS spectra.

Spectral mismatch between template and object can seriously degrade the cross-correlation results. Therefore, the possibility of using a composite M31 globular cluster spectrum as a template was investigated to see if this provided a better match for the targets. A dozen or so of the higher S/N ARGUS spectra of M31 GCs with published high-precision velocities were each shifted to zero velocity, and then co-added to form the composite spectrum. However, this composite spectrum did not yield any significant improvement over the cross-correlation results for the M31 globular clusters.

5.4 Metallicities from the ARGUS Data

Due to residual sky lines and the large external uncertainties associated with most of the derived velocities from the ARGUS data, it was reasonable to investigate absorption feature strengths for only the Galactic template spectra and some of the high S/N M31 globular cluster spectra.

5.4.1 Flux Calibration and Absorption Corrections

Observations of spectrophotometric standards were obtained to provide a means of transforming the output spectra from the ARGUS task in scaled photon counts into real flux units. Good spectrophotometric standards such as white dwarf stars have

relatively thin stellar atmospheres and nearly featureless spectra with few absorption features. The observed flux standards include BD+25 3941 (B1.5 V), Feige 25 (B6 V), Kopff 27 (A3 V), and Wolf 1346 (DA white dwarf).

The IRAF task **standard** was used to generate a file containing flux calibration information, including observational data (e.g. spectrum name, airmass, exposure time, wavelength range), central bandpass wavelength, tabulated absolute flux per Angstrom, bandpass width, and the observed counts (i.e. instrumental intensity) in the bandpass. Pre-defined calibration data were available under the **onedspec** task in IRAF and consisted of wavelengths, calibration magnitudes and bandpass widths for commonly-used flux calibrators. The output observed instrumental intensities were integrated within the set of bandpasses listed in these calibration tables which fell entirely within the spectral range observed. A correction was made for the gradient in extinction across the bandpasses: this was accomplished by weighting the integral by the ratio of the extinction correction at each pixel to that at the central bandpass wavelength.

Next, the IRAF task **sensfunc** was used to determine the system sensitivity as a function of wavelength based on the flux calibrator measurements tabulated by **standard**. The sensitivity function calibration factor $\mathcal{SF}$ at each data point was calculated by:

$$\mathcal{SF}(\lambda) = 2.5 \log_{10} \frac{\text{counts}}{f_\nu \, \Delta\lambda \, t_{\text{exp}}}, \tag{5.2}$$

where f_ν is the flux per Å at a given bandpass, $\Delta\lambda$ is the width of the bandpass, and t_{exp} is the exposure time of the observation in seconds. Figure 5.15 shows a plot of the sensitivity function and its residuals.

Finally, the IRAF task **calibrate** was used to perform the flux calibration on the M31 globular cluster and template spectra. The spectra were each divided by the sensitivity function spectrum $\mathcal{SF}$, yielding output in flux units of ergs cm^{-2} sec^{-1} Å^{-1}.

One advantage of working in the red spectral region is that atmospheric extinc-

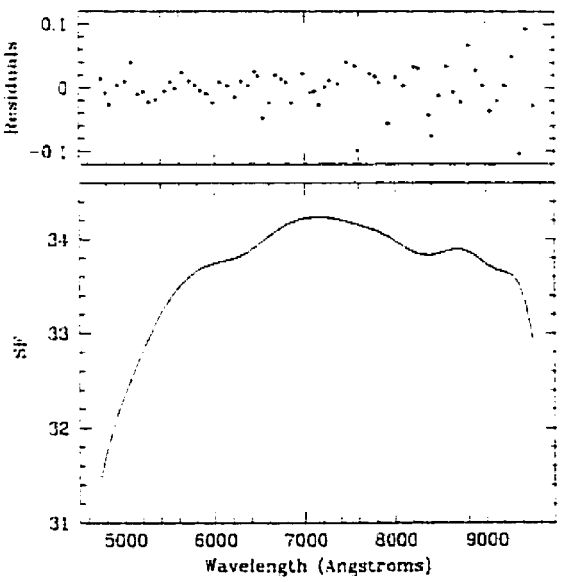

Figure 5.15: The sensitivity function derived for the MOS/ARGUS observations based on the observed flux calibrators (bottom). The residuals of the fit as a function of wavelength are shown in the top plot.

tion is somewhat less severe (refer to Figure 4.5). Nonetheless, it is still necessary to correct for the effects of atmospheric extinction and this was accomplished in the same manner as described in Section 4.2.1, applying corrections appropriate to the observatory location and target airmass. An example of a flux calibrated and extinction corrected M31 globular cluster spectrum obtained using MOS/ARGUS is shown in Figure 5.16. Reddening corrections for the M31 GCs were performed in the same manner as described in Section 4.2.2, incorporating additional unpublished E_{B-V} values where available (P. Barmby, private communication).

5.4.2 *Line Index Estimates*

Line indices were calculated from the generalized feature index defined in Equation 4.7. Feature bandpasses in the wavelength range relevant to the ARGUS data are listed in Table 5.4. Due to poor efficiency of the R300-2 grism at short wave-

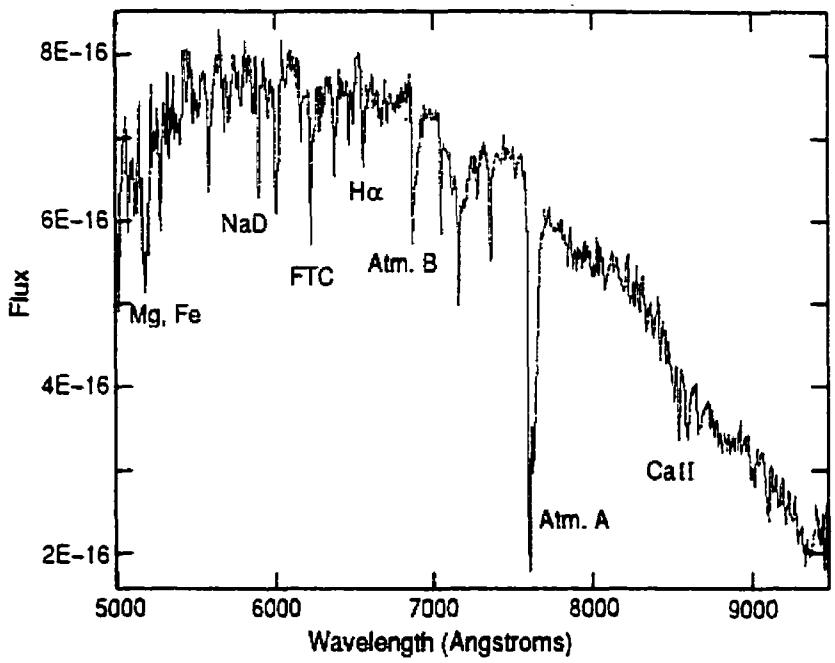

Figure 5.16: A flux calibrated and extinction corrected ARGUS spectrum of M31 globular cluster B225, with some of the absorption features labelled. Flux is measured in units of ergs cm^{-2} sec^{-1} $Å^{-1}$.

lengths (Figure 5.3), it was found that the S/N was too low to investigate lines below $\sim$ 5000 Å. The FTC feature listed in Table 5.4 represents the combined strength of the FeI+TiO+CaI absorption features (Brodie & Hanes 1986).

The CaII triplet lines are among the strongest features in near-infrared spectra and are sensitive metallicity indicators (Rutledge, Hesser & Stetson 1997). Several common definitions of the CaII triplet bandpass were investigated to probe the lines at λ8498, λ8542, and λ8662. The bandpasses defined by Armandroff & Zinn (1988: AZ88) and those from Rutledge, Hesser & Stetson (1997: R97) were found to provide the best measures of these features. Unfortunately, strong residual sky lines in this region and the washing out of spectral features due to second-order blue light prevented accurate CaII triplet feature strength determinations for most of the M31 globular cluster spectra.

Table 5.4: ARGUS line index definitions (Angstroms)

Index	C1	I	C2	Source
Mgb	5144.50 - 5162.00	5162.00 - 5193.25	5193.25 - 5207.00	BFGK
Fe52	5235.50 - 5249.25	5248.00 - 5286.75	5288.00 - 5319.25	BFGK
Fe53	5307.25 - 5317.25	5314.75 - 5353.50	5356.00 - 5364.75	BFGK
NaD	5863.00 - 5876.75	5879.25 - 5910.50	5924.50 - 5949.25	BFGK
FTC	5950.00 - 6100.00	6100.00 - 6330.00	6330.00 - 6480.00	BH86
Hα	6480.00 - 6515.00	6515.00 - 6575.00	6575.00 - 6610.00	BH86
CaAZ1	8474.00 - 8489.00	8490.00 - 8506.00	8521.00 - 8531.00	AZ88
CaAZ2	8521.00 - 8531.00	8532.00 - 8552.00	8555.00 - 8595.00	AZ88
CaAZ3	8626.00 - 8650.00	8653.00 - 8671.00	8695.00 - 8725.00	AZ88
CaR1	8346.00 - 8489.00	8490.00 - 8506.00	8563.00 - 8642.00	R97
CaR2	8346.00 - 8489.00	8532.00 - 8552.00	8563.00 - 8642.00	R97
CaR3	8563.00 - 8642.00	8653.00 - 8671.00	8697.00 - 8754.00	R97

Line indices were calculated for the Galactic globular cluster templates (Table 5.5), as well as for the M31 clusters which met the following requirements:

1. A minimum of 10 successful ($CC \geq 0.3$) cross-correlation results were obtained from the 12 templates, yielding an uncertainty in the weighted mean velocity of $\lesssim 15$ km s^{-1}. This demonstrated that most or all of the cross-correlations with the templates were internally consistent.

2. The target had a published velocity of reasonably high precision ($\lesssim 20$ km s^{-1}), and the absolute difference between the known velocity and that measured from the ARGUS spectra was $\lesssim 30$ km s^{-1}.

3. Visual inspection of the spectrum revealed that it was of sufficiently high S/N (e.g. it had visible absorption features), and did not suffer from strong residual sky lines.

Metallicity determinations for targets with uncertain or inaccurate cross-correlation velocities were not pursued, since a velocity uncertainty of 100 km s^{-1} corresponds

Table 5.5: Milky Way GC calibrating line indices

Name	Mgb CaAZ1	Fe52 CaAZ2	Fe53 CaAZ3	NaD CaR1	FTC CaR2	Hα CaR3
N5272	0.031	0.011	−0.011	0.021	0.015	0.050
	0.031	0.060	0.071	0.022	0.109	0.074
N6171	0.062	0.049	0.028	0.051	−0.001	0.042
	−0.015	0.071	0.152	0.041	0.141	0.148
N6341	0.039	0.015	0.011	0.021	0.006	0.031
	0.027	0.063	0.050	0.022	0.110	0.058
N6356	0.115	0.061	0.038	0.108	0.037	0.010
	0.026	0.141	0.110	0.043	0.218	0.116
N7078	0.015	0.009	0.003	0.045	0.008	0.046
	−0.003	0.013	0.024	0.002	0.067	0.034
N7089	0.030	0.017	0.005	0.030	0.010	0.043
	−0.004	0.045	0.048	0.015	0.111	0.066

to a potential shift of about $5 - 20\%$ of the feature bandpasses for most of the line indices listed in Table 5.4. A total of 17 M31 GCs satisfied the criteria listed above, and their calculated line indices are presented in Table 5.6[2].

All 17 of the M31 GCs used in the ARGUS line index measurements already had published metallicities; these values are provided along with the relevant references in the final column of Table 5.6 (WHT: the WYFFOS data: HBK: Huchra, Brodie & Kent 1991; B00: Barmby et al. 2000). The derived line indices from the ARGUS data were compared against these values of [Fe/H] to ascertain whether there was any significant correlation between our feature strengths and known metallicity. The results are presented graphically in Figure 5.17. Linear correlation coefficients were calculated for each of the indices, and Table 5.7 provides the results for the Milky Way + M31 GCs (column 2) as well as for the Milky Way calibrators only (column 3).

Despite the relatively high correlation coefficients for the Milky Way globular clus-

[2] The primary interest for the ARGUS study was to investigate the kinematics of a large sample of M31 GCs. Since MOS/ARGUS was not a multiplex instrument, the observation of 200 targets filled the available nights. It was thus not possible to achieve the S/N necessary for a full metallicity analysis.

Table 5.6: Line indices for some of the M31 globular clusters

Name	Mgb	Fe52	Fe53	NaD	FTC	Hα	[Fe/H]
	CaAZ1	CaAZ2	CaAZ3	CaR1	CaR2	CaR3	Ref.
B8	0.196	0.049	0.003	0.080	0.012	−0.005	−0.41 ± 0.38
	0.012	0.231	0.128	0.040	0.272	0.092	WHT
B10	−0.013	0.030	0.014	−0.032	0.036	0.019	−1.77 ± 0.14
	—	—	−0.055	0.147	—	−0.019	WHT
B16	0.114	0.143	0.084	−0.043	−0.020	0.009	−0.78 ± 0.19
	0.330	0.166	0.116	0.372	0.374	0.139	WHT
B28	0.141	−0.065	−0.019	0.109	0.021	0.051	−1.87 ± 0.29
	0.203	0.120	0.046	0.087	0.066	0.084	WHT
B33	0.416	0.142	0.213	0.040	0.006	0.040	−1.33 ± 0.24
	−0.024	0.076	0.103	0.034	0.171	0.051	WHT
B37	0.117	0.077	−0.021	0.144	0.041	−0.019	−1.07 ± 0.20
	0.048	0.166	0.164	0.086	0.224	0.173	WHT
B50	0.090	0.116	−0.057	0.111	0.023	−0.013	−1.42 ± 0.37
	0.024	0.114	0.063	0.050	0.143	0.062	WHT
B129	0.448	−0.205	0.180	0.050	−0.039	−0.054	−1.21 ± 0.32
	0.032	0.043	0.097	0.074	0.174	0.074	WHT
B130	0.057	0.007	0.006	−0.011	0.125	0.041	−1.28 ± 0.19
	−0.072	0.116	0.082	0.032	0.178	0.086	WHT
B190	−0.003	0.094	0.006	0.038	0.036	0.020	−1.03 ± 0.09
	0.031	0.099	0.110	0.007	0.128	0.087	WHT
B225	0.213	0.091	0.051	0.096	0.008	−0.006	−0.67 ± 0.12
	0.074	0.197	0.100	0.038	0.236	0.073	WHT
B234	0.126	0.033	−0.060	0.060	0.004	0.002	−0.95 ± 0.13
	−0.031	0.078	0.199	−0.035	0.140	0.182	WHT
B304	0.140	0.043	0.000	0.086	−0.117	0.035	−1.32 ± 0.22
	0.028	−0.002	0.074	0.080	0.138	0.041	B00
B313	0.117	0.072	0.083	0.073	0.040	0.003	−1.09 ± 0.10
	0.019	0.163	0.114	−0.016	0.152	0.093	WHT
B358	−0.024	−0.088	−0.056	0.059	0.015	0.030	−1.83 ± 0.22
	−0.119	−0.104	—	0.043	0.166	—	HBK
B383	−0.029	−0.080	−0.117	0.123	0.044	—	−0.48 ± 0.20
	0.037	0.139	0.152	0.000	0.203	0.142	B00
B400	0.100	0.250	−0.053	0.054	0.035	0.040	−2.01 ± 0.21
	0.166	0.222	0.057	0.139	0.204	0.053	WHT

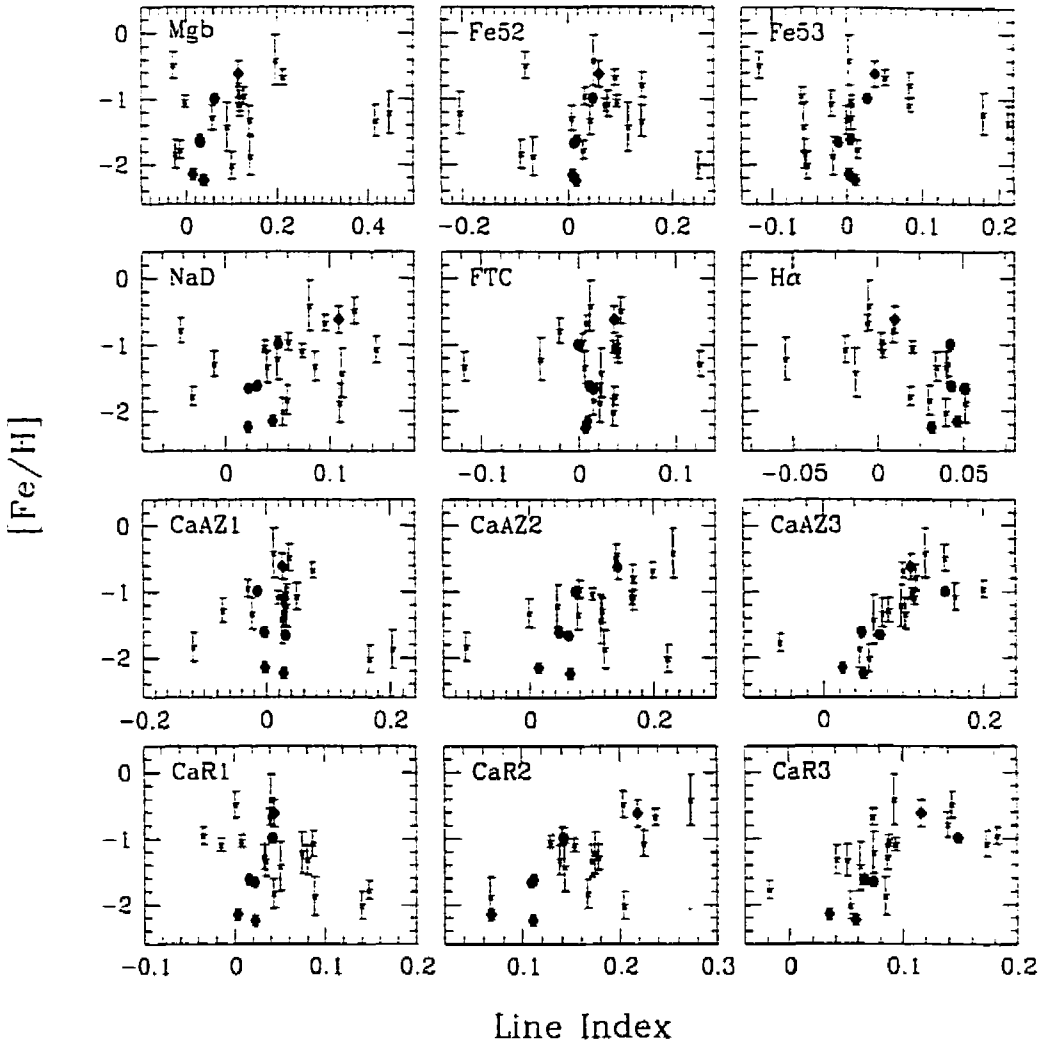

Figure 5.17: Measured line indices from the Galactic GC templates (filled diamonds) and several of the M31 cluster spectra (asterisks) as compared with their known [Fe/H] values. Linear correlation coefficients for these line indices and metallicities are provided in Table 5.7.

Table 5.7: Linear correlation coefficients

	(MW+M31)	(MW)
Index	r	r
Mgb	0.24	0.87
Fe52	0.05	0.92
Fe53	0.10	0.74
NaD	0.31	0.79
FTC	0.02	0.53
Hα	-0.53	-0.55
CaAZ1	0.06	-0.07
CaAZ2	0.49	0.81
CaAZ3	0.72	0.84
CaR1	0.02	0.86
CaR2	0.65	0.88
CaR3	0.61	0.87

ters, most of the M31 line indices did not demonstrate strong correlations with metallicity. The strongest correlations were for several of the CaII triplet lines (CaAZ3, CaR2 and CaR3), lines known to be sensitive metallicity indicators. The scatter in the remaining CaII lines may be due to contamination by residual sky lines and washing out by second-order light in this region of the target spectra. The Mgb, Fe52 and Fe53 features have all suffered from the low efficiency of the R300-2 grism at wavelengths $\sim$ 5000 Å. The large scatter in the NaD feature strengths shown in Figure 5.17 is possibly due to contamination by interstellar absorption lines, an effect noted also by Burstein et al. (1984). The FTC line index is defined over a large wavelength range and is therefore somewhat more sensitive to uncertainties in the adopted cluster reddening values. Note the distinct negative correlation in Hα with metallicity, an effect which is similar to that found for the Hβ Balmer feature measured for the WYFFOS spectra (Figure 4.14, see also Brodie & Hanes 1986).

Metallicity calibration for the ARGUS line indices was not pursued due to their (generally) poor correlation with [Fe/H]. Furthermore, the M31 GCs in the ARGUS

sample with high-S/N spectra and accurate velocities already have published metallicities, and we could not hope to improve upon these results with the current data.

5.5 Globular Cluster Widths

Integral field spectroscopy has the advantage of providing some degree of spatial information for extended targets, in addition to wavelength information. It is therefore possible to provide some measure of the relative sizes of M31 globular clusters in the MOS/ARGUS sample using the reconstructed images shown in Appendix C

The IRAF task `imexam` and the radial profile plotting option were used to estimate values of the full-width-at-half-maximum (FWHM) for the M31 GCs. Direct measurements of the FWHM for each cluster were obtained, each based on the azimuthally averaged flux profile in the direct image. The radius at which the profile dropped to half of its peak value was doubled to get the observed FWHM in pixels. The conversion from pixels to arcseconds was made using the image scale set by the image reconstruction technique. Centre-to-centre fibre separation is set to be 10.0 units in the rebuilt image, a distance which corresponds to 0.4″ (the angle subtended by each fibre after the focal enlarger). This yields a scale of 0.04″/pix in the reconstructed image.

The true width (W) of a cluster profile was estimated by deconvolving a simple Gaussian seeing profile from the observed cluster shape. The seeing can be characterized by the measured FWHM of point sources. In this case, the template stars and flux calibrators yielded a mean value of FWHM $\sim 0.6''$. Note that the reconstructed images are somewhat "steppy" due to the finite size of the fibres. The widths are estimates only, and can be considered accurate to $\gtrsim 0.5''$. The ARGUS M31 globular cluster results are presented in Table 5.8.

Table 5.8: M31 GC velocities and widths from the ARGUS data

ID	X (′)	Y (′)	v_r (km s^{-1})	W (″)	ID	X (′)	Y (′)	v_r (km s^{-1})	W (″)
B2	-22.0	21.4	-356.4 ± 33.0	0.8	B71	-7.4	3.1	-510.9 ± 8.5	0.6
B3	-21.9	19.9	-584.3 ± 10.3	0.9	B72	1.0	9.6	—	—
B4	-11.7	25.7	-346.9 ± 7.6	0.5	B74	17.3	22.1	-412.8 ± 35.7	1.1
B8	-15.5	19.9	-291.1 ± 5.2	0.8	B75	-0.8	7.8	-176.5 ± 18.9	1.3
B9	1.1	32.5	-236.3 ± 12.4	2.6	B77	-10.6	-0.4	-458.0 ± 6.4	2.5
B10	-16.7	18.6	-185.2 ± 3.8	1.8	B78	-2.2	5.9	-243.5 ± 5.5	0.6
B11	3.1	33.7	-342.1 ± 9.3	0.7	B80	-1.4	6.5	—	3.6
B13	-7.2	24.3	—	4.3	B81	-25.2	-12.4	59.2 ± 4.6	6.6
B16	-9.0	21.4	-429.1 ± 14.2	0.7	B84	-0.9	5.7	-437.5 ± 12.5	0.9
B25	-23.0	4.0	-164.3 ± 11.8	0.6	B85	-31.5	-18.4	-482.8 ± 5.6	1.1
B26	-3.6	18.5	-324.4 ± 12.7	0.7	B91	2.1	7.0	-336.4 ± 8.3	1.3
B28	-23.6	2.5	-414.0 ± 8.4	1.1	B96	0.3	4.6	-254.5 ± 7.0	0.6
B30	-24.8	1.1	-372.2 ± 17.9	1.3	B97	5.4	8.3	-239.3 ± 4.6	0.7
B31	-23.1	1.9	-283.3 ± 22.4	0.9	B99	-6.8	-1.3	-127.1 ± 5.9	1.5
B33	-21.6	1.8	-410.0 ± 10.1	1.0	B100	-22.4	-13.9	-348.5 ± 27.1	1.6
B35	9.4	24.4	-48.2 ± 21.4	0.6	B101	-8.0	-2.6	-456.9 ± 7.0	3.4
B36	-0.4	16.7	-320.8 ± 4.6	1.8	B102	12.6	13.3	-115.5 ± 13.3	0.7
B37	-9.0	9.5	-312.9 ± 3.0	1.8	B104	-0.7	2.9	-118.3 ± 31.6	1.4
B38	-5.5	12.0	-243.7 ± 8.3	0.8	B105	9.7	10.8	-392.3 ± 5.4	1.6
B40	-35.4	-11.9	-598.8 ± 27.8	0.7	B108	-7.2	-2.6	-442.5 ± 5.8	1.0
B43	-33.6	-11.4	—	4.6	B111	-13.6	-8.1	-51.8 ± 4.2	0.8
B46	17.1	27.4	—	0.8	B114	-3.8	-0.6	-119.1 ± 15.4	—
B47	13.7	24.6	-405.8 ± 13.1	1.7	B117	-16.1	-10.2	-566.4 ± 3.9	0.8
B49	-27.5	-7.4	-392.0 ± 24.4	1.7	B118	-2.2	0.3	-192.7 ± 43.6	—
B50	6.0	18.5	-139.3 ± 5.2	—	B119	0.2	2.1	-358.2 ± 7.8	1.5
B52	10.7	22.0	—	1.2	B122	13.4	11.5	-517.2 ± 4.2	1.1
B53	-1.4	12.5	-166.7 ± 9.3	0.2	B123	-4.8	-2.9	-542.3 ± 16.1	1.1
B55	-9.3	5.6	-244.2 ± 2.6	1.1	B124	-0.9	0.0	-29.3 ± 5.0	0.9
B56	-20.7	-3.5	-444.6 ± 19.5	3.0	B125	-8.6	-6.2	-468.3 ± 3.6	0.6
B57	-24.9	-7.2	-436.2 ± 6.5	0.7	B126	-2.8	-2.0	-147.0 ± 4.6	—
B59	-9.9	4.3	—	2.7	B128	-3.5	-3.6	-109.1 ± 91.7	4.8
B60	-14.1	0.3	—	1.4	B129	7.5	4.9	-65.6 ± 10.0	2.8
B62	12.6	20.3	—	1.0	B130	11.3	7.8	-44.6 ± 9.2	2.9
B66	-29.5	-13.2	-424.4 ± 14.0	0.7	B133	6.7	3.4	-376.8 ± 19.9	0.3
B67	-14.0	-1.1	-304.3 ± 5.6	2.3	B134	-0.8	-2.4	-212.4 ± 10.0	0.7
B70	-10.8	0.5	-77.3 ± 9.2	0.6	B136	3.8	0.7	-575.5 ± 12.8	7.3

CONTINUED ON NEXT PAGE

Table 5.8 –(CONTINUED FROM PREVIOUS PAGE)

ID	X (′)	Y (′)	v_r (km s^{-1})	W (″)	ID	X (′)	Y (′)	v_r (km s^{-1})	W (″)
B137	13.8	8.5	-272.7 ± 4.6	1.2	B215	21.8	-2.5	-254.4 ± 8.8	0.8
B138	3.2	-0.2	-323.2 ± 4.5	1.4	B216	26.9	1.0	-167.8 ± 18.4	2.7
B141	14.8	8.1	-726.0 ± 3.5	3.5	B220	22.4	-5.1	-218.1 ± 10.3	1.7
B144	1.8	-2.3	-6.7 ± 2.2	0.2	B222	10.2	-16.1	—	2.5
B146	1.6	-3.2	-58.3 ± 11.3	0.7	B223	26.4	-3.7	49.2 ± 24.9	1.3
B149	16.9	8.2	-78.4 ± 31.5	2.9	B225	16.5	-12.2	-134.9 ± 7.3	1.2
B150	6.0	-0.9	-227.0 ± 20.5	0.7	B226	8.3	-18.9	—	2.3
B156	-8.3	-13.5	-280.9 ± 27.8	0.9	B229	30.2	-2.3	-110.0 ± 9.7	3.2
B157	-0.3	-7.4	-202.2 ± 13.8	1.2	B231	22.4	-9.7	-310.5 ± 9.9	1.9
B159	10.7	1.1	-271.0 ± 28.2	0.8	B234	24.5	-9.8	-210.0 ± 8.1	0.8
B162	10.0	0.1	-167.7 ± 10.1	0.9	B236	-3.3	-37.3	—	1.1
B164	1.1	-7.3	-206.9 ± 19.2	0.8	B237	21.9	-17.4	—	0.9
B165	-0.2	-8.3	-70.5 ± 7.2	1.1	B239	32.6	-10.4	-104.9 ± 7.4	2.7
B167	2.7	-6.7	-158.6 ± 32.1	0.7	B289	-32.0	94.1	-177.8 ± 6.2	1.3
B168	26.4	11.6	-102.8 ± 34.2	2.6	B290	-47.7	82.4	—	1.9
B169	3.9	-6.2	—	2.6	B291	-8.9	87.2	-297.4 ± 5.1	1.2
B170	-15.5	-21.5	-374.0 ± 94.7	2.6	B292	-58.5	47.1	-467.7 ± 7.4	1.3
B172	9.1	-2.9	-313.1 ± 6.1	1.0	B294	-83.4	24.4	-151.7 ± 6.5	0.6
B173	10.2	-2.6	—	1.1	B296	-77.1	25.9	-485.2 ± 20.1	0.8
B176	-15.8	-23.5	49.3 ± 6.0	1.2	B297	-118.2	-6.3	-388.6 ± 10.8	1.2
B181	15.8	0.9	—	2.9	B298	-58.2	22.7	-510.3 ± 5.0	0.9
B184	22.2	4.8	-175.1 ± 16.9	2.0	B299	-59.8	21.2	—	3.1
B186	22.1	4.6	—	—	B300	-107.0	-18.8	-332.4 ± 71.6	1.6
B187	17.1	0.4	—	2.5	B301	-87.8	-4.9	-360.9 ± 29.5	2.7
B188	13.2	-3.3	-166.7 ± 8.0	3.3	B303	-65.5	5.2	—	1.1
B189	21.9	3.3	-70.3 ± 3.9	1.4	B304	-30.7	30.4	-355.9 ± 11.3	1.1
B190	20.9	2.4	-85.7 ± 6.1	0.7	B309	-71.9	-7.9	-662.8 ± 7.3	1.7
B194	-0.8	-15.2	-50.7 ± 20.8	3.1	B310	-17.0	34.0	-539.8 ± 10.5	3.1
B196	-18.9	-30.2	—	2.1	B313	-39.1	12.5	-440.6 ± 3.9	0.8
B197	18.6	-1.0	-194.2 ± 7.1	1.1	B314	-69.9	-11.1	-176.3 ± 11.0	3.1
B198	20.0	0.0	-49.1 ± 28.9	1.5	B315	-55.6	-1.1	-672.4 ± 5.5	2.1
B199	-6.5	-20.8	-395.0 ± 17.3	1.1	B316	-47.0	4.3	-389.5 ± 14.9	—
B203	21.2	-0.4	-172.5 ± 7.0	1.2	B317	5.6	44.4	-72.1 ± 10.9	0.8
B207	0.9	-17.3	-210.2 ± 16.5	3.2	B318	-52.1	-1.4	-172.3 ± 54.8	3.3
B208	14.3	-6.8	-271.2 ± 15.9	1.0	B319	-52.0	-1.8	-563.7 ± 10.8	1.2
B214	17.2	-5.5	-265.2 ± 8.1	0.8	B323	-51.2	-4.9	—	1.9

CONTINUED ON NEXT PAGE

Table 5.8 –(CONTINUED FROM PREVIOUS PAGE)

ID	X (′)	Y (′)	v_r (km s^{-1})	W (″)	ID	X (′)	Y (′)	v_r (km s^{-1})	W (″)
B324	3.0	36.4	—	2.1	B375	39.5	-12.0	-373.7 ± 28.8	0.8
B327	-47.6	-3.5	-425.4 ± 13.0	1.3	B377	-8.3	-50.8	-272.2 ± 7.4	2.4
B330	5.2	36.9	-315.9 ± 14.5	1.1	B378	51.7	-5.1	—	1.3
B337	30.9	51.5	—	1.2	B380	58.5	-1.8	-60.4 ± 28.3	3.5
B339	-75.4	-33.8	-227.8 ± 5.6	2.8	B382	40.8	-16.9	—	1.4
B340	-88.9	-46.2	—	0.9	B383	27.0	-28.4	-234.3 ± 3.5	1.7
B341	-42.8	-10.6	-399.9 ± 3.1	1.3	B385	40.6	-20.6	—	0.9
B342	-40.4	-12.3	-562.8 ± 7.0	—	B387	1.9	-53.7	—	3.0
B345	-49.6	-31.6	-276.3 ± 8.4	—	B389	53.7	-14.6	—	0.8
B346	-38.8	-24.5	—	1.0	B390	-12.0	-69.2	41.9 ± 18.3	0.7
B347	27.7	26.8	-195.0 ± 12.3	1.5	B391	43.5	-26.2	—	1.6
B348	26.1	25.5	-288.6 ± 6.3	0.6	B392	60.0	-13.6	—	5.4
B350	-42.2	-29.2	-414.0 ± 11.2	1.6	B393	36.2	-32.8	—	2.5
B351	42.9	35.1	-305.5 ± 9.0	2.0	B394	24.3	-43.5	—	1.3
B352	35.6	29.3	-198.1 ± 7.4	1.0	B395	27.7	-40.9	-233.3 ± 7.6	2.2
B354	35.2	26.8	—	1.4	B396	-9.6	-75.5	-647.0 ± 12.1	0.8
B355	33.9	24.6	-164.2 ± 8.0	0.8	B397	30.0	-44.1	-30.7 ± 4.6	1.3
B356	30.1	17.4	-30.5 ± 11.9	2.9	B398	62.0	-25.6	-11.7 ± 19.0	1.3
B357	-47.9	-44.5	-230.5 ± 11.8	1.0	B399	51.9	-34.2	-472.9 ± 6.3	2.1
B358	-64.4	-58.7	-316.7 ± 5.5	1.8	B400	91.1	-3.0	-249.1 ± 3.8	0.8
B360	-50.4	-56.8	—	1.3	B401	57.0	-32.2	-469.2 ± 10.9	3.3
B361	-40.3	-49.2	-483.1 ± 164.4	2.8	B402	76.5	-23.1	-343.9 ± 28.4	1.6
B362	29.9	3.3	-32.9 ± 5.0	0.7	B406	97.3	-26.0	-48.4 ± 15.1	1.5
B365	61.0	21.4	-103.2 ± 6.3	0.9	B408	23.3	-94.1	—	0.8
B366	51.6	11.6	61.1 ± 17.7	2.3	NB6	-2.2	0.3	62.0 ± 17.4	1.5
B369	-48.0	-73.6	-236.4 ± 12.6	2.3	NB16	2.0	4.2	-291.7 ± 7.2	2.5
B370	50.0	3.7	—	1.6	NB21	-0.9	0.8	-600.3 ± 6.8	0.3

6. ANALYSIS OF THE COMBINED SAMPLE

The results derived in the previous chapters are now combined with published values from other sources in order to provide a comprehensive analysis of the kinematics and abundance properties of the M31 globular cluster system.

6.1 The Best Current Spectroscopic Sample

The WYFFOS results were merged with the velocities and [Fe/H] values from the literature to produce the best available sample of spectroscopic data for the globular clusters of M31. The ARGUS results were not incorporated in this sample due to the large scatter in their final velocities. Wherever data from other publications overlapped with the WYFFOS sample *and* demonstrated smaller associated uncertainties, these data superseded the WYFFOS results; such cases are noted in the final column of Table 4.7. In this final sample, 191 WYFFOS velocities and 189 metallicities were combined with additional data from Peterson (1989), Huchra, Brodie & Kent (1991), Federici et al. (1993), Dubath & Grillmair (1997), and Barmby et al. (2000) to yield a complete M31 globular cluster spectroscopic database comprising 321 velocities and 301 metallicities.

Barmby et al. (2000) identified the following targets as having spectral properties which are inconsistent with globular clusters (e.g. strong NaD absorption, narrow absorption line widths, unusual continuum slope, and/or radial velocities inappropriate to M31 membership): B55-S116 (stellar), B308 (galaxy), B341-S81 (stellar) and B392-S329 (stellar). I concur with the identification of B308 as a definite non-cluster and with that of B392-S329 as a probable non-cluster, and do not carry these through

the remainder of the analysis. However, based on the WYFFOS spectra, there is no clear indication that the other objects should be rejected as confirmed non-clusters.

In an effort to verify that there are no obvious biases in the metallicity sample studied here, the colour distribution of the WYFFOS sample was compared to that of the overall M31 GCS. The mean estimated intrinsic colour of 412 M31 globular clusters with $(B-V)$ data from Barmby et al. (2000) is found to be $(B-V)_0 = 0.67 \pm 0.04$, while that for the clusters with [Fe/H] values used in the metallicity analysis presented herein (264 clusters with colours) is $(B-V)_0 = 0.65 \pm 0.05$. Based on this and a comparison of the colour histograms for the metallicity sample and the overall GCS shown in Figure 6.1, there do not appear to be any significant population biases with respect to the colour of the metallicity sample presented herein. A Kolmogorov-Smirnov two-sample test on the distributions in Figure 6.1 confirms what the eye suggests: the colour distribution of the metallicity sample is drawn from the same parent population as the overall colour sample at a high confidence level (99.5%).

Clearly, the globular clusters at small galactocentric radii will suffer from more severe effects of incompleteness due to obscuration by the disk and bulge of M31. Depending on the colour/metallicity distribution as a function of position within the galaxy, this observational effect will conceivably bias the observed metallicity sample. This point will be discussed further in Section 6.2.2.

6.2 M31 Cluster Metallicities

The metal abundance properties of M31's globular clusters are of interest as they bespeak the galaxy's formative processes and enrichment history. The metallicity distribution for the M31 GCS is presented in Figure 6.2 along with a similar plot of the Milky Way GCS for comparison. The mean metallicity of the full complement of 301 M31 globular clusters is [Fe/H] $= -1.21 \pm 0.03$, in excellent agreement with the

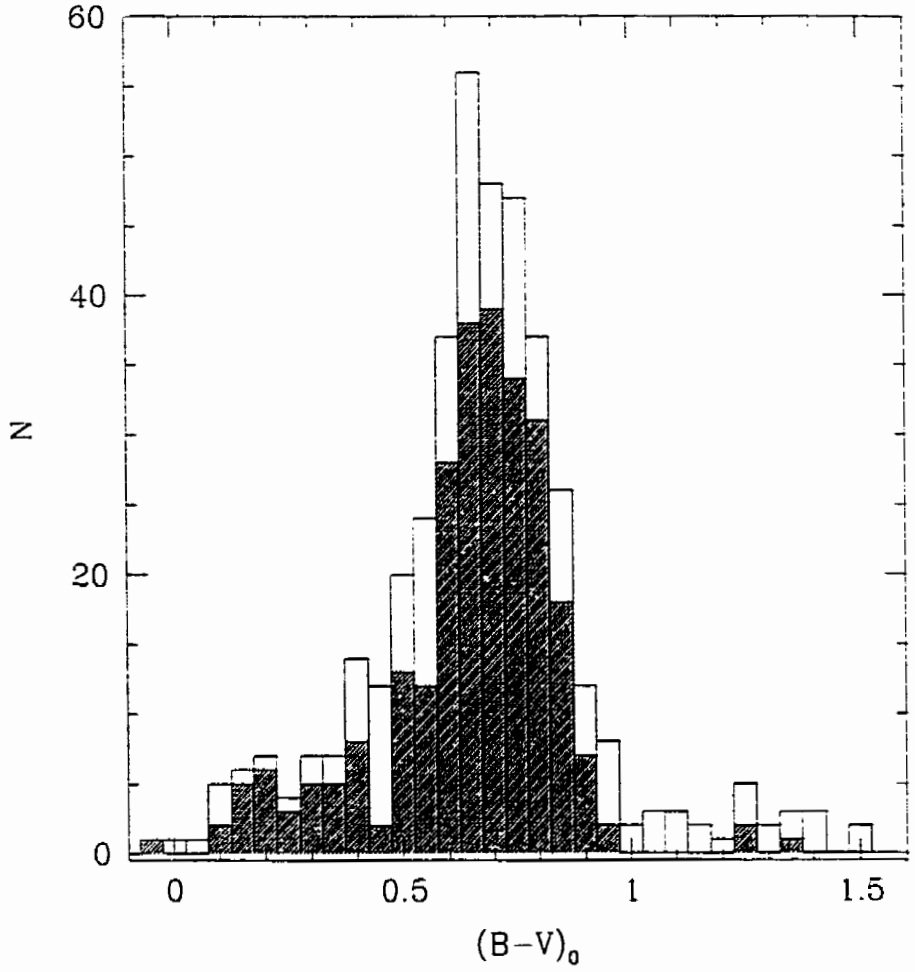

Figure 6.1: The colour distribution of the M31 globular clusters for which there are spectroscopic metallicities (shaded) as compared to the overall colour distribution of the GCS (solid line). There is no sign of a colour bias in the metallicity sample as compared to the overall M31 cluster population with available $(B-V)$ colours from Barmby et al. (2000).

value of [Fe/H] = −1.2 obtained by Huchra, Brodie & Kent (1991) for their sample of 150 spectra. The M31 cluster system's mean [Fe/H] is also comparable to the value of -1.27 ± 0.05 obtained for the Milky Way GCS (based on data supplied in Harris 1996, revised 1999). However, a Kolmogorov-Smirnov test reveals that the Galactic and M31 globular clusters have [Fe/H] distributions which are *not* drawn from the same parent population. This difference will be explored in the upcoming section.

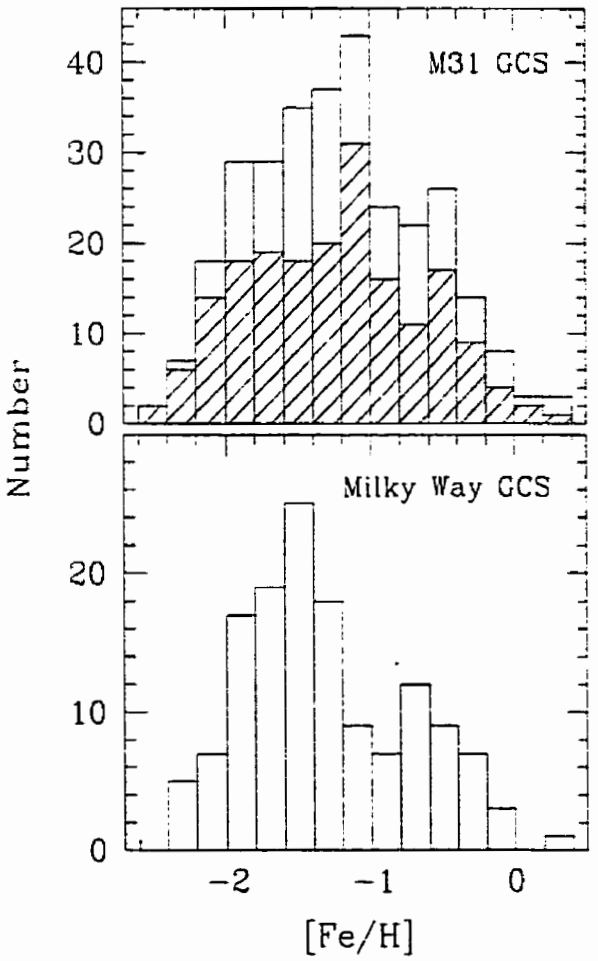

Figure 6.2: The metallicity histogram for the M31 cluster system (top) and the Milky Way GCS (bottom) for comparison. The shaded area in the top plot represents the M31 WYFFOS data.

6.2.1 KMM Mixture-modeling

As is frequently the case with binned data, the appearance of a histogram can be ambiguous and potentially misleading, and thus a more robust method of analysis is desirable. In order to examine the shape of the metallicity distribution without relying on binning methods, the KMM algorithm used by Ashman, Bird & Zepf (1994) is employed.

KMM mixture-modeling provides a method of quantifying the significance of multi-modality in data sets. The usefulness of the KMM algorithm as applied to astronomical data sets is described in Nemec & Nemec (1991) and Ashman, Bird & Zepf (1994). In brief, KMM fits a specified number of Gaussian distributions to the data, calculates maximum likelihood estimates of their respective means and variances, and then determines the improvement of the fit over a single Gaussian fit to the data. The significance of the result is tested over the null hypothesis which states that "a unimodal Gaussian parent population is a good description of the observational data".

The KMM algorithm for astronomical univariate data sets has kindly been made available for download by Ashman, Bird & Zepf. The code accepts user-specified initial estimates for parameters such as the number of groups (N_g), the mean, variance and mixing proportions. The *a posteriori* probability that each object belongs to any given group is determined and the object is "assigned" to the group for which it has the largest residence probability. The program re-fits the data and continues to iterate through this procedure until the object assignments stabilize.

The output from the KMM routine provides a value for the likelihood ratio test statistic (LRTS), an estimator of the improvement of an n-modal fit over the unimodal case. The significance of the multi-modal fit over the null hypothesis is given by the p-value, the probability that the LRTS would be greater than or equal to the one computed for the data in the event that the null hypothesis is true. Small p-values

($p < 0.05$) indicate that the unimodal case can be rejected at high ($> 95\%$) confidence (Ashman, Bird & Zepf 1994).

The KMM technique presumes that each data point is independently drawn from a parent population which is composed of an admixture of Gaussian distributions. This means that although this analysis is not plagued by the biases presented by binning methods, it assumes an underlying Gaussian probability density for each sub-sample. The KMM test has previously been applied to the M31 globular cluster metallicity distribution by Ashman & Bird (1993), albeit with a significantly smaller data sample.

First, a bimodal distribution was tested against the assumption of a unimodal shape (the null hypothesis) for the GCS metallicities. Since there is no obvious reason to assume that both [Fe/H] groups in a bimodal fit would exhibit a common variance, heteroscedastic fitting was applied such that the variances for the two distributions were not constrained to be identical. The KMM results revealed that this 2-group fit demonstrated a marginal improvement over a single group fit, although Ashman, Bird & Zepf (1994) caution that the output probability in the heteroscedastic case is more difficult to interpret and may, in and of itself, be suspect. The KMM test was repeated on more than 1500 simulations with bootstrap resampling and revealed that the bimodal case is significantly preferred over the unimodal distribution at a median confidence level higher than 97%. The bimodal test returned Gaussian fits characterized by means at [Fe/H] $= -1.44$ ($\sigma = 0.47$) for the metal-poor distribution and at [Fe/H] $= -0.50$ ($\sigma = 0.36$) for the metal-rich clusters. The *a posteriori* probabilities of group membership returned by KMM assigned 231 clusters to the metal-poor distribution and 70 to the metal-rich population (Figure 6.3).

In their analysis, Elson & Walterbos (1988) treated the M31 GCS as comprising three distinct metallicity sub-populations: metal-poor, intermediate, and metal-rich. The KMM test was used to ascertain whether a trimodal distribution is also con-

sistent with the measured [Fe/H] values for the M31 cluster system. The trimodal KMM results with bootstrap resampling demonstrated that a 3-group fit was indeed preferred over a single Gaussian distribution at a relatively high confidence level (96%). The output population means obtained for the best 3-group fit are located at [Fe/H] $= -1.59$ ($\sigma = 0.44$), -1.18 ($\sigma = 0.42$) and -0.47 ($\sigma = 0.35$). The numbers of clusters assigned to each group were N =153, 76 and 72, respectively. The trimodal fits are shown in Figure 6.4.

In light of the variation in the magnitude of [Fe/H] uncertainties quoted within the WYFFOS sample and others, it is appropriate to test the effects of these uncertainties on the inferred shape of the distribution. There were 229 GCs which had metallicity uncertainties less than 0.45 dex, a value roughly equal to the variance of one of the populations as determined from the bimodal results. KMM was applied to this higher-precision sample to test the stability of the earlier conclusions. The bimodal case was again found to represent a statistically significant improvement over the unimodal assumption with peaks similar to those found when incorporating the complete sample. The input assumption of three peaks, however, did not return adequate fits: the *a posteriori* probabilities of group membership in the trimodal case only allocated two clusters into the intermediate higher-precision population.

There is an unavoidable smearing of the metallicity distribution due to metallicity calibration uncertainties, absorption and reddening of bulge/disk clusters and other line-of-sight problems. Therefore, as a further test, simulations were run in which the high-precision [Fe/H] sample data were shuffled by a random fraction of their associated uncertainties. This returned a result of marginal significance (median p-value ~ 0.1) for the 2-group case, and an insignificant result (p-value ~ 0.4) for the 3-group heteroscedastic trial. Note that the shapes of the 2-group Gaussian fits were once again consistent with those of the original bimodal test using the full sample.

In light of these KMM results, the possibility of a trimodal GC metallicity distri-

bution is tentatively rejected for the purposes of the analysis which follows. While it may yet be reasonable to separate the cluster system into more than two populations — say, by culling out the intermediate targets with group membership probabilities between 0.4 and 0.6 in the bimodal case — this is not done so here, as it is not clear that these represent a *bona fide* intermediate population. Based on the available data, it appears that the metallicity distribution of the M31 globular cluster system is not unimodal and better resembles a bimodal distribution similar in general shape to that of the Milky Way (e.g. Zinn 1985). Therefore, "metal-poor" and "metal-rich" populations shall refer to those objects separated into two groups based on the *a posteriori* probabilities returned from the 2-group heteroscedastic KMM test with the complete available sample. Each population was independently fit using an adaptive kernel smoothing procedure[1] with results shown in Figure 6.3. For reference, the trimodal results are shown in Figure 6.4.

It is interesting to see if there are signs of multi-modality in the abundance distributions derived from the WYFFOS data independently of the other datasets. Based on formal KMM results, the WYFFOS [Fe/H] distribution itself (shown by the shaded area in Figure 6.2) is not clearly better represented by either a bimodal or trimodal distribution. This is likely due to the smaller sample size and to the relative undersampling of (metal-poor) halo GCs above and below the major axis in the WYFFOS sample with respect to the full metallicity sample, in combination with smearing from uncertainties on the individual WYFFOS line indices. Visual inspection of the adaptive kernel fits to histograms of the [Fe/H] values derived for each of the CHG, Mgb and Fe53 line indices separately does hint at signs of bimodality, however (Figure 6.5).

Armandroff & Zinn (1988) and Armandroff (1989) selected a metallicity division at [Fe/H] = −0.8 to separate the metal-rich Milky Way clusters from the metal-poor population. At this value, they observed changes in the spatial distribution

[1] Adaptive kernel smoothing code kindly made available by K. Gebhardt.

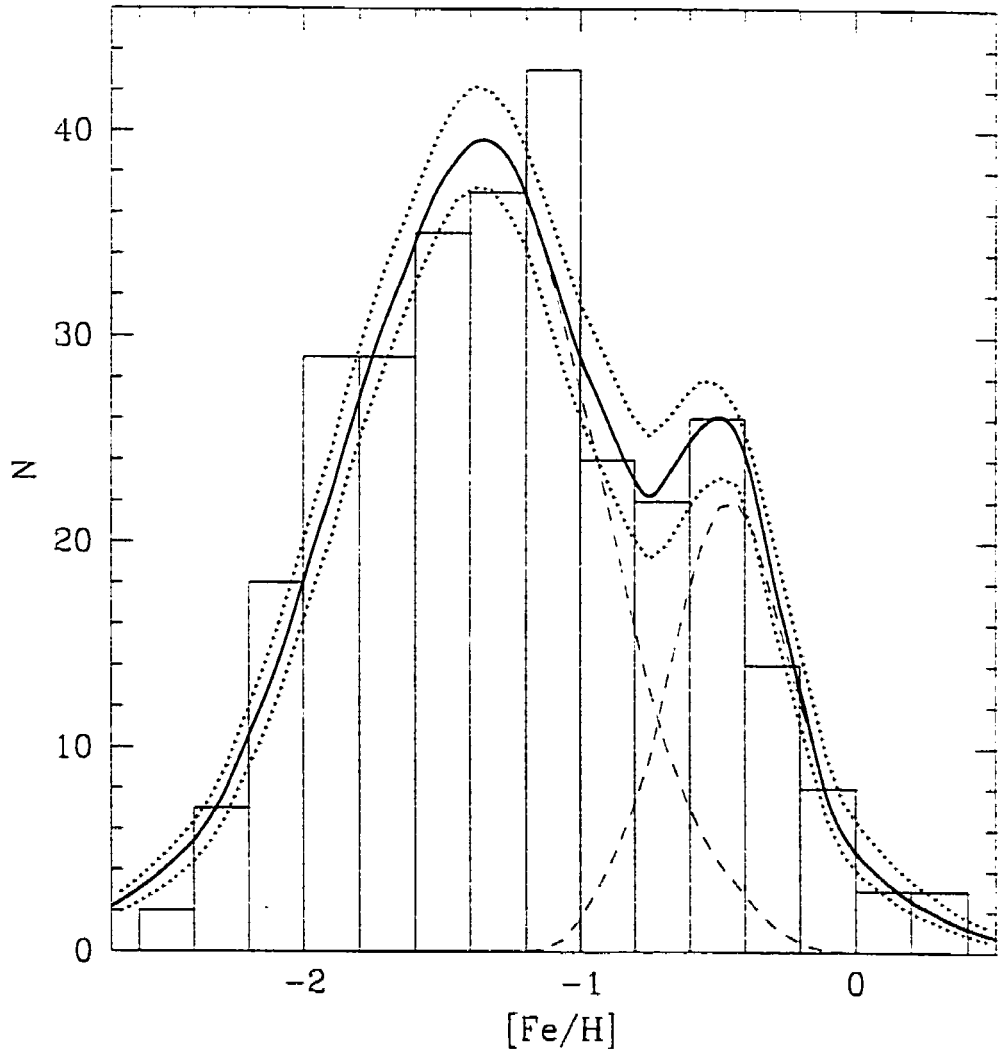

Figure 6.3: Adaptive kernel fits to the M31 metal-poor and metal-rich GC populations (dashed lines), separated according to the KMM mixture-modeling results. The sum of the individual fits is shown (solid line) along with its 5% and 95% confidence intervals (dotted lines).

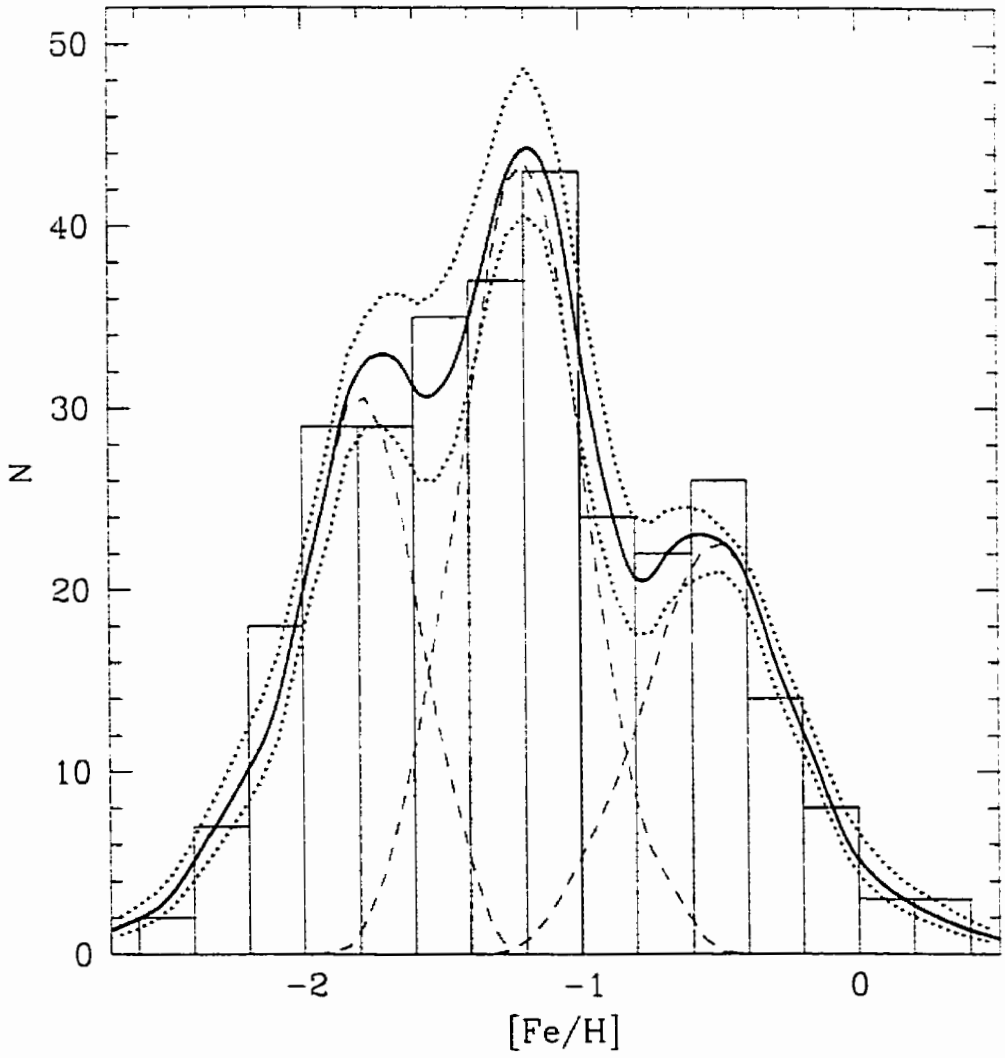

Figure 6.4: Adaptive kernel fits to the metal-poor, intermediate and metal-rich M31 globular cluster populations (dashed lines), separated according to the homoscedastic KMM mixture-modeling results. The sum of the individual fits is shown (solid line) along with its 5% and 95% confidence intervals (dotted lines).

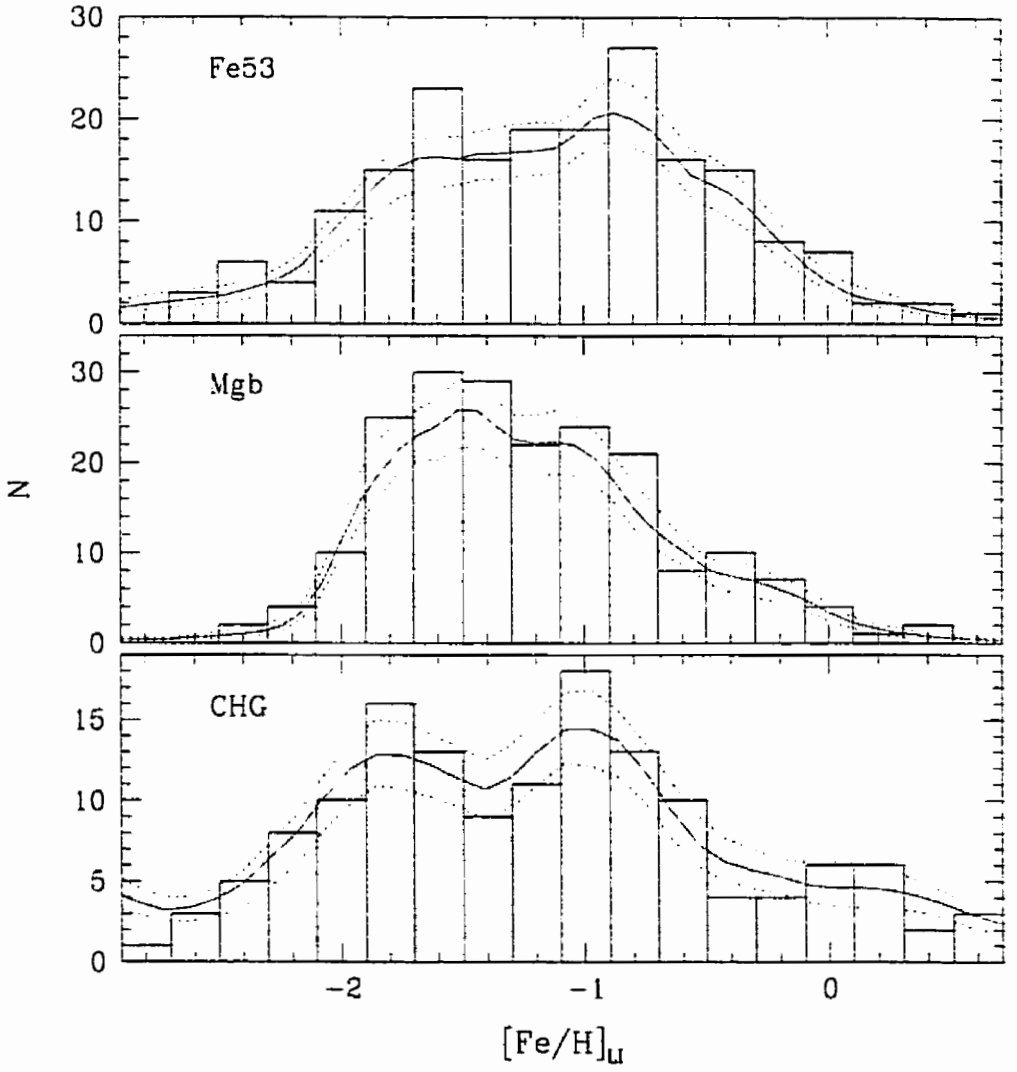

Figure 6.5: Histograms of the [Fe/H] results derived independently from each of the three best abundance indicators for the WYFFOS sample, based on the fits of Table 4.6. Adaptive kernel fits to the data are shown (solid line) along with the 5% and 95% confidence intervals (dotted lines).

and kinematics of the cluster sub-systems. The division between rich and poor in the bimodal distribution shown in Figure 6.3 for the M31 globular clusters is also at roughly this value. The positions of the two peaks returned by KMM ([Fe/H] = -1.44 ± 0.03 and -0.50 ± 0.04) differ only slightly from those quoted by Barmby et al. (2000), who found a bimodal distribution in M31 GC metallicities and metallicity-sensitive colours with peaks at [Fe/H] = -1.4 and -0.6.

For comparison with the M31 results, a KMM mixture-modeling test was performed on the metallicities of the Milky Way globular cluster system (from Harris 1996). The KMM results indicate that the Milky Way GCS is better represented by a bimodal [Fe/H] distribution than by a single population at an extremely high confidence level ($\sim$ 100%). KMM returned Milky Way peaks at [Fe/H] = -1.59 ($\sigma = 0.31$) and -0.56 ($\sigma = 0.25$), with metal-poor and metal-rich population sizes of 100 and 45, respectively. These populations are shown in Figure 6.6. The metal-rich peak in the Milky Way GCS is comparable to that found in M31. The metal-poor distribution, however, peaks at a higher metallicity for M31 than for its Milky Way counterpart. In both the Milky Way and M31, metal-rich clusters represent $\sim 1/3$ of the overall cluster population.

6.2.2 Spatial Distribution

The projected spatial distributions of the metal-poor and metal-rich cluster populations are shown in Figure 6.7. The metal-rich population is clearly more centrally concentrated, an effect which has been demonstrated previously with a smaller dataset by Huchra, Brodie & Kent (1991). In the Milky Way, the metal-rich clusters are also more centrally concentrated (refer to Figure 1.3) and have been ascribed as belonging to a thick disk system (Zinn 1985; Elson & Walterbos 1988; Armandroff 1989). Later work has suggested that this population is better described as a bulge/bar cluster system (Minniti 1995; Côté 1999; Forbes, Brodie & Larsen 2001). The spatial con-

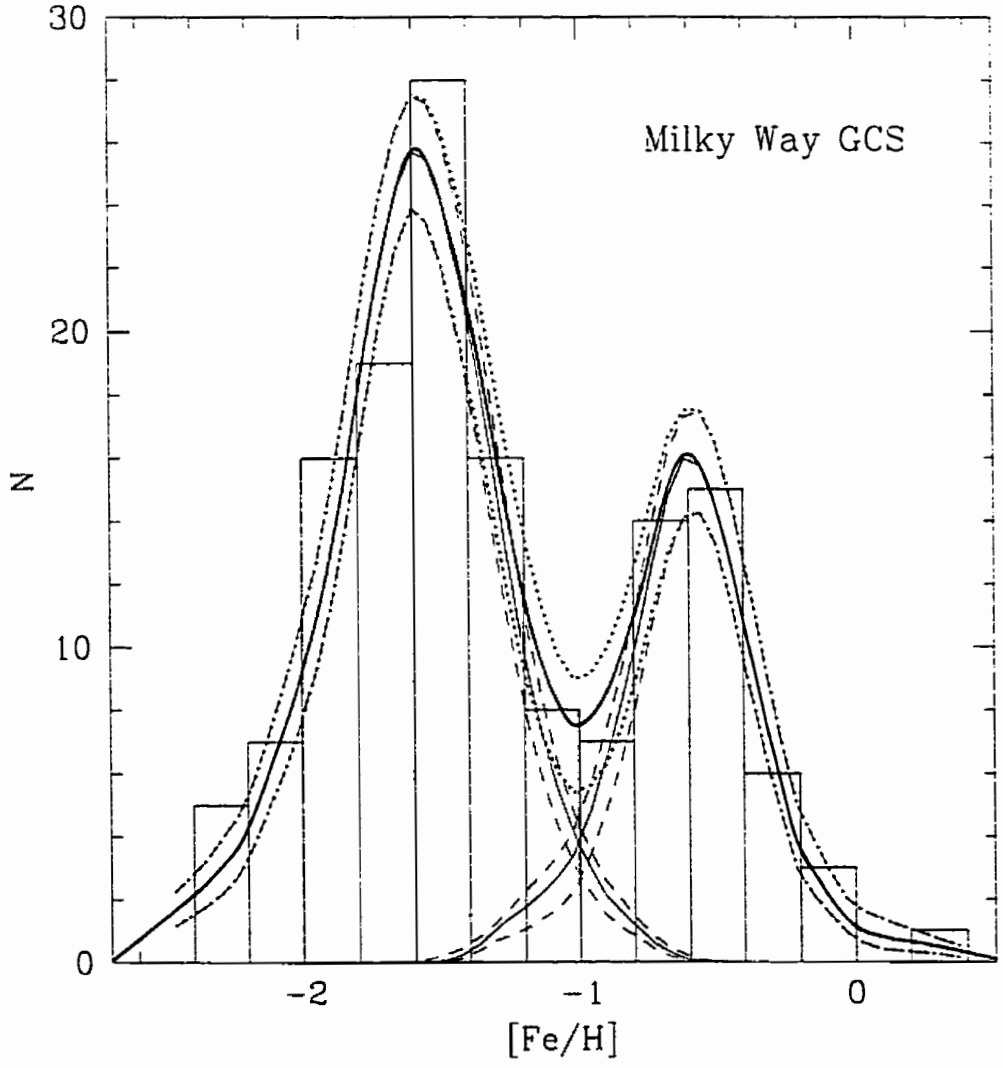

Figure 6.6: Adaptive kernel fits to the Milky Way's metal-poor and metal-rich GC populations (dashed lines), separated according to the KMM mixture-modeling results. The sum of the individual fits is shown (solid line) along with its 5% and 95% confidence intervals (dotted lines).

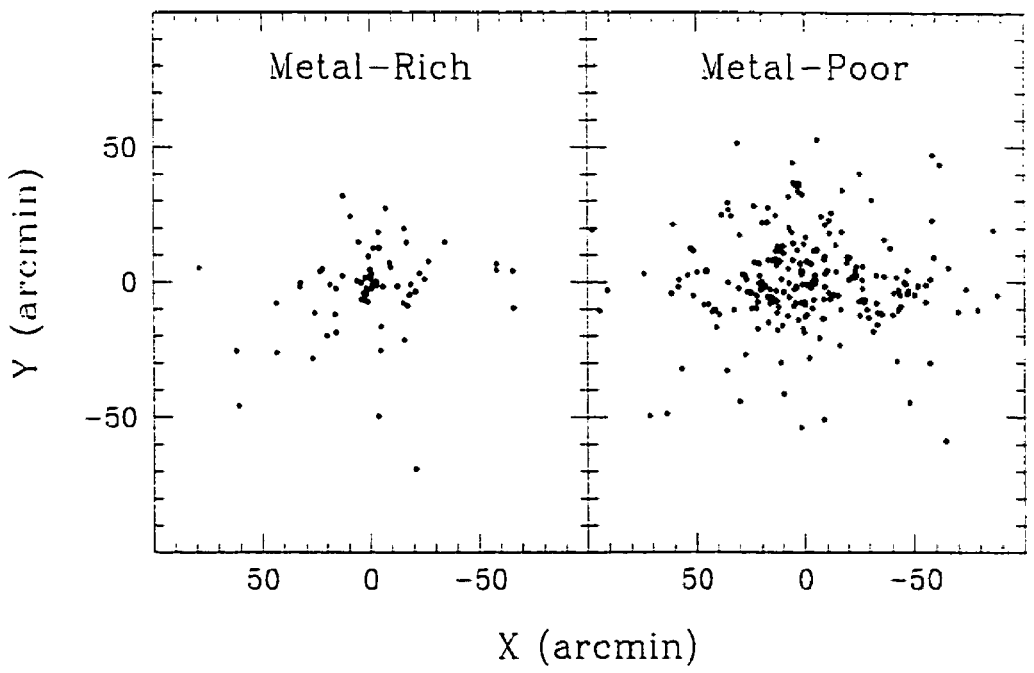

Figure 6.7: The projected spatial distributions of the metal-rich and metal-poor cluster populations in the M31 frame (refer to Figure 2.1 for the orientation). At an M31 distance of 770 kpc, 5′ corresponds to just over 1 kpc.

centration and distribution of the metal-rich clusters in M31 appear to be consistent with the latter interpretation.

There is a notable deficit of metal-poor clusters in the central radial bin shown in Figure 6.8. The already strong central concentration in the metal-rich GC population might mask any analogous deficit of metal-rich clusters. A similar lack of central clusters was reported by Elson & Walterbos (1988) within the inner 15′ of the GCS and is at least partially attributable to sampling restrictions towards the middle of the galaxy, as well as to observational biases incurred as a result of obscuration by the bulge and disk (see also Aurière, Coupinot & Hecquet 1992). The cluster sample at large galactocentric radii is likely to be more complete at faint magnitudes due to the lower degree of absorption as compared with the inner cluster system.

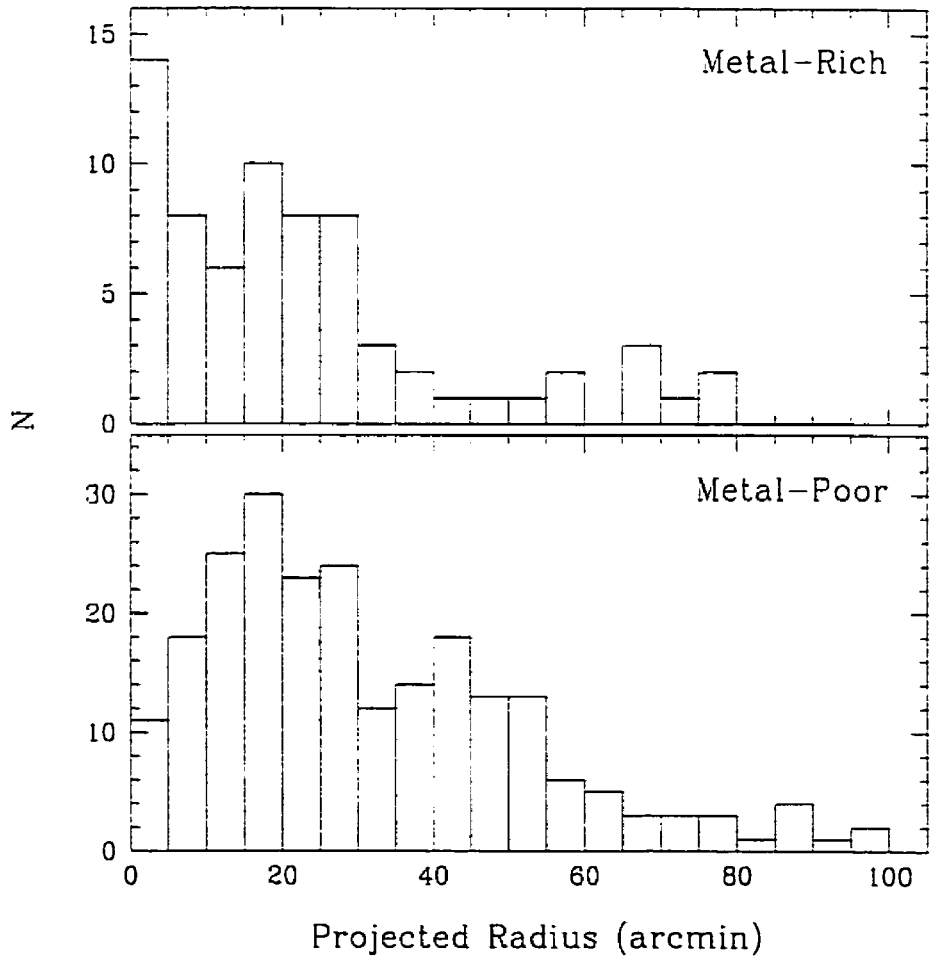

Figure 6.8: The radial distributions for the metal-rich and metal-poor M31 globular cluster populations.

Examination of the plot of magnitude versus radius in Figure 6.9 reveals a modest deficiency of clusters fainter than $V \approx 17$ within the inner 10′ or so of the GCS. An attempt is made to estimate the incompleteness at small radii in the following manner. Available V photometry (Barmby et al. 2000) is used to construct the observed luminosity functions (LFs) for the metal-rich and metal-poor clusters beyond a galactocentric radius of 15′. These outer LFs are normalized to the same scale as the distributions within the inner 15′ by summing under the brighter end of the inner and outer histograms ($V < 16.75$ mag) and multiplying by the ratio of these values. The observed histograms for the inner metal-rich and metal-poor clusters are shown by the solid lines in Figure 6.10, and the scaled outer histograms are represented by the dotted lines. Note that this method provides only a very crude estimate of the number of missing clusters at $V \geq 16.75$, as it naïvely presumes that the shape of the globular cluster LF does not change within the inner region of the galaxy. Dynamical friction and tidal interactions will more severely affect the inner clusters and thus change the overall shape of the luminosity function. Evidence for this effect has previously been noted by Kavelaars & Hanes (1997).

From the scaled outer LFs in Figure 6.10, we can infer that there are possibly ~ 30 missing metal-poor clusters at $V \geq 16.75$, whereas there may be only ~ 8 faint, metal-rich clusters which are missing within the inner 15′ of the galaxy. Barmby, Huchra & Brodie (2001) noted that their sample of metal-rich clusters in M31 were brighter on average by $V \sim 0.4$ than the metal-poor clusters. Selection effects may thus provide a reasonable explanation for the dip in the central bin of the metal-poor radial profile.

Comparing simple counts of the cluster populations within quadrants centred on the major and minor axes reveals that there is a slight enhancement in the major axis fields for the metal-rich population: 40 clusters in the major axis sectors versus 30 along the minor axis. If one takes into account only the inner 30′ of the GCS, this

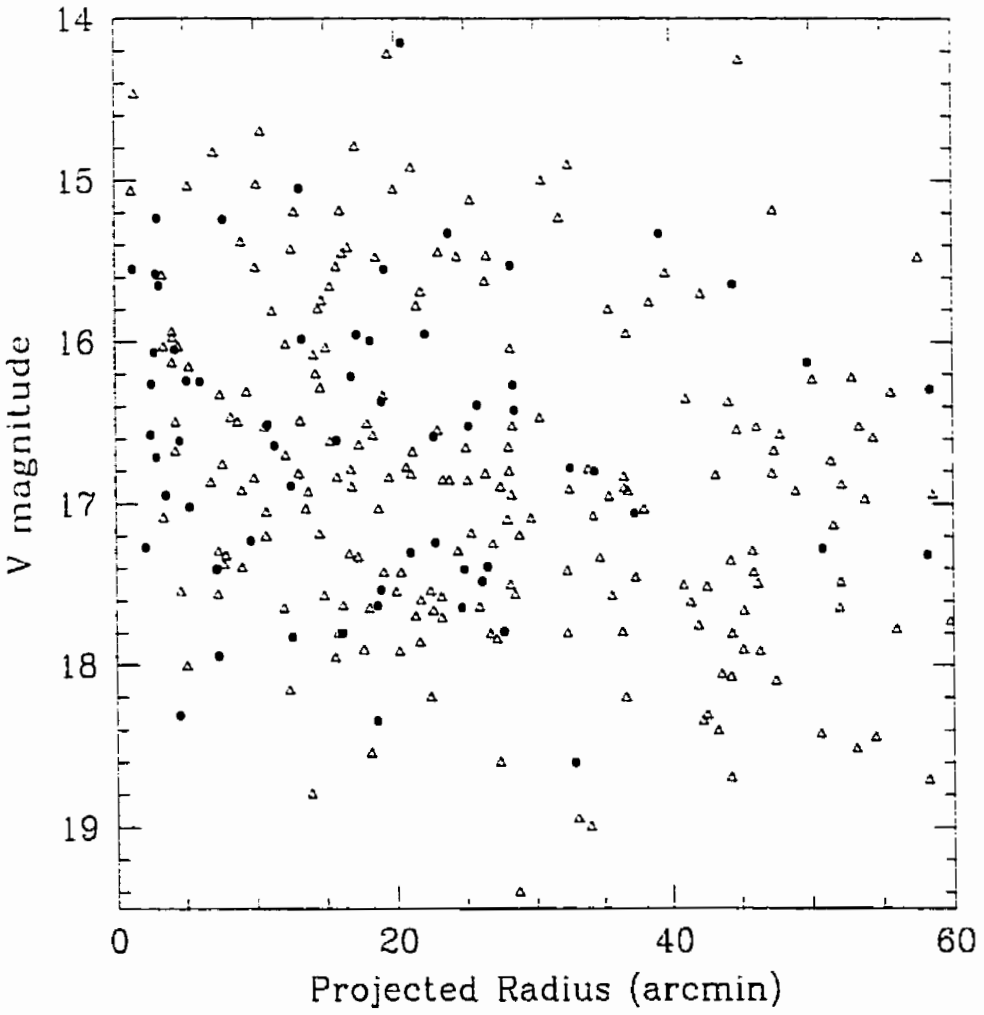

Figure 6.9: Apparent V magnitude of the clusters as a function of galactocentric radius. The filled circles represent the metal-rich clusters and the metal-poor clusters are shown by the open triangles.

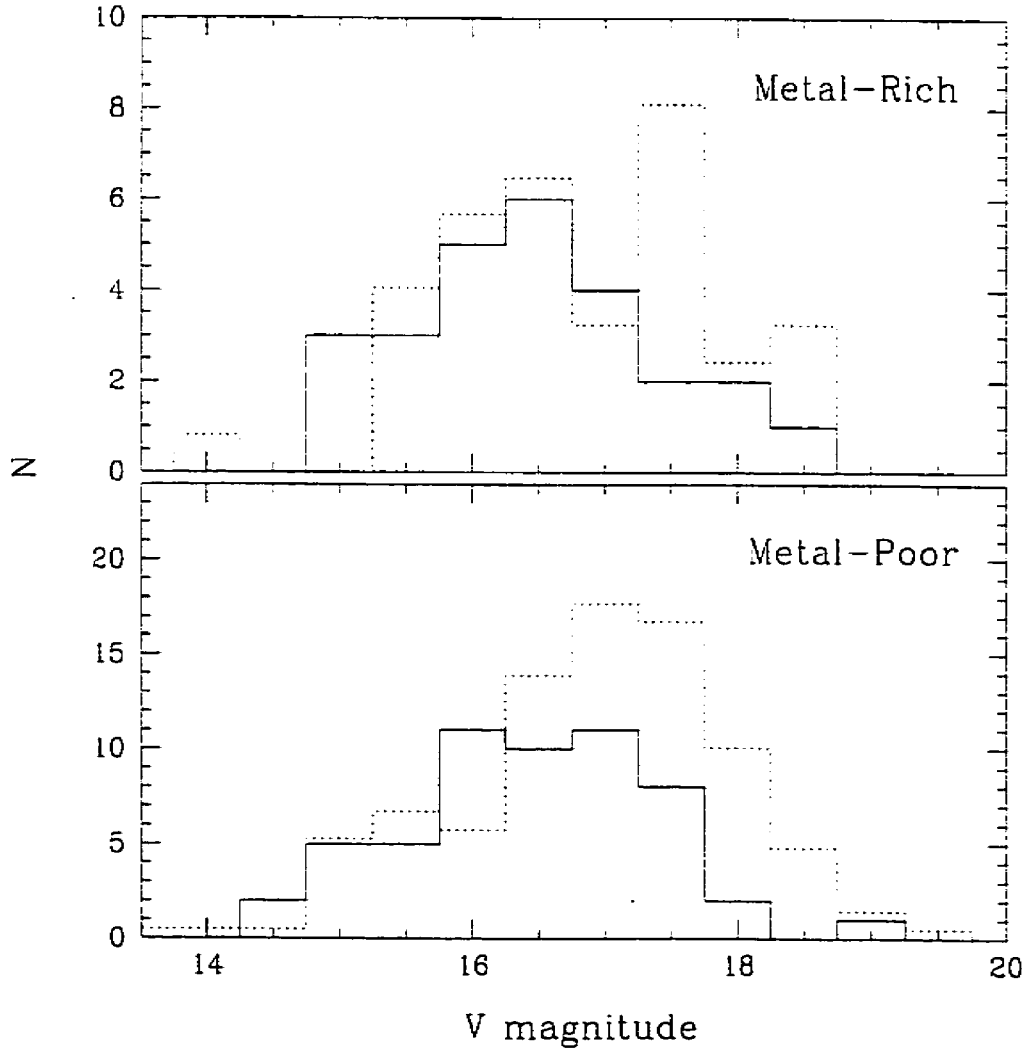

Figure 6.10: The observed luminosity functions of the metal-rich and metal-poor clusters within the inner 15′ of the galaxy are represented by the solid lines. The outer cluster LFs, scaled as described in the text, are shown by the dotted lines.

enhancement largely vanishes for the metal-rich clusters: 28 clusters in the major axis sectors compared to 26 along the minor axis. Based on their photometric metallicity estimates. Elson & Walterbos (1988) discovered that their sample of clusters classified as metal-rich defined a flattened system with an ellipticity of $\epsilon \gtrsim 0.4$ within a major axis radius of 30′. Our cluster counts are not consistent with such a large degree of flattening of the metal-rich system in this region. At present, reasonable limits on the flattening of metal-poor cluster distribution cannot be provided. since the arrangement of the WYFFOS fields has preferentially oversampled the major axis sectors at radii beyond about 30′.

6.2.3 *Metallicity Gradient*

Several previous studies have suggested the presence of a weak metallicity gradient in the M31 cluster system out to radii of $\sim$ 10 kpc (Sharov 1988: Huchra. Brodie & Kent 1991). In Figure 6.11, the M31 globular cluster metallicities are plotted as a function of galactocentric radius for the full sample and separate metallicity sub-populations. The large scatter in these plots is due at least in part to the fact that we can only measure projected positions, but nonetheless it seems that the mean [Fe/H] does indeed decrease with radius.

A sliding-bin method was used to fit the mean metallicity in 12 arcminute bins centred on each data point, with results shown in Figure 6.11. Robust estimates of the mean metallicity in radial bins are also consistent with the presence of a modest gradient in [Fe/H] within the full sample. Separating the data into sub-populations reveals no clear evidence for a gradient in the metal-rich GCS, although the spread in metallicity does seem to increase towards the center of the galaxy. There is an apparent trend towards decreasing metallicity within the inner metal-poor sample with a gradient of roughly −0.015 dex/arcmin. Poor sampling of the clusters at large radii makes it difficult to comment decisively on the results beyond a radius of about

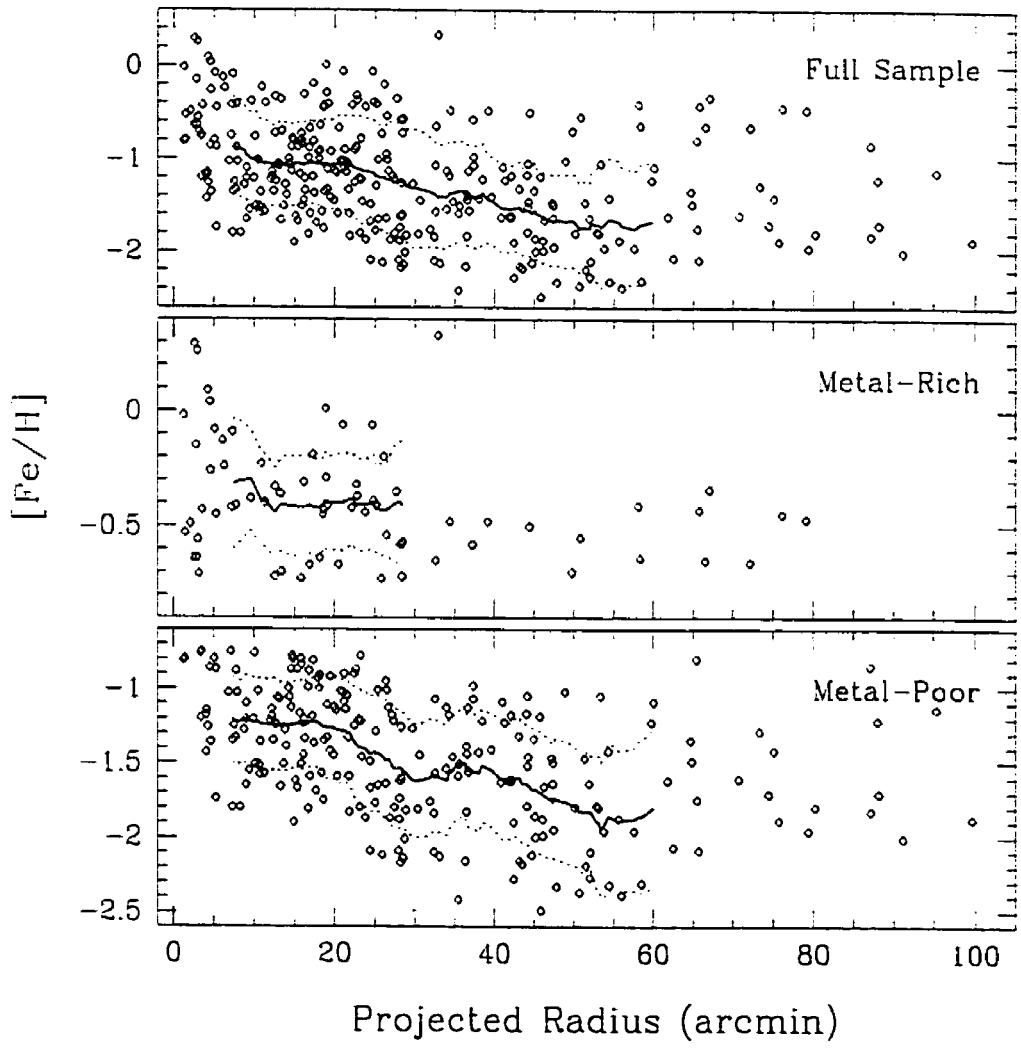

Figure 6.11: [Fe/H] as a function of projected radius for the full sample and metallicity populations of the M31 GCS. A sliding-bin fit was used to determine the mean and RMS at each data point (shown by the solid and dotted curves, respectively).

60′, although the metal-poor sample appears to level off at a lower mean metallicity beyond this distance.

6.2.4 Metallicity versus Cluster Luminosity

As Huchra, Brodie & Kent (1991) pointed out, correlations between metallicity and luminosity (i.e. mass) within a globular cluster system may reveal certain aspects of its formation and enrichment processes. For example, in a scenario in which self-enrichment is a predominant factor in cluster evolution, one would expect that more massive clusters would have higher metallicities. Furthermore, the preferential destruction of less massive clusters in the central region of the galaxy might have more devastating implications for any low luminosity, metal-rich GCs which might tend to reside at smaller radii.

Figure 6.12 shows a plot of metallicity versus apparent cluster V magnitude for the M31 GCS. There is no discernible trend of [Fe/H] with luminosity, confirming the earlier results of Huchra, Brodie & Kent (1991) and Barmby et al. (2000). There is a similar lack of correlation between cluster luminosity and [Fe/H] found in the Milky Way globular cluster system (Armandroff 1989; van den Bergh 1991).

A plot of cluster metallicity versus $(B-V)$ colour is shown in Figure 6.13. At a given age, more metal-rich stellar systems are redder. For reference, the $(B-V)_0$ colour-metallicity relation

$$[\mathrm{Fe/H}] = 5.50\,(\pm 0.33)\,(B-V)_0 - 5.26\,(\pm 0.23) \tag{6.1}$$

derived by Barmby et al. (2000) for a sample of 88 Galactic globular clusters is superimposed over the data. Note that the uncertainties on the reddening corrections for the M31 clusters can be quite large.

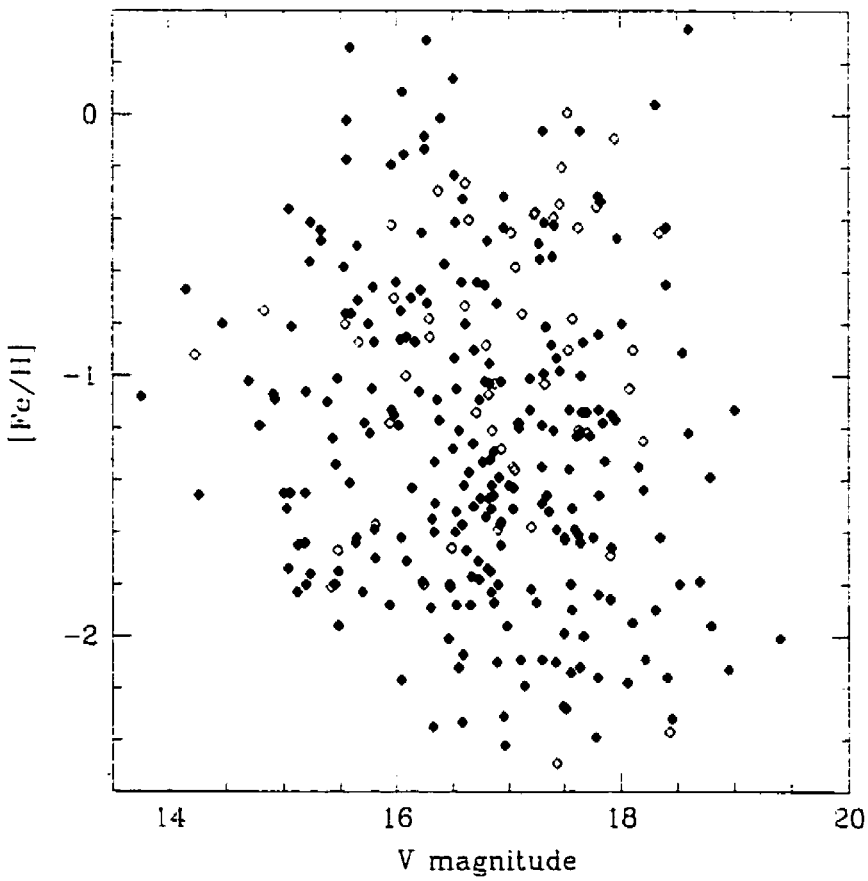

Figure 6.12: M31 globular cluster metallicity as a function of apparent V magnitude. The open symbols represent clusters with higher reddenings ($E_{B-V} > 0.25$).

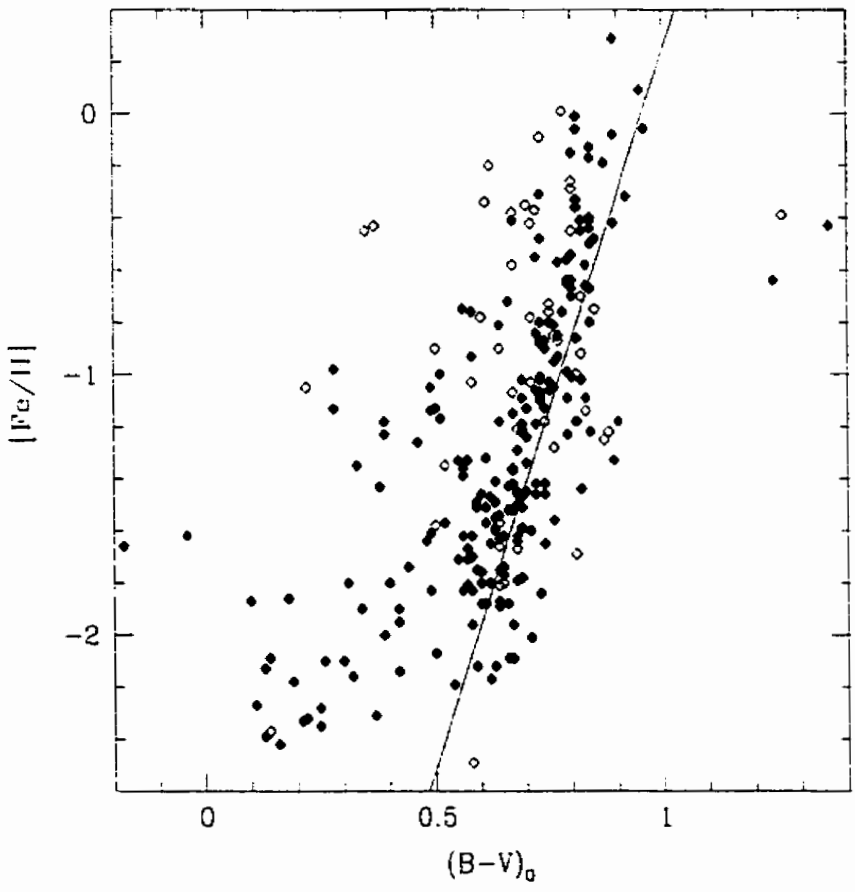

Figure 6.13: M31 globular cluster metallicity as a function of reddening-corrected $(B-V)$ colour. The open symbols represent clusters with higher reddening corrections. where $E_{B-V} > 0.25$. The solid line represents the colour-metallicity relation for Galactic globular clusters in Equation 6.1.

6.3 GCS Kinematics

The Andromeda Galaxy itself has a systemic velocity of -300 ± 4 km s^{-1} (RC3). The maximum likelihood value for the mean M31 cluster radial velocity is somewhat higher, at $\langle v_r \rangle = -284 \pm 9$ km s^{-1}. The globular cluster system as a whole has a velocity dispersion of $\sigma_v = 156 \pm 6$ km s^{-1}. The kinematics of the metal-rich and metal-poor GCS populations will be discussed later in this section. First, the global kinematic properties of the M31 GCS are examined.

6.3.1 GCS Rotation

A histogram of the cluster line-of-sight velocities is presented in Figure 6.14. There is strong evidence for bimodality in the velocity distribution, a feature which is attributable to the fact that the cluster system is rotating with respect to the line of sight. Considering, for the moment, a purely rotating disk population of globular clusters in the reference frame of the galaxy:

$$v_{GC} = \overbrace{v_{rot} \sin(i) \sin(\theta + \delta)}^{v'} + v_\sigma \tag{6.2}$$

where v_{rot} is the rotation velocity of the population, i is the inclination of the rotation axis to the line of sight (77.7°), θ is the angle about the angular momentum axis, δ is an arbitrary phase offset, and v_σ incorporates the velocity dispersion plus random measurement errors. The combined probability distribution $P(v_{GC})$ for the M31 globular cluster radial velocities is the convolution of $P(v')$ with $P(v_\sigma)$. The probability function $P(v_\sigma)$ is Gaussian and serves to broaden the combined distribution. $P(v')dv' = P(\theta)d\theta$ and the probability $P(\theta)$ is uniform, so this gives:

$$\frac{dv'}{d\theta} = v_{rot}\sin(i)\cos(\theta) = v_{rot}\sin(i)\frac{\sqrt{v_{rot}^2\sin^2 i - v'^2}}{v_{rot}\sin(i)}$$

$$\text{and } P(v') = \frac{1}{2\pi}\frac{1}{\sqrt{v_{rot}^2\sin^2 i - v'^2}}. \tag{6.3}$$

This represents a bimodal distribution with maxima at $\pm v_{\rm rot}\sin(i)$ about the systemic velocity of the population. The peaks of the (unshifted) velocity histogram in Figure 6.14 lie at -413 and -170 km s^{-1}, yielding an estimated rotation amplitude of $v_{\rm rot} \sim 125$ km s^{-1}.

The fact that M31 is rotating has been established by various studies (see review by Hodge 1992, and references therein). Using a sample of $\sim$ 150 M31 clusters as dynamical tracers, Huchra, Brodie & Kent (1991) noted a rapid rotation of the handful of inner ($R \lesssim 7'$) clusters in their sample with [Fe/H] ≥ -0.8. They also found that the metal-poor population had no rotation signature within the inner galaxy, but shared a moderate rotation of $\sim$ 60 km s^{-1} with the bulk of the GCS beyond this radius. With this increased sample of 321 velocities, a more comprehensive look at the kinematics of the system is now possible.

Perhaps not surprisingly, there appears to be no significant rotation of the GCS about the major axis of M31 as shown in the left panel of Figure 6.15. A robust fit to the targets within the inner 25′ along the minor axis (dropping four objects at extreme radii) gives $v_r = -298 + 0.27\,Y$ km s^{-1}, where Y is the distance along the minor axis in arcminutes. Such a small deviation from a slope of zero may simply be due to statistical imprecision or a variation in the position angle for the galaxy (Hodge & Kennicutt 1982).

A plot of the observed cluster radial velocities as a function of projected distance along the major axis of M31 is shown in the right panel of Figure 6.15. A basic 2σ culled robust linear fit to the velocities along the major axis reveals that the globular cluster system does indeed have a significant rotational component about the minor axis. This rotation will now be investigated in more detail.

An adaptive binning technique[2] was used to generate the GCS rotation curve shown in Figure 6.16. Before fitting the rotation curve, the globular cluster coor-

[2] The srotate code was kindly made available by K. Gebhardt.

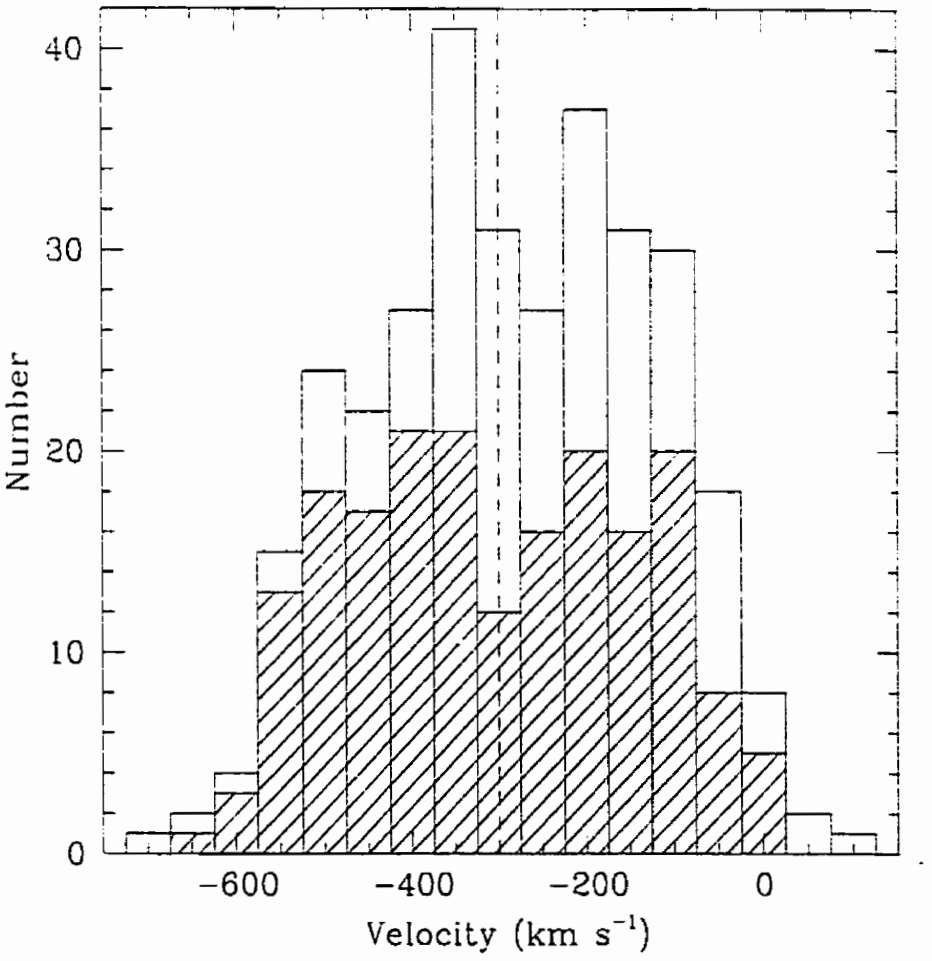

Figure 6.14: The velocity histogram for the M31 cluster system. The solid-line histogram is that for the available sample of 321 M31 globular cluster velocities, while the shaded area shows our contribution of 191 WYFFOS velocities to the overall sample. The M31 systemic velocity of -300 ± 4 km s^{-1} is shown by the dashed line.

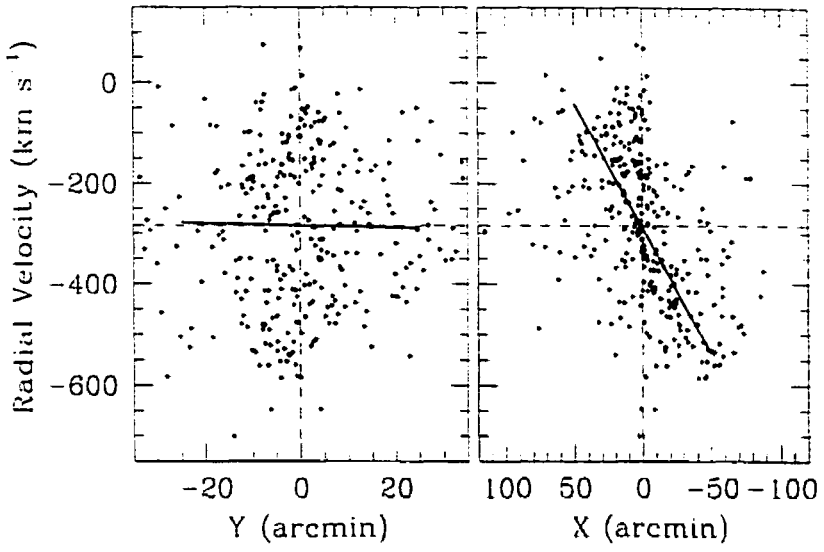

Figure 6.15: Radial velocity of the M31 globular clusters versus projected radius along the minor axis (left) and the major axis (right). Culled robust fits to the data are shown by the solid lines.

dinates were transformed into the reference frame of the galaxy and the data were folded about each axis. The function $v = v_{\rm sys} + v_{\rm rot} \sin\phi$ was fit to the radial velocities of the clusters within radial bins outwards from the galaxy center (Kissler-Patig & Gebhardt 1998). The angle ϕ represents the position angle of the target object in the projected frame of the galaxy, and $v_{\rm sys}$ is the mean velocity of the cluster system. The kinematic properties were determined in a series of annuli centred on each cluster in the projected frame and encompassing a specified number of data points (79 points, with a minimum of 39 at the extrema). This method yields a rotation amplitude of 136 km s^{-1} where the curve flattens off beyond $R = 30'$. Plots of the velocity dispersion and v/σ_v as a function of radius are shown in Figures 6.17 and 6.18, respectively.

Robust biweight estimators of location and scale were employed as measures of mean velocity and dispersion in 10 arcminute bins along the major axis of the galaxy (Hoaglin, Mosteller & Tukey 2000; see also Beers, Flynn & Gebhardt 1990).

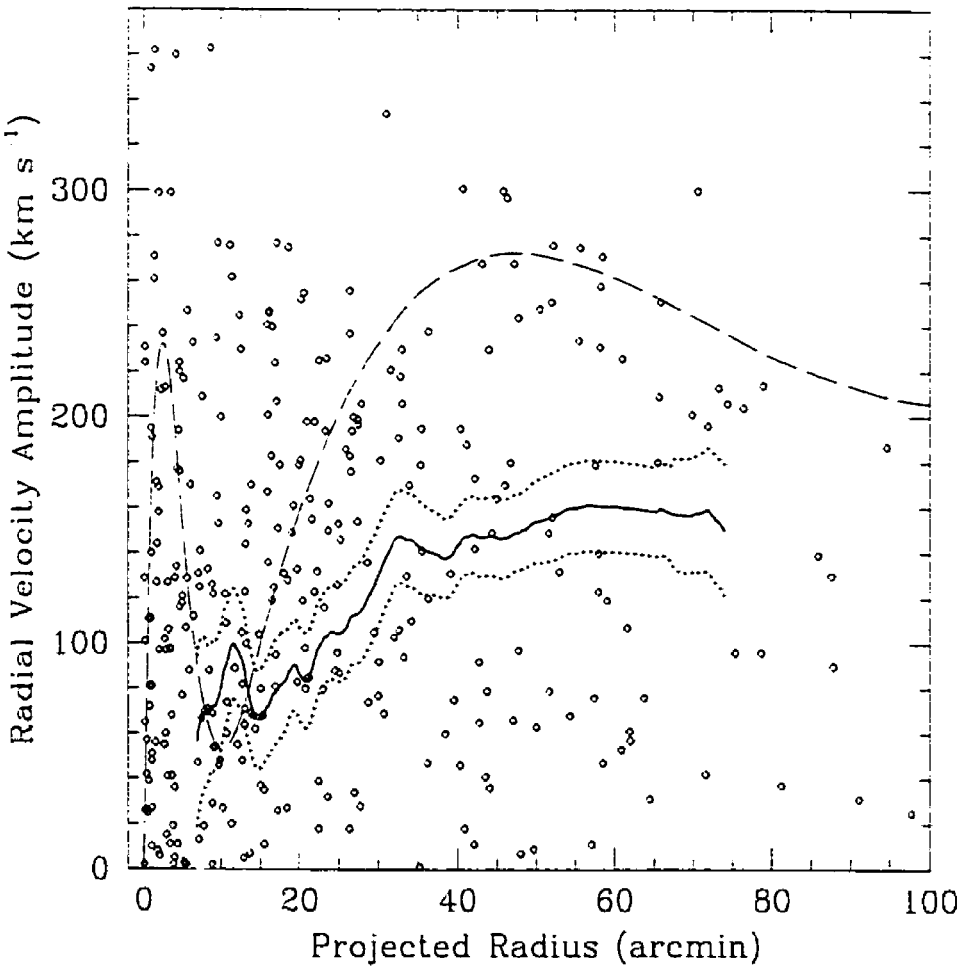

Figure 6.16: The projected rotation curve of the M31 GCS and its 90% confidence limits are shown by the solid and dotted lines, respectively (see the text for details). The dashed line represents the stellar rotation curve from Rubin & Ford (1970) for comparison.

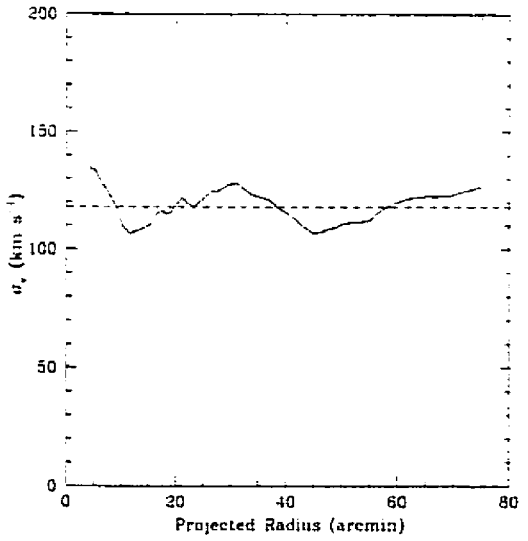

Figure 6.17: The projected velocity dispersion (solid line) and the 90% confidence bands (dotted lines) as a function of radius. The dashed line indicates the "typical" velocity dispersion level of ~ 118 km s^{-1} at any given major axis distance.

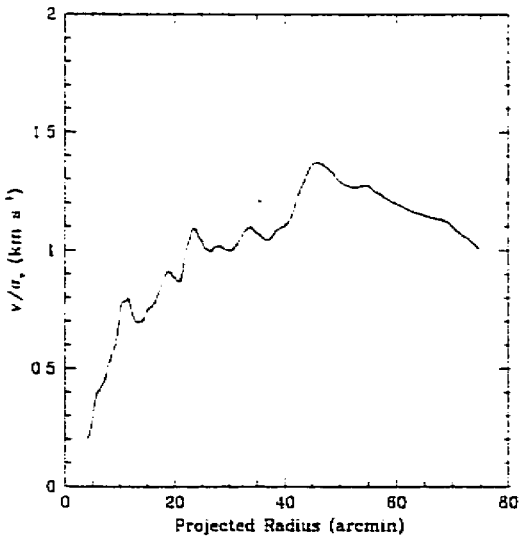

Figure 6.18: A plot of v/σ_v as a function of projected radius. The dotted lines represent the 90% confidence limits.

Table 6.1: Mean velocity and dispersion (in $\mathrm{km\,s^{-1}}$) in radial bins

	Full Sample			Metal-Poor			Metal-Rich		
$X(')$	N	$\langle v_r \rangle$	σ_v	N	$\langle v_r \rangle$	σ_v	N	$\langle v_r \rangle$	σ_v
-60 to -50	13	-467^{+57}_{-73}	108^{+75}_{-35}	10	-486^{+81}_{-58}	110^{+87}_{-76}	—	—	—
-50 to -40	17	-432^{+48}_{-85}	130^{+19}_{-42}	14	-461^{+106}_{-93}	135^{+56}_{-59}	—	—	—
-40 to -30	12	-398^{+82}_{-90}	144^{+41}_{-66}	10	-444^{+50}_{-62}	95^{+81}_{-34}	—	—	—
-30 to -20	23	-432^{+37}_{-34}	81^{+51}_{-20}	18	-441^{+42}_{-38}	84^{+52}_{-31}	5	-381^{+18}_{-128}	66^{+9}_{-7}
-20 to -10	24	-371^{+46}_{-46}	129^{+21}_{-27}	15	-355^{+72}_{-69}	132^{+24}_{-56}	9	-399^{+107}_{-140}	128^{+112}_{-37}
-10 to 0	55	-295^{+38}_{-38}	155^{+26}_{-27}	32	-307^{+54}_{-64}	159^{+54}_{-33}	17	-293^{+39}_{-50}	127^{+48}_{-46}
0 to 10	55	-211^{+28}_{-30}	134^{+37}_{-21}	38	-224^{+38}_{-47}	140^{+46}_{-23}	16	-186^{+49}_{-40}	99^{+22}_{-14}
10 to 20	34	-199^{+37}_{-60}	131^{+26}_{-15}	31	-212^{+45}_{-54}	135^{+33}_{-19}	6	-138^{+129}_{-47}	99^{+38}_{-89}
20 to 30	24	-165^{+40}_{-52}	119^{+70}_{-29}	18	-177^{+50}_{-78}	126^{+76}_{-45}	5	-111^{+56}_{-139}	90^{+33}_{-16}
30 to 40	13	-203^{+85}_{-86}	157^{+36}_{-34}	11	-198^{+74}_{-113}	138^{+51}_{-42}	—	—	—
40 to 50	11	-167^{+52}_{-138}	101^{+35}_{-13}	9	-128^{+20}_{-94}	63^{+102}_{-44}	—	—	—
50 to 60	7	-152^{+98}_{-61}	97^{+81}_{-24}	7	-152^{+98}_{-61}	97^{+81}_{-24}	—	—	—

The biweight results and their 90% confidence intervals (from bootstrap errors) are presented in Table 6.1 and Figure 6.19 for the full sample and the two metallicity sub-populations. Based on the appearance of these plots, it seems reasonable to approximate the shape of the curve as consisting of solid-body rotation within the central 25′, with a flattening beyond this radius. One-half of the velocity difference between the flat regions of the curve in Figure 6.19 yields a rotation amplitude of $v_{\rm rot} = 138 \pm 13\ \mathrm{km\,s^{-1}}$ for the full sample.

Significant differences between the kinematic properties of the metal-rich and metal-poor clusters would imply that these populations underwent dissimilar formation mechanisms. The maximum likelihood value for the mean velocity of the 70 clusters in the metal-rich sample is $\langle v_r \rangle = -260 \pm 18\ \mathrm{km\,s^{-1}}$ with a dispersion of $\sigma_v = 146 \pm 12\ \mathrm{km\,s^{-1}}$. For comparison, the larger metal-poor sample (231 clusters) demonstrates a somewhat lower mean velocity of $\langle v_r \rangle = -290 \pm 10\ \mathrm{km\,s^{-1}}$ and a slightly higher dispersion of $\sigma_v = 155 \pm 7\ \mathrm{km\,s^{-1}}$, although these values are still consistent with those of the higher metallicity sample within the quoted errors. A

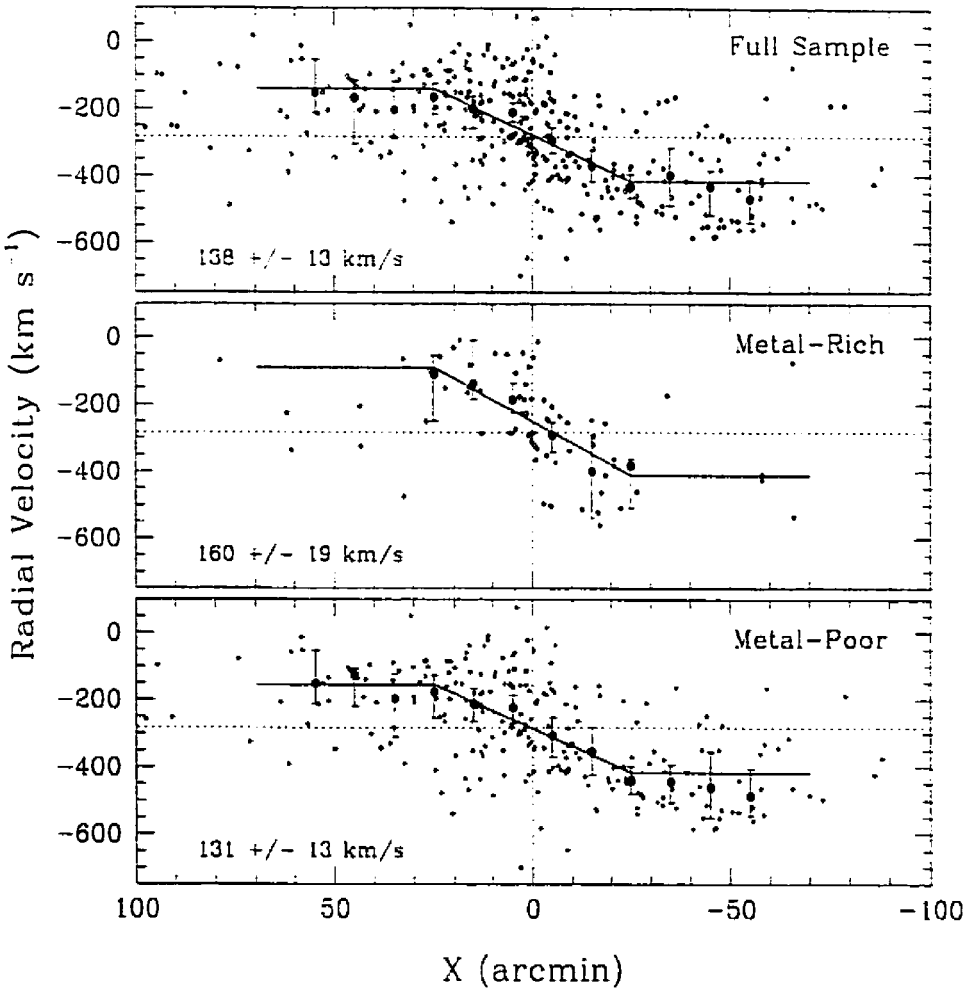

Figure 6.19: The rotation curve of the M31 GCS based on robust biweight estimates of the mean ("location") in radial bins of 10 arcmin for the full dataset and separate metallicity populations. The error bars represent the 90% confidence interval. The solid line shows the best fit to the data assuming solid-body rotation in the inner 25 arcmin and a flattening beyond. The derived rotation amplitudes are provided in the lower-left corner of each plot.

rotation amplitude of $v_{\rm rot} = 160 \pm 19$ km s^{-1} for the metal-rich population is obtained from fits to the biweight results shown in the middle panel of Figure 6.19. This value is somewhat larger than the metal-poor amplitude of $v_{\rm rot} = 131 \pm 13$ km s^{-1}, although these values are also not inconsistent within their formal errors.

The projected position angle of each cluster was determined as the angle of maximum positive rotation obtained from maximum likelihood sinusoid fits. Plots of the variation of position angle with radius for the full sample and metallicity subpopulations are presented in Figure 6.20. The input GC positions already incorporate a de-rotation of $PA_{M31} = 38°$ for the galaxy and, all else being equal, one would expect to find that the PA for the cluster system is roughly zero. Despite the sizeable spread at low radius in the full sample, there is a relatively clear increase in PA within the central region of the metal-poor cluster system. This effect is consistent with studies of the central bulge and inner disk region of M31 which demonstrate a similar increase in PA to 50° (Hodge & Kennicutt 1982; Kent 1989). The M31 GCS shows a notable decrease in the PA of the rotation axis beyond about 30′. Interestingly, the metal-rich clusters seem to be rotating about an axis which is tilted at a slightly lower PA with respect to the major axis throughout the full radial extent of the population.

6.4 The Mass of M31

The kinematics of M31's GCS provide us with a dynamical probe of the underlying mass distribution of the host galaxy. The projected mass estimator (PME) was used to place constraints on the underlying mass of the system (Bahcall & Tremaine 1981; Heisler et al. 1985):

$$M_{\rm PME} = \frac{f_p}{NG} \sum_{i=1}^{N} r_i v_i^2 \tag{6.4}$$

where N is the number of bodies, G is the gravitational constant, r is the projected galactocentric radius and v is the radial velocity of the body relative to the systemic

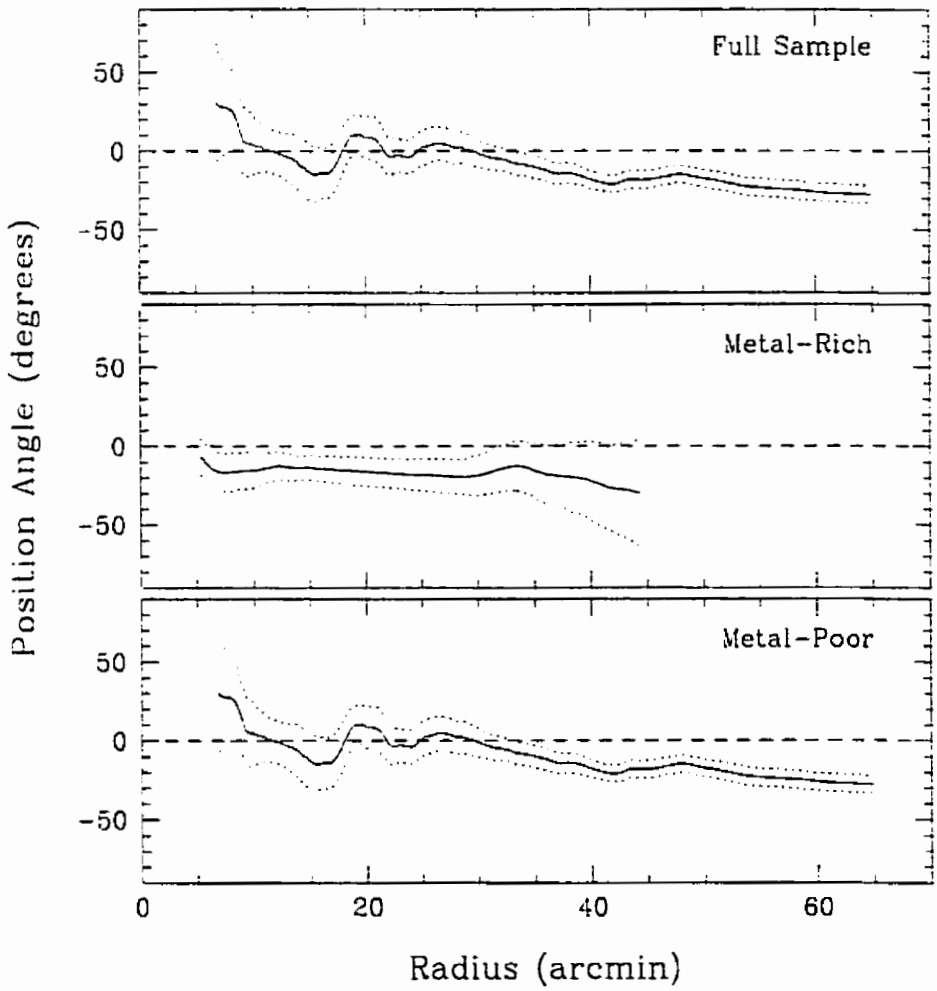

Figure 6.20: The projected position angle of the rotation axis (solid line) and its 90% confidence bands (dotted lines) as a function of radius for the full sample, as well as for the metal-rich and metal-poor populations.

velocity of the galaxy (-300 ± 4 km s^{-1} according to RC3). The empirical scale factor f_p depends on the assumptions made regarding the distribution of orbits, and is equal to $32/\pi$ and $64/\pi$ for isotropic and radial orbits within a continuous density distribution, respectively.

Admittedly, this projected mass estimate is hampered by our limited sample size and coverage, as well as a lack of detailed understanding of the cluster orbits. Recent work by Evans & Wilkinson (2000) has shown that the dynamical tracers in the M31 halo exhibit a predominantly isotropic velocity dispersion. Applying the PME to the available cluster data and assuming isotropic orbits within an extended mass distribution yields an estimated mass of $M_{\rm M31} = (4.1 \pm 0.1) \times 10^{11}\ M_\odot$ using 319 dynamical targets out to a radius of $\sim 120'$ from the galaxy center (~ 27 kpc at 770 kpc). This result is comparable to previous mass estimates obtained out to similar radii as summarized in Table 6 of Evans & Wilkinson (2000). In the unlikely case of purely radial orbits, our mass estimate would increase to twice the value quoted above.

A more detailed study of the mass distribution of M31 based on a large sample of kinematic probes — including the current sample of globular clusters velocities as well as a large number of planetary nebulae from Halliday et al. (in preparation) — is currently underway by Wilkinson et al. (in preparation).

6.5 M31 Globular Cluster Sizes

Globular cluster sizes depend on factors such as mass segregation within the cluster and truncation due to the tidal influence of the parent galaxy (see Section 6.1.10 of Binney and Merrifield 1998). The FWHM values measured in Section 5.5 from the ARGUS reconstructed images were used as estimates of the relative widths (W) of the M31 globular clusters in that sample. A histogram of the results is presented in Figure 6.21. The mean and median sample values for 189 clusters are found to be

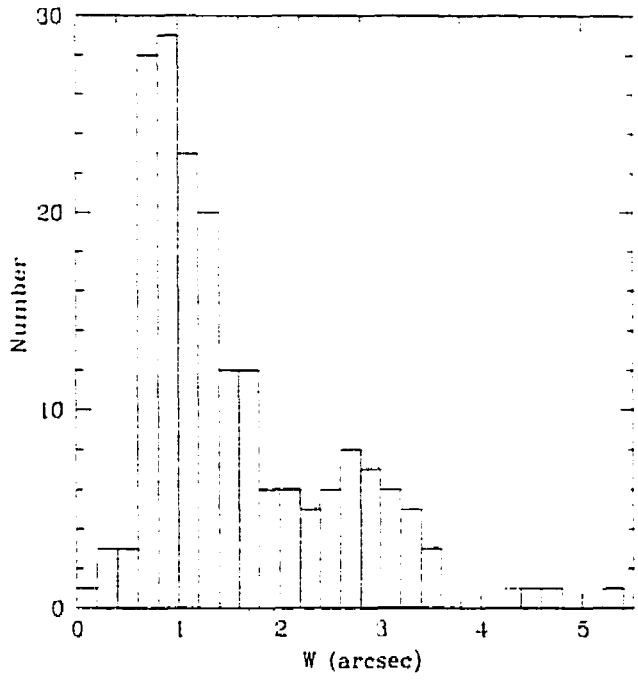

Figure 6.21: A histogram showing the distribution of cluster widths estimated from the ARGUS direct images.

$W = 1.6''$ and $1.3''$, respectively.

Studies have shown that the radii of individual globular clusters tend to increase, on average, towards larger galactocentric distances (van den Bergh 1994). This effect has been demonstrated in both the Milky Way GCS (van den Bergh, Morbey & Pazder 1991) and in M31 (Crampton et al. 1985). Tidal destruction of extended globular clusters within the inner galaxy would explain the relative absence of large clusters at small galactocentric radii. The lack of compact clusters (with half-light radii $\lesssim 3$ pc) beyond the solar radius is suggestive of a formation mechanism wherein more extended clusters preferentially form within the less dense regions of galaxies (van den Bergh, Morbey & Pazder 1991).

The correlation between cluster size and metallicity is investigated in Figure 6.22. Sliding-bin fits to the M31 data reveal that despite an increase in the scatter towards

decreasing metallicity. GC diameter does not appear to correlate with [Fe/H]. This is in agreement with the conclusions drawn by van den Bergh, Morbey & Pazder (1991) for their sample of Milky Way globular clusters. A plot of Galactic GC half-mass radius versus [Fe/H] is shown in the lower panel of Figure 6.22, for comparison. Plots of cluster size versus V magnitude (from Barmby et al. 2001) for the full sample and metallicity sub-populations are shown in Figures 6.23 and 6.24, and reveal that these parameters are also uncorrelated. Sampling biases may contribute to the lack of M31 GCs at magnitudes fainter than $V \sim 17.6$ with large values of W; faint distended objects are less likely to provide good targets for observation.

Figure 6.25 shows a plot of GC diameter versus projected galactocentric distance for the clusters in the ARGUS sample. A robust fit to the data reveals a modest increase in the average size of the clusters at larger radii of the form:

$$W = 0.37 \frac{R_{gc}}{100} + 1.1 \tag{6.5}$$

where galactocentric radius (R_{gc}) is measured in arcminutes and W is in arcseconds. The significant scatter at small R_{gc} compared to similar plots for the Milky Way GCS (e.g. Figure 1 of van den Bergh 1994) is mostly due to projection effects in M31.

Separating the cluster sample with available metallicities into metal-rich and metal-poor sub-populations reveals a small difference in the mean GC diameter: $\langle W_{rich} \rangle \sim 1.2''$ versus $\langle W_{poor} \rangle \sim 1.7''$. This is consistent with the findings of Larsen et al. (2001) in their HST WFPC2 study of the globular cluster systems of 17 galaxies; they found that the blue (metal-poor) clusters tended to be on average $\sim 20\%$ larger than red (metal-rich) clusters. Interestingly, robust fits to plots of size against galactocentric radius in Figure 6.26 demonstrate a measurable gradient within the metal-rich population, while the metal-poor clusters are consistent with a slope of zero. More details about the orbits of the clusters in each sample would help to ascertain whether this difference is due to dynamical processes in the M31 GCS.

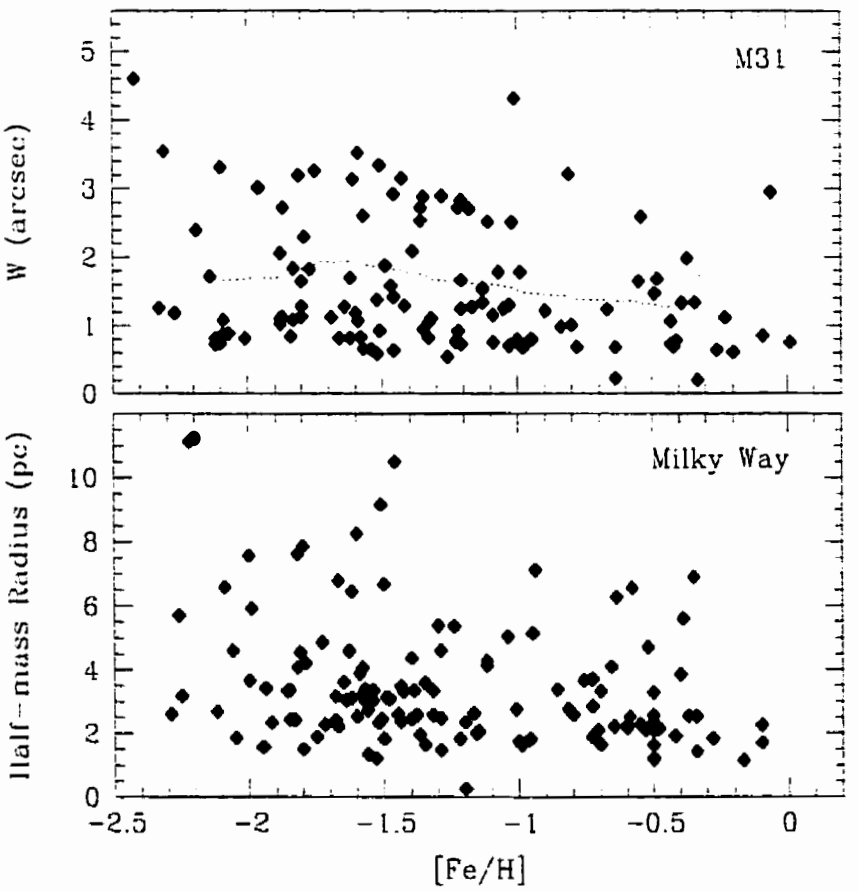

Figure 6.22: Globular cluster size versus metallicity. The upper panel shows the width values from the ARGUS direct images. A sliding-bin fit to the data is represented by the dotted line, and reveals that the mean cluster size does not change significantly with [Fe/H]. The lower panel shows a plot of half-mass radius versus metallicity for the Milky Way GCS (Harris 1996).

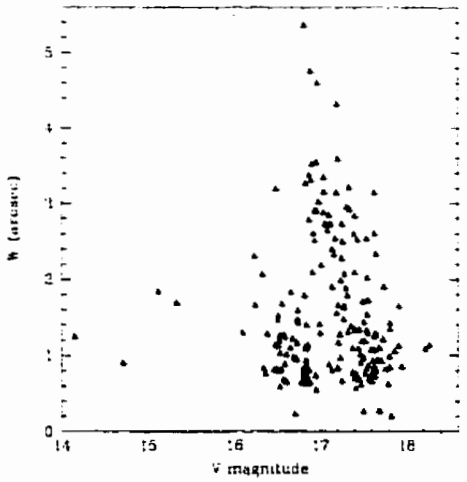

Figure 6.23: Globular cluster width versus V magnitude, showing no apparent trend.

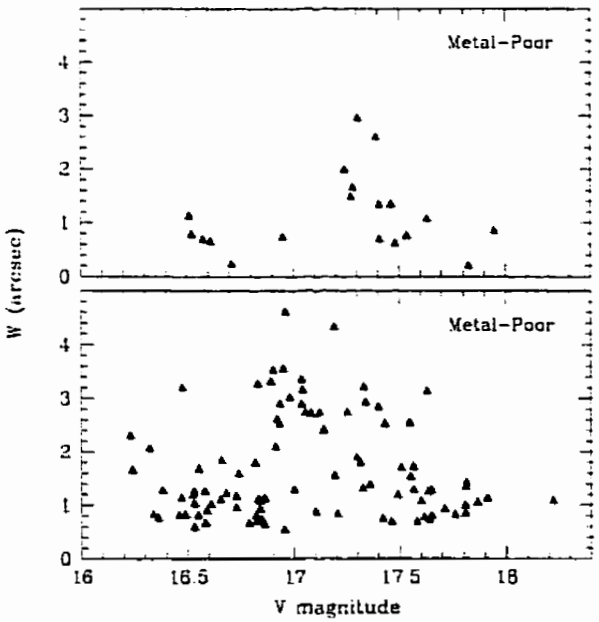

Figure 6.24: Globular cluster width versus V magnitude for the metal-rich and metal-poor populations.

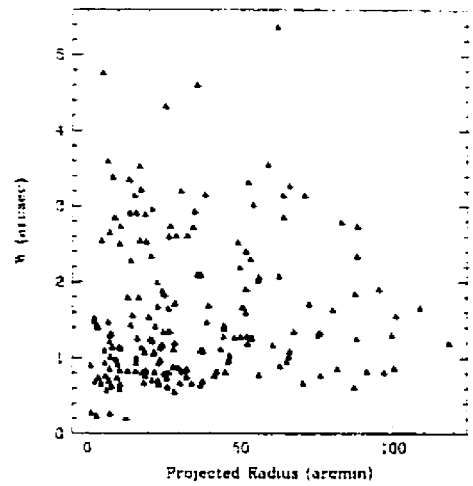

Figure 6.25: Globular cluster size versus projected galactocentric radius. A robust fit to the data is given by the dotted line, showing a modest increase in GC width with distance.

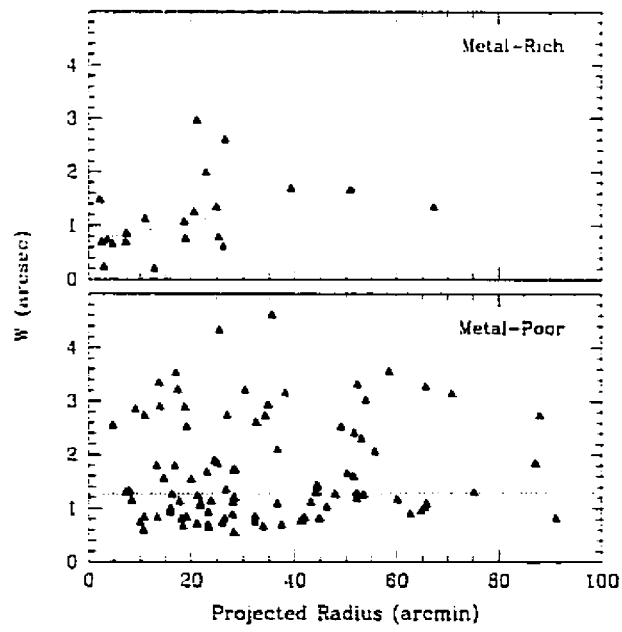

Figure 6.26: Globular cluster size versus projected galactocentric radius for the metal-rich and metal-poor globular clusters. Robust fits to the data are shown by the dotted lines.

7. SUBSTRUCTURE IN THE M31 GCS

In the hierarchical structure formation scenario, galaxies form at least in part from the merger and accretion of smaller lumps (see for example Cole et al. 2000). Clumping in the early Universe is believed to have resulted from small perturbations in the primordial density field, which in turn caused gravitational instabilities and the growth of structure from the "bottom-up". These clumps then evolved into dwarf galaxies like those observed in the present epoch, or they could have merged to form more massive galaxies. Such accretion would, at some level, likely continue during the present epoch.

Globular clusters have been identified within some of the dwarf galaxy satellites of the Milky Way (Da Costa & Armandroff 1995; Hodge et al. 1999; Oh, Lin & Richer 2000) and M31 (Grebel, Dolphin & Guhathakurta 2000), as well as in the dwarf members of distant galaxy clusters (e.g. Durrell et al. 1996; Miller et al. 1998). In the context of hierarchical galaxy formation, one would expect that the GCSs of massive galaxies might incorporate the cannibalized globular clusters of past accreted dwarfs. Of course, this presumes that a significant fraction of the early satellites were able to form globular clusters of their own, and that these clusters do not get destroyed during the merger.

Is it reasonable to search for grouping in the globular cluster system of M31? Are these likely to represent remnants of dwarf galaxy GCSs and, if so, what might this tell us about the formation and evolutionary history of M31? These questions are addressed in this chapter. The chapter begins with a brief review of the properties of the local dwarf galaxies and presents a "case study" of an accretion event: the Sagit-

tarius dwarf in the Milky Way. The plausibility of identifying remnants of recently accreted dwarf galaxies in M31 by way of their globular clusters is investigated, and a search is conducted for position/velocity/metallicity grouping in the M31 GCS.

7.1 Dwarf Galaxies

Dwarf galaxies are the most commonly found members of the present-day Universe, and are believed to have been even more prevalent in past epochs. There are several types of dwarf galaxies: spheroidals, ellipticals and irregulars. Dwarf spheroidal galaxies (dSph) are diffuse, low-surface-brightness galaxies with total masses of order $\sim 10^7 M_\odot$. These galaxies are thought to have a significant dark matter component due to their sizeable internal velocity dispersions (Grebel 2001). Dwarf elliptical galaxies (dE) are more massive, brighter and more compact galaxies with $M_{\rm tot} \sim 10^9 M_\odot$. The gas-rich dwarf irregulars (dIrr) tend to be dominated by star formation and have extended dark matter halos (Côté, Carignan, & Freeman 2000).

7.1.1 Local Group Dwarfs

The Local Group is a small group of galaxies dominated by the Milky Way and M31 which contains $\sim$ 45 known or suspected members. The vast majority of this population consists of dwarf galaxies, the general properties of which are listed in Table 7.1: the galaxy's subgroup affiliation, type, Galactic longitude (l) and latitude (b), distance (D), heliocentric radial velocity (v_r), core radius (R_c), total mass ($M_{\rm tot}$) and the number of globular clusters (N_{GC}) which are currently known to be associated with the satellite. The data in Table 7.1 is a summary of the tables in the review by Mateo (1998) on the subject of Local Group dwarf galaxies, with some additional recent data from the sources indicated in the table notes.

The Local Group dwarfs display a wide range of properties, with differing star

Table 7.1: Local Group dwarf galaxy parameters (Mateo 1998 and references therein).

Galaxy Name	Group	Type	l	b	D (kpc)	v_r ($\mathrm{km\,s^{-1}}$)	R_c (pc)	M_{tot} ($10^6\,M_\odot$)	N_{GC}
Sagittarius	MW	dSph	5.6	−14.1	24 ± 2	140 ± 5	550	—	4
UKS 2323-326	LG	dIrr	11.9	−70.9	1320 ± 350	62 ± 6	150	—	—
SagDIG	LG	dIrr	21.1	−16.3	1060 ± 160	−75 ± 5	125	9.6	—
NGC 6822	LG	IrrIV-V	25.3	−18.4	490 ± 40	−53 ± 4	260	1640	1
DDO 210	LG	dIrr/dSph	34.0	−31.3	800 ± 250	−137 ± 3	95	5.4	1
WLM	LG	IrrIV-V	75.9	−73.6	925 ± 40	−123 ± 3	710	150	1
Draco	MW	dSph	86.4	34.7	82 ± 6	−293 ± 2	180	22	—
Pegasus	LG	dIrr/dSph	94.8	−43.5	955 ± 50	−182 ± 2	280	58	—
Ursa Minor	MW	dSph	105.0	44.8	66 ± 3	−248 ± 2	200	23	—
And VI[a,b]	M31	dSph	106.0	−36.3	775 ± 35	—	—	—	—
And VII[a,c]	M31	dSph	109.5	−9.9	760 ± 70	—	—	—	—
IC 10	M31	dIrr	119.0	−3.3	825 ± 50	−344 ± 5	475	1580	—
And III	M31	dSph	119.3	−26.2	760 ± 40	—	180	—	—
NGC 147	M31	dSph/dE5	119.8	−14.3	725 ± 45	−193 ± 3	170	110	3
NGC 205	M31	E5p/dSph	120.7	−21.1	815 ± 35	−242 ± 3	260	740	12
NGC 185	M31	dSph/dE3p	120.8	−14.5	620 ± 25	−210 ± 7	155	130	9
M32	M31	E2	121.2	−22.0	805 ± 35	−197 ± 3	635	2120	0
And I	M31	dSph	121.7	−24.9	805 ± 40	—	375	—	1[d]
And V[a,c]	M31	dSph	126.2	−15.1	810 ± 45	—	—	—	—
LG S3	M31	dIrr/dSph	126.8	−40.9	810 ± 60	−282 ± 4	160	13	—
And II	M31	dSph	128.9	−29.2	525 ± 110	−188 ± 3[f]	205	—	—
IC 1613	M31/LG	IrrV	129.8	−60.6	700 ± 35	−237 ± 5	585	795	0
EGB 0427+63	M31	dIrr/dSph	144.7	10.5	1300 ± 700	−87 ± 6	85	—	—
Leo A	MW/N3109	dIrr	196.9	52.4	690 ± 100	26 ± 2	185	11	—
Leo II	MW	dSph	220.2	67.2	205 ± 12	76 ± 2	160	9.7	—
Leo I	MW	dSph	226.0	49.1	250 ± 30	286 ± 2	215	22	—
Sextans B	N3109	dIrr	233.2	43.8	1345 ± 100	303 ± 2	445	885	—
Fornax	MW	dSph	237.1	−65.7	138 ± 8	53 ± 3	460	68	5
Sextans	MW	dSph	243.5	42.3	86 ± 4	227 ± 3	335	19	—
Sextans A	N3109	dIrr/dSph	246.2	39.9	1440 ± 110	328 ± 5	700	395	—
Carina	MW	dSph	260.1	−22.2	101 ± 5	224 ± 3	210	13	—
NGC 3109	N3109	IrrIV-V	262.1	23.1	1250 ± 165	404 ± 2	630	6550	0-10
Antlia	N3109	dIrr/dSph	263.1	22.3	1235 ± 65	361 ± 2	230	12	—
Phoenix	MW/LG	dIrr/dSph	272.2	−68.9	445 ± 30	56 ± 3	310	33	—
Sculptor	MW	dSph	287.5	−83.2	79 ± 4	108 ± 3	110	6.4	0
GR 8	GR 8	dIrr	310.7	77.0	1590 ± 600	215 ± 3	110	7.6	—
Tucana	LG	dSph	322.9	−47.4	880 ± 40	—	130	—	—
NGC55	LG	IrrIV	332.7	−75.7	1480 ± 150	124 ± 6	875	15600	5
IC 5152	LG	dIrr	343.9	−50.2	1590 ± 200	124 ± 3	390	400	—

Notes: The Large and Small Magellanic Clouds (IrrIII-IV and IrrIV-V, respectively) have intentionally been excluded from this tabulation.

Additional references: *a)* RC3; *b)* Armandroff, Jacoby & Davies 1999; *c)* Grebel & Guhathakurta 1999; *d)* Grebel, Dolphin, & Guhathakurta 2000; *e)* Armandroff, Davies & Jacoby 1998; *f)* Da Costa et al. 2000.

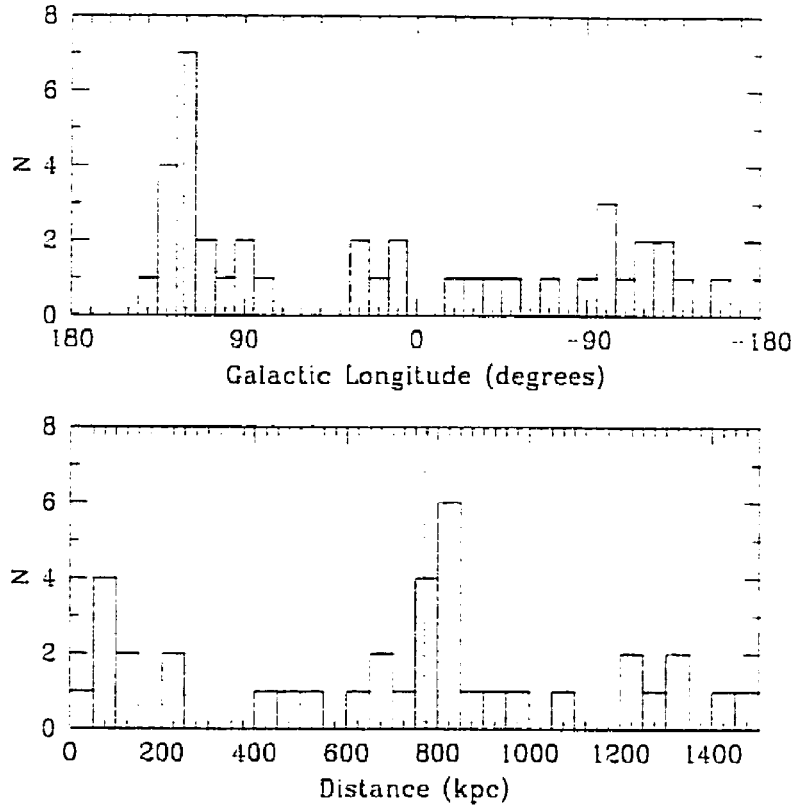

Figure 7.1: The distribution of Local Group dwarf galaxies in Galactic longitude (top) and distance from the Milky Way (bottom). In both plots, the concentration of dwarf galaxies about M31 (dotted line) is apparent.

formation and enrichment histories (Mateo 1998). They generally tend to have an old population and are, on average, of similar age to old Galactic globular clusters. The detailed orbits of these galaxies currently remain poorly understood due to a lack of proper motion data and large distance uncertainties. However, dwarf galaxies within $\sim$ 200 kpc from massive galaxies like the Milky and M31 are likely to be gravitationally-bound satellites of that parent galaxy (Grebel 2001). The concentration of satellites about M31 is apparent in histograms showing the number of dwarfs as a function of position and distance from the Milky Way (Figure 7.1).

7.1.2 A Current Merger: the Sagittarius Dwarf

The random accretion of dwarf galaxies may indeed be ongoing in many large galaxies. The fact that we are currently witnessing the assimilation of the Sagittarius dwarf spheroidal (Sgr dSph) galaxy by the Milky Way is evidence for such occurrences in the present day. There are also indications of tidal distortions in M31's companion, NGC 205 (Walterbos & Kennicutt 1987; Bender, Paquet & Nieto 1991). Either the process of satellite accretion is not uncommon, or we are observing our Galaxy and M31 at unique stages of their evolution.

Ibata, Gilmore & Irwin (1995) discovered the Sgr dSph as a large co-moving group of stars at a Galactocentric distance of 16 ± 2 kpc. The group has a major axis length of $\gtrsim 9$ kpc, an extent which indicates that it is being disrupted. Further, isodensity contours reveal that this object is elongated in a direction perpendicular to the plane of the Galaxy due to the spreading of stripped material along its orbit. Its stars are moderately old ($\sim$ 10 Gyr) and have a mean metallicity of $[\mathrm{Fe/H}] = -1.1 \pm 0.3$ (Mateo et al. 1995). The mean velocity of the group is 176 $\mathrm{km\,s^{-1}}$ with a dispersion of 10 $\mathrm{km\,s^{-1}}$ which is typical of many dwarf galaxies. The orbital period of the Sgr dSph is $\lesssim 1$ Gyr and it is believed to have survived over many ($\sim$ 10) orbits through the Milky Way (Ibata et al. 1997). The timescale for the complete disruption of the Sgr dSph is currently not known (Ibata 1999).

There are four globular clusters which are believed to be associated with the Sgr dSph based on their positions, distances and radial velocities (Ibata, Gilmore & Irwin 1994; Ibata et al. 1997). Ultimately, these clusters — M54, Arp 2, Terzan 7 and Terzan 8 — will have their orbits randomized by the strong potential of the Milky Way and they will take their place in the Galactic globular cluster system. The Sagittarius dwarf's globular clusters have a luminosity distribution which is similar to that of the outer halo of the Galaxy at $R > 80$ kpc (van den Bergh 1998), consistent with the identification of this satellite as a potential Searle-Zinn remnant. However, only one

of the four globular clusters associated with the Sgr dSph has a large half-light radius which is commonly associated with the outer halo clusters (van den Bergh, Morbey & Pazder 1991).

There is a substantial stellar stream associated with the Sagittarius dwarf (e.g. Ibata et al. 2001; Dohm-Palmer et al. 2001) and it is possible that the Sgr dSph has lost more of its original globular clusters along its orbit due to a strong and lengthy interaction with the Milky Way. Moreover, if the debris from accreted satellites constitutes a significant portion of the Galaxy's halo material, it may be reasonable to search for remaining signs of these mergers in the globular cluster system. A hunt for groups of globular clusters in position/velocity/metallicity parameter space may point to recent or even ancient mergers of satellite galaxies and their globular cluster systems.

How frequently might such accretion events have occurred, and how much (if any) residual evidence might remain? It has been found that the majority of the dwarf satellites in M31 and the Milky Way are on polar orbits: this would seem to suggest that these represent the survivors of a once much richer satellite population (Grebel, Kolatt, & Brandner 1998). Numerical simulations have shown that the signatures of such disrupted satellites can survive even over large timescales. Helmi and White (1999) simulated the destruction of satellites in the potential of the Milky Way over a timescale of $\sim$ 10 Gyr. They found that velocity correlations remained, despite the fact that the final density of debris was not significantly greater than the background. Based on numerical simulations of the Sgr dSph disruption in the Milky Way, Johnston et al. (1995) confirmed that debris from at least the dwarf's most recent passage is observable as moving groups in the halo of the Galaxy.

Interestingly, further numerical studies of the survival of dark matter halos have shown that fewer dwarfs are observed in the current epoch than models would predict. A numerical study by Klypin et al. (1999) predicted a population of low-mass,

dark halos within the Local Group which exceeds the observed number by an order of magnitude (see also Moore et al. 1999). They propose the existence of "dark satellites" which failed to accrete gas to form stars due to processes such as gas heating from ionization or mass-loss by supernovae-driven winds during the early formation stages of the Galaxy. Either the model assumptions are incorrect, or we are unable to observe these faint halos if they have no clear optical counterparts. The latter possibility would imply that there may be many more ongoing mergers than we currently observe.

7.2 Modeling the Fate of the Satellites

The continuing infall of clumps is a consequence of the hierarchical model of formation in the Universe. As a satellite galaxy (or, equivalently, a small dark matter halo) gets caught in the potential well of a galaxy, it will suffer a gradual stripping of its material due to tidal forces. It is thus necessary to consider the evolution of a dwarf galaxy's small globular cluster population in the presence of the large galaxian potential to determine if there is any point in searching for merger remnants over reasonable timescales (e.g. $\gtrsim 10^9$ yr after the initial encounter). To test this possibility, N-body simulations are used to follow the evolution of satellite globular cluster systems in an external potential similar to that of the Milky Way. The results of these simulations will be used in Section 7.3 to investigate the effectiveness of group retrieval over the course of an accretion event.

7.2.1 The Model Dwarf and the External Potential

The dwarf satellite galaxy in each simulation was modeled as a Hernquist sphere with a density distribution given by:

$$\rho(r) = \frac{M}{2\pi}\frac{s}{r}\frac{1}{(r+s)^3} \tag{7.1}$$

(Hernquist 1990), which corresponds to a cumulative mass distribution of

$$M(r) = \frac{Mr^2}{(r+s)^2}. \tag{7.2}$$

In the above equations, M is the total mass and s is a scale length which defines the half-mass radius of the distribution: i.e. setting $M(r_{1/2}) = M/2$ in Equation 7.2 gives $r_{1/2} = (1+\sqrt{2})s$. The potential, found by integrating Poisson's equation $\nabla^2\phi(r) = 4\pi G\rho(r)$, is given by

$$\phi(r) = -\frac{GM}{r+s}. \tag{7.3}$$

This analytical mass model is an approximation of the de Vaucouleurs $R^{1/4}$ profile which is applicable to galaxies and bulges (de Vaucouleurs 1953). In each simulation, roughly 10 000 particles were generated within this density profile to compose the dwarf galaxy. An extra 10 objects with a somewhat more extended distribution about the dwarf were designated to be the globular clusters; these GCs were each assigned masses of $5 \times 10^5 M_\odot$.

The galactic potential was assumed to be rigid and time-independent, and was built from three components: a spheroidal bulge potential (Hernquist 1990), a Miyamoto & Nagai (1975) thick disk, and a logarithmic halo. The forms of these potentials were adopted based on the modeling of the Sgr dSph by Johnston et al. (1995) and Helmi & White (2001):

$$\phi_{\rm disk} = \frac{-GM_{\rm disk}}{\sqrt{R^2 + (a + \sqrt{z^2+b^2})^2}} \tag{7.4}$$

$$\phi_{\rm bulge} = \frac{-GM_{\rm bulge}}{(r+c)} \tag{7.5}$$

$$\phi_{\rm halo} = v_{\rm halo}^2 \ln(r^2 + d^2) \tag{7.6}$$

In these equations, G is the gravitational constant, r and R represent radii, and z is the height above the disk. The masses (M), scale lengths (a, b, c, d) and velocity ($v_{\rm halo}$) in the above potentials were selected to reproduce the characteristics of the

Table 7.2: Galaxy model parameters

Parameter	Adopted Value
$M_{\rm bulge}$	$3.4 \times 10^{10} M_{\odot}$
$M_{\rm disk}$	$1 \times 10^{11} M_{\odot}$
$v_{\rm halo}$	$128\ {\rm km\,s^{-1}}$
a	6.5 kpc
b	0.26 kpc
c	0.7 kpc
d	12.0 kpc

Milky Way. The components of our Galaxy are better understood than those of M31, and we can expect the overall effects of satellite disruption within M31 to be quite similar. The adopted component parameters are provided in Table 7.2 and have been selected following Johnston (1998).

The representation here of the massive galaxy by a fixed potential of course neglects any exchange of energy between the satellite and its parent galaxy. Typical masses of dwarf satellites are orders of magnitude smaller than that of the Milky Way or M31. As a result, the effects of dynamical friction and energy exchange between the satellite and the massive galaxy are generally taken to be negligible, and can be ignored over the timescales of interest here (Helmi & White 2001).

7.2.2 *Initial Conditions*

Numerical simulations were executed in order to illustrate the effects of an interaction between a dwarf galaxy with a massive spiral like the Milky Way or M31. These N-body simulations were performed using the Barnes-Hut `treecode` version 1.4 distributed by J. Barnes[1] and modified by D. Stiff to include an external potential. The `treecode` algorithm is based on the commonly-used hierarchical force method described by Barnes & Hut (1986). An adaptive timestep was used, such that smaller

[1] *http://www.ifa.hawaii.edu/~barnes/treecode/treeguide.html*

Table 7.3: Initial conditions for N-body simulations

Parameter	Initial Conditions
$M_{\rm dw}$	$10^7 - 10^9 M_\odot$
$R_{\rm hm}$	$0.2 - 0.4$ kpc
R_{GC}	$1 - 2R_{\rm hm}$
D	$20 - 100$ kpc
θ	$0 - 90°$
α	$0 - 0.9$
β	$0 - 0.9$

timesteps were taken for larger global maximum accelerations. The external potential is a combination of the disk, bulge and halo potentials ($\phi_{\rm disk}$, $\phi_{\rm bulge}$, and $\phi_{\rm halo}$) as described in the previous section.

A series of $\sim$ 85 simulations were run in order to explore a reasonable range of parameter space by altering the initial conditions of the incident satellite. The ranges of initial conditions which were tested are given in Table 7.3. The total dwarf masses ($M_{\rm dw}$) were selected to span a range between a typical dwarf spheroidal and a dwarf elliptical and incorporate the mass of 10 globular clusters, each GC having $M = 5 \times 10^5 M_\odot$. The range in satellite half-mass radius ($R_{\rm hm}$) was chosen to correspond to a typical range of dwarf galaxy core radii (R_c provided in Table 7.1), a reasonable assumption if light follows mass. R_{GC} is the scale radius of the dwarf's globular cluster system. The satellites were given an initial galactocentric distance of D and a position angle θ above the plane of the disk. The parameters α and β dictate the initial partition of velocity in the XZ and XY plane, respectively, in units of circular velocity such that $\alpha^2 + \beta^2 = 1$ for circular orbits.

It should be noted that the simulations presented herein are intended to be illustrative, and *not* to reproduce the detailed characteristics of what would be a complex interaction. Further in-depth studies would benefit from the following additions and improvements:

1. The addition of evolving potentials for the bulge, disk and halo components. This would permit longer simulation timescales and a more informative and realistic evolution of the merger remnant.

2. The inclusion of the effects of dynamical friction, disk-shocking, gas dynamics, globular cluster destruction and formation during the interaction.

3. A more complete sampling of satellite parameter space (masses, scale lengths, initial velocities and position angles).

7.2.3 *N-body Simulation Results*

During the early stages of the interaction, stars from the dwarf are lost into leading or trailing streams. The satellite becomes flattened and disrupted, dispersing material until only a small fraction of the original mass remains within a small clump: the principal remnant of the original dwarf. Note that no particles "escape" from the simulation; no matter how far a particle might get from the centre of the satellite, its effect is still considered in the calculations.

The disruption progresses more rapidly when the satellite is given a more radial orbit with a low inclination, and the dwarf spends more time within the potential of the disk or travels through the bulge. However, the effects of the halo potential are sufficient to disrupt the satellite even on polar orbits with large galactocentric radii. Examples of the simulation results for various incidence angles and satellite masses as viewed face-on (the XY plane) and edge-on (XZ plane) to the disk are shown in Figures 7.2 to 7.7. The particle and GCS distributions extend beyond the fields of view shown in these figures.

The simulation snapshots show that depending on the characteristics of the orbit of the dwarf and its initial mass, its GCS will remain relatively spatially coherent over timescales of a few Gyr at most (a typical orbital period for the dwarf remnant is $\sim$ 1 Gyr). The more interesting question is whether the addition of kinematic

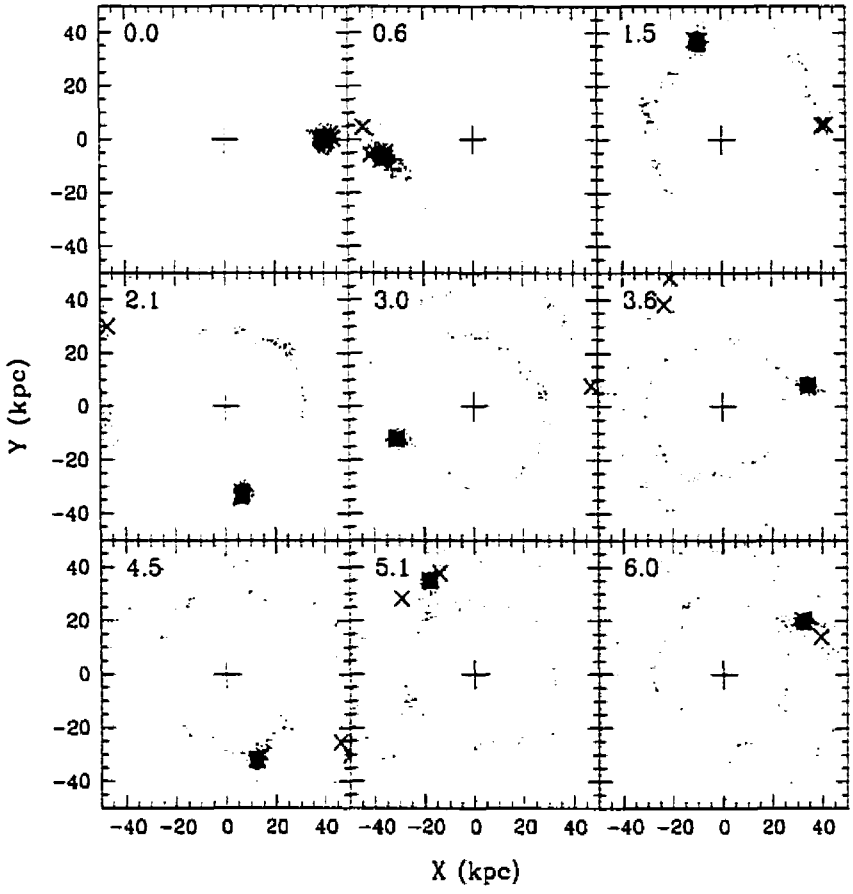

Figure 7.2: A sample of the simulation results for the case of a dwarf incident in the plane of the disk ($\theta = 0°$, $\alpha = 0$ and $\beta = 0.9$) as viewed in the XY plane, face-on to the disk. In this case, the satellite has an initial mass of $M_{\rm dw} = 10^9 M_\odot$ and a half-mass radius $R_{\rm hm} = 0.2$ kpc (its motion is counter-clockwise). The globular cluster system was given a scale radius of $2R_{\rm hm}$, and the GCs are represented by the large red crosses. The time in Gyr is given in each panel. Note that even though only two of the ten original satellite GCs remain within the field of view at $T = 6$ Gyr, all are considered in the analysis.

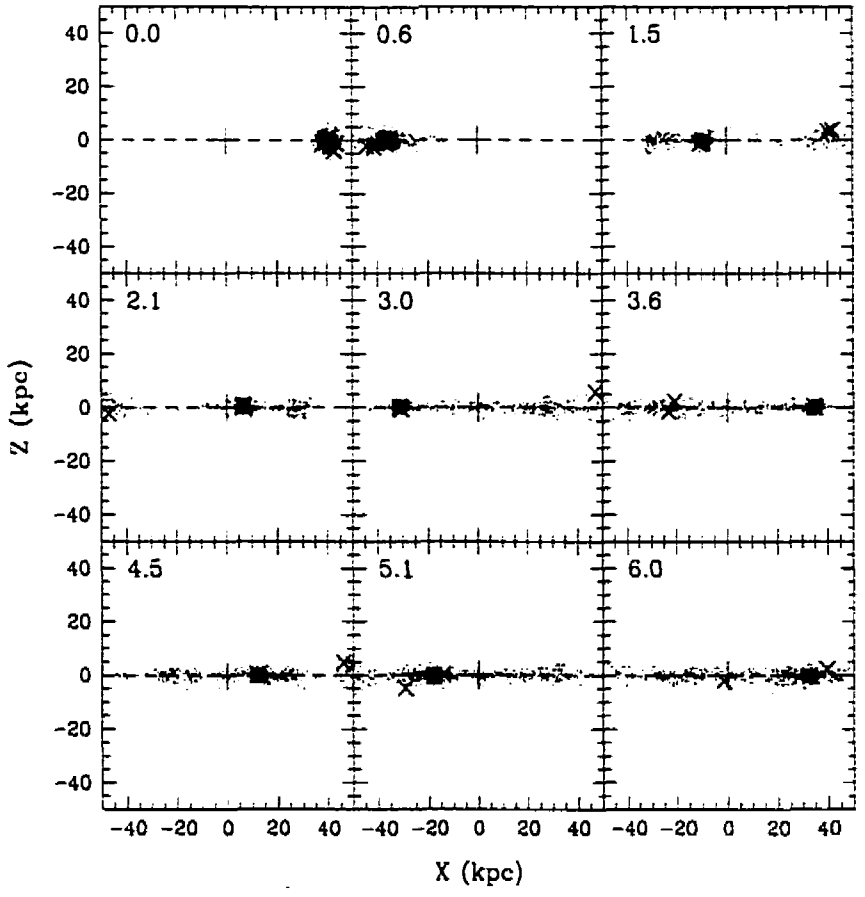

Figure 7.3: A sample of the simulation results for the case of a dwarf incident in the plane of the disk ($\theta = 0°$, $\alpha = 0$ and $\beta = 0.9$) as viewed in the XZ plane, edge-on to the disk (shown by the dashed line). In this case, the satellite has an initial mass of $M_{\rm dw} = 10^9 M_\odot$ and a half-mass radius $R_{\rm hm} = 0.2$ kpc. The globular cluster system was given a scale radius of $2R_{\rm hm}$, and the GCs are represented by the large red crosses. The time in Gyr is given in each panel.

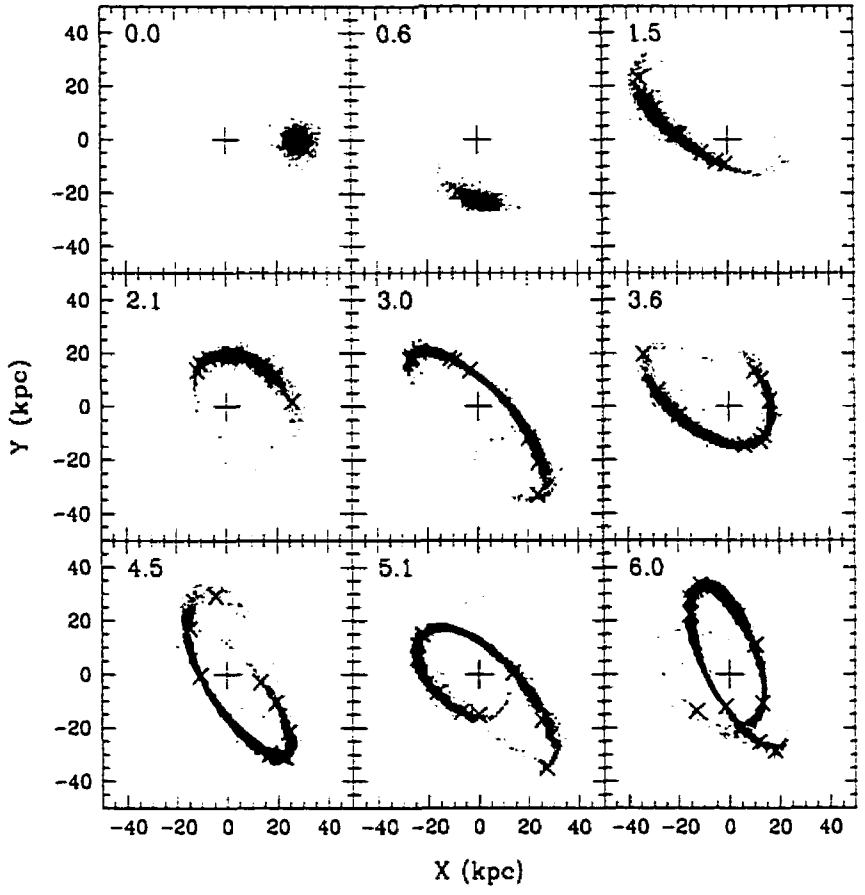

Figure 7.4: A sample of the simulation results for the case of a dwarf with an initial position angle of $\theta = 45°$ ($\alpha = 0.45$ and $\beta = 0.45$), as viewed in the XY plane, face-on to the disk. In this case, the satellite has an initial mass of $M_{\rm dw} = 10^7 M_\odot$ and a half-mass radius $R_{\rm hm} = 0.4$ kpc (its motion is counter-clockwise). The globular cluster system was given a scale radius of $1R_{\rm hm}$, and the GCs are represented by the large red crosses. The time in Gyr is given in each panel.

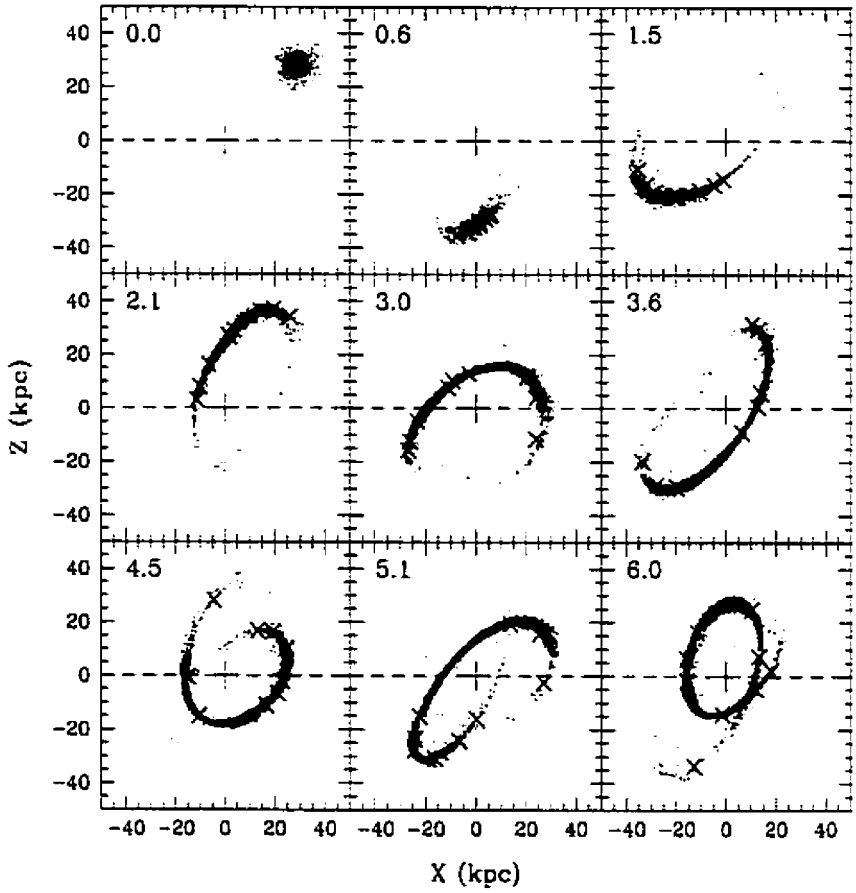

Figure 7.5: A sample of the simulation results for the case of a dwarf with an initial position angle of $\theta = 45°$ ($\alpha = 0.45$ and $\beta = 0.45$), as viewed in the XZ plane, edge-on to the disk (shown by the dashed line). In this case, the satellite has an initial mass of $M_{\rm dw} = 10^7 M_\odot$ and a half-mass radius $R_{\rm hm} = 0.4$ kpc (its motion is counter-clockwise). The globular cluster system was given a scale radius of $1R_{\rm hm}$, and the GCs are represented by the large red crosses. The time in Gyr is given in each panel.

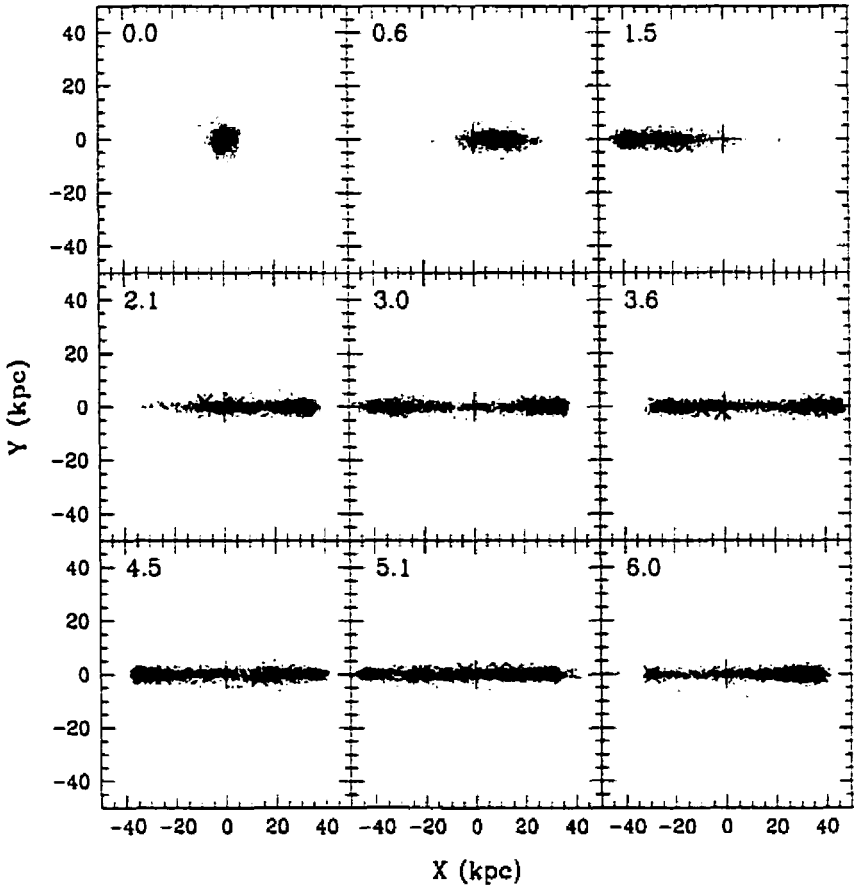

Figure 7.6: A sample of the simulation results for the case of a dwarf with an initial position angle of $\theta = 90°$ ($\alpha = 0.9$ and $\beta = 0$), as viewed in the XY plane, face-on to the disk. In this case, the satellite has an initial mass of $M_{\rm dw} = 10^8 M_\odot$ and a half-mass radius $R_{\rm hm} = 0.3$ kpc. The globular cluster system was given a scale radius of $1R_{\rm hm}$, and the GCs are represented by the large red crosses. The time in Gyr is given in each panel.

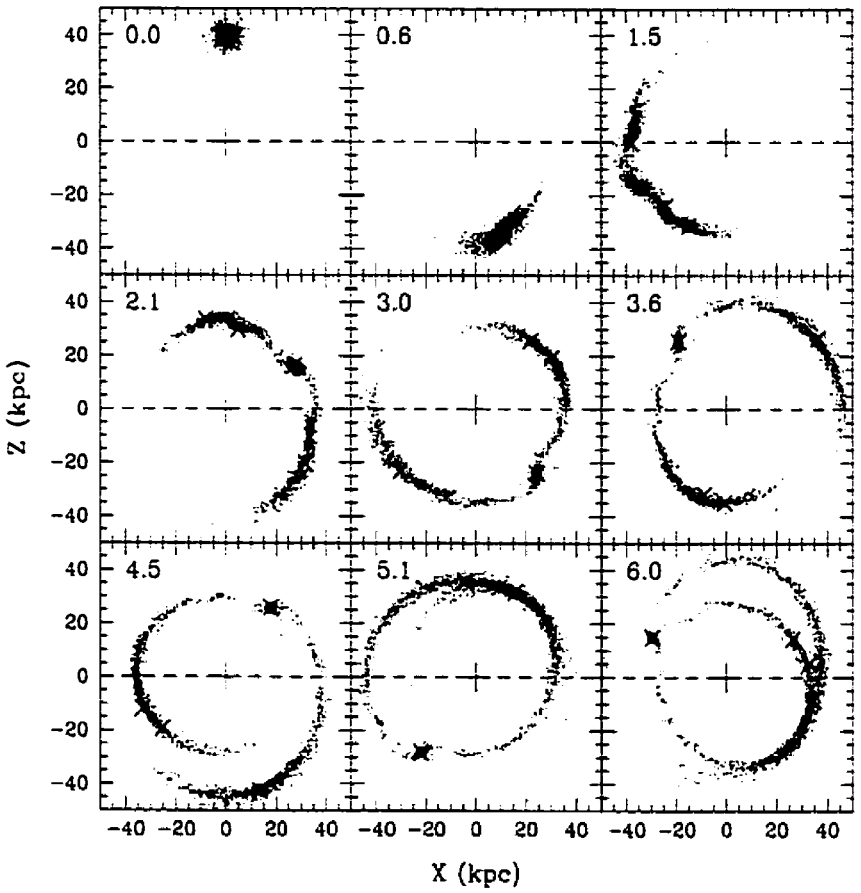

Figure 7.7: A sample of the simulation results for the case of a dwarf with an initial position angle of $\theta = 90°$ ($\alpha = 0.9$ and $\beta = 0$), as viewed in the XZ plane, edge-on to the disk (shown by the dashed line). In this case, the satellite has an initial mass of $M_{\rm dw} = 10^8 M_\odot$ and a half-mass radius $R_{\rm hm} = 0.3$ kpc (its motion is counter-clockwise). The globular cluster system was given a scale radius of $1R_{\rm hm}$, and the GCs are represented by the large red crosses. The time in Gyr is given in each panel.

data will help to affirm this apparent coherence, enough to enable the identification of a group of globular clusters which are associated with this cannibalized dwarf, using only projected positions and radial velocities. This question is addressed in the upcoming sections.

7.3 The Hunt for Groups

7.3.1 The Group-Finding Algorithm

The search for groups in parameter space was facilitated by a group-finding program (written by D. Stiff) which is based on a friends-of-friends algorithm. This algorithm links the neighbours of each particle which fall within a specified distance in parameter space, and each distinct set of joined particles constitutes a group.

The difficulty lies in determining what are appropriate limits on the parameters of interest. In the case of the M31 globular cluster system, these parameters include X and Y (projected) positions, radial velocity v_r, and, possibly to a lesser degree, metallicity [Fe/H]. The appropriate weighting of these parameters must be determined in advance in order to set the group linking criteria. For example, if X and Y each span a range of 100 arcmin, the velocities range over 600 $\mathrm{km\,s^{-1}}$, and metallicities span only 3 dex, an appropriate metric must be devised such that the group is not defined principally based on [Fe/H] owing to its comparatively small numerical range. In essence, the metric puts all of the parameters onto the same effective scale. In addition to the metric, the group-finding algorithm requires the input of a "linking length" which defines the smallest scaled distance between successive group members in parameter space. The linking length is expressed as a fraction of the mean inter-particle spacing.

Therefore, for each particle, the algorithm links a nearby particle to its group if

$$(\Delta s)^2 = \sum_i \gamma_i^2 (\Delta x_i)^2 < \Lambda^2 (\overline{\Delta s})^2, \qquad (7.7)$$

where Δs is the total separation of the neighbour to the particle in question, γ_i is the scaling or weighting factor defined for parameter i, Δx_i is the separation between the particle and its neighbour in parameter i, Λ is the specified linking length, and $\overline{\Delta s}$ is the mean inter-particle spacing for the entire collection of particles.

In this manner, the procedure is able to follow grouping along elongated streams. Error bars on the input parameters are accommodated by the addition of an "uncertainty ellipsoid" around each particle. A particle's parameter space neighbours are grouped with it if the minimum distance between their uncertainty ellipsoids are less than the linking length.

7.3.2 Metric and Linking Length Determinations

Since we have no *a priori* knowledge of what would be a suitable metric or linking length for the definition of a group in parameter space, a method was devised to test the group-finding algorithm on known groups using a range of scalings and linking lengths. Groups of objects with various spatial distributions (e.g. spherical, linear and curved streams), membership sizes, galactocentric positions and orientations were created with general parameters similar to those of Local Group dwarf galaxies. The groups were given internal velocity dispersions of $\sigma_v = 6$ to 12 km s^{-1}, mean metallicities of $\langle$[Fe/H]$\rangle = -1.2$ to -1.6 dex, and [Fe/H] spreads of $\sigma_{\rm [Fe/H]} = 0.3$ to 0.5 dex (e.g. Mateo 1998; Da Costa et al. 2000). The particles in these groups were then superimposed over a background of a few hundred particles consisting of a metal-poor random spherical halo distribution, a rotating metal-rich thick disk distribution inclined at 12.3° to the line-of-sight ($i = 77.7°$), and a rotating intermediate-metallicity ellipsoidal bulge distribution. A sample plot of the projected positions of a set of these simulated groups is shown in Figure 7.8.

Projected positions, radial velocities and metallicities for the fabricated group members and additional background objects were input to the group-finding proce-

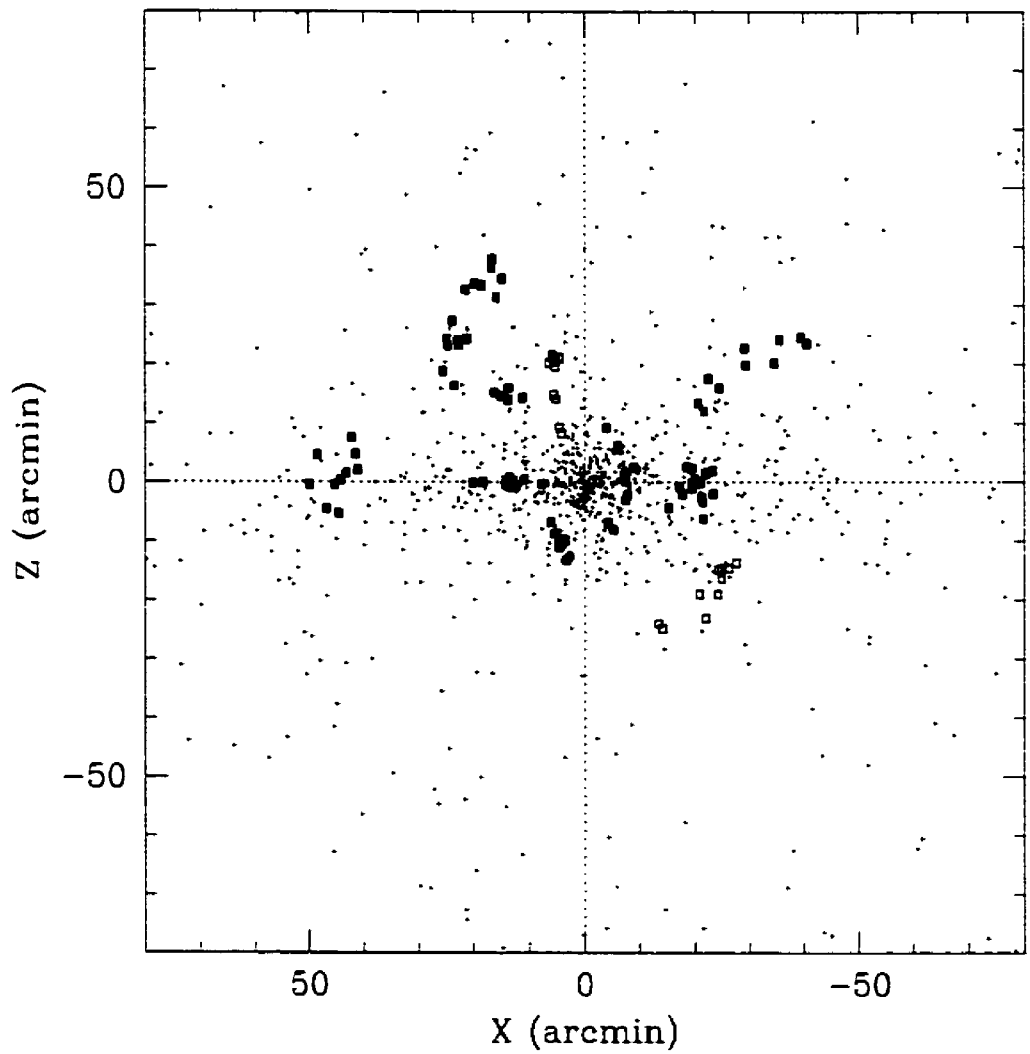

Figure 7.8: A sample plot showing projected positions for a set of simulated groups (coloured points) over a background distribution of particles. A series of parameter scalings and linking lengths were tested to determine the optimal parameters for the retrieval of these known groups.

dure, cycling through a range of linking lengths (Λ) and parameter scalings to determine the optimal combination for group retrieval. A minimum group membership of $n_{GC} = 4$ clusters was specified to define a group. Setting the X and Y scaling to $\gamma_X = \gamma_Y = 1.0$ to define the baseline, it was found that the best recovery rate occurred when $\Lambda = 0.1$ and the velocities were scaled by $\gamma_v = 0.13$ for cases when metallicities were *not* considered. With the addition of metallicity information, the optimal velocity and [Fe/H] scalings were $\gamma_v = 0.14$ and $\gamma_{[Fe/H]} = 9.7$, respectively, with a linking length of $\Lambda = 0.09$. Raising the minimum group membership to $n_{GC} = 6$ clusters did not significantly change these values.

As a further test, some of the simulation results from Section 7.2 were then examined to verify these optimal scalings and linking lengths for GC group retrieval over time. The globular cluster projected positions and radial velocities at various stages during the simulation were superimposed over a background of objects similar to that used in the fabricated group procedure described above. The optimal settings were determined based on the fraction of satellite GCs which were correctly allocated into one or more groups with $n_{GC} \geq 4$ members, with as little background contamination and false positive detections as possible. A sample of this variation in "optimal" linking length and velocity scaling with timestep is shown in Figure 7.9 for one of the simulations. Since the simulations did not include metallicity information, [Fe/H] scalings were not determined here.

Encouragingly, the simulation results for early timesteps generally yielded optimal linking lengths and velocity scalings which were very similar to those determined from the fabricated groups (see Figure 7.9). Their magnitudes did tend to increase with time, and in some cases the linking length started at values of $\sim 0.15 - 0.18$. Nonetheless, the somewhat more conservative linking length defined above was kept in order to minimize possible group contamination and the detection of false positives.

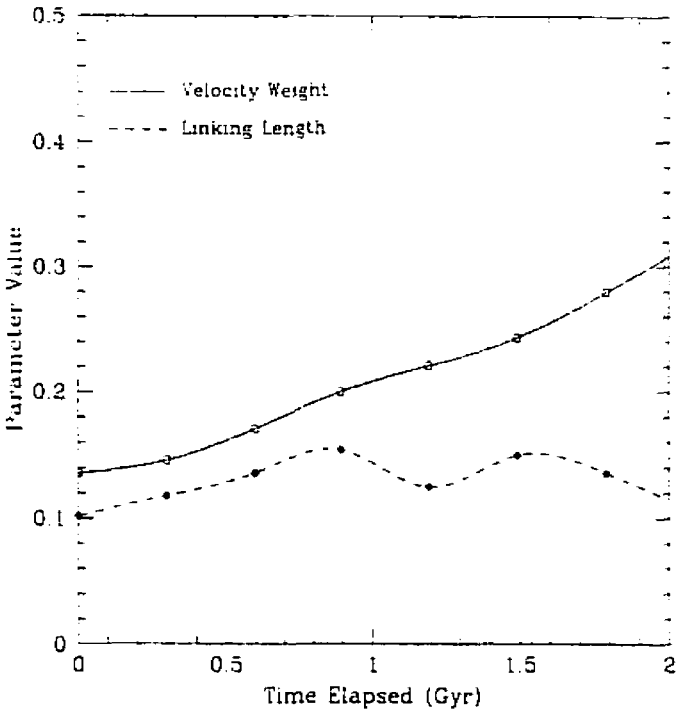

Figure 7.9: The variation of optimal linking length (solid line) and velocity weighting (dashed line) as a function of time for the simulation shown in Figures 7.4 and 7.5. At timestep zero, the best group recovery for the simulated dwarf's GCS occurred using $\lambda \sim 0.1$ and $\gamma_v \sim 0.14$, similar to the linking length and velocity weighting selected based on the fabricated group testing. The velocity weighting increases with time as the dwarf's GCS disperses (spatially) in the external potential.

7.3.3 Grouping in the Simulation Results

Using the scaling and linking lengths determined in the previous step ($\Lambda = 0.1$, $\gamma_v = 0.13$), the N-body simulation results were analyzed to investigate the likelihood of identifying the cannibalized dwarf's globular clusters as a group in parameter space. The three-dimensional positions and velocities were projected in an orientation similar to that of M31 with $i = 77.7°$, and were superimposed over the background components described in the previous section. The group-finding algorithm was then applied to the simulation results at various timesteps.

Two parameters, Q and Q_{max}, are defined as follows to reflect the retrieval efficiency of the satellite's GCS:

$$Q = \frac{1}{N}\sum_k \left(\frac{n_{GC}}{n_g}\right)_k \tag{7.8}$$

$$Q_{max} = \max\left(\frac{n_{GC}}{n_g}\right)_k \tag{7.9}$$

where N is the total number of groups containing globular clusters, n_{GC} is the number of globular clusters in group k, and n_g is the total number of objects (including background) which were found in group k. The sum in Q is calculated only over those groups which contain one or more globular clusters, and reflects the general contamination of the GC groups by background objects. Q_{max} is the maximum ratio of the number of GCs in any group to the total number of objects allocated to that group, and more appropriately indicates whether a *bona fide* group has been found. For perfect group recovery with no contamination, $Q = Q_{max} = 1$.

To demonstrate, let us examine a particular simulation with an initial dwarf position angle 90° ($\alpha = 0.9$, $\beta = 0$) with $M_{\rm dw} = 10^9 M_\odot$ above the plane at a timestep of 1.2 Gyr. The group-finding algorithm returned globular cluster group memberships as follows: 6 of the 10 dSph GCs were in the same group and had 1 additional background object included, 1 GC was allocated to a background group with 3 additional members, 1 GC was allocated to a background group with 4 additional members, and 2 GCs were not identified as members of any group. For this case with $N = 3$ groups containing one or more globular clusters:

$$Q = \frac{1}{3}\left[\frac{6}{7} + \frac{1}{4} + \frac{1}{5}\right] = 0.44$$

$$Q_{max} = \max\left(\frac{6}{7}, \frac{1}{4}, \frac{1}{5}\right) = 0.86$$

The high Q_{max} indicates that it is very likely that we can detect a group containing, by definition ($n_{GC} > 4$), a significant fraction of the disrupting satellite's GCS, here

with only $\sim$ 14% contamination by background objects. The moderate to low Q ratio reflects the fact that some of the satellite's GCs were allocated to other groups to which they do not truly belong. Plots of the evolution of Q and Q_{max} with time for a series of initial conditions are provided in Figures 7.10, 7.11, and 7.12.

The orbital periods of the satellite debris within the potential of the parent galaxy are of order 1 Gyr, apparent in the periodicity seen in most of the Q plots. This periodicity is largely dictated by the initial galactocentric radius of the dwarf in the potential of the parent galaxy, as well as by its initial velocity. The effects of varying the starting radius of the dwarf are demonstrated in Figure 7.13. In general, it appears that the GCSs of the simulated satellites given initial galactocentric distances of $\lesssim$ 20 kpc are very difficult to recover after one orbit. For instance, if a Sgr dSph equivalent was located in M31 at a radius of 16 kpc, it would be unlikely that we could discover the remnant based on its globular clusters. The association of a stellar stream would be necessary in such a case. According to the simulation results, satellite globular cluster groups would be more easily observable at galactocentric radii of $\gtrsim$ 60 kpc due to their significantly lower degree of disruption over the relevant timescales.

The probability of detection clearly depends to a large degree on the relic's location in its orbit, as there is a decreased likelihood of finding a group if the GCS debris is fore or aft of the bulge, or obscured in the rotating disk particles. Therefore, the likelihood that the detection of grouping in a galaxy's GCS reflects the remnant of a *bona fide* accretion event is comparatively low if the group is superimposed over the dense part of the disk or the bulge of the galaxy.

In reality, the orbital parameters of past or even present satellites are rarely known. Therefore, the average Q values of a large sample of simulations having a variety of initial position angles and incident velocities can be examined to get some idea of the likelihood of group detection for a satellite on a random orbit. The mean and

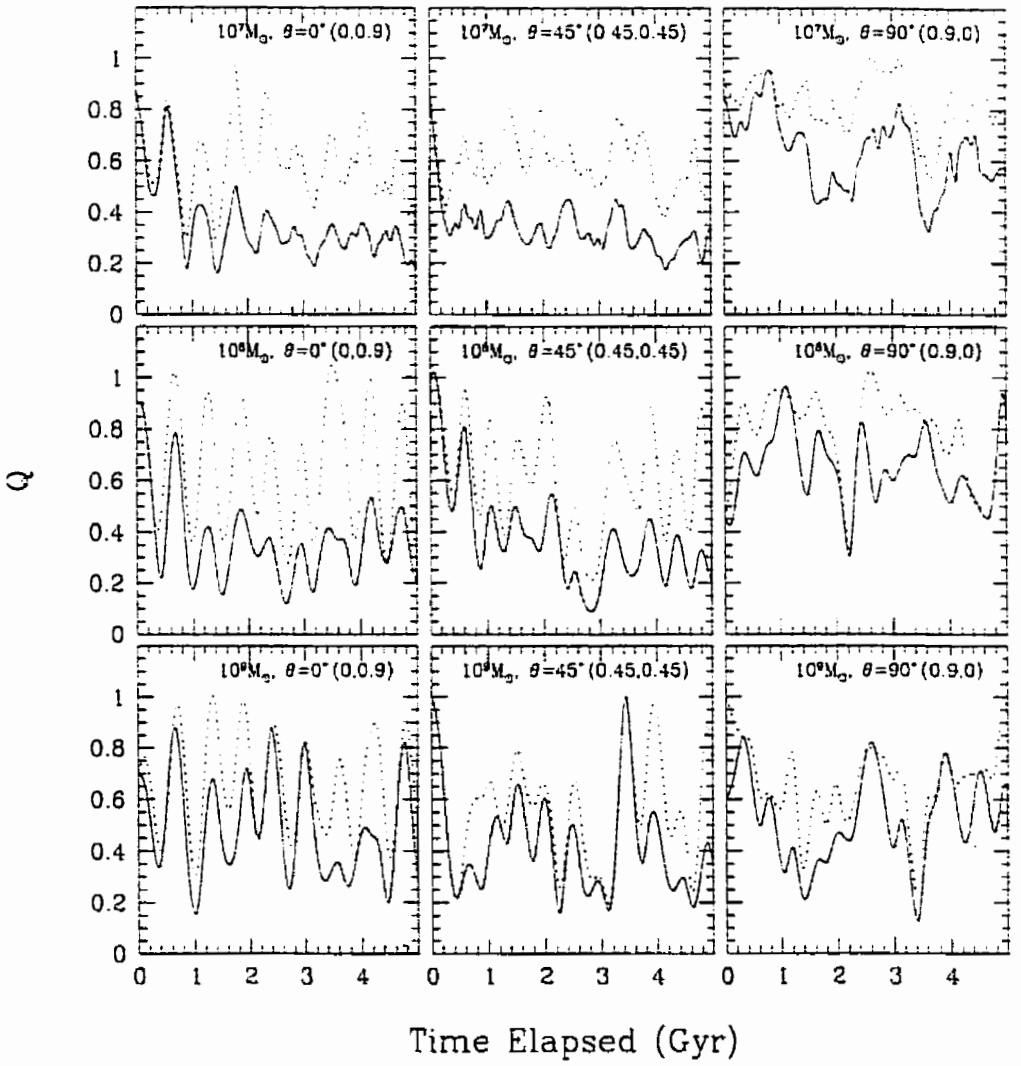

Figure 7.10: The Q ratio values for a representative sample of the simulations run using a dwarf half-mass radius of $R_{\rm hm} = 0.2$ kpc and a globular cluster scale radius of $R_{GC} = 2\,R_{\rm hm}$. The solid lines represent smoothed fits to the Q values obtained at each timestep, and the dotted lines are smoothed fits of Q_{max}. In each panel, the satellite masses, initial position angles (θ) and velocity partitions (α, β in parentheses) are provided.

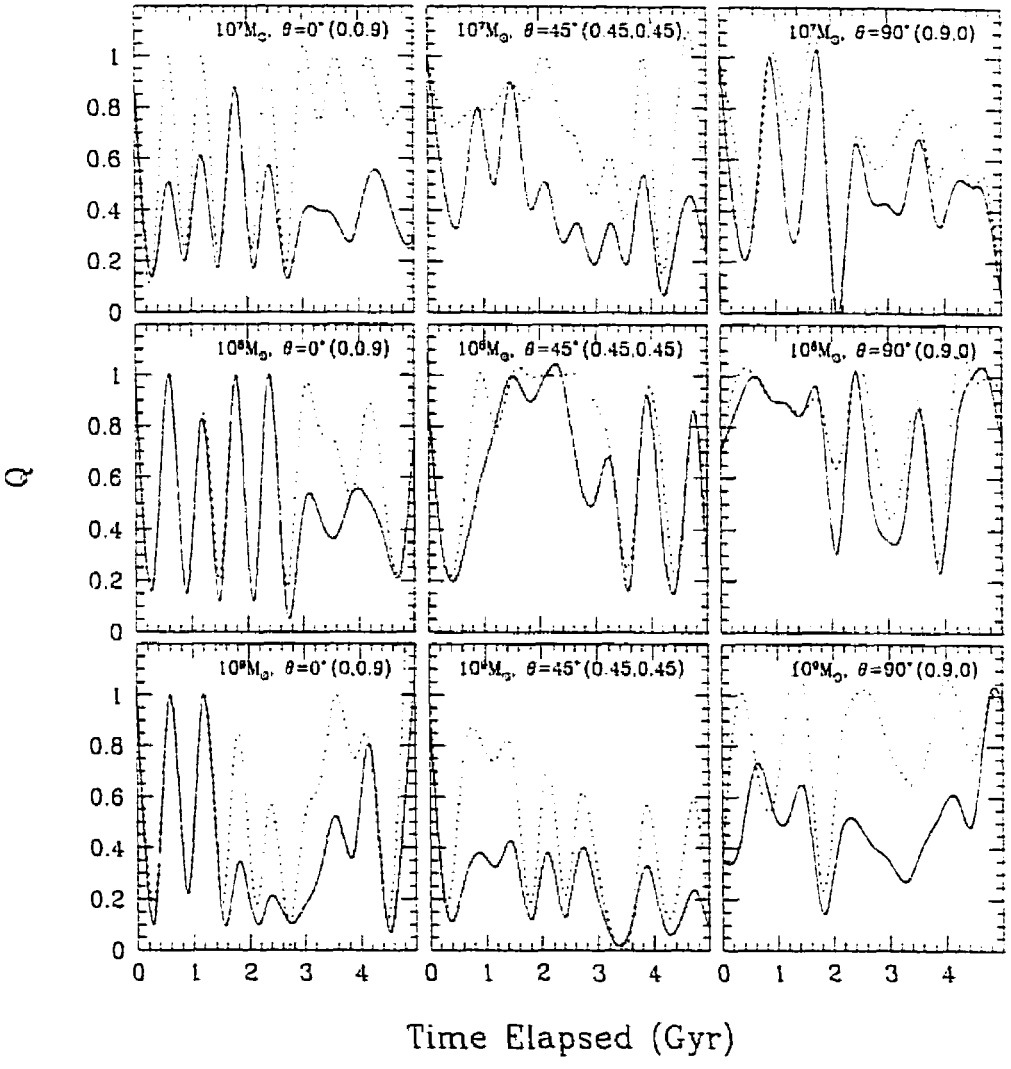

Figure 7.11: The Q ratio values for a representative sample of the simulations run using a dwarf half-mass radius of $R_{\rm hm} = 0.3$ kpc and a globular cluster scale radius of $R_{GC} = 1\, R_{\rm hm}$. The solid lines represent smoothed fits to the Q values obtained at each timestep, and the dotted lines are smoothed fits of Q_{max}. In each panel, the satellite masses, initial position angles (θ) and velocity partitions (α, β in parentheses) are provided.

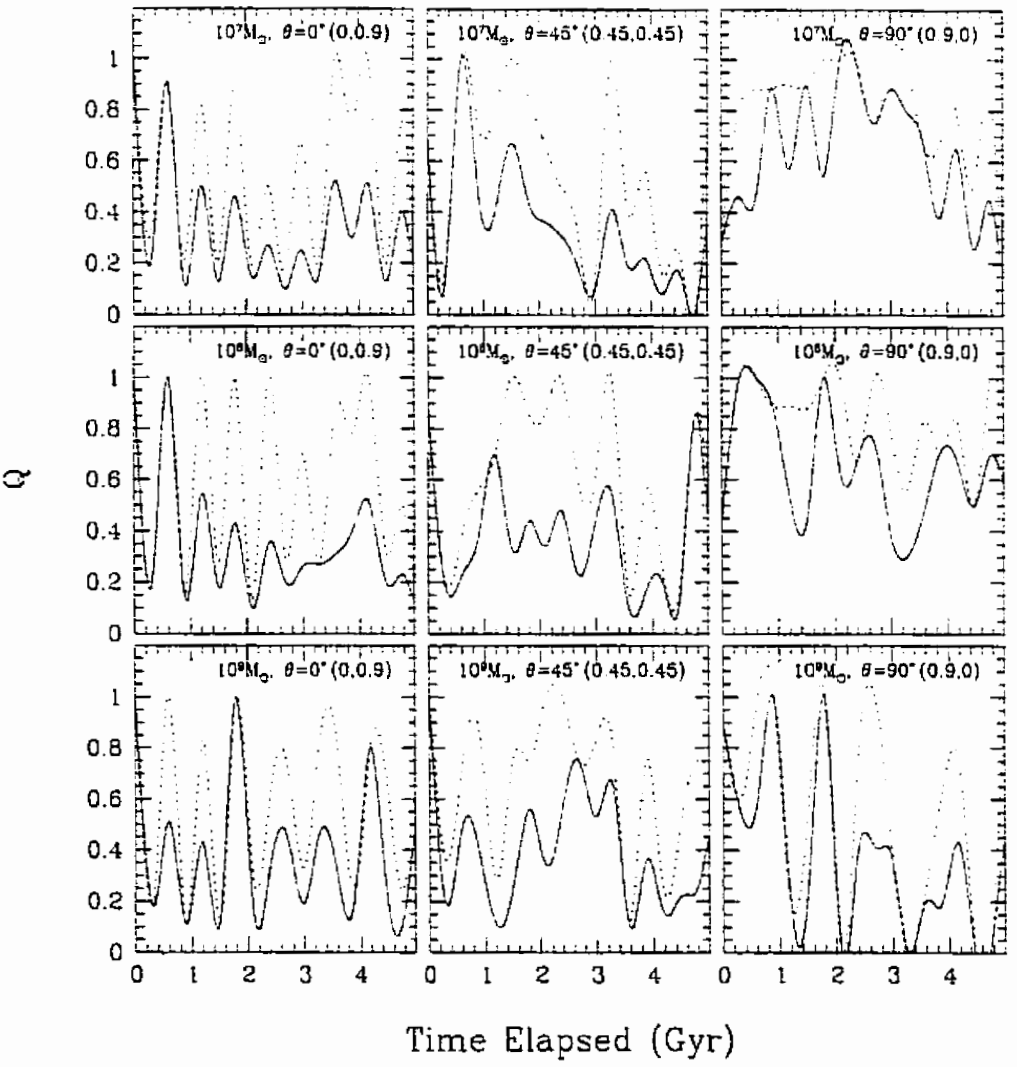

Figure 7.12: The Q ratio values for a representative sample of the simulations run using a dwarf half-mass radius of $R_{\rm hm} = 0.4$ kpc and a globular cluster scale radius of $R_{GC} = 1\,R_{\rm hm}$. The solid lines represent smoothed fits to the Q values obtained at each timestep, and the dotted lines are smoothed fits of Q_{max}. In each panel, the satellite masses, initial position angles (θ) and velocity partitions (α, β in parentheses) are provided.

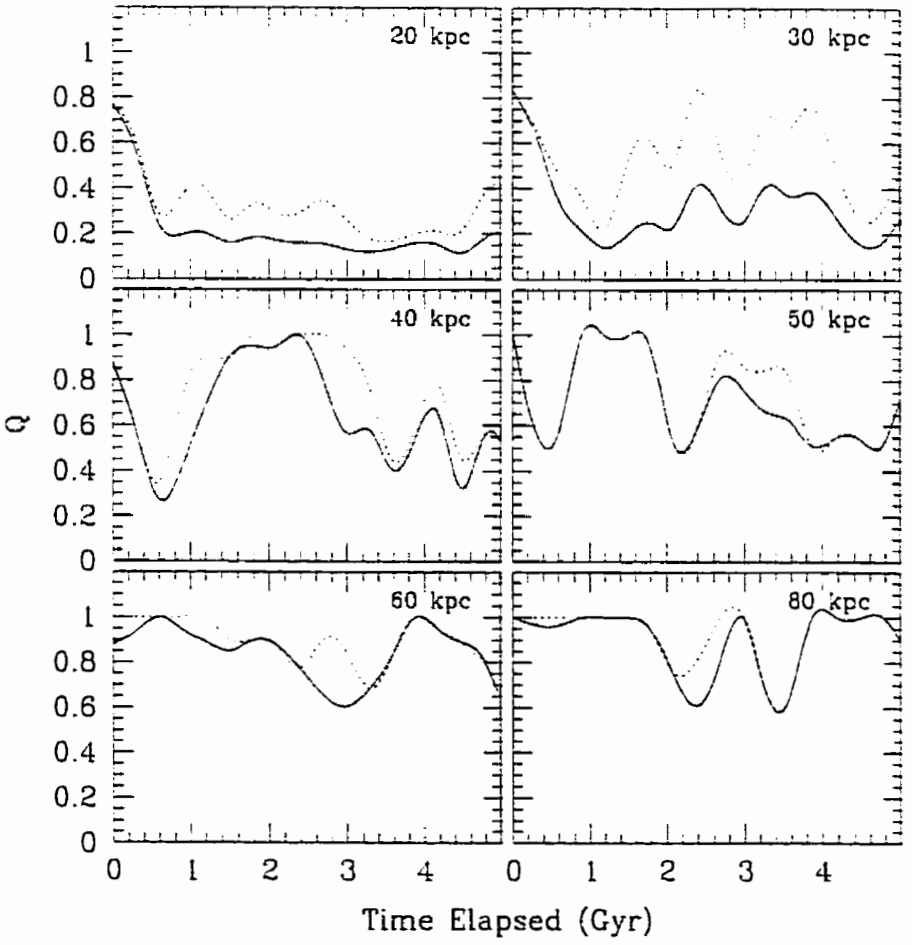

Figure 7.13: The Q ratio (solid line) and Q_{max} values (dotted lines) of a series of simulations with different dwarf initial distances. The galactocentric radius of the satellite at the start of the simulation is provided in the corner of each panel. All of the simulations shown were given similar initial conditions (other than initial distance): $M_{\rm dw} = 10^8 M_\odot$, $R_{\rm hm} = 0.3$ kpc, $R_{GC} = 1\,R_{\rm hm}$, $\theta = 45°$, $\alpha = \beta = 0.45$.

median Q and Q_{max} values for satellites with an initial galactocentric radius of 40 kpc are shown in Figure 7.14. The average and median Q values decrease with time, as expected. The Q results indicate that it is not likely that the complete GCS of the satellite dwarf can be recovered in a single uncontaminated group. However, the Q_{max} plot shows that one significant grouping of clusters associated with the cannibalized dwarf can generally be found up to several Gyr after the initial encounter. Again, this presumes that the initial satellite galaxy was initially massive enough to form and retain at least a handful of globular clusters, and that these GCs are not destroyed during the encounter.

7.4 Substructure in the M31 GCS

Having shown that it is in principle possible to detect grouping in the globular cluster system of a large galaxy which may have resulted from the recent accretion of a dwarf satellite with its own GCS, the available data for the M31 GCS were tested for the presence of such grouping. The "best spectroscopic sample" of available radial velocities and spectroscopic metallicities defined in Section 6.1 was examined for substructure. Quoted errors on velocity and metallicity were used to define the uncertainty ellipsoids about each data point in parameter space; no position uncertainties were incorporated in the analysis. Note that grouping based strongly on metallicity will not necessarily improve the quality of the substructure results. The dwarf galaxies of the Local Group exhibit a wide variety of star formation histories and metallicities (Mateo 1998). For example, Grebel & Guhathakurta (1999) report a large (1 dex) spread in metallicity within both And VI and And VII.

Applying the parameter scalings and linking lengths determined in Section 7.3.2, the data were analyzed using the group-finding algorithm. A minimum of four clusters was required to define a group. The complete available sample of M31 positions and velocities were examined for grouping both with and without the inclusion of [Fe/H]

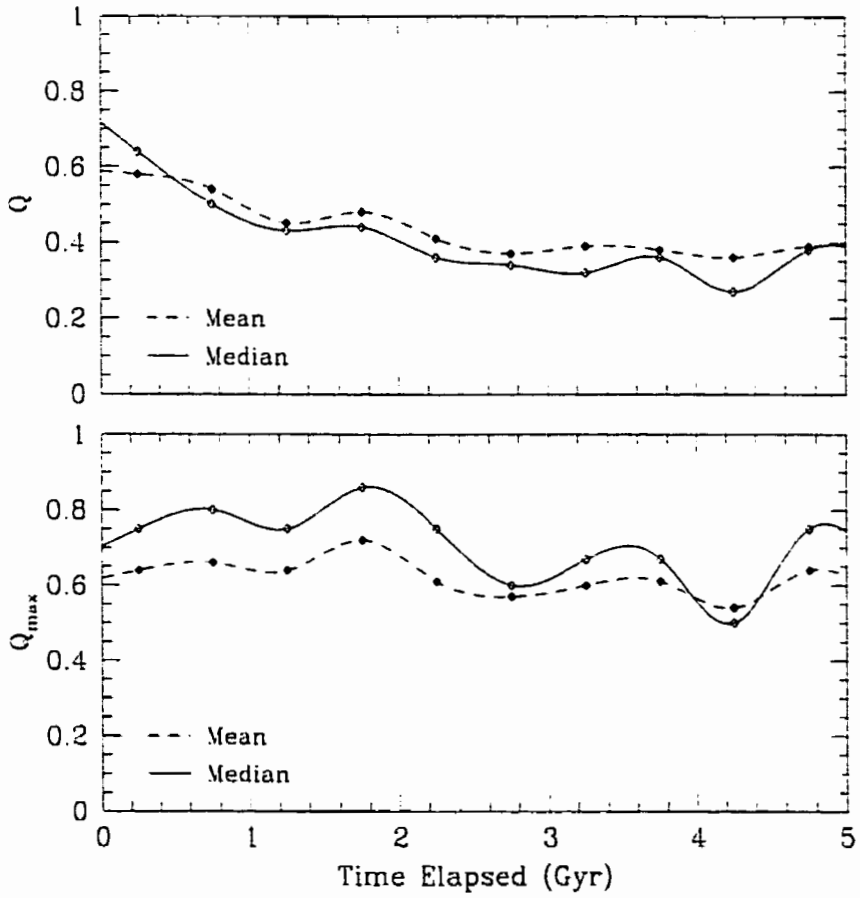

Figure 7.14: The average Q ratio (top plot) and Q_{max} values (bottom plot) of a series of simulations with a range of initial conditions at an initial distance of 40 kpc. The dashed and solid lines show smoothed fits to the mean and median values in timestep bins, respectively.

information. These results are shown in Figures 7.15 and 7.16. The results of a similar analysis on the 231 M31 globular clusters in the metal-poor population are shown in Figure 7.17 (without [Fe/H]) and Figure 7.18 (including [Fe/H]).

Not surprisingly, at least one group was found in the full sample of Figures 7.15 and 7.16 which corresponded to a sizeable portion of the metal-rich bulge population. Groupings remained within the central region even for the metal-poor population of the galaxy's GCS shown Figures 7.17 and 7.18. Several of these innermost groups are rejected here due to inconsistency in the membership allocations between the metal-poor and full sample determinations. As confirmed by the simulation results, cannibalized dwarf GCSs would be extremely difficult to recover in the dense inner regions of the galaxy regardless. Furthermore, final grouping results were required to be resistant to small changes in linking length and parameter scalings.

Of the groupings shown in Figures 7.15 to 7.18, there is convincing evidence for the presence of four confirmed and four tentative globular cluster groups of $n_{GC} \geq 4$ members in position/velocity/metallicity parameter space. The positions of these final groups are shown in Figure 7.19, and the data for group members are provided in Table 7.4.

The association of a group of globular clusters with NGC 205 is clearly evident in Figure 7.19. The mean velocity of the NGC 205 group is $v_r = -258$ km s^{-1}, comparable to NGC 205's systemic velocity of -242 ± 3 km s^{-1} (RC3).

It is interesting to note that none of the groups recovered in this analysis overlap with the associations found by Ashman & Bird (1993). This is at least partly attributable to the larger sample size presented here. Ashman & Bird used the 144 M31 cluster velocities and metallicities presented by Huchra, Brodie & Kent (1991), and then removed 49 of the metal-rich GCs from their grouping analysis as "non-halo" objects. Of the remaining 95 GCs in their sample, many had velocity uncertainties larger than ± 20 km s^{-1}.

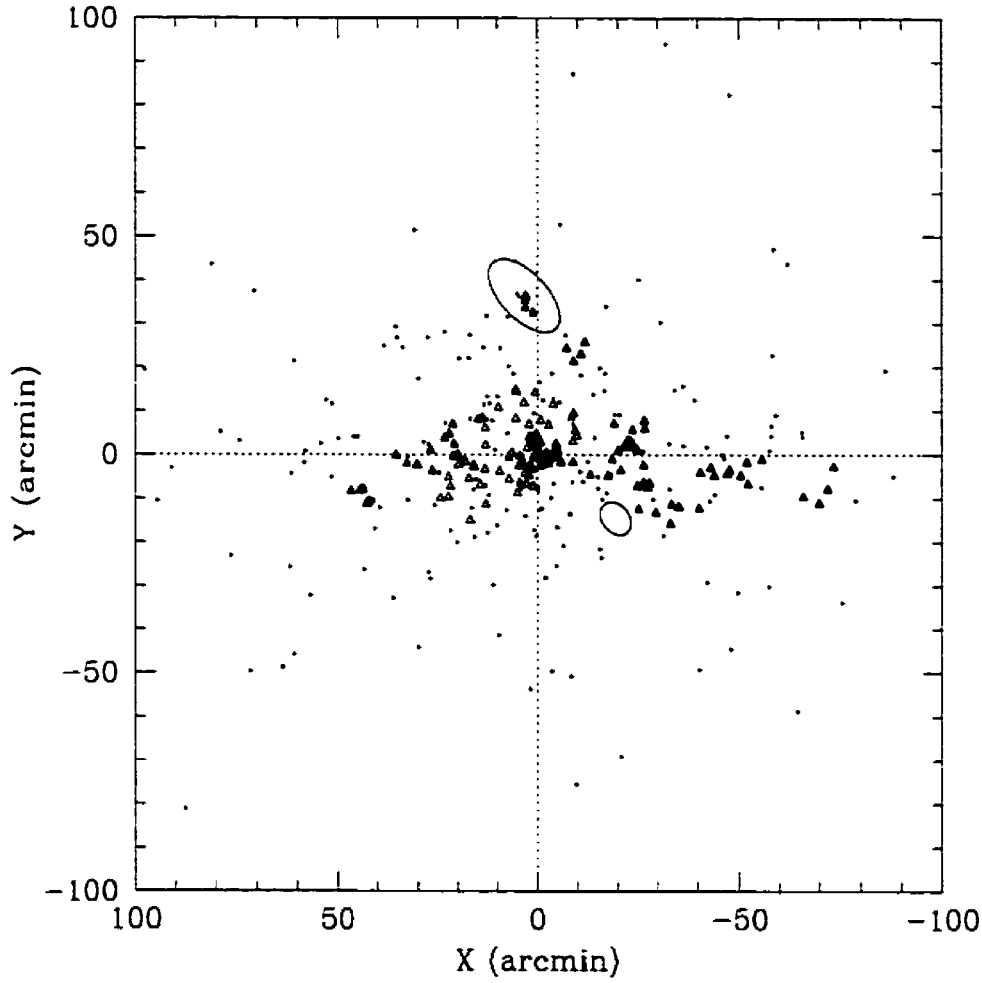

Figure 7.15: The locations of groups found in position and velocity parameter space for the entire sample of M31 GCS data. The blue ellipses represent the M31 companions NGC 205 (north) and M32 (southwest). Coloured symbols represent individual group members.

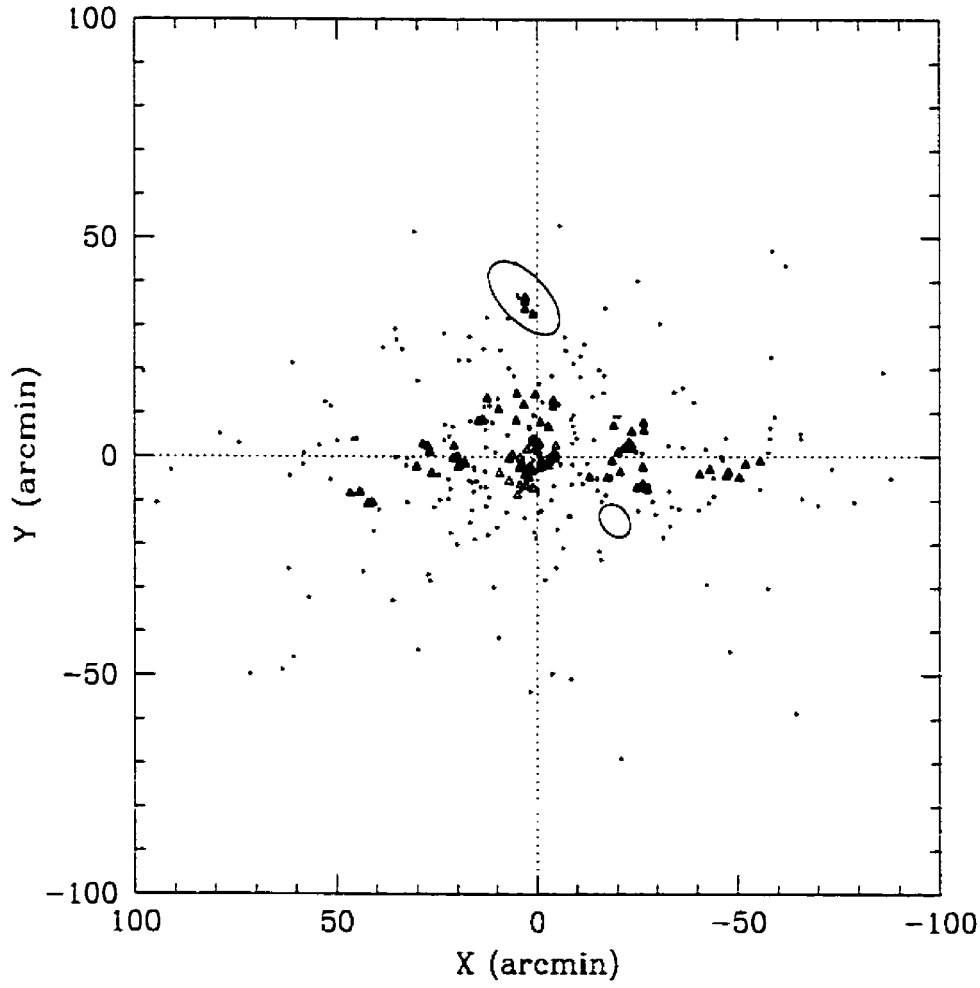

Figure 7.16: As in Figure 7.15 for the full M31 GCS, but with the addition of [Fe/H] information to the parameter space grouping.

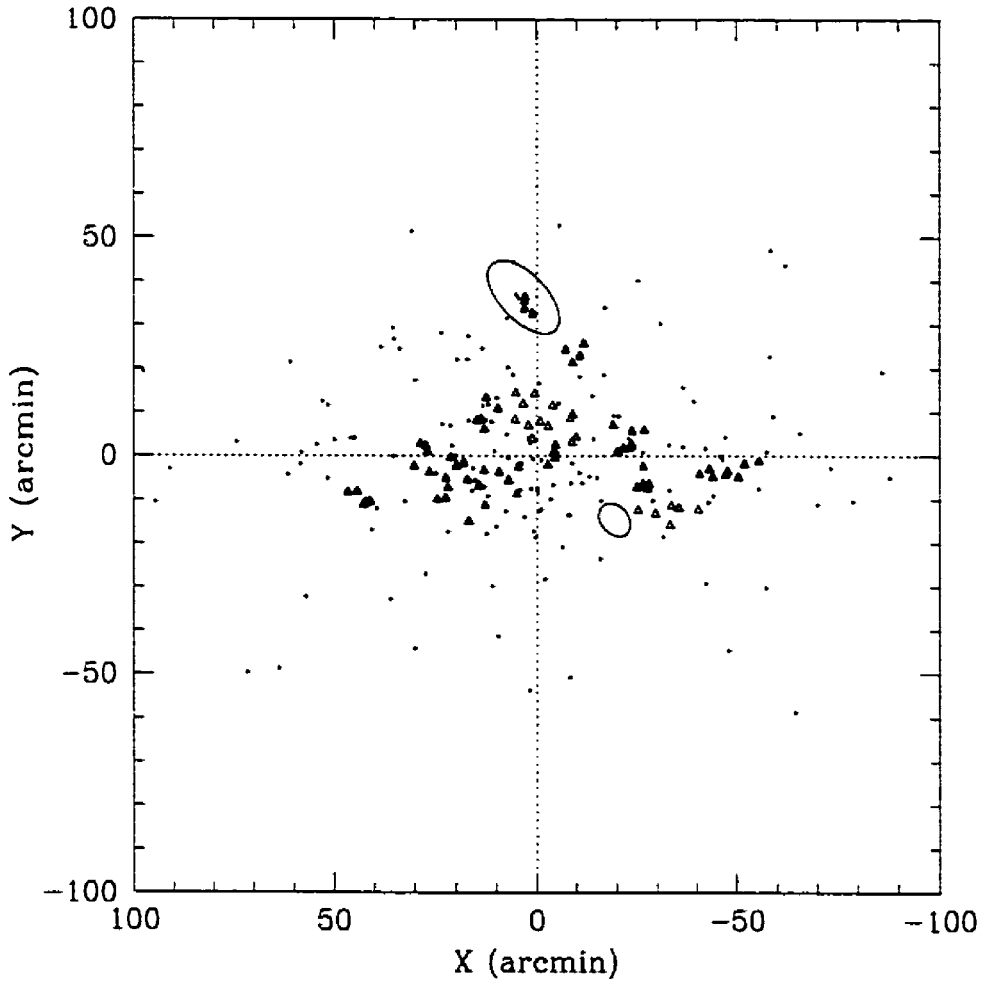

Figure 7.17: The locations of groups found in position and velocity parameter space for the 231 metal-poor M31 globular clusters. The blue ellipses represent the M31 companions NGC 205 (north) and M32 (southwest). Coloured symbols represent individual group members.

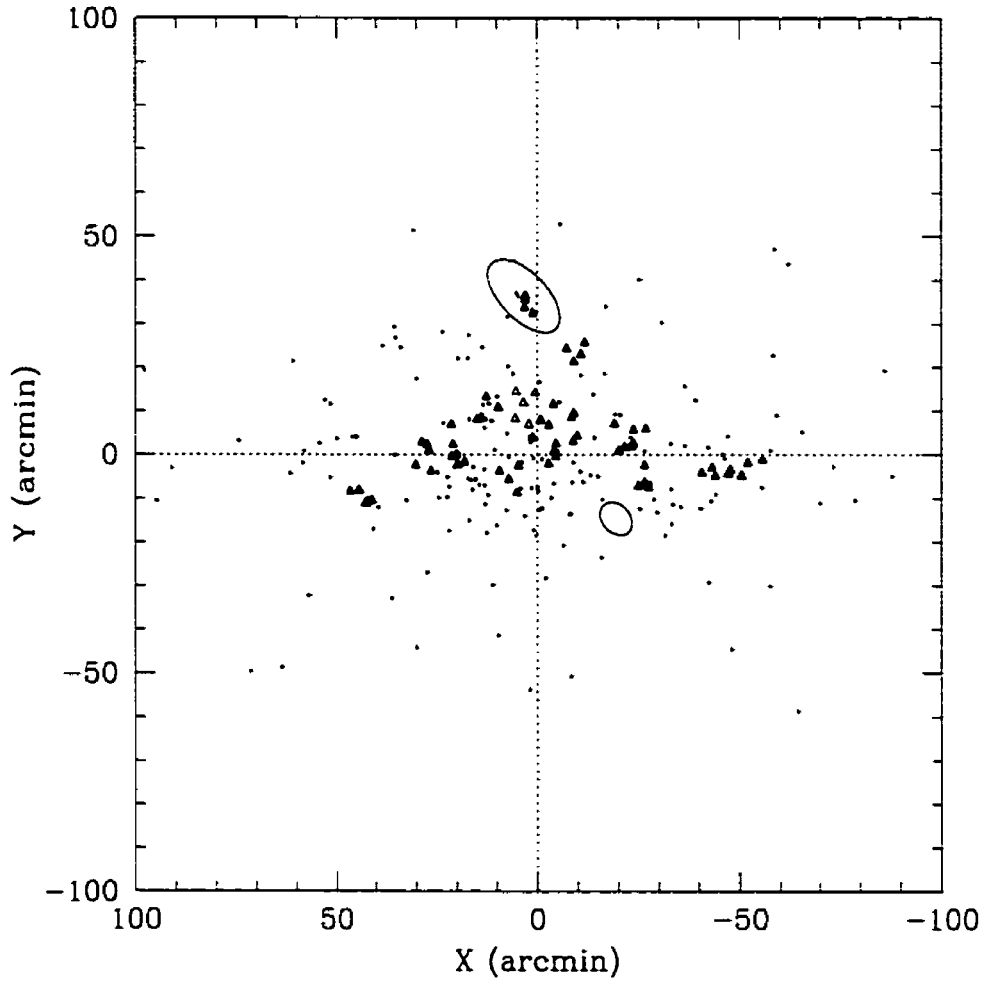

Figure 7.18: As in Figure 7.17 for the metal-poor M31 GCS, but with the addition of [Fe/H] information to the parameter space grouping.

The majority of the clusters in the inner and outer subsystems found by Saito & Iye (2000) are included in the metal-rich (bulge) population inferred from the KMM results discussed in Section 6.2.1. The bulk of inner subsystem found by Saito & Iye was recovered here as two of the central groups shown in Figure 7.15: the memberships of these inner groups were not stable and they are not listed in Table 7.4 for reasons discussed previously.

Do the M31 globular cluster groups listed in Table 7.4 represent the signatures of past accretion events? Without distance information or the identification of a coincident stellar stream, the correlation of M31 GCS grouping with past accretion events is somewhat tenuous. For the Sagittarius dwarf merger occurring within our Galaxy, we have three-dimensional data for a clear stellar stream. It is somewhat easier to pick out the globular clusters which coincide with this stream based on their distances and velocities. although even here the results are controversial (see. for example, Minniti, Meylan & Kissler-Patig 1996). At the distance of M31. we have projected data and are only now beginning to uncover signs of stellar streams (Ibata et al. 2001b). Note that this recently-discovered stream in M31 extends beyond the spatial limits of the observed cluster sample on a line connecting NGC 205 and M32 (Ibata et al. 2001b), and thus cannot be directly matched with any of the GC groupings found here.

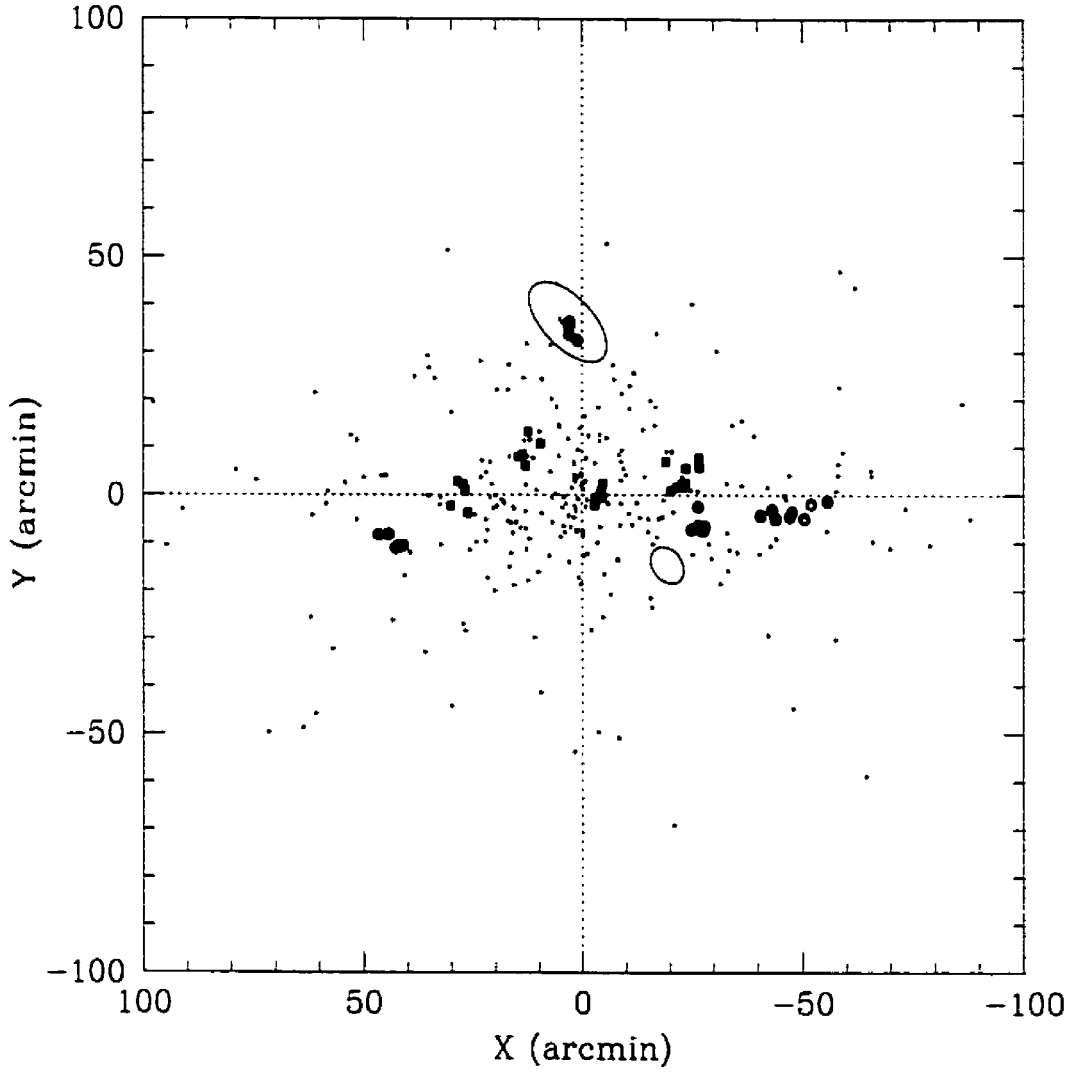

Figure 7.19: The positions of the confirmed groups (with members shown as coloured circles) and tentative groups (coloured squares) in the M31 globular cluster system. Group membership data are presented in Table 7.4.

Table 7.4: M31 groups in position/velocity/metallicity

GC	X (arcmin)	Y (arcmin)	v_r (km s^{-1})	[Fe/H]
		Group 1		
B484-S310	46.69	-8.31	-104 ± 12	-1.95 ± 0.59
B480	44.36	-8.18	-135 ± 12	-1.86 ± 0.66
DAO84	42.76	-11.08	-192 ± 12	-1.79 ± 0.72
B376-S309	42.22	-10.64	-142 ± 20	-2.18 ± 0.99
B374-S306	41.14	-10.50	-96 ± 12	-1.90 ± 0.67
		Group 2: NGC 205		
B11-S63	3.12	33.74	-157 ± 52	-1.54 ± 0.34
B328-S54	3.11	35.50	-243 ± 23	-1.51 ± 0.28
B324-S51	2.95	36.42	-299 ± 35	-1.39 ± 0.40
B9-S61	1.11	32.47	-335 ± 52	-1.57 ± 0.26
		Group 3		
B57-S118	-24.94	-7.16	-437 ± 12	-2.12 ± 0.32
B34-S96	-26.43	-2.40	-540 ± 12	-1.01 ± 0.22
B458	-26.44	-6.37	-521 ± 12	-1.18 ± 0.67
B49-S112	-27.49	-7.41	-481 ± 12	-2.14 ± 0.55
DAO48	-27.91	-6.55	-490 ± 12	-2.01 ± 0.99
		Group 4		
B18-S71	-40.63	-4.15	-585 ± 12	-1.63 ± 0.77
B448	-43.13	-3.01	-552 ± 12	-2.16 ± 0.19
B335	-43.95	-4.87	-514 ± 12	-1.05 ± 0.26
BoD195	-47.14	-4.38	-552 ± 12	-1.64 ± 0.19
B327-S53	-47.65	-3.51	-528 ± 12	-2.33 ± 0.49
B443	-50.41	-4.85	-532 ± 12	-2.37 ± 0.46
B319-S44	-51.99	-1.81	-535 ± 12	-2.27 ± 0.47
B315-S38	-55.62	-1.13	-559 ± 12	-1.88 ± 0.52
		Group 5: tentative		
B229-S282	30.25	-2.30	-103 ± 88	-1.81 ± 0.74
DAO66	28.68	2.88	-148 ± 12	-1.82 ± 0.26
DAO65	27.37	2.32	-130 ± 12	-1.80 ± 0.36
B216-S267	26.90	1.02	-84 ± 12	-1.87 ± 0.39
B223-S278	26.45	-3.68	-101 ± 12	-1.13 ± 0.51
		Group 6: tentative		
B141-S197	14.83	8.06	-180 ± 12	-1.59 ± 0.21
B137-S195	13.79	8.50	-215 ± 12	-1.21 ± 0.29
DAO58	13.13	6.19	-125 ± 12	-0.87 ± 0.07
B102	12.63	13.34	-236 ± 12	-1.57 ± 0.10
B105-S166	9.71	10.83	-238 ± 12	-1.13 ± 0.32
		Group 7: tentative		
B126-S184	-2.76	-2.04	-182 ± 14	-1.20 ± 0.47
NB91	-2.93	-1.19	-187 ± 10	-0.71 ± 0.33
NB83	-4.23	0.84	-150 ± 14	-1.26 ± 0.16
B106-S168	-4.54	-0.43	-90 ± 43	-0.86 ± 0.68
B86-S148	-4.64	2.48	-168 ± 21	-1.74 ± 0.17
		Group 8: tentative		
V31	-19.06	7.11	-433 ± 12	-1.59 ± 0.06
V216	-20.17	0.96	-465 ± 12	-1.15 ± 0.26
B33-S95	-21.57	1.78	-439 ± 12	-1.33 ± 0.24
B31-S92	-23.12	1.88	-400 ± 12	-1.22 ± 0.40
B28-S88	-23.64	2.54	-434 ± 12	-1.87 ± 0.29
B453	-23.69	5.64	-446 ± 12	-2.09 ± 0.53
B15	-26.57	7.78	-460 ± 12	-0.35 ± 0.96
DAO39	-26.73	5.92	-478 ± 12	-1.22 ± 0.41

8. SUMMARY AND CONCLUSIONS

This study has presented a significant sample of new spectroscopic observations of M31 globular clusters, contributing $\sim$ 200 high-precision velocities and [Fe/H] values for what represents a large fraction of the dynamical tracers of the galaxy. A comprehensive analysis of the kinematics and abundance properties of M31's GCS demonstrates both some interesting similarities and differences when compared with the Milky Way's globular cluster population.

The Galactic and M31 globular cluster systems have comparable mean metallicities of [Fe/H] ~ -1.2 to -1.3, although it has been shown that the two distributions are not drawn from the same parent population. A KMM mixture-modeling test reveals that the M31 GCS metallicity distribution can convincingly be separated into two groups, a bimodality which is analogous to that found in the Milky Way GCS. The peaks in the M31 metallicity distribution lie at [Fe/H] $= -1.44$ and -0.50. However, a KMM test on the Milky Way GCS metallicities returns peaks at [Fe/H] $= -1.59$ and -0.56, indicating that the metal-poor Galactic globulars have, on average, a somewhat lower metal abundance than their M31 counterparts.

M31's metal-rich globular clusters appear to constitute a distinct kinematic subsystem which is centrally-concentrated, consistent with membership in a bulge population akin to the inner metal-rich clusters of the Milky Way (Minniti 1995; Côté 1999; Forbes, Brodie & Larsen 2001). Furthermore, the velocity dispersion of the metal-rich cluster system, $\sigma_v = 146 \pm 12$ km s^{-1}, is indistinguishable from the mean bulge dispersion of σ_v(bulge) $= 156 \pm 23$ km s^{-1} as determined from the kinematics of faint planetary nebulae (Lawrie 1983). The mean metallicity of this population is

quite similar to its Milky Way counterpart and these metal-rich clusters demonstrate no obvious abundance gradient with galactocentric radius. Contrary to observations in the Milky Way, however, there are no clear signs of flattening in the metal-rich component of the M31 GCS *despite* the sampling bias towards major axis fields in the WYFFOS dataset. The rotation axis of the metal-rich cluster population is tilted by an angle of $\sim 10 - 15^{\circ}$ with respect to that of the minor axis of M31 and the rotation axis of the bulk of its GCS. This observation points to a disparate origin for these clusters.

The origin of this metal-rich population represents an intriguing mystery. Did these clusters form *in situ* in a second phase of collapse in an enriched medium and, if so, how? Or do they instead represent a population that formed independently of the parent galaxy (e.g. within the large protogalactic remnants) which fell in towards the centre of the potential well? Further searches for potential cluster candidates hidden by the bulge of M31 may be helpful in providing a clearer understanding of the origin and nature of these metal-rich inner clusters.

In M31, there are more than three times as many metal-poor clusters as there are metal-rich. The peak of the metal-poor GC distribution is at a significantly lower [Fe/H] than the average field star metallicity within the (inner) halo of [Fe/H] ~ -1.0 with a spread of $\sigma_{[Fe/H]} \sim 0.3$ (Pritchet & van den Bergh 1988). It is not clear if it is necessary (or even possible) to further separate this larger, more spatially distended metal-poor population into sub-components. If the metal-poor cluster distribution does indeed incorporate a thick disk component in addition to halo clusters, this would account for the relatively high net rotation amplitude and large velocity dispersion observed therein. While grouping the clusters based on metallicity remains an instructive exercise, [Fe/H] alone is not an adequate discriminator of membership in the spatially or kinematically defined components of the galaxy. This is primarily a result of the substantial spread and measurable gradient in [Fe/H] within the

metal-poor cluster system.

There is evidence for a radial metallicity gradient of roughly −0.015 dex/arcmin within the metal-poor population of M31 out to about 60′ from the galaxy center. Despite a notable lack of cluster data beyond this radius, it does seem that mean metallicity levels off, although the scatter remains large. This gradient in the metal-poor clusters is not inconsistent with a large-scale single collapse event in which the enrichment timescale is less than the collapse time (ELS). However, a metallicity gradient, in and of itself, is not sufficient to confirm an early dissipational collapse. Such a gradient could be mimicked by hierarchical halo formation if the metallicity of the accreting fragments correlates with their mass and mean density (Freeman 1996). The search for substructure in position/velocity/metallicity parameter space is clearly of interest in the investigation of the accretion history of the galaxy.

Numerical simulations in the present study have shown that spatial and kinematic grouping in the globular cluster systems of accreting dwarf satellites can be detected for several Gyr after the initial encounter. This is true even when considering only projected positions and radial velocities, provided the clump is not on an excessively radial orbit.

The discovery of grouping within the M31 globular cluster system points to a formation bolstered by the accretion of sub-clumps or dwarf satellites. This scenario is supported by the recent detection of a stellar stream in the Andromeda Galaxy by Ibata et al. (2001b), evidence of recently stripped material from M31's dwarf companions or of a past accretion event. The present-day disruption and accretion of the Sagittarius dwarf spheroidal in the Milky Way demonstrates that such minor mergers may be an ongoing process. Improved orbital parameters for the individual M31 GCS group members are required in order to ascertain if these clusters are dynamically correlated. The search for associated stellar or gaseous streams would provide useful corroborative evidence as to whether these groups do indeed reflect

recent merger events, or whether they are mere coincidental associations borne of a rotating globular cluster system.

A comprehensive investigation of the kinematics of the dynamical tracers in M31 would not be complete without the addition of planetary nebulae data. Fortunately, the study of a large sample of PNe in M31 is currently underway (Halliday, Carter, & Bridges in preparation). Moreover, these data can be combined with the globular cluster sample to better probe the underlying mass distribution of the galaxy (Wilkinson et al. in preparation).

The galaxy formation question remains largely an issue of timescale. Age determinations from high-resolution spectroscopy of a large sample M31 globular clusters would make a valuable contribution towards characterizing the formation timescales involved. Fortunately, an analysis of M31 cluster ages is in progress (Bridges et al. in preparation), which should provide a better sense of the chronology of GC formation within the galaxy.

Despite its long and rich history of investigation, there is little doubt that there are missing globulars in M31's database which are awaiting discovery and identification. Ongoing searches and surveys for M31 cluster candidates (e.g. Lee et al. 2001) promise to help remedy this situation and to further fuel this "booming industry". It is clear that detailed studies of the kinematics, metallicities and ages of the globular cluster systems of a large sample of galaxies can provide us with the clues necessary for a more complete understanding of the mechanisms which form and evolve galaxies of all kinds.

REFERENCES

Aaronson, M., Cohen, J. G., Mould, J., & Malkan, M. 1978, *Astrophys. J.*, 223, 824.

Alfaro, E. J., Cabrera-Caño, J., & Delgado, A. J. 1993, *Astrophys. J.*, 402, 53.

Armandroff, T. E. 1989, *Astr. J.*, 97, 375.

Armandroff, T. E., & Zinn, R. 1988, *Astr. J.*, 96, 92.

Armandroff, T. E., Davies, J. E., & Jacoby, G. H. 1998, *Astr. J.*, 116, 2287.

Armandroff, T. E., Jacoby, G. H., & Davies, J. E. 1999, *Astr. J.*, 118, 1220.

Ashman, K. M., & Bird, C. M. 1993, *Astr. J.*, 106, 2281.

Ashman, K. M., & Zepf, S. E. 1992, *Astrophys. J.*, 384, 50.

Ashman, K. M., & Zepf, S. E. 1998, *Globular Clusters* (New York: Cambridge Univ. Press).

Ashman, K. M., Bird, C. M., & Zepf, S. E. 1994, *Astr. J.*, 108, 2348.

Astronomical Almanac, 1998, (Washington: US Government), p. H42.

Aurière, M., Coupinot, G., & Hecquet, J. 1992, *Astr. & Astrophys.*, 256, 95.

Baade, W. 1944, *Astrophys. J.*, 100, 137.

Baade, W., & Arp, H. 1964, *Astrophys. J.*, 139, 1027.

Bahcall, J. N., & Tremaine, S. 1981, *Astrophys. J.*, 244, 805.

Barmby, P., Huchra, J. P., Brodie, J. P., Forbes, D. A., Schroder, L. L., Grillmair, C. J. 2000, *Astr. J.*, 119, 727.

Barmby, P., Huchra, J. P., & Brodie, J. P. 2001, *Astr. J.*, 121, 1482.

Barnes, J., & Hut, P. 1986, *Nature*, 324, 446.

Battistini, P., Bònoli, F., Braccesi, A., Fusi Pecci, F., & Malagnini, M. L. 1980, *Astr. Ap. Supp.*, 42, 357.

Battistini, P., Bònoli, F., Braccesi, A., Federici, L., Fusi Pecci, F., Marano, B., & Börngen, F. 1987, *Astr. Ap. Supp.*, 67, 447.

Battistini, P., Bònoli, F., Casavecchia, M., Ciotti, L., Federici, L., & Fusi Pecci, F. 1993, *Astr. & Astrophys.*, 272, 77.

Beaulieu, S. F., Freeman, K. C., Kalnajs, A. J., Saha, P. & Zhao, H. 2000, *Astr. J.*, 120, 855.

Beers, T. C., Flynn, K., & Gebhardt, K. 1990, *Astr. J.*, 100, 32.

Bekki, K. 2000, *Astrophys. J.*, 540, L79.

Bender, R., Paquet, A., & Nieto, J.-L. 1991, *Astr. & Astrophys.*, 246, 349.

Berendzen, R., Hart, R., & Seeley, D. 1976. *Man Discovers the Galaxies* (New York: Science History Publ.).

Binney, J., & Merrifield, M. 1998, *Galactic Astronomy*, (Princeton: Princeton Univ. Press).

Binney, J., & Tremaine, S. 1987, *Galactic Dynamics*, (Princeton: Princeton Univ. Press).

Binney, J., Gerhard, O. E., Stark, A. A., Bally, J., & Uchida, K. I. 1991, *Mon. Not. R. Astr. Soc.*, 252, 210.

Binney, J., Gerhard, O., & Spergel, D. 1997, *Mon. Not. R. Astr. Soc.*, 288, 365.

Binney, J., Dehnen, W., & Bertelli, G. 2000, *Mon. Not. R. Astr. Soc.*, 318, 658.

Blitz, L., Binney, J., Lo, K. Y., Baily, J., & Ho, P. T. P. 1993, *Nature*, 361, 417.

Bònoli, F., Delpino, F., Federici, L., & Fusi Pecci, F. 1987, *Astr. & Astrophys.*, 187, 25.

Bònoli, F., Delpino, F., Federici, L., Fusi Pecci, F., & Longmore, A. J. 1992, *Astr. & Astrophys.*, 96, 163.

Braun, R. 1990, *Astrophys. J. Supp.*, 72, 755.

Braun, R. 1991, *Astrophys. J.*, 372, 54.

Brewer, J. P., Richer, H. B., & Crabtree, D. R. 1995, *Astr. J.*, 109, 2480.

Bridges, T. J. 1998, in *Fibre Optics in Astronomy III*, ASP Conf. Ser. 152, eds. S. Arribas, E. Mediavilla and F. Watson, 104.

Brodie, J. P., & Hanes, D. A. 1986, *Astrophys. J.*, 300, 258.

Brodie, J. P., & Huchra, J.P. 1990, *Astrophys. J.*, 362, 503.

Brodie, J. P., & Huchra, J.P. 1991, *Astrophys. J.*, 379, 157.

Bullock, J. S., Kravtsov, A. V., & Weinberg, D. H. 2001, *Astrophys. J.*, 548, 33.

Buonanno, R., Corsi, C. E., Battistini, P., Bònoli, F., & Fusi Pecci, F. 1982, *Astr. Ap. Supp.*, 47, 451.

Burstein, D. 1979, *Astrophys. J.*, 234, 829.

Burstein, D., Faber, S. M., Gaskell, C. M., & Krumm, N. 1984, *Astrophys. J.*, 287, 586.

Cardelli, J. A., Clayton, G. C., & Mathis, J. S., 1989, *Astrophys. J.*, 345, 245.

Carney, B. W., Laird, J. B., Latham, D. W., & Aguilar, L. A. 1996, *Astr. J.*, 112, 668.

Chaboyer, B., Demarque, P. Kernan, P. J., Krauss, L. M., & Sarajedini, A. 1996, *Mon. Not. R. Astr. Soc.*, 283, 683.

Chen, B., Stoughton, C., Smith, J. A., Uomoto, A., Pier, J. R., Yanny, B., Ivezic, Z., York, D. G., Anderson, J. E., Annis, J., Brinkmann, J., Csabai, I., Fukugita, M., Hindsley, R., Lupton, R., Munn, J. A. 2001, *Astrophys. J.*, 553, 184.

Chiappini, C., Matteucci, F., & Romano, D. 2001, *Astrophys. J.*, 554, 1044.

Chiba, M., & Beers, T. C. 2000, *Astr. J.*, 119, 2843.

Cohen, J. G. & Matthews, K. 1994, *Astr. J.*, 108, 128.

Cohen, J. G., Frogel, J. A., & Persson, S. E. 1978, *Astrophys. J.*, 165, 165.

Cole, S., Lacey, C. G., Baugh, C. M., & Frenk, C. S. 2000, *Mon. Not. R. Astr. Soc.*, 319, 168.

Combes, F., Debbasch, F., Friedli, D., & Pfenniger, D. 1990, *Astr. & Astrophys.*, 233, 82.

Côté, P. 1999, *Astr. J.*, 118, 406.

Côté, P., Marzke, R. O., & West, M. J. 1998, *Astrophys. J.*, 501, 554.

Côté, P., Mateo, M., Sargent, W. L. W., & Olszewski, E. W. 2000, *Astrophys. J.*, 537, L91.

Côté, P., Marzke, R. O., West, M. J., & Minniti, D. 2000b, *Astrophys. J.*, 533, 869.

Côté, S., Carignan, C., & Freeman, K. C. 2000, *Astr. J.*, 120, 3027.

Cram, T. R., Roberts, M. S., & Whitehurst, R. N. 1980, *Astr. Ap. Supp.*, 40, 215.

Crampton, D., Cowley, A. P., Schade, D., Chayer, P. 1985, *Astrophys. J.*, 288, 494.

Curtis, H. D. 1917, *Publ. Astron. Soc. Pac.*, 29, 206.

Curtis, H. D. 1921, Bull. of the Nat. Res. Coun., 2, 194.

Da Costa, G. S., & Armandroff, T. E. 1995, *Astr. J.*, 109, 2533.

Da Costa, G. S., Armandroff, T. E., Caldwell, N., & Seitzer, P. 2000, *Astr. J.*, 119, 705.

de Freitas Pacheco, J. A. 1997, *Astr. & Astrophys.*, 319, 394.

de Vaucouleurs, G. 1953, *Mon. Not. R. Astr. Soc.*, 113, 134.

de Vaucouleurs, G. 1958, *Astrophys. J.*, 128, 465.

de Vaucouleurs, G., de Vaucouleurs, A., Corwin Jr., H.G., Buta, R. J., Paturel, G., & Fouque, P., Third Reference Catalogue of Bright Galaxies, 1991, Version 3.9 (RC3).

Djorgovski, S. G., Gal, R. R., McCarthy, J. K., Cohen, J. G., de Carvalho, R. R., Meylan, G., Bendinelli, O., & Parmeggiani, G. 1997, *Astrophys. J.*, 474, L19.

Dohm-Palmer, R. C., Helmi, A., Morrison, H., Mateo, M., Olszewski, E. W., Harding, P., Freeman, K. C., Norris, J., Shectman, S. A. 2001, *Astrophys. J.*, 555, 37.

Dubath, P., & Grillmair, C. J. 1997 *Astr. & Astrophys.*, 321, 379.

Dubinski, J., Mihos, J. C., & Hernquist, L. 1996, *Astrophys. J.*, 462, 576.

Durrell, P. R., Harris, W. E., & Pritchet, C. J. 1994, *Astr. J.*, 108, 2114.

Durrell, P. R., Harris, W. E., Geisler, D., & Pudritz, R. E. 1996, *Astr. J.*, 112, 972.

Durrell, P. R., Harris, W. E., & Pritchet, C. J. 2001, *Astr. J.*, 121, 2557.

Eggen, O. J., Lynden-Bell, D., & Sandage, A. R. 1962, *Astrophys. J.*, 136, 748 (ELS).

Elson, R. A. W., & Walterbos, R. A. M. 1988, *Astrophys. J.*, 333, 594.

Evans, N. W., & Wilkinson, M.I. 2000, *Mon. Not. R. Astr. Soc.*, 316, 929.

Fall, S. M. & Rees, M. J. 1985, *Astrophys. J.*, 298, 18.

Federici, L., Fusi Pecci, F., & Marano, B. 1990, *Astr. & Astrophys.*, 236, 99.

Federici, L., Bònoli, F., Ciotti, L., Fusi Pecci, F., Marano, B., Lipovetsky, V. A., Neizvestny, S. I., & Spassova, N. 1993, *Astr. & Astrophys.*, 274, 87.

Feltzing, S., & Gilmore, G. 2000, *Astr. & Astrophys.*, 355, 949.

Forbes, D. A., & Forte, J. C. 2001, *Mon. Not. R. Astr. Soc.*, 322, 257.

Forbes, D. A., Brodie, J. P., & Grillmair, C. J. 1997, *Astr. J.*, 113, 1652.

Forbes, D. A., Masters, K. L., Minniti, D., & Barmby, P. 2000, *Astr. & Astrophys.*, 358, 471.

Forbes, D. A., Brodie, J. P., & Larsen, S. S. 2001, *Astrophys. J.*, 556, L83.

Freedman, W. L., & Madore, B. F. 1990, *Astrophys. J.*, 365, 186.

Freeman, K. C. 1996, in *Formation of the Galactic Halo...Inside and Out*. ASP Conf. Ser. 92, eds. H. Morrison and A. Sarajedini, 3.

Frogel, J. A., Persson, S. E., & Cohen, J. G. 1980, *Astrophys. J.*, 240, 785.

Fusi Pecci, F., Cacciari, C., Federici, L., & Pasquali, A. 1993, in *The Globular Cluster-Galaxy Connection*, ASP Conf. Ser. 48, eds. G. H. Smith and J. P. Brodie, p. 410.

Genzel, R., & Townes, C. H. 1987, *Ann. Rev. Astr. & Astrophys.*, 25, 377.

Ghez, A. M., Klein, B. L., Morris, M., & Becklin, E. E. 1998, *Astrophys. J.*, 509, 678.

Gilmore, G. 1996, in *Formation of the Galactic Halo...Inside and Out*, ASP Conf. Ser. 92, eds. H. Morrison and A. Sarajedini, 161.

Gilmore, G., & Reid, N. 1983, *Mon. Not. R. Astr. Soc.*, 202, 1025.

Gilmore, G., King, I. R., & van der Kruit, P. C. 1989, *The Milky Way as a Galaxy* (California: University Science Books), Ch. 2.

Gilmore, G., Wyse, R. F. G., & Jones, J. B. 1995 *Astr. J.*, 109, 1095.

Grebel, E. K. 2001, Preprint: astro-ph\0107208.

Grebel, E. K., & Guhathakurta, P. 1999, *Astrophys. J.*, 511, L101.

Grebel, E. K., Kolatt, T. S., & Bradner, W. 1998, in *The Stellar Content of Local Group Galaxies*, IAUS 192, eds. P. Whitelock and R. Cannon, p. 30.

Grebel, E. K., Dolphin, A. E., & Guhathakurta, P. 2000, *Astronomische Gesellschaft Abstract Series*, 17, 61.

Harris, W. E. 1991, *Ann. Rev. Astr. & Astrophys.*, 29, 543.

Harris, W. E. 1996, *Astr. J.*, 112, 1487 (McMaster catalogue, revised June 1999) *http://physun.physics.mcmaster.ca/~harris/mwgc.dat.*

Harris, W. E. 1998, lecture notes from the *Saas-Fee Advanced Course* held in Les Diablerets.

Harris, W. E., & Canterna, R. 1979, *Astrophys. J.*, 231, L19.

Harris, W. E., & Pudritz, R. E. 1994, *Astrophys. J.*, 429, 177.

Harris, W. E., Bell, R. A. Vandenberg, D. A., Bolte, M., Stetson, P. B., Hesser, J. E., van den Bergh, S., Bond, H. E., Fahlman, G. G., & Richer, H. B. 1997, *Astr. J.*, 114, 1030.

Hayakawa, S., Matsumoto, T., Murakami, H., Uyama, K., Yamagami, T., Thomas, J. A. 1979, *Nature*, 279, 510.

Hearnshaw, J. B. 1986, *The Analysis of Starlight: One Hundred and Fifty Years of Astronomical Spectroscopy*, (Cambridge: Cambridge Univ. Press).

Heisler, J., Tremaine, S., & Bahcall, J. N. 1985, *Astrophys. J.*, 298, 8.

Helmi, A., & White, S. D. M. 2001, *Mon. Not. R. Astr. Soc.*, 323, 529.

Hernquist, L. 1990, *Astrophys. J.*, 356, 359.

Hiltner, W. A. 1960, *Astrophys. J.*, 131, 163.

Hoaglin, D. C., Mosteller, F. & Tukey, J. 2000, *Understanding Robust and Exploratory Data Analysis* (New York: Wiley & Sons).

Hodge, P. 1992, *The Andromeda Galaxy*, (Dordrecht: Kluwer), Ch. 7.

Hodge, P. W., & Kennicutt, R. C. 1982, *Astr. J.*, 87, 264.

Hodge, P., & Lee, M. G. 1998, *Astrophys. J.*, 329, 651.

Hodge, P. W., Dolphin, A. E., Smith, T. R., & Mateo, M. 1999, *Astrophys. J.*, 521, 577.

Hoessel, J. G., & Melnick, J. 1980, *Astr. & Astrophys.*, 84, 317.

Horne, K. 1986, *Publ. Astron. Soc. Pac.*, 98, 609.

Hubble, E. P. 1929, *Astrophys. J.*, 69, 103.

Hubble, E. 1932, *Astrophys. J.*, 76, 44.

Huchra, J., Stauffer, J., & Van Speybroeck, L. 1982, *Astrophys. J.*, 259, L57.

Huchra, J. P., Brodie, J. P., & Kent, S. M. 1991, *Astrophys. J.*, 370, 495.

Huchra, J. P., Brodie, J. P., Caldwell, N., Christian, C., & Schommer, R. 1996, *Astrophys. J. Supp.*, 102, 29.

Ibata, R. A. 1999, in *Galaxy Interactions at Low and High Redshift*, IAU Symp. 186, eds. J. E. Barnes and D. B. Sanders, p.39

Ibata, R. A., & Gilmore, G. 1995, *Mon. Not. R. Astr. Soc.*, 275, 605.

Ibata, R. A., Gilmore, G., & Irwin, M. J. 1994, *Nature*, 370, 194.

Ibata, R. A., Gilmore, G., & Irwin, M. J. 1995, *Mon. Not. R. Astr. Soc.*, 277, 781.

Ibata, R. A., Wyse, R. F. G., Gilmore, G., Irwin, M. J. & Suntzeff, N. B. 1997, *Astr. J.*, 113, 634.

Ibata, R., Irwin, M., Lewis, G. F., & Stolte, A. 2001, *Astrophys. J.*, 547, 133L.

Ibata, R., Irwin, M., Lewis, G., Ferguson, A., & Tanvir, N. 2001b, Preprint: astro-ph\0107090.

Iye, M., & Richter, O. G. 1985, *Astr. & Astrophys.*, 144, 471.

Johnston, K. V. 1998, *Astrophys. J.*, 495, 297.

Johnston, K. V., Spergel, D. N., Hernquist, L. 1995, *Astrophys. J.*, 451, 598.

Jones, B. J. T., & Wyse, R. F. G. 1983, *Astr. & Astrophys.*, 120, 165.

Josey, S. A., & Arimoto, N. 1992, *Astr. & Astrophys.*, 255, 105.

Kapteyn, J. C. 1909. *Astrophys. J.*, 29, 46.

Kapteyn, J. C., & van Rhijn, P. J. 1920, *Astrophys. J.*, 52, 23.

Kavelaars, J., & Hanes, D. A. 1997, *Mon. Not. R. Astr. Soc.*, 285, 31.

Kent, S. 1986, *Astr. J.*, 91, 1301.

Kent, S. 1989, *Astr. J.*, 97, 1614.

Kent, S. M., Huchra, J. P., & Stauffer, J. 1989, *Astr. J.*, 98, 2080.

Kissler-Patig, M., & Gebhardt, K. 1998, *Astr. J.*, 116, 2237.

Klypin, A. A., Kravtsov, A. V., Valenzuela, O., & Prada, F. 1999, *Astrophys. J.*, 522, 82.

Kormendy, J. 1988, *Astrophys. J.*, 325, 128.

Kormendy, J., & Bender, R. 1999, *Astrophys. J.*, 522, 772.

Kron, G. E., & Mayall, N. U. 1960, *Astr. J.*, 65, 581.

Laird, J. B., Rupen, M. P., Carney, B. W., & Latham, D. W. 1988, *Astr. J.*, 96, 1908.

Larsen, S. S., Brodie, J. P., Huchra, J. P., Forbes, D. A., & Grillmair, C. J. 2001, *Astr. J.*, 121, 2974.

Larson, R. B. 1976, *Mon. Not. R. Astr. Soc.*, 176, 31.

Lauer, T. R., Faber, S. M., Groth, E. J., Shaya, E. J., Campbell, B., Code, A., Currie, D. G., Baum, W. A., Ewald, S. P., Hester, J. J., Holtzman, J. A., Kristian, J., Light, R. M., Lynds, C. R., O'Neil, E. J. Jr., & Westphal, J. A. 1993, *Astr. J.*, 106, 1436.

Lawrie, D. G. 1983, *Astrophys. J.*, 273, 562.

Lee, M. G., Kim, S. C., Geisler, D., Seguel, J., Sarajedini, A., & Harris, W. E. 2001, in *Extragalactic Star Clusters*, IAU Symp. Ser. 207, eds. E. Grebel, D. Geisler and D. Minniti, in press.

Lewis, J. R. 1996, *WYFFOS Data Reduction Manual*, (Cambridge: Royal Greenwich Observatory).

Liu, W. M., & Chaboyer, B. 2000, *Astrophys. J.*, 544, 818.

Loinard, L., Dame, T. M., Heyer, M. H. Lequeux, J., & Thaddeus, P. 1999, *Astr. & Astrophys.*, 351, 1087.

Lynden-Bell, D., & Lynden-Bell, R. M. 1995, *Mon. Not. R. Astr. Soc.*, 275, 429.

Majewski, S. R. 1992, *Astrophys. J. Supp.*, 78, 87.

Majewski, S. R. 1994, *Astrophys. J.*, 431, L17.

Marsh, T. R. 1989, *Publ. Astron. Soc. Pac.*, 101, 1032.

Mateo, M. 1996, in *Formation of the Galactic Halo...Inside and Out*, ASP Conf. Ser. 92, eds. H. Morrison and A. Sarajedini, p. 434.

Mateo, M. 1998, *Ann. Rev. Astr. & Astrophys.*, 36, 435.

Mateo, M., Udalski, A., Szymanski, M., Kaluzny, J., Kubiak, M., & Krzeminski, W. 1995, *Astr. J.*, 109, 588.

Mathewson, D. S., Schwarz, M. P., & Murray, J. D. 1977, *Astrophys. J.*, 217, L5.

Mayall, N. U., & Eggen, O. J. 1953, *Publ. Astron. Soc. Pac.*, 65, 24.

McLaughlin, D. E., & Pudritz, R. E. 1996, *Astrophys. J.*, 457, 578.

Miller, B. W., Lotz, J. M., Ferguson, H. C., Stiavelli, M., & Whitmore, B. C. 1998, *Astrophys. J.*, 508, L133.

Minniti, D. 1995, *Astr. J.*, 109, 1663.

Minniti, D. 1996, *Astrophys. J.*, 459, 175.

Minniti, D., White, S. D. M., Olszewski, E. W., & Hill, J. M. 1992, *Astrophys. J.*, 393, 47.

Minniti, D., Olszewski, E. W., Liebert, J., White, S. D. M., Hill, J. M., & Irwin, M. J. 1995, *Mon. Not. R. Astr. Soc.*, 277, 1293.

Minniti, D., Meylan, G., & Kissler-Patig, M. 1996, *Astr. & Astrophys.*, 312, 49.

Miyamoto, M. & Nagai, R. 1975, *Publ. Astron. Soc. Japan*, 27, 533.

Mochejska, B. J., Kaluzny, J., Krockenberger, M., Sasselov, D. D., & Stanek, K. Z. 1998, *Acta Astr.*, 48, 455.

Moore, B., Ghigna, S., Governato, F., Lake, G., Quinn, T., Stadel, J., & Tozzi, P. 1999, *Astrophys. J.*, 524, 19.

Morrison, H. L. 1996, in *Formation of the Galactic Halo...Inside and Out*. ASP Conf. Ser. 92, eds. H. Morrison and A. Sarajedini, 453.

Nemec, J., & Nemec, A. F. L. 1991, in *The Formation and Evolution of Star Clusters*. ASP Conf. Ser. 13, ed. K. A. Janes, 512.

Oh, K. S., Lin, D. N. C., & Richer, H. B. 2000, *Astrophys. J.*, 531, 727.

Parmentier, G., Jehin, E., Magain, P., Noels, A., & Thoul, A. A. 2000, *Astr. & Astrophys.*, 363, 526.

Pascarelle, S. M., Windhorst, R. A., Keel, W. C., & Odewahn, S. C. 1996, *Nature*, 383, 45.

Peterson, R. 1989, in *Dynamics of Dense Stellar Systems*, ed. D. Merritt (Cambridge: Cambridge Univ. Press), 161.

Pilachowski, C. A. 1984, *Astrophys. J.*, 281, 614.

Pollacco, D., Bridges, T. J., Rees, P. C. T., Lewis, J. R., Boyle, B. J., Lewis, I., King, D. L., Telting, J., & Corradi, R. 2000, *AUTOFIB2/WYFFOS User Manual*.

Preston, G. W., Shectman, S. A., & Beers, T. C. 1991, *Astrophys. J.*, 375, 121.

Pritchet, C. J., & van den Bergh, S. 1988, *Astrophys. J.*, 331, 135.

Pritchet, C. J., & van den Bergh, S. 1994, *Astr. J.*, 107, 1730.

Prochaska, J. X., Naumov, S. O., Carney, B. W., McWilliam, A., & Wolfe, A. M. 2000, *Astr. J.*, 12, 2513.

Quinn, P. J., Hernquist, L., & Fullagar, D. P. 1993, *Astrophys. J.*, 403, 74.

Racine, R. 1991, *Astr. J.*, 101, 865.

Racine, R., & Harris, W. E., 1992, *Astr. J.*, 104, 1068.

Reed, L. G., Harris, G. L. H., & Harris, W. E. 1992, *Astr. J.*, 103, 824.

Reed, L. G., Harris, G. L. H., & Harris, W. E. 1994, *Astr. J.*, 107, 555.

Reid, I. N. 1997, *Astr. J.*, 114, 161.

Richer, H. B., Harris, W. E., Fahlman, G. G., Bell, R. A., Bond, H. E., Hesser, J. E., Holland, S., Pryor, C., Stetson, P. B., VandenBerg, D. A., & van den Bergh, S. 1996, *Astrophys. J.*, 463, 602.

Rood, R. & Iben, I. Jr., 1968, *Astrophys. J.*, 154, 215.

Rosenberg, A., Saviane, I., Piotto, G., & Aparicio, A. 1999, *Astr. J.*, 118, 2306.

Rubin, V. C. 1995, *Astrophys. J.*, 451, 419.

Rubin, V. C., & Ford, W. K. Jr. 1970, *Astrophys. J.*, 159, 379.

Rubin, V. C., & Ford, W. K. Jr. 1971, *Astrophys. J.*, 170, 25.

Rubin, V. C., Burstein, D., Ford, W. K. Jr., & Thonnard, N. 1985, *Astrophys. J.*, 289, 81.

Rutledge, G. A., Hesser, J. E., Stetson, P. B., Mateo, M. Simard, L., Bolte, M., Friel, E. D., & Chopin, Y. 1997, *Publ. Astron. Soc. Pac.*, 109, 883.

Rutledge, G. A., Hesser, J. E., & Stetson, P. B. 1997, *Publ. Astron. Soc. Pac.*, 109, 907.

Saito, Y., & Iye, M. 2000, *Astrophys. J.*, 535, L95.

Salaris, M., & Weiss, A. 1998, *Astr. & Astrophys.*, 335, 943.

Sarajedini, A., & King, C. R. 1989, *Astr. J.*, 98, 1624.

Sarajedini, A., Chaboyer, B., & Demarque, P. 1997, *Publ. Astron. Soc. Pac.*, 109, 1321.

Sargent, W., Kowal, S., Hartwick, F., & van den Bergh, S. 1977, *Astr. J.*, 82, 947.

Schweizer, F. 1987, in *Nearly Normal Galaxies*, ed. S. M. Faber (New York: Springer), 18.

Schweizer, F., & Seitzer, P. 1993, *Astrophys. J.*, 417, L29.

Searle, L., & Zinn, R. 1978, *Astrophys. J.*, 225, 357 (SZ).

Sellwood, J. A., Nelson, R. W., & Tremaine, S. 1998, *Astrophys. J.*, 506, 590.

Seyfert, C. K., & Nassau, J. J. 1945, *Astrophys. J.*, 102, 377.

Shapley, H. 1918, *Publ. Astron. Soc. Pac.*, 30, 42.

Shapley, H. 1921, *Bull. of the Nat. Res. Coun.*, 2, 171.

Sharov, A. S. 1988, *Sov. Astron. Lett.*, 14, 339.

Sharov, A. S., Lyutyi, V. M. 1983, *Astr. Ap. Supp.*, 90, 371.

Sharov, A. S., Lyutyi, V. M., & Esipov, V. F. 1983, *Sov. Astron. Lett.*, 9, 208.

Sharov, A. S., Lyutyi, V. M., & Esipov, V. F. 1984, *Sov. Astron. Lett.*, 10, 243.

Sharov, A. S., Lyutyi, V. M., & Esipov, V. F. 1987, *Sov. Astron. Lett.*, 13, 270.

Sharov, A. S., Lyutyi, V. M., & Esipov, V. F. 1995, *Astron. Lett.*, 21, 240.

Sharov, A. S., Lyutyi, V. M., & Esipov, V. F. 1996, *Astron. Lett.*, 22, 409.

Sitko, M. L. 1984, *Astrophys. J.*, 286, 209.

Sofue, Y., & Kato, T. 1981, *Publ. Astron. Soc. Japan*, 33, 449.

Sommer-Larsen, J., Beers, T. C., Flynn, C., Wilhelm, R. & Christensen, P. R. 1997, *Astrophys. J.*, 481, 775.

Spinrad, H. & Schweizer, F. 1972, *Astrophys. J.*, 171, 403.

Stetson, P. B., Bolte, M., Harris, W. E., Hesser, J. E., van den Bergh, S., Vanden-Berg, D. A., Bell, R. A., Johnson, J. A., Bond, H. E., Fullton, L. K., Fahlman, G. G., & Richer, H. B. 1999, *Astr. J.*, 117, 247.

Tonry, J., & Davis, M. 1979, *Astr. J.*, 84, 1511.

Toomre, A. 1977, in *The Evolution of Galaxies and Stellar Populations*, ed. B. M. Tinsley and R. B. Larson, 420.

Tremaine, S. 1995, *Astr. J.*, 110, 628.

Trimble, V. 1987, *Ann. Rev. Astr. & Astrophys.*, 25, 425.

Twarog, B., Anthony-Twarog, B. 1994, *Astr. J.*, 107, 1371.

Unavane, M., Wyse, R. F. G., & Gilmore, G. 1996 *Mon. Not. R. Astr. Soc.*, 278, 727.

van den Bergh, S. 1969, *Astrophys. J. Supp.*, 171, 145.

van den Bergh, S. 1991, *Publ. Astron. Soc. Pac.*, 103, 1053.

van den Bergh, S. 1994, *Astr. J.*, 108, 2145.

van den Bergh, S. 1996, *Publ. Astron. Soc. Pac.*, 108, 986.

van den Bergh, S. 1998, *Astrophys. J.*, 505, L127.

van den Bergh, S. 1999, *Astr. Astrophys. Rev.*, 9, 273.

van den Bergh, S., Morbey, C., & Pazder, J. 1991, *Astrophys. J.*, 375, 594.

Vanderriest, C. 1993, in *Fiber Optics in Astronomy*, ASP Conf. Ser. 37, ed. Peter M. Gray, 338.

Vanderriest, C. 1995, in *3D Optical Spectroscopic Methods in Astronomy*, ASP Conf. Ser. 71, eds. G. Comte and M. Marcelin, 209.

Vanderriest, C., & Bohlender, D. 1996, *Users' Manual for the CFHT Multi-Object Imaging Spectrograph (MOS) Version 3.20*, The Canada-France-Hawaii Telescope Corporation *www.cfht.hawaii.edu*.

Vetešnik, M. 1962, *Bull. Astron. Inst. Czechoslovakia*, 13, 180.

Walker, G. 1987, *Astronomical Observations. An Optical Perspective*, (Cambridge: Cambridge Univ. Press).

Walterbos, R. A. M., & Kennicutt, R. C. Jr. 1987, *Astr. Ap. Supp.*, 69, 311.

Walterbos, R. A. M., & Kennicutt, R. C. Jr. 1988, *Astr. & Astrophys.*, 198, 61.

Weiland, J. L., Arendt, R. G., Berriman, G. B., Dwek, E., Freudenreich, H. T., Hauser, M. G., Kelsall, T., Lisse, C. M., Mitra, M., Moseley, S. H., Odegard, N. P., Silverberg, R. F., Sodroski, T. J., Spiesman, W. J., & Stemwedel, S. W. 1994, *Astrophys. J.*, 425, 81.

Whitmore, B. C. 1980, *Astrophys. J.*, 242, 53.

Whitmore, B. C., & Schweizer, F. 1995, *Astr. J.*, 109, 960.

Worthey, G. 1994, *Astrophys. J. Supp.*, 95, 107.

Yoss, K. M., Neese, C. L., & Hartkopf, W. I. 1997, *Astr. J.*, 94, 1600.

Zinn, R. 1985, *Astrophys. J.*, 293, 424.

Zinn, R., & West, M. J. 1984, *Astrophys. J. Supp.*, 55, 45.

A. WYFFOS TARGET DATA AND RESULTS

Table A.1: Target data for the WYFFOS M31 GCS sample. Column 1 lists the target name(s), columns 2 and 3 list the sky coordinates, columns 4 and 5 list the X and Y positions in the galaxy frame, columns 6 and 7 list the apparent V magnitude and (B-V) colour (Barmby et al. 2000, and references therein), and column 8 lists the WYFFOS fibre(s) through which the target was observed.

Target	$\alpha_{(B1950)}$	$\delta_{(B1950)}$	X (′)	Y (′)	V	(B-V)	Fibre*
DAO1	00:32:36.85	39:52:40.6	-104.46	26.28	—	—	S2-117
DAO3	00:33:09.83	40:04:29.1	-91.22	28.31	—	—	S2-98
B294-S12	00:33:50.55	40:08:23.7	-83.42	24.44	—	—	S2-91
DAO5	00:33:53.24	40:11:45.2	-80.43	26.05	—	—	S2-108
B295-S14	00:34:04.29	40:03:12.6	-85.98	19.22	16.72	0.69	S2-95
DAO6	00:34:13.62	39:52:22.7	-93.55	11.26	—	—	S2-113
DAO8	00:34:19.30	39:31:36.6	-109.45	-2.13	—	—	S2-18
S18	00:34:35.90	40:04:50.3	-81.04	15.37	—	—	S2-104
DAO9	00:34:43.31	39:48:25.1	-93.27	4.33	—	—	S2-123
B419	00:34:44.85	39:26:39.7	-110.42	-9.05	18.40	—	S2-24
DAO11	00:34:46.70	39:40:32.3	-99.15	-0.95	19.70	—	S2-23
DAO12	00:34:57.00	39:30:01.8	-106.32	-8.88	—	—	S2-26
DAO13	00:35:03.45	39:48:43.3	-90.69	1.43	—	—	S2-111
DAO14	00:35:07.97	39:54:10.8	-85.82	4.04	—	—	S2-88
DAO16	(00:35:14.41)	(40:08:23.0)	-74.06	11.41	18.50	—	S2-87
B298-S21	00:35:17.40	40:27:26.8	-58.24	22.73	16.59	0.64	S1-77
B424	00:35:20.52	39:28:54.3	-104.48	-13.17	18.38	1.12	S2-31
B301-S22	00:35:38.86	39:47:08.4	-87.83	-4.94	17.12	1.01	S2-59
B427	00:35:39.98	39:41:41.9	-92.03	-8.41	18.18	1.18	S2-46
DAO20	00:35:42.42	39:24:22.6	-105.52	-19.28	18.70	—	S2-33
DAO21	00:35:45.50	39:27:37.5	-102.57	-17.78	—	—	S2-35
B303-S26	00:36:07.55	40:11:02.8	-65.50	5.19	18.22	0.24	S1-106
							S2-76
DAO22	00:36:10.99	39:35:02.3	-93.70	-17.20	—	—	S2-42

CONTINUED ON NEXT PAGE

Table A.1 (CONTINUED FROM PREVIOUS PAGE)

Target	$\alpha_{(B1950)}$	$\delta_{(B1950)}$	X (′)	Y (′)	V	(B-V)	Fibre
DAO23	00:36:11.34	40:10:18.4	-65.65	4.16	18.40	—	S1-107
							S2-78
B305	00:36:15.91	40:00:04.0	-73.25	-2.75	18.11	1.02	S1-95
							S2-46
B306-S29	00:36:25.62	40:17:52.5	-57.98	6.59	16.30	1.21	S1-100
DAO25	00:36:30.37	39:51:03.8	-78.71	-10.42	18.80	—	S2-62
DAO27	00:36:33.28	40:24:36.5	-51.75	9.53	18.00	—	S1-84
B435	00:36:35.20	40:31:57.4	-45.69	13.71	18.61	1.52	S1-71
B307-S30	00:36:35.34	40:16:29.9	-57.95	4.29	17.32	0.78	S1-105
B308	00:36:35.80	40:13:04.9	-60.60	2.14	—	—	S1-91
B309-S31	(00:36:40.42)	(39:58:12.5)	-72.01	-7.74	17.50	0.97	S1-98
							S2-67
B311-S33	00:36:50.55	40:14:46.7	-57.55	0.94	15.48	0.90	S1-92
B439	00:36:56.78	40:45:46.0	-32.24	18.86	—	—	S1-57
B312-S35	00:36:56.82	40:40:34.3	-36.36	15.69	15.58	0.87	S1-59
B314-S37	00:37:01.17	39:57:40.2	-69.88	-11.09	17.63	0.59	S2-64
B313-S36	00:37:01.29	40:36:26.9	-39.11	12.51	16.36	1.05	S1-61
B315-S38	00:37:05.29	40:15:02.5	-55.62	-1.13	16.32	0.35	S1-97
B1-S39	00:37:07.61	40:41:42.7	-34.21	14.76	17.06	1.27	S1-56
DAO30	00:37:07.65	40:01:47.4	-65.86	-9.56	18.40	—	S1-111
							S2-68
B316-S40	00:37:10.26	40:25:11.1	-47.00	4.29	16.82	0.84	S1-76
B319-S44	00:37:19.72	40:17:30.7	-51.99	-1.81	17.49	0.21	S1-112
B321-S46	00:37:32.05	40:11:18.6	-55.47	-7.46	17.78	0.23	S1-116
S47	00:37:32.09	40:23:32.0	-45.78	-0.01	17.30	—	S1-113
B4-S50	00:37:34.27	41:06:12.6	-11.72	25.70	16.95	0.92	C1-90
B5-S52	00:37:36.71	40:27:30.1	-42.10	1.72	15.71	0.97	S1-52
B443	00:37:37.38	40:16:54.8	-50.41	-4.85	18.43	0.97	S1-120
B327-S53	00:37:40.69	40:19:55.0	-47.65	-3.51	16.58	0.31	S1-121
B6-S58	00:37:42.76	41:10:59.1	-6.96	27.35	15.53	0.96	C1-87
B7	(00:37:43.03)	(41:12:37.6)	-5.63	28.31	—	—	C1-86
BoD195	00:37:45.92	40:19:47.4	-47.14	-4.38	15.19	—	S1-122
B8-S60	00:37:46.61	40:59:41.3	-15.46	19.88	16.52	1.03	C1-104
B10-S62	00:37:47.90	40:57:55.1	-16.72	18.61	16.66	0.84	C1-106
							C2-85
B12-S64	00:37:48.75	41:05:16.7	-10.79	22.98	15.13	0.73	C2-78
B245	00:37:52.46	40:51:06.0	-21.59	13.76	—	—	C1-93
							S1-49
B448	00:37:53.06	40:23:47.9	-43.13	-3.01	18.41	0.42	S1-22
DAO36	00:37:53.77	40:32:17.5	-36.33	2.07	17.80	—	S1-36

CONTINUED ON NEXT PAGE

Table A.1 (CONTINUED FROM PREVIOUS PAGE)

Target	$\alpha_{(B1950)}$	$\delta_{(B1950)}$	X (′)	Y (′)	V	(B-V)	Fibre
B13-S65	00:37:54.70	41:08:56.4	-7.21	24.32	17.19	0.87	C1-88
B14	00:37:54.93	40:56:18.4	-17.18	16.57	18.09	1.57	C2-86
B335	00:37:58.18	40:22:01.1	-43.95	-4.87	18.08	1.99	S1-17
B15	00:38:01.36	40:43:30.0	-26.57	7.78	17.79	1.41	C1-98
							S1-46
B16-S66	00:38:01.40	41:05:42.7	-8.99	21.35	17.58	1.00	C1-89
							C2-74
B451	00:38:02.83	40:35:13.5	-32.95	2.50	18.95	0.23	S1-39
B17-S70	00:38:05.00	40:55:39.8	-16.53	14.67	15.95	1.09	C1-91
B18-S71	00:38:05.85	40:25:05.1	-40.63	-4.15	17.51	0.74	S1-71
DAO39	00:38:08.62	40:42:14.4	-26.73	5.92	18.60	—	C2-105
							S1-44
B19-S72	00:38:08.75	41:02:26.2	-10.73	18.25	14.93	1.01	C1-100
							C2-77
B22-S74	00:38:15.24	41:08:15.0	-5.39	20.84	17.36	0.73	C2-81
B21-S75	00:38:15.30	40:49:12.3	-20.45	9.18	17.54	0.80	C1-96
							S1-45
B338-S76	00:38:15.44	40:19:22.3	-44.03	-9.09	14.26	0.84	S1-10
DAO41	00:38:18.97	40:50:09.1	-19.27	9.21	17.70	—	C2-100
B453	00:38:19.63	40:44:28.6	-23.69	5.64	17.30	0.87	C1-110
							S1-41
S83	(00:38:25.13)	(40:53:28.9)	-15.93	10.33	—	—	C2-89
B341-S81	00:38:25.62	40:19:26.3	-42.79	-10.58	16.38	—	S1-11
V31	00:38:28.45	40:49:02.1	-19.06	7.11	17.43	—	C1-97
							S1-42
B25-S84	00:38:28.81	40:44:01.3	-22.98	3.99	16.86	0.95	C1-111
							S1-40
B26-S86	00:38:30.63	41:08:13.2	-3.64	18.53	17.53	1.07	C2-80
B28-S88	00:38:32.72	40:42:36.5	-23.64	2.54	16.86	0.88	C1-112
B29-S90	00:38:34.06	40:43:56.3	-22.44	3.15	16.58	1.04	C2-107
B30-S91	00:38:34.98	40:40:48.9	-24.80	1.10	17.41	1.92	C1-113
B31-S92	00:38:37.15	40:42:37.4	-23.12	1.88	17.71	1.37	C2-108
B32-S93	00:38:37.64	41:01:03.4	-8.49	13.10	17.61	1.14	C2-82
B456	00:38:37.90	39:58:42.0	-57.75	-25.14	18.09	0.66	S1-123
B342-S94	00:38:40.46	40:20:20.1	-40.35	-12.27	18.35	0.06	S1-15
B33-S95	00:38:42.58	40:43:46.9	-21.57	1.78	17.86	0.99	S1-38
B34-S96	00:38:44.32	40:37:23.0	-26.43	-2.40	15.47	0.95	C2-95
							S1-33
DAO47	00:38:45.74	40:28:50.5	-33.01	-7.85	19.00	—	S1-27

CONTINUED ON NEXT PAGE

Table A.1 (CONTINUED FROM PREVIOUS PAGE)

Target	$\alpha_{(B1950)}$	$\delta_{(B1950)}$	X (′)	Y (′)	V	(B-V)	Fibre
B35	00:38:48.50	41:22:06.0	9.39	24.38	17.48	0.89	C1-75
B36	00:38:48.84	41:09:38.0	-0.42	16.69	17.32	0.94	C1-82
V216	00:38:50.52	40:44:23.2	-20.17	0.96	17.92	—	C2-91
							S1-37
B37	00:38:51.04	40:58:28.1	-8.99	9.52	16.82	2.05	C1-107
B38-S98	00:38:52.00	41:02:48.0	-5.45	12.03	16.49	0.91	C2-76
B39-S101	00:38:53.89	41:04:23.0	-3.99	12.72	15.98	1.31	C2-75
B40-S102	00:38:55.10	40:24:27.6	-35.38	-11.94	17.46	0.38	S1-21
DAO48	00:38:56.78	40:33:40.3	-27.91	-6.55	19.40	—	C1-117
B41-S103	00:38:56.85	40:58:18.8	-8.44	8.56	17.65	0.97	C2-87
B42-S104	00:38:57.76	40:50:59.6	-14.11	3.93	16.29	1.48	C2-104
B43-S106	00:38:58.56	40:26:13.4	-33.58	-11.38	16.96	0.26	S1-23
B45-S108	00:38:59.03	41:17:53.4	7.28	20.24	15.78	0.94	C1-73
B458	00:39:00.80	40:34:56.4	-26.44	-6.37	17.84	0.48	S1-32
B47-S111	00:39:01.41	41:25:37.2	13.66	24.63	17.51	0.72	C1-72
B48-S110	00:39:01.55	40:57:04.1	-8.88	7.09	16.64	1.16	C1-92
B49-S112	00:39:01.73	40:33:28.3	-27.49	-7.41	17.56	0.52	S1-30
							C2-97
B50-S113	00:39:02.19	41:15:51.7	6.04	18.52	16.84	0.92	C2-63
B51-S114	00:39:02.64	41:08:52.5	0.57	14.17	16.08	1.16	C1-79
B52	00:39:02.83	41:21:43.2	10.74	22.02	17.21	1.41	C1-80
B53	00:39:03.19	41:06:18.7	-1.39	12.52	17.82	0.91	C1-85
B54-S115	00:39:03.77	40:44:28.8	-18.56	-0.96	18.34	0.73	S1-35
B55-S116	00:39:06.42	40:55:45.8	-9.34	5.56	16.51	—	C2-90
B56-S117	00:39:07.27	40:41:13.9	-20.72	-3.48	17.30	1.06	C1-116
B57-S118	00:39:08.93	40:35:38.7	-24.94	-7.16	17.64	0.69	C1-119
B59-S120	00:39:10.06	40:54:34.7	-9.86	4.29	17.05	0.94	C2-103
B61-S122	00:39:15.96	41:13:09.2	5.49	14.82	16.61	1.12	C2-61
B62-S123	00:39:16.09	41:22:05.8	12.56	20.29	17.23	1.34	C1-71
							C2-58
B65-S126	00:39:18.06	40:23:46.7	-33.24	-15.81	16.93	0.86	S1-20
B66-S128	00:39:19.19	40:28:20.9	-29.50	-13.18	17.42	0.36	S1-25
B69-S132	00:39:21.40	41:09:42.8	3.40	11.90	18.16	0.43	C2-64
V246	00:39:22.49	41:01:40.3	-2.82	6.80	17.30	—	C2-73
V228	00:39:23.12	40:43:49.6	-16.83	-4.26	—	—	S1-34
B72	00:39:23.27	41:06:21.3	0.97	9.56	17.23	1.25	C1-77
B74-S135	00:39:23.80	41:26:55.4	17.26	22.11	16.66	0.75	C1-68
B75-S136	00:39:24.69	41:03:54.9	-0.79	7.85	17.33	0.92	C2-72
DAO52	00:39:24.88	40:34:26.5	-24.03	-10.29	18.42	0.14	C1-121
							S1-29

CONTINUED ON NEXT PAGE

Table A.1 (CONTINUED FROM PREVIOUS PAGE)

Target	$\alpha_{(B1950)}$	$\delta_{(B1950)}$	X (′)	Y (′)	V	(B-V)	Fibre
DAO53	00:39:26.04	40:21:37.9	-34.00	-18.33	18.80	—	S1-18
B76-S138	00:39:26.21	40:48:55.8	-12.44	-1.58	16.89	0.87	C2-96
B79	00:39:27.97	41:13:01.1	6.77	12.95	17.82	1.42	C2-59
B81-S142	00:39:29.65	40:32:13.5	-25.22	-12.36	16.80	0.54	C1-122
B82-S144	00:39:31.80	40:44:48.5	-15.04	-4.95	15.54	1.56	C1-120
B83-S146	00:39:32.14	41:28:54.4	19.78	22.10	17.09	0.76	C2-54
B346-S149	00:39:36.30	40:14:04.9	-38.75	-24.51	17.51	1.67	S1-12
B88-S150	00:39:36.82	41:15:48.2	9.99	13.35	15.42	1.12	C1-69
B90	00:39:37.04	40:46:31.7	-13.07	-4.68	18.80	—	C2-98
B91-S151	00:39:37.51	41:05:38.8	2.06	7.01	17.56	0.41	C1-76
B93-S155	00:39:38.94	41:05:17.3	1.94	6.57	16.87	0.97	C2-68
NB20	00:39:40.46	40:56:16.3	-4.99	0.80	18.01	—	C2-106
B94-S156	00:39:41.01	40:40:51.8	-17.08	-8.75	15.55	0.97	C2-111
NB33	00:39:41.89	41:02:39.5	0.21	4.52	18.31	—	C1-84
B97-S159	00:39:43.21	41:09:06.2	5.44	8.29	16.85	1.10	C1-70
B102	00:39:45.51	41:17:52.5	12.63	13.34	16.58	0.62	C2-53
V234	00:39:45.74	40:49:25.4	-9.78	-4.20	—	—	C2-110
B105-S166	00:39:46.46	41:14:01.8	9.71	10.83	17.19	0.89	C2-56
B109-S170	00:39:48.05	40:54:02.0	-5.88	-1.70	16.25	1.02	C1-118
B110-S172	00:39:48.99	40:47:02.4	-11.28	-6.15	15.20	0.88	C2-112
B112-S174	(00:39:49.26)	(40:59:24.4)	-1.49	1.41	16.26	1.07	C2-88
B113	00:39:49.33	41:05:12.9	3.09	4.99	—	—	C2-57
B116-S178	00:39:50.25	41:16:25.5	12.03	11.75	16.79	1.40	C1-64
B117-S176	00:39:50.31	40:40:43.6	-16.10	-10.23	16.34	0.65	C2-113
B119	00:39:51.89	41:01:09.8	0.19	2.11	17.27	—	C2-70
B122-S181	00:39:55.74	41:17:21.1	13.40	11.50	17.91	1.40	C2-52
B125-S183	00:39:58.10	40:49:05.4	-8.60	-6.24	16.53	0.77	C1-123
B127-S185	00:40:00.28	40:58:15.7	-1.12	-0.92	14.47	0.99	C2-115
B354-S186	00:40:03.08	41:44:00.0	35.24	26.83	17.81	0.70	N1-89
B129	00:40:04.01	41:08:41.3	7.53	4.94	17.40	2.16	C2-46
B130-S188	00:40:04.51	41:13:26.9	11.34	7.80	16.93	1.15	C1-63
B134-S190	00:40:07.41	40:57:37.9	-0.79	-2.37	16.57	0.91	C2-116
B135-S192	00:40:07.56	41:14:42.2	12.68	8.12	16.04	0.92	C2-47
B355-S193	00:40:08.33	41:41:34.1	33.93	24.56	17.76	0.66	N1-100
B137-S195	00:40:09.60	41:15:48.7	13.79	8.50	17.64	1.23	C1-62
B140	00:40:14.47	40:52:27.3	-4.04	-6.61	17.38	—	C2-118
B141-S197	00:40:14.88	41:16:21.9	14.83	8.06	16.90	1.00	C1-60
B144	00:40:15.55	40:59:40.1	1.76	-2.33	16.71	1.34	C1-27
							C2-21
DAO58	00:40:17.12	41:13:52.0	13.13	6.19	15.80	—	C2-45

CONTINUED ON NEXT PAGE

Table A.1 (CONTINUED FROM PREVIOUS PAGE)

Target	$\alpha_{(B1950)}$	$\delta_{(B1950)}$	X (′)	Y (′)	V	(B-V)	Fibre
B148-S200	00:40:19.51	41:01:39.1	3.78	-1.69	15.98	0.84	C2-26
B149-S201	00:40:21.03	41:18:01.7	16.86	8.18	17.04	0.89	C1-59
B467-S202	00:40:21.81	41:45:23.7	38.49	24.93	17.43	0.88	N1-88
B356-S206	00:40:25.80	41:34:05.8	30.06	17.38	17.34	0.78	N2-106
B156-S211	00:40:29.45	40:44:52.5	-8.27	-13.51	16.84	0.79	C2-122
B158-S213	00:40:30.05	40:50:55.1	-3.44	-9.88	14.70	0.86	C1-11
							C2-123
B159	00:40:30.20	41:08:48.1	10.66	1.13	17.20	0.88	C2-40
B160-S214	00:40:30.64	40:45:10.2	-7.89	-13.51	17.96	0.61	C1-10
B161-S215	00:40:31.06	40:54:59.6	-0.11	-7.51	16.33	0.81	C2-10
B164	00:40:33.77	40:56:03.9	1.05	-7.26	17.94	1.04	C2-11
B469-S220	00:40:34.64	41:53:52.1	46.64	28.28	17.58	0.53	N1-79
B166	00:40:36.09	40:56:08.2	1.37	-7.56	16.76	0.67	C1-22
B167	00:40:36.73	40:57:42.9	2.69	-6.68	17.41	1.02	C1-25
B168	00:40:37.87	41:27:39.6	26.39	11.63	17.63	1.60	C1-58
							N1-95
B170-S221	00:40:39.24	40:34:16.5	-15.46	-21.52	17.39	0.98	C2-119
DAO60	00:40:39.76	41:29:29.7	28.05	12.49	16.65	1.33	N1-92
B272-V294	00:40:40.94	41:20:46.4	21.32	6.93	18.20	1.32	C2-44
							N1-100
B171-S222	00:40:41.17	40:59:11.8	4.37	-6.42	15.24	0.98	C2-17
B174-S226	(00:40:46.13)	(41:22:02.4)	22.92	6.92	15.47	1.00	C1-56
B176-S227	00:40:46.17	40:32:45.6	-15.84	-23.49	16.52	0.73	C2-120
B179-S230	00:40:46.67	41:01:49.5	7.08	-5.62	15.38	0.83	C1-33
							C2-24
B180-S231	00:40:47.36	40:51:21.8	-1.07	-12.18	16.02	0.88	C1-16
B182-S233	00:40:52.24	40:51:47.1	-0.17	-12.64	15.43	0.93	C1-18
B470	00:40:52.74	41:53:22.0	48.32	25.32	17.89	0.99	N1-76
B185-S235	00:40:52.82	40:58:17.3	5.02	-8.71	15.54	0.94	C2-16
B184-S236	00:40:52.91	41:20:09.6	22.23	4.78	17.24	1.15	C2-42
B471-S238	00:40:56.86	41:51:31.7	47.35	23.58	17.12	1.22	N1-77
B188-S239	00:40:56.99	41:08:00.6	13.15	-3.33	17.04	0.71	C1-45
B190-S241	00:40:58.79	41:17:40.5	20.95	2.38	16.82	0.88	C1-53
							N1-111
B193-S244	00:41:00.91	41:20:32.4	23.45	3.84	15.33	0.97	C1-54
							C2-41
S245	00:41:02.94	41:10:42.7	15.96	-2.54	17.80	—	C2-34
B472	00:41:03.85	41:10:27.8	15.87	-2.83	15.19	0.78	C1-46
B197-S247	00:41:05.13	41:13:45.2	18.61	-0.98	17.63	1.08	C1-49

CONTINUED ON NEXT PAGE

Table A.1 (CONTINUED FROM PREVIOUS PAGE)

Target	$\alpha_{(B1950)}$	$\delta_{(B1950)}$	X (′)	Y (′)	V	(B-V)	Fibre
B199-S248	00:41:05.43	40:41:49.7	-6.45	-20.76	17.60	0.77	C1-12
B198-S249	00:41:05.45	41:15:27.3	19.98	0.02	17.55	0.60	N1-113
B200	00:41:05.82	41:12:57.7	18.07	-1.57	18.55	—	C2-36
							N1-114
B201-S250	(00:41:08.54)	(40:53:43.6)	3.25	-13.89	16.20	0.85	C1-23
B203-S252	00:41:11.05	41:16:10.0	21.19	-0.36	16.68	0.93	C2-37
B204-S254	00:41:11.84	41:05:37.8	13.00	-7.00	15.75	0.92	C1-39
B207-S258	00:41:14.96	40:49:45.7	0.90	-17.27	17.33	0.74	C1-20
B208-S259	00:41:15.48	41:06:46.5	14.33	-6.83	17.81	0.92	C1-40
B209-S261	00:41:18.01	41:09:01.5	16.39	-5.81	16.64	0.77	C2-29
B210	00:41:18.22	40:57:59.4	7.74	-12.67	17.57	0.52	C1-28
B213-S264	00:41:18.85	41:14:13.8	20.58	-2.71	16.78	1.05	N1-115
B214-S265	00:41:19.32	41:09:53.5	17.22	-5.47	17.65	0.61	N1-117
DAO65	00:41:20.19	41:22:40.7	27.37	2.32	16.90	—	C2-39
							N1-110
DAO66	00:41:22.14	41:24:03.4	28.68	2.88	17.20	—	C1-52
B216-S267	00:41:24.07	41:21:30.2	26.90	1.02	17.25	0.20	N1-112
DAO67	00:41:25.41	41:42:25.6	43.49	13.77	—	—	N1-86
B217-S269	00:41:25.96	41:07:26.2	16.07	-7.97	16.51	0.92	C2-27
B218-S272	00:41:29.69	41:02:54.7	12.95	-11.32	14.79	0.87	C2-23
B219-S271	00:41:30.54	40:40:22.5	-4.65	-25.40	16.39	0.94	C1-15
B220-S275	00:41:34.73	41:14:10.2	22.38	-5.10	16.55	0.79	N1-118
							C2-33
B221-S276	00:41:38.30	41:16:41.7	24.78	-4.06	16.86	0.90	C1-47
B222-S277	00:41:40.72	40:57:47.7	10.22	-16.12	17.43	0.68	C1-29
B223-S278	00:41:42.27	41:18:14.7	26.45	-3.68	17.81	0.38	C2-35
B224-S279	00:41:42.34	41:12:25.0	21.89	-7.30	15.45	0.74	C1-44
							C2-31
							N1-119
B225-S280	00:41:44.85	41:05:11.1	16.50	-12.16	14.15	0.95	C1-38
							C2-25
B226	00:41:45.86	40:54:34.8	8.30	-18.88	17.65	1.05	C1-26
DAO69	00:41:49.85	41:37:02.9	42.09	6.85	16.60	—	N1-105
B230-S283	00:41:50.60	40:40:48.0	-1.96	-28.12	16.05	0.72	C1-17
B365-S284	00:41:51.34	42:00:56.3	61.01	21.44	16.73	0.79	N1-70
B231-S285	00:41:53.81	41:11:22.3	22.40	-9.65	17.30	0.69	C2-28
							N1-120
B232-S286	00:41:55.52	40:58:36.1	12.58	-17.82	15.70	0.68	C1-31
DAO70	00:41:55.70	41:24:19.0	32.78	-1.90	18.60	—	N1-116
B281-S288	00:41:58.08	41:03:44.2	16.91	-15.01	17.67	0.84	C1-35

CONTINUED ON NEXT PAGE

Table A.1 (CONTINUED FROM PREVIOUS PAGE)

Target	$\alpha_{(B1950)}$	$\delta_{(B1950)}$	X (′)	Y (′)	V	(B-V)	Fibre
B234-S290	00:42:01.58	41:12:53.7	24.51	-9.85	16.82	0.92	C1-42
							N1-121
B366-S291	00:42:01.61	41:47:26.1	51.60	11.57	16.23	0.78	N1-81
B367-S292	00:42:02.08	41:49:07.7	52.98	12.55	18.45	0.32	N1-80
B368-S293	00:42:02.77	41:34:45.0	41.79	3.53	18.04	0.23	N1-96
B283-S296	00:42:10.56	41:00:36.3	15.92	-18.80	17.64	1.06	C2-20
B475	00:42:11.00	41:37:36.3	44.98	4.10	17.67	0.49	N1-103
B235-S297	00:42:13.09	41:13:00.0	25.93	-11.48	16.27	0.85	C1-41
							N1-123
DAO73	00:42:14.40	41:38:22.9	45.98	4.08	17.50	—	N1-84
B477	00:42:23.35	41:23:13.9	35.15	-6.64	18.46	—	N1-122
B237-S299	00:42:24.34	41:06:10.4	21.89	-17.38	17.10	0.77	C1-37
B478	00:42:27.44	42:07:44.1	70.49	20.41	17.50	1.09	N2-47
B370-S300	00:42:29.27	41:41:16.9	49.98	3.71	16.24	0.92	N1-69
B238-S301	00:42:29.81	41:03:13.0	20.22	-20.02	16.42	0.97	C1-34
							C2-22
DAO78	00:42:36.87	42:04:33.0	69.09	17.06	—	—	N1-63
							N2-50
B479	00:42:42.67	41:50:39.4	58.88	7.58	17.35	2.19	N1-60
DAO81	00:42:44.89	41:57:56.3	64.83	11.78	—	—	N1-62
							N2-55
B372-S304	00:42:48.14	41:44:00.7	54.31	2.64	16.60	0.84	N1-59
V129	00:42:58.98	41:35:43.9	49.09	-4.09	—	—	N1-37
B374-S306	00:42:59.36	41:25:31.5	41.14	-10.50	18.31	0.44	N1-11
B480	00:43:00.36	41:29:29.2	44.36	-8.18	17.91	0.28	N1-18
B375-S307	00:43:00.42	41:23:18.8	39.53	-12.03	17.61	0.90	N1-10
DAO84	00:43:07.14	41:26:25.6	42.76	-11.08	18.70	—	N1-15
B483	00:43:08.60	41:45:54.6	58.17	0.84	18.71	0.29	N1-50
B484-S310	00:43:08.66	41:31:13.8	46.69	-8.31	18.10	0.52	N1-24
B378-S311	00:43:11.94	41:37:07.4	51.68	-5.12	17.65	0.58	N1-38
DAO86	00:43:20.02	42:13:15.6	80.88	16.22	—	—	N2-44
B380-S313	00:43:20.76	41:44:29.3	58.47	-1.82	16.95	0.47	N1-49
B382-S317	00:43:25.09	41:21:17.3	40.83	-16.92	17.36	0.79	N1-12
DAO87	00:43:36.01	42:17:56.7	86.38	16.83	—	—	N2-38
B385-S321	00:43:39.62	41:18:46.3	40.57	-20.62	17.67	1.25	N1-14
B386-S322	00:43:41.55	41:45:29.0	61.66	-4.23	15.64	0.75	N1-46
BoD289	00:43:53.07	42:00:02.1	74.37	3.18	16.09	0.67	N1-53
							N2-61
DAO88	00:43:56.26	41:59:16.8	74.15	2.24	—	—	N1-52
							N2-63

CONTINUED ON NEXT PAGE

Table A.1 (CONTINUED FROM PREVIOUS PAGE)

Target	$\alpha_{(B1950)}$	$\delta_{(B1950)}$	X (′)	Y (′)	V	(B-V)	Fibre
B389-S326	00:43:58.33	41:32:47.4	53.71	-14.60	17.38	1.40	N1-29
BoD292	00:43:59.97	42:04:53.1	78.96	5.21	17.97	—	N2-58
DAO89	00:44:00.44	42:32:08.2	100.28	22.16	—	—	N2-24
S327	00:44:03.60	42:28:24.3	97.73	19.38	15.94	0.73	N2-25
B391-S328	00:44:12.68	41:17:34.4	43.51	-26.21	17.28	0.86	N1-17
B392-S329	00:44:15.32	41:38:22.0	60.04	-13.60	16.81	—	N1-36
B493	00:44:28.69	42:00:43.3	79.04	-1.56	18.11	1.49	N2-68
DAO91	00:44:38.86	42:23:22.2	97.87	11.15	—	—	N2-22
S337	00:44:44.04	41:26:59.1	54.53	-24.91	—	—	N1-25
DAO92	00:44:51.51	42:31:32.5	105.70	14.45	—	—	N2-15
DAO93	00:45:00.04	42:28:34.1	104.37	11.36	—	—	N2-14
DAO94	00:45:08.19	42:27:39.7	104.61	9.62	18.58	0.70	N2-12
DAO95	00:45:11.35	41:50:35.7	76.12	-14.09	—	—	N2-76
B400-S343	00:45:15.36	42:09:11.1	91.06	-3.00	16.46	0.81	N2-95
DAO97	00:45:22.74	42:38:57.8	115.08	14.63	—	—	N2-11
DAO98	00:45:43.02	42:02:20.4	88.96	-11.29	—	—	N2-100
B402-S346	00:45:50.00	41:45:13.5	76.47	-23.07	17.27	0.88	N2-82
BA11	00:45:59.35	42:07:16.9	94.70	-10.54	17.66	0.59	N2-92
DAO99	00:46:02.00	42:16:24.1	102.09	-5.18	19.03	—	N2-117
DAO100	00:46:14.98	41:59:18.6	90.33	-17.81	—	—	N2-103
DAO101	00:46:20.09	42:14:12.4	102.50	-9.17	—	—	N2-112
B505	00:46:28.99	42:02:43.5	94.62	-17.68	—	—	N2-107
DAO104	00:46:34.96	41:59:56.0	93.16	-20.30	18.79	0.87	N2-105
DAO106	00:46:49.57	41:59:59.2	94.91	-22.38	—	—	N2-106
DAO107	00:46:54.67	42:29:11.2	118.14	-4.68	—	—	N2-122
B406	00:47:12.80	41:59:36.0	97.33	-25.97	—	—	N2-108
S353	00:47:31.42	42:19:24.6	114.86	-16.11	17.15	0.65	N2-113

* The field name and fibre number are provided (e.g. "C1-10" designates Central Field 1, fibre number 10, "N2-123" refers to Northeast Field 2, fibre number 123 etc.) for cross-reference with Table 3.2.

Table A.2: WYFFOS Line Indices: H2400B grating

GC	H&K	CNR	CaI	CHG	Δ
B1	0.051	0.328	-0.119	0.200	1.213
B4	—	0.022	0.085	0.349	—
B5	0.380	0.105	0.013	0.155	1.176
B6	0.449	0.129	0.032	0.206	1.251
B8	0.476	-0.004	0.048	0.255	1.056
B10	0.468	0.0005	-0.006	0.087	1.016
B12	0.125	-0.007	-0.031	0.102	0.889
B13	0.347	-0.020	0.125	0.137	1.208
B15	—	—	—	—	—
B16	—	—	—	—	—
B17	0.199	-0.161	-0.153	0.290	1.065
B18	0.314	-0.219	0.050	-0.019	1.152
B19	0.329	0.069	0.018	0.155	1.018
B21	-0.076	0.0004	-0.043	0.167	1.473
B25	0.129	0.025	-0.007	0.146	0.733
B26	—	—	—	—	—
B28	0.373	-0.020	-0.028	0.109	1.067
B29	—	—	—	—	—
B30	—	—	—	—	—
B31	—	—	—	—	—
B33	0.273	0.197	0.027	0.118	0.841
B34	0.257	0.162	0.036	0.131	0.962
B35	0.771	-0.082	0.154	0.275	1.747
B37	—	—	—	—	—
B38	0.238	0.072	0.041	0.180	1.033
B39	0.150	—	-0.020	0.245	0.931
B40	0.316	-0.186	—	0.231	0.662
B41	-0.066	0.016	-0.002	0.144	0.396
B42	—	0.003	-0.154	0.229	—
B43	0.172	-0.130	-0.034	-0.048	0.672
B45	0.435	0.003	0.030	0.189	1.064
B47	—	-0.183	-0.118	0.075	—
B48	0.205	0.083	0.113	0.275	1.049
B49	—	—	—	—	—
B50	—	0.105	0.006	0.063	—
B51	0.413	0.025	-0.015	0.185	1.103
B53	0.457	-0.143	0.091	0.205	1.163

CONTINUED ON NEXT PAGE

Table A.2 (CONTINUED FROM PREVIOUS PAGE)

GC	H&K	CNR	CaI	CHG	Δ
B54	0.463	0.342	-0.087	0.182	1.048
B55	0.222	0.137	-0.023	0.242	0.757
B56	0.766	0.085	-0.016	0.262	1.785
B57	0.555	-0.0006	-0.015	0.067	0.893
B59	0.886	0.240	-0.002	0.084	0.832
B61	0.160	0.131	-0.063	0.229	1.029
B65	0.427	-0.030	-0.056	0.109	0.842
B66	0.143	-0.032	0.005	—	0.547
B69	0.188	-0.039	-0.053	0.077	0.966
B72	0.896	0.029	0.136	0.258	1.775
B74	0.271	-0.057	0.012	0.096	0.979
B75	0.259	0.028	-0.005	0.130	0.727
B76	—	—	—	—	—
B81	0.191	-0.034	-0.106	0.047	0.988
B82	0.645	0.053	-0.022	0.204	1.375
B83	0.498	-0.115	-0.084	0.071	0.526
B88	0.238	-0.041	0.002	0.085	0.807
B90	—	—	-0.212	-0.012	—
B91	0.359	-0.110	0.006	-0.015	0.862
B93	0.181	-0.0007	-0.0005	0.156	1.001
B94	—	0.318	-0.164	0.314	1.296
B97	0.371	0.033	0.025	0.166	1.251
B102	0.226	0.065	-0.027	0.096	0.794
B105	—	—	—	—	—
B109	0.515	-0.143	-0.007	0.307	1.369
B110	—	0.076	0.057	0.143	1.226
B116	0.481	0.047	0.044	0.161	1.257
B117	0.289	0.002	0.159	0.207	0.858
B119	0.369	0.107	0.024	0.214	1.225
B122	—	—	—	—	—
B125	0.363	-0.035	-0.023	0.129	1.120
B127	0.406	0.100	0.007	0.192	1.195
B129	—	0.078	0.278	0.173	—
B130	0.114	0.004	0.073	0.124	1.069
B134	0.381	0.111	0.025	0.206	1.237
B135	0.226	-0.004	—	0.116	0.876
B137	0.280	-0.049	0.016	0.166	1.024
B140	—	—	—	—	—

CONTINUED ON NEXT PAGE

Table A.2 (CONTINUED FROM PREVIOUS PAGE)

GC	H&K	CNR	CaI	CHG	Δ
B141	0.299	-0.043	-0.011	0.104	0.975
B144	0.424	0.082	-0.020	0.159	1.003
B148	0.272	0.027	-0.060	0.093	1.099
B149	0.472	0.021	-0.025	0.107	1.165
B156	—	0.266	-0.023	0.053	—
B158	0.378	0.081	-0.017	0.158	0.987
B159	0.161	0.131	0.065	0.041	0.942
B160	—	0.073	0.142	0.332	—
B161	0.151	-0.030	0.144	0.026	1.264
B164	0.293	0.009	-0.078	0.312	1.301
B166	0.282	-0.049	0.062	0.189	0.946
B167	0.338	0.144	0.049	0.253	1.329
B170	—	—	—	—	—
B171	0.422	0.120	-0.016	0.215	1.169
B176	—	0.002	-0.042	0.094	—
B179	0.330	0.041	0.021	0.153	0.942
B180	0.347	0.025	0.070	0.158	1.022
B182	0.323	0.008	0.0007	0.131	0.905
B184	0.591	0.208	0.084	0.159	1.095
B185	0.382	0.073	0.005	0.179	1.104
B188	0.268	-0.023	0.032	0.089	0.897
B190	0.361	0.020	0.077	0.169	1.028
B193	0.396	0.135	-0.006	0.183	1.268
B197	—	-0.059	-0.082	0.152	—
B198	0.598	0.050	-0.029	0.102	0.914
B199	0.472	-0.098	0.043	0.119	1.075
B200	0.254	0.126	-0.003	0.072	1.252
B203	0.230	0.070	-0.022	0.210	1.024
B204	0.387	0.077	0.002	0.178	1.185
B207	0.475	-0.061	0.059	0.282	1.023
B208	0.453	0.215	0.220	—	0.906
B209	0.263	-0.030	0.011	0.113	0.937
B210	0.206	-0.154	-0.027	0.034	0.700
B213	0.525	0.054	0.004	0.172	1.332
B214	—	0.221	0.453	—	—
B216	0.251	-0.077	-0.028	0.019	0.723
B217	0.300	-0.005	0.051	0.194	1.109
B218	0.357	0.051	0.005	0.135	1.029

CONTINUED ON NEXT PAGE

Table A.2 (CONTINUED FROM PREVIOUS PAGE)

GC	H&K	CNR	CaI	CHG	Δ
B219	0.321	0.014	0.010	0.349	1.207
B220	0.213	0.052	0.021	0.160	0.891
B221	0.316	-0.055	0.035	0.138	1.083
B222	—	0.223	-0.213	0.253	0.984
B223	-0.018	-0.115	0.018	0.071	0.905
B224	0.260	0.004	0.008	0.087	0.998
B225	0.401	0.129	0.006	0.171	1.164
B230	0.133	-0.091	0.048	0.034	0.931
B231	0.449	0.012	-0.045	0.048	0.824
B232	0.237	-0.033	0.042	0.109	0.821
B234	0.439	0.013	0.060	0.146	1.159
B235	0.179	0.052	0.036	0.176	1.018
B237	0.188	0.351	0.238	0.054	0.708
B238	0.442	0.080	0.043	0.317	0.931
B281	0.479	0.082	0.059	0.264	1.006
B283	—	—	—	—	—
B295	—	—	—	—	—
B298	0.225	-0.059	0.011	0.055	0.668
B301	0.221	0.116	0.019	0.195	0.879
B303	0.605	-0.295	0.076	0.013	0.837
B305	0.454	-0.085	0.065	0.093	1.060
B306	0.077	-0.116	0.055	0.300	1.080
B307	—	-0.021	-0.004	—	—
B311	0.189	-0.011	0.043	0.088	0.637
B312	0.275	0.068	0.008	0.114	0.954
B313	0.299	0.059	0.030	0.174	1.064
B314	0.452	-0.094	0.064	0.055	0.925
B315	0.063	-0.080	-0.074	-0.055	0.630
B316	0.335	0.190	0.003	0.092	1.096
B319	0.139	0.068	-0.051	-0.025	0.626
B321	0.200	-0.145	0.026	-0.034	0.802
B327	0.102	-0.083	-0.006	-0.038	0.697
B335	—	—	—	—	—
B338	0.271	0.065	0.004	0.143	1.267
B341	0.350	0.033	0.031	0.139	1.008
B342	0.176	—	-0.020	—	0.459
B355	0.505	-0.024	-0.121	0.164	0.818
B356	-0.068	0.042	-0.143	0.170	1.180

CONTINUED ON NEXT PAGE

Table A.2 (CONTINUED FROM PREVIOUS PAGE)

GC	H&K	CNR	CaI	CHG	Δ
B365	0.202	0.117	0.020	0.065	0.894
B366	0.140	-0.028	—	0.094	0.655
B367	0.326	-0.106	-0.007	-0.039	0.601
B370	0.240	-0.031	-0.014	0.096	0.852
B372	0.273	0.086	0.034	0.099	0.933
B374	0.208	-0.061	-0.028	-0.032	0.881
B378	0.144	0.044	0.031	0.074	0.905
B380	0.212	-0.229	-0.097	-0.032	0.738
B382	0.400	-0.034	0.087	0.074	0.811
B386	0.304	0.014	0.011	0.113	0.999
B391	0.267	-0.107	0.033	0.217	0.848
B400	—	—	—	0.072	—
B443	0.213	-0.050	-0.119	-0.011	1.124
B448	0.112	0.052	-0.072	0.053	0.844
B451	—	0.033	-0.080	-0.008	0.514
B453	0.160	-0.063	0.047	-0.024	0.809
B458	0.062	0.242	-0.051	—	0.326
B467	0.318	-0.071	-0.031	-0.051	0.716
B472	0.302	0.007	0.011	0.127	0.932
B475	—	-0.211	-0.113	—	—
B480	0.245	-0.135	-0.054	-0.015	0.740
B483	0.208	-0.179	0.115	-0.048	0.727
B484	0.156	-0.140	-0.075	-0.023	0.621
S47	0.187	-0.042	-0.037	0.134	0.358
S245	0.365	0.195	0.071	0.250	0.935
S327	0.201	-0.009	0.016	0.087	0.852
BoD195	0.132	-0.066	-0.025	—	0.706
BoD289	0.262	-0.019	0.013	0.127	0.908
BoD292	—	0.045	0.151	0.260	—
DAO23	0.249	-0.220	—	0.202	1.351
DAO25	—	—	—	—	—
DAO30	—	-0.029	-0.137	0.165	—
DAO36	0.147	0.160	0.038	—	0.415
DAO39	0.486	-0.230	0.011	—	0.730
DAO41	—	—	—	—	—
DAO47	0.466	-0.005	0.061	0.097	0.801
DAO48	—	—	—	—	—
DAO58	0.370	0.093	-0.011	0.165	1.098

CONTINUED ON NEXT PAGE

Table A.2 (CONTINUED FROM PREVIOUS PAGE)

GC	H&K	CNR	CaI	CHG	Δ
DAO65	0.177	-0.075	-0.015	0.030	0.579
DAO66	—	0.083	0.017	0.051	—
DAO70	—	0.074	0.123	0.268	—
DAO73	0.107	-0.086	0.077	—	1.214
DAO84	0.259	0.019	0.034	-0.034	0.759
BA11	—	—	—	—	—
NB20	0.204	0.093	0.029	0.145	1.150
NB33	—	0.398	0.049	0.315	—
V31	0.475	—	-0.220	—	1.207
V216	—	—	—	—	—
V246	-0.045	0.160	-0.190	0.178	0.767
V294	—	—	—	—	—

Table A.3: WYFFOS Line Indices: R1200R grating

GC	$H\beta$	MgH	Mg2	Mgb	MgG	Fe52	Fe53
B1	0.082	0.140	0.132	0.121	0.086	0.079	0.080
B4	0.125	0.064	0.024	0.099	0.058	0.032	0.053
B5	0.077	0.114	0.123	0.115	0.068	0.069	0.029
B6	0.067	0.070	0.098	0.160	0.088	0.059	0.059
B8	0.148	0.072	0.110	0.094	0.080	0.095	0.087
B10	0.118	0.068	0.012	0.020	0.003	0.055	0.029
B12	0.102	0.014	-0.064	0.019	0.009	-0.002	0.037
B13	0.113	0.148	0.167	0.044	0.014	0.141	0.089
B15	-0.021	0.165	0.266	0.080	0.096	0.156	0.117
B16	0.063	0.075	0.091	0.148	0.051	0.065	0.051
B17	0.057	0.084	0.102	0.106	0.083	0.055	0.063
B18	0.092	0.055	0.036	0.079	0.041	0.068	0.071
B19	0.086	0.090	0.101	0.105	0.061	0.075	0.045
B21	0.071	0.060	0.062	0.131	0.079	0.046	0.051
B25	0.113	0.083	0.015	0.060	0.041	0.043	0.024
B26	0.053	0.157	0.205	0.240	0.121	0.063	0.076
B28	0.162	0.081	0.039	0.058	0.032	0.061	-0.011
B29	0.013	0.110	0.147	0.187	0.148	0.129	0.072
B30	0.066	0.119	0.226	0.133	0.084	0.123	0.090
B31	0.025	0.081	0.065	0.126	0.069	0.0002	0.024
B33	0.131	0.067	0.021	0.051	0.014	0.062	0.056
B34	0.069	0.077	0.069	0.106	0.058	0.057	0.066
B35	0.094	0.036	0.022	0.084	0.049	0.046	0.108
B37	-0.010	0.123	0.050	0.084	0.040	0.113	0.055
B38	0.113	0.071	0.036	0.028	0.036	0.047	-0.004
B39	0.103	0.085	0.046	0.111	0.075	0.052	0.048
B40	0.341	0.025	-0.062	0.026	-0.0007	0.0009	0.057
B41	0.106	0.040	-0.023	0.051	0.042	0.056	0.057
B42	0.105	0.089	0.074	0.080	0.056	0.057	0.059
B43	0.244	0.009	-0.033	0.014	0.006	0.033	0.016
B45	0.093	0.101	0.098	0.059	-0.002	0.068	0.054
B47	0.149	—	—	0.011	0.018	0.031	0.058
B48	0.118	0.088	0.104	0.111	0.058	0.072	0.071
B49	0.449	0.053	-0.017	0.054	0.024	0.057	-0.022
B50	0.069	0.074	0.034	0.091	0.062	0.014	0.053
B51	0.061	0.117	0.122	0.105	0.062	0.078	0.041
B53	0.086	0.116	0.221	0.221	0.122	0.101	0.064

CONTINUED ON NEXT PAGE

Table A.3 (CONTINUED FROM PREVIOUS PAGE)

GC	$H\beta$	MgH	Mg2	Mgb	MgG	Fe52	Fe53
B54	0.065	0.137	0.196	0.174	0.123	0.099	0.081
B55	0.109	0.101	0.133	0.175	0.106	0.055	0.079
B56	0.065	0.162	0.227	0.196	0.114	0.124	0.082
B57	0.245	0.147	0.016	0.055	0.020	0.092	-0.015
B59	0.042	0.088	0.110	0.174	0.057	0.064	0.014
B61	0.123	0.178	0.169	0.135	0.095	0.086	0.041
B65	0.084	0.032	0.022	0.061	0.049	0.058	0.027
B66	0.202	0.004	-0.012	0.039	0.027	0.019	-0.013
B69	0.328	0.146	0.097	0.060	0.009	0.060	0.069
B72	0.081	0.131	0.137	0.130	0.087	0.107	0.073
B74	0.167	0.091	0.019	0.019	0.017	0.043	0.012
B75	0.082	-0.001	-0.022	0.077	0.054	-0.012	0.076
B76	0.127	0.135	0.095	0.130	0.103	0.017	0.064
B81	0.372	0.057	-0.038	0.021	-0.010	0.037	0.051
B82	0.103	0.105	0.048	0.096	0.060	0.041	0.061
B83	0.159	0.006	0.035	0.142	0.079	-0.002	0.057
B88	0.108	0.051	-0.029	0.030	0.010	0.013	0.021
B90	0.138	0.215	0.212	0.169	0.079	0.110	0.057
B91	0.335	0.087	0.072	0.060	0.043	0.066	0.054
B93	0.124	0.103	0.081	0.090	0.055	0.073	0.058
B94	0.088	0.116	0.092	0.139	0.102	0.086	0.069
B97	0.112	0.102	0.082	0.070	0.052	0.080	0.040
B102	0.114	0.054	0.050	0.069	0.052	0.022	0.028
B105	0.061	0.175	0.077	0.067	0.020	0.069	0.058
B109	—	0.229	0.256	0.134	0.095	0.093	0.079
B110	0.083	0.093	0.113	0.126	0.079	0.074	0.044
B116	0.106	0.149	0.147	0.112	0.090	0.086	0.065
B117	0.112	0.049	-0.003	0.070	0.031	0.038	0.006
B119	0.060	0.150	0.222	0.182	0.115	0.084	0.057
B122	0.101	0.137	0.147	0.076	0.044	0.071	0.007
B125	0.127	0.022	-0.001	0.063	0.052	-0.0004	0.022
B127	0.062	0.128	0.163	0.143	0.093	0.084	0.046
B129	0.106	0.136	0.163	0.119	0.087	0.099	0.015
B130	0.137	0.083	0.009	0.064	0.033	0.035	0.054
B134	0.068	0.118	0.142	0.143	0.091	0.062	0.059
B135	0.086	0.064	0.017	0.048	0.033	0.048	0.022
B137	0.111	0.095	0.048	0.035	0.025	0.068	0.055
B140	0.0004	0.116	0.251	0.193	0.170	0.106	0.023

CONTINUED ON NEXT PAGE

Table A.3 (CONTINUED FROM PREVIOUS PAGE)

GC	$H\beta$	MgH	Mg2	Mgb	MgG	Fe52	Fe53
B141	0.115	0.071	0.011	0.023	0.028	0.025	0.042
B144	0.069	0.123	0.172	0.168	0.119	0.073	0.072
B148	0.080	0.093	0.107	0.113	0.082	0.073	0.063
B149	0.115	0.085	0.036	0.057	0.041	0.074	0.056
B156	0.034	0.038	0.029	0.091	0.054	0.054	0.047
B158	0.072	0.056	0.085	0.110	0.075	0.066	0.050
B159	0.099	0.149	0.156	0.100	0.083	0.077	0.039
B160	—	0.238	-0.124	0.107	0.002	0.014	-0.046
B161	0.074	0.149	0.160	0.107	0.075	0.073	0.041
B164	0.060	0.113	0.209	0.169	0.090	0.055	0.067
B166	0.125	0.052	0.069	0.081	0.046	0.053	0.009
B167	0.076	0.108	0.159	0.153	0.090	0.103	0.060
B170	0.195	0.082	0.072	0.176	0.099	0.020	0.059
B171	0.067	0.122	0.164	0.159	0.102	0.077	0.077
B176	0.085	-0.021	-0.073	0.068	0.040	0.005	0.026
B179	0.084	0.045	0.036	0.098	0.063	0.046	0.047
B180	0.068	0.105	0.119	0.089	0.057	0.080	0.038
B182	0.102	0.041	0.021	0.075	0.049	0.038	0.050
B184	0.066	0.133	0.213	0.236	0.100	0.084	0.074
B185	0.080	0.100	0.120	0.124	0.064	0.094	0.066
B188	0.093	0.047	0.041	0.073	0.044	0.011	0.037
B190	0.097	0.074	0.042	0.089	0.062	0.070	0.052
B193	0.080	0.134	0.189	0.186	0.124	0.091	0.077
B197	0.046	0.145	0.233	0.211	0.096	0.098	0.081
B198	0.089	0.080	0.132	0.108	0.078	0.084	0.063
B199	0.125	0.113	0.006	0.033	0.028	0.024	0.031
B200	0.082	0.089	0.065	0.135	0.083	0.050	0.093
B203	0.035	0.137	0.153	0.136	0.074	0.080	0.028
B204	0.078	0.057	0.073	0.102	0.063	0.048	0.071
B207	0.128	0.014	0.020	0.062	0.060	0.066	0.038
B208	0.127	0.134	0.215	0.128	0.079	0.118	0.055
B209	0.076	0.039	0.036	0.098	0.048	0.055	0.033
B210	0.310	0.063	-0.017	0.028	0.0003	0.044	0.035
B213	0.044	0.105	0.131	0.116	0.077	0.075	0.040
B214	0.136	0.040	0.010	0.051	0.027	0.066	0.075
B216	0.250	0.065	0.048	0.058	0.034	0.072	0.032
B217	0.074	0.055	0.043	0.104	0.065	0.056	0.046
B218	0.071	0.063	0.050	0.092	0.058	0.050	0.047

CONTINUED ON NEXT PAGE

Table A.3 (CONTINUED FROM PREVIOUS PAGE)

GC	$H\beta$	MgH	Mg2	Mgb	MgG	Fe52	Fe53
B219	0.080	0.065	0.070	0.133	0.074	0.054	0.075
B220	0.086	0.052	0.039	0.080	0.049	0.050	0.038
B221	0.078	0.098	0.097	0.088	0.055	0.084	0.035
B222	0.400	—	—	0.027	0.013	—	—
B223	0.191	0.111	0.114	0.102	0.079	0.058	0.080
B224	0.110	0.058	0.009	0.030	0.026	0.043	0.021
B225	0.073	0.098	0.139	0.148	0.089	0.090	0.070
B230	0.117	0.016	-0.020	0.023	-0.0003	0.052	0.003
B231	0.100	0.028	0.052	0.098	0.066	0.057	0.049
B232	0.131	0.043	-0.015	0.034	0.020	0.034	0.005
B234	0.051	0.069	0.095	0.124	0.076	0.059	0.059
B235	0.085	0.050	0.062	0.102	0.061	0.074	0.082
B237	0.342	0.088	0.008	-0.030	-0.070	0.106	0.027
B238	0.051	0.098	0.114	0.092	0.066	0.085	0.039
B281	0.245	0.148	0.132	0.091	0.086	0.128	0.027
B283	-0.032	0.105	0.175	0.179	0.117	0.006	0.097
B295	0.207	0.035	-0.048	0.057	0.038	0.028	0.014
B298	0.110	0.025	-0.039	0.027	0.0004	0.052	0.004
B301	0.075	0.138	0.109	0.087	0.053	0.061	0.074
B303	0.256	0.032	0.075	0.079	0.069	0.055	-0.002
B305	0.108	-0.031	-0.016	0.094	0.066	-0.015	0.102
B306	0.095	0.121	0.084	0.071	0.051	0.074	0.021
B307	0.255	-0.057	-0.015	0.131	0.088	0.062	0.089
B311	0.113	0.034	-0.023	0.022	0.009	0.026	0.005
B312	0.120	0.085	0.050	0.072	0.034	0.060	0.038
B313	0.095	0.110	0.103	0.091	0.057	0.069	0.042
B314	0.227	0.110	0.083	0.069	0.042	0.052	0.043
B315	0.207	0.086	0.036	0.027	0.015	0.040	0.019
B316	0.102	0.076	0.119	0.107	0.065	0.081	0.026
B319	0.236	0.036	0.003	0.033	0.010	0.029	0.017
B321	0.282	-0.002	-0.041	0.017	0.020	0.015	0.009
B327	0.175	0.053	0.026	0.030	0.017	0.036	0.015
B335	0.088	0.048	0.105	0.129	0.085	0.044	0.037
B338	0.085	0.079	0.079	0.059	0.035	0.052	0.024
B341	0.077	0.057	0.081	0.096	0.050	0.046	0.046
B342	0.322	-0.001	-0.072	0.049	-0.005	-0.024	0.025
B355	0.189	0.077	0.038	0.070	0.038	0.083	-0.014
B356	0.138	0.073	0.018	0.050	0.031	0.059	0.015

CONTINUED ON NEXT PAGE

Table A.3 (CONTINUED FROM PREVIOUS PAGE)

GC	$H\beta$	MgH	Mg2	Mgb	MgG	Fe52	Fe53
B365	0.143	0.073	0.041	0.036	0.023	0.024	0.031
B366	0.121	0.001	-0.067	0.027	0.0005	0.0004	0.021
B367	0.278	0.029	-0.019	0.001	0.004	0.082	0.029
B370	0.112	0.020	-0.033	0.030	0.011	0.004	0.017
B372	0.106	0.087	0.066	0.074	0.050	0.063	0.044
B374	0.174	0.033	0.042	0.061	0.009	0.066	0.050
B378	0.122	0.048	0.005	0.038	0.019	0.049	0.044
B380	0.294	0.089	0.076	0.036	0.006	0.069	0.011
B382	0.122	0.001	-0.025	0.068	0.033	0.043	0.046
B386	0.097	0.080	0.069	0.071	0.047	0.058	0.013
B391	0.107	0.032	0.018	0.049	0.054	0.048	0.107
B400	0.019	0.085	0.054	0.050	0.014	0.109	-0.006
B443	0.304	-0.052	-0.034	0.066	0.044	0.012	-0.020
B448	0.303	0.075	0.032	0.035	0.029	0.041	-0.014
B451	0.148	0.005	0.024	0.060	0.075	-0.018	0.012
B453	0.176	0.069	0.056	0.039	0.035	0.078	0.034
B458	0.277	0.073	0.053	0.030	0.006	0.078	0.070
B467	0.089	0.049	0.014	0.005	0.020	0.009	0.011
B472	0.092	0.076	0.058	0.067	0.040	0.054	0.030
B475	0.265	0.066	0.062	0.002	0.024	0.041	0.014
B480	0.227	-0.006	-0.040	0.046	0.044	0.059	0.057
B483	0.246	0.085	0.034	-0.012	-0.012	0.039	-0.035
B484	0.252	-0.033	-0.028	0.052	0.035	0.038	0.044
S47	0.182	0.026	0.021	0.051	0.022	0.033	0.065
S245	0.064	0.138	0.177	0.168	0.092	0.087	0.069
S327	0.118	0.035	-0.015	0.036	0.018	0.035	0.009
BoD195	0.184	0.017	-0.040	0.031	0.009	0.001	0.031
BoD289	0.142	0.121	0.108	0.129	0.050	0.085	-0.035
BoD292	0.081	0.113	0.227	0.207	0.132	0.110	0.027
DAO23	-0.040	0.202	—	—	—	0.086	0.079
DAO25	0.066	0.158	-0.006	0.110	0.033	0.047	-0.031
DAO30	0.144	0.139	0.120	0.109	0.063	0.121	0.092
DAO36	0.220	-0.0002	-0.035	-0.028	0.018	-0.031	0.015
DAO39	0.324	0.017	0.017	0.050	0.022	0.065	0.058
DAO41	0.336	—	—	0.096	0.055	0.042	—
DAO47	0.172	0.002	-0.028	0.049	0.059	0.009	0.091
DAO48	0.105	0.223	-0.034	-0.076	-0.018	-0.041	0.049
DAO58	0.074	0.064	0.066	0.118	0.072	0.047	0.061

CONTINUED ON NEXT PAGE

Table A.3 (CONTINUED FROM PREVIOUS PAGE)

GC	$H\beta$	MgH	Mg2	Mgb	MgG	Fe52	Fe53
DAO65	0.245	0.040	0.008	0.066	0.034	0.039	0.033
DAO66	0.075	0.013	-0.029	0.073	0.029	0.015	0.017
DAO70	-0.005	0.256	0.305	0.184	0.136	0.108	0.133
DAO73	0.242	0.026	-0.033	0.034	0.013	-0.028	0.001
DAO84	-0.067	-0.012	-0.057	0.126	0.030	-0.014	0.036
BA11	0.036	0.014	0.077	0.154	0.091	0.059	0.019
NB20	0.071	0.172	0.225	0.166	0.127	0.099	0.058
NB33	0.096	0.185	0.197	0.198	0.147	0.070	0.068
V31	0.259	-0.009	-0.016	0.059	0.025	0.019	0.023
V216	-0.006	0.131	0.167	0.120	0.116	0.061	0.033
V246	-0.005	0.106	0.050	0.075	0.047	0.059	0.015
V294	0.077	0.096	0.124	0.101	0.062	0.077	0.033

B. ARGUS OBSERVING RECORDS

Table B.1: M31 globular clusters observed with MOS/ARGUS at CFHT

Target	Date	Start (UT)	Exp. Time (sec)	Airmass
B225	19/08/95	8:22	60	2.35
B124	19/08/95	8:32	100	2.18
B358	19/08/95	8:36	100	2.13
B176	19/08/95	8:40	100	2.11
B383	19/08/95	8:44	100	2.06
B370	19/08/95	8:48	100	1.90
B289	19/08/95	8:52	100	1.85
B347	19/08/95	8:56	150	1.89
B315	19/08/95	9:01	150	1.81
B38	19/08/95	9:06	200	1.79
B366	19/08/95	9:12	200	1.77
B397	19/08/95	9:17	200	1.74
B341	19/08/95	9:24	200	1.65
B352	19/08/95	9:29	200	1.62
B400	19/08/95	9:35	200	1.62
B117	19/08/95	9:41	200	1.54
B291	19/08/95	9:48	200	1.48
B165	19/08/95	9:55	200	1.48
B96	19/08/95	10:16	200	1.37
B298	19/08/95	10:23	300	1.33
B229	19/08/95	10:30	300	1.33
B350	19/08/95	10:38	300	1.29
B220	19/08/95	10:45	300	1.28
B74	19/08/95	10:52	300	1.25
B125	19/08/95	11:00	300	1.23
B317	19/08/95	11:07	300	1.21

CONTINUED ON NEXT PAGE

Table B.1 (CONTINUED FROM PREVIOUS PAGE)

Target	Date	Start (UT)	Exp. Time (sec)	Airmass
B337	19/08/95	11:14	300	1.20
B111	19/08/95	11:22	300	1.18
B134	19/08/95	11:29	300	1.17
B365	19/08/95	11:47	300	1.15
B150	19/08/95	11:54	300	1.13
B10	19/08/95	12:02	300	1.11
B50	19/08/95	12:09	300	1.11
B172	19/08/95	12:16	300	1.10
B37	19/08/95	12:24	300	1.09
B144	19/08/95	12:31	300	1.09
B55	19/08/95	12:38	300	1.08
B60	19/08/95	12:46	300	1.08
B11	19/08/95	12:53	300	1.08
B8	19/08/95	13:10	300	1.07
B70	19/08/95	13:17	300	1.07
B85	19/08/95	13:25	300	1.07
B28	19/08/95	13:32	300	1.08
B203	19/08/95	13:39	300	1.08
B4	19/08/95	13:47	300	1.09
B99	19/08/95	13:54	300	1.09
B304	19/08/95	14:01	300	1.09
B156	19/08/95	14:09	300	1.10
B190	19/08/95	14:16	300	1.11
B340	19/08/95	14:23	300	1.10
B97	19/08/95	14:31	300	1.12
B146	19/08/95	14:38	300	1.13
B294	19/08/95	14:45	300	1.15
B25	19/08/95	14:53	300	1.16
B234	19/08/95	15:00	300	1.17
B357	19/08/95	15:07	300	1.18
B401	20/08/95	9:10	300	1.78
B136	20/08/95	9:17	300	1.68
B126	20/08/95	9:25	300	1.63
B130	20/08/95	9:32	300	1.58
B9	20/08/95	9:39	300	1.53

CONTINUED ON NEXT PAGE

Table B.1 (CONTINUED FROM PREVIOUS PAGE)

Target	Date	Start (UT)	Exp. Time (sec)	Airmass
B339	20/08/95	9:47	300	1.48
B310	20/08/95	9:55	300	1.44
B318	20/08/95	10:11	300	1.36
B149	20/08/95	10:18	300	1.35
B356	20/08/95	10:26	300	1.33
B361	20/08/95	10:33	300	1.30
B141	20/08/95	10:40	300	1.28
B118	20/08/95	10:56	300	1.23
B43	20/08/95	11:03	300	1.21
B81	20/08/95	11:10	300	1.19
B114	20/08/95	11:18	300	1.18
B13	20/08/95	11:25	300	1.16
B392	20/08/95	11:32	300	1.16
B301	20/08/95	11:47	300	1.12
B188	20/08/95	11:55	300	1.12
B101	20/08/95	12:02	300	1.11
B128	20/08/95	12:10	300	1.10
B387	20/08/95	12:17	300	1.10
B80	20/08/95	12:24	300	1.10
B194	20/08/95	12:32	300	1.09
B129	20/08/95	12:39	300	1.08
B181	20/08/95	12:46	300	1.08
B59	20/08/95	12:54	300	1.08
B207	20/08/95	13:07	300	1.07
B170	20/08/95	13:16	300	1.07
B239	20/08/95	13:22	300	1.08
B382	20/08/95	13:36	300	1.08
B292	20/08/95	13:43	300	1.08
B394	20/08/95	13:51	300	1.08
B105	20/08/95	13:58	300	1.09
B299	20/08/95	14:05	300	1.10
B67	20/08/95	14:12	300	1.10
B231	20/08/95	14:20	300	1.11
B184	20/08/95	14:27	300	1.12

CONTINUED ON NEXT PAGE

Table B.1 (CONTINUED FROM PREVIOUS PAGE)

Target	Date	Start (UT)	Exp. Time (sec)	Airmass
B187	20/08/95	14:34	300	1.13
B77	20/08/95	14:42	300	1.14
B169	20/08/95	14:49	300	1.15
B196	20/08/95	14:57	300	1.16
B36	20/08/95	15:04	300	1.19
B327	20/08/95	15:11	300	1.20
B30	21/08/95	8:30	300	2.09
B108	21/08/95	8:39	300	1.99
B216	21/08/95	8:46	300	1.93
B215	21/08/95	8:54	300	1.85
B157	21/08/95	9:04	300	1.76
B189	21/08/95	9:11	300	1.70
B75	21/08/95	9:21	300	1.64
B72	21/08/95	9:28	300	1.57
B26	21/08/95	9:42	300	1.49
B236	21/08/95	9:50	300	1.47
B159	21/08/95	9:57	300	1.43
B123	21/08/95	10:05	300	1.39
B222	21/08/95	10:21	300	1.33
B47	21/08/95	10:38	300	1.27
B104	21/08/95	10:45	300	1.25
B173	21/08/95	10:52	300	1.23
B297	21/08/95	11:00	300	1.19
B198	21/08/95	11:16	300	1.18
B31	21/08/95	11:24	300	1.16
B16	21/08/95	11:31	300	1.15
B214	21/08/95	11:38	300	1.14
B2	21/08/95	11:47	300	1.12
B398	21/08/95	11:54	300	a.12
B35	21/08/95	12:03	300	1.11
B162	21/08/95	12:10	300	1.10
B57	21/08/95	12:17	300	1.09
B78	21/08/95	12:25	300	1.09
B362	21/08/95	12:44	300	1.08
B62	21/08/95	12:51	300	1.08

CONTINUED ON NEXT PAGE

Table B.1 (CONTINUED FROM PREVIOUS PAGE)

Target	Date	Start (UT)	Exp. Time (sec)	Airmass
B389	21/08/95	12:59	300	1.08
B378	21/08/95	13:06	300	1.08
B309	21/08/95	13:14	300	1.07
B66	21/08/95	13:21	300	1.07
B319	21/08/95	13:29	300	1.07
B40	21/08/95	13:36	300	1.08
B91	21/08/95	13:45	300	1.09
B314	21/08/95	13:52	300	1.09
B122	21/08/95	14:06	300	1.11
B137	21/08/95	14:14	300	1.11
B313	21/08/95	14:22	200	1.12
B102	21/08/95	14:29	200	1.13
B324	21/08/95	14:37	200	1.15
B345	21/08/95	14:42	200	1.14
B348	21/08/95	14:47	200	1.16
B138	21/08/95	14:53	200	1.17
B408	21/08/95	14:59	200	1.16
B395	21/08/95	15:06	200	1.19
B393	22/08/95	8:14	200	2.34
B377	22/08/95	8:20	200	2.23
NB6	22/08/95	8:25	200	2.10
B316	22/08/95	8:31	200	2.01
B56	22/08/95	8:37	200	1.96
B369	22/08/95	8:42	300	1.94
B290	22/08/95	8:56	300	1.71
B300	22/08/95	9:04	300	1.68
B186	22/08/95	9:11	300	1.67
B380	22/08/95	9:21	300	1.63
B167	22/08/95	9:27	300	1.56
B390	22/08/95	9:35	300	1.54
B402	22/08/95	9:42	300	1.51
B391	22/08/95	9:49	300	1.46
B199	22/08/95	9:57	300	1.41
B237	22/08/95	10:04	300	1.39
B399	22/08/95	10:12	300	1.37

CONTINUED ON NEXT PAGE

Table B.1 (CONTINUED FROM PREVIOUS PAGE)

Target	Date	Start (UT)	Exp. Time (sec)	Airmass
B406	22/08/95	10:28	300	1.32
B52	22/08/95	10:35	300	1.27
B396	22/08/95	10:44	300	1.25
B351	22/08/95	10:51	300	1.23
B133	22/08/95	10:59	300	1.21
B375	22/08/95	11:06	300	1.20
B360	22/08/95	11:14	300	1.18
B226	22/08/95	11:21	300	1.16
B119	22/08/95	11:28	300	1.15
B223	22/08/95	11:36	300	1.14
B100	22/08/95	11:43	300	1.12
B355	22/08/95	11:52	300	1.12
B296	22/08/95	12:06	300	1.09
B168	22/08/95	12:14	300	1.10
NB21	22/08/95	12:21	300	1.09
B346	22/08/95	12:32	300	1.08
B385	22/08/95	12:39	300	1.08
B33	22/08/95	12:47	300	1.07
B323	22/08/95	12:54	300	1.07
B342	22/08/95	13:01	300	1.07
B164	22/08/95	13:09	300	1.07
B354	22/08/95	13:35	300	1.09
B3	22/08/95	13:49	300	1.09
B53	22/08/95	13:57	300	1.10
B49	22/08/95	14:04	300	1.11
B46	22/08/95	14:12	300	1.12
B84	22/08/95	14:19	300	1.12
B197	22/08/95	14:26	300	1.13
B330	22/08/95	14:33	300	1.15
B208	22/08/95	14:41	300	1.15
NB16	22/08/95	14:48	300	1.17
B303	22/08/95	14:56	300	1.19
B71	22/08/95	15:03	300	1.20

C. GALLERY OF ARGUS RECONSTRUCTED IMAGES

Reconstructed globular cluster images from the MOS/ARGUS frames, as discussed in Chapter 5. Darker areas represent illuminated fibres.

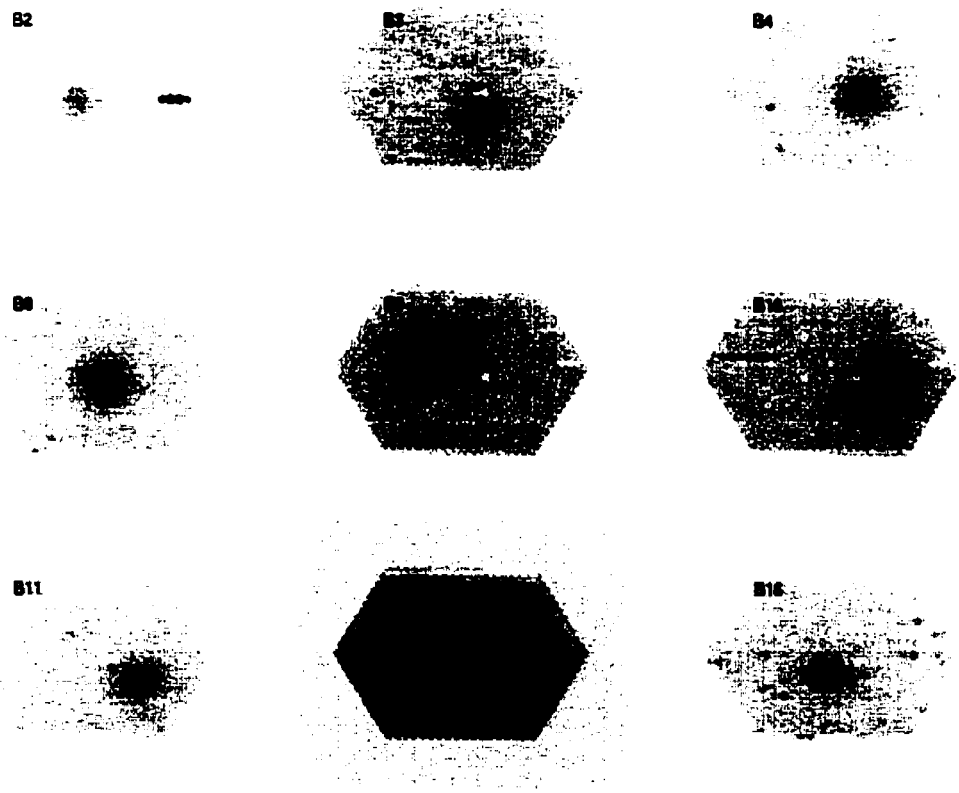

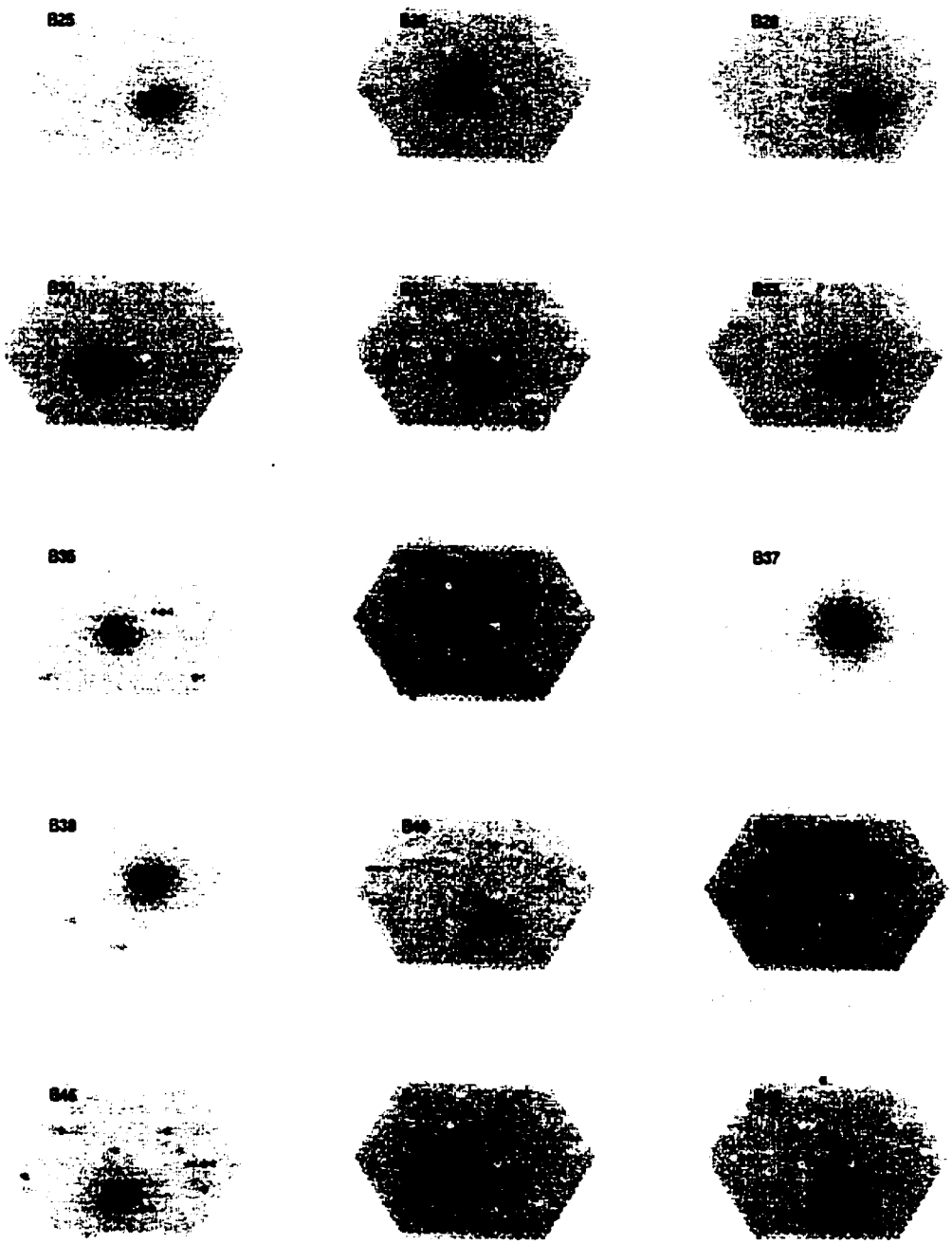
B25
B36
B37
B38
B46

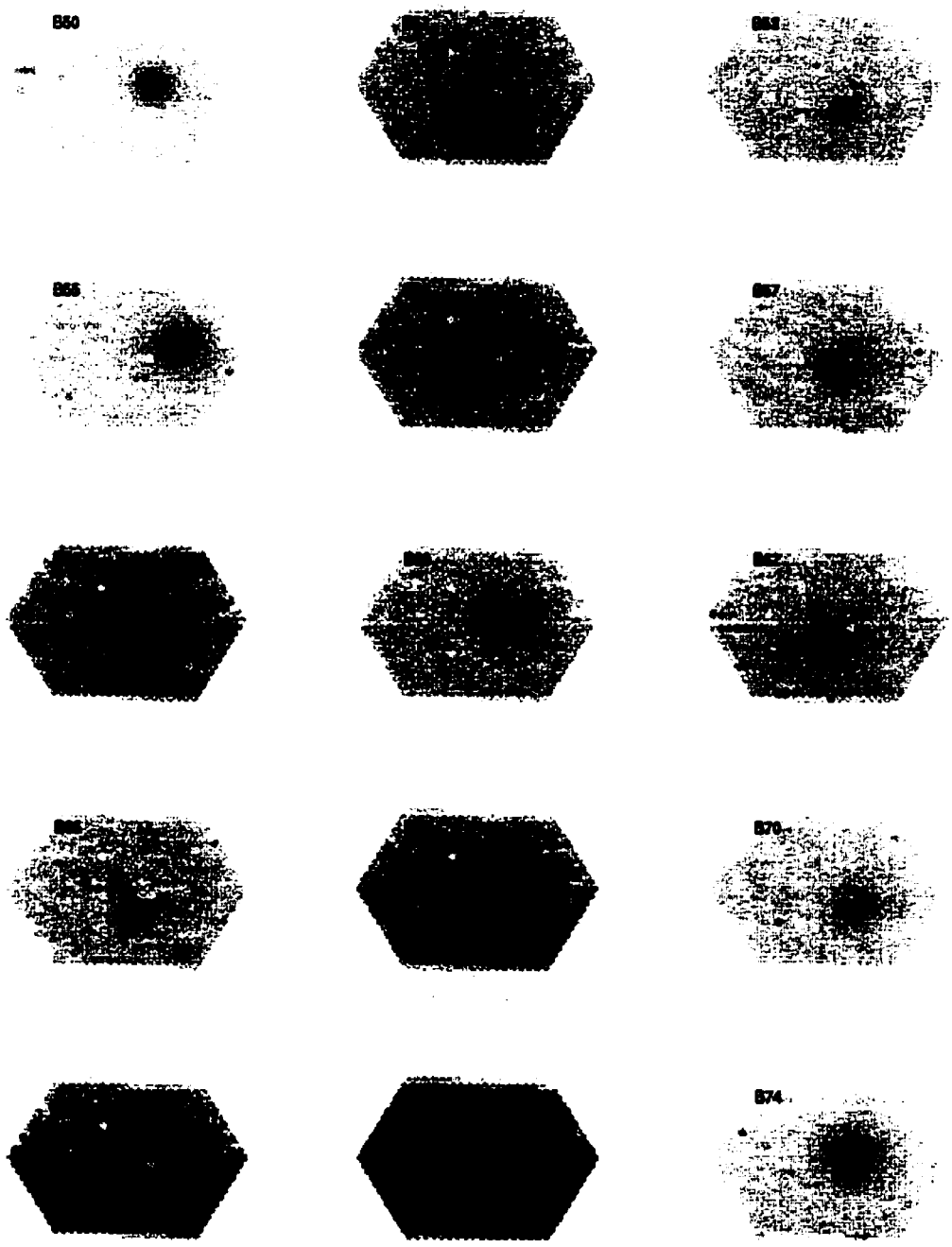
B50
B74

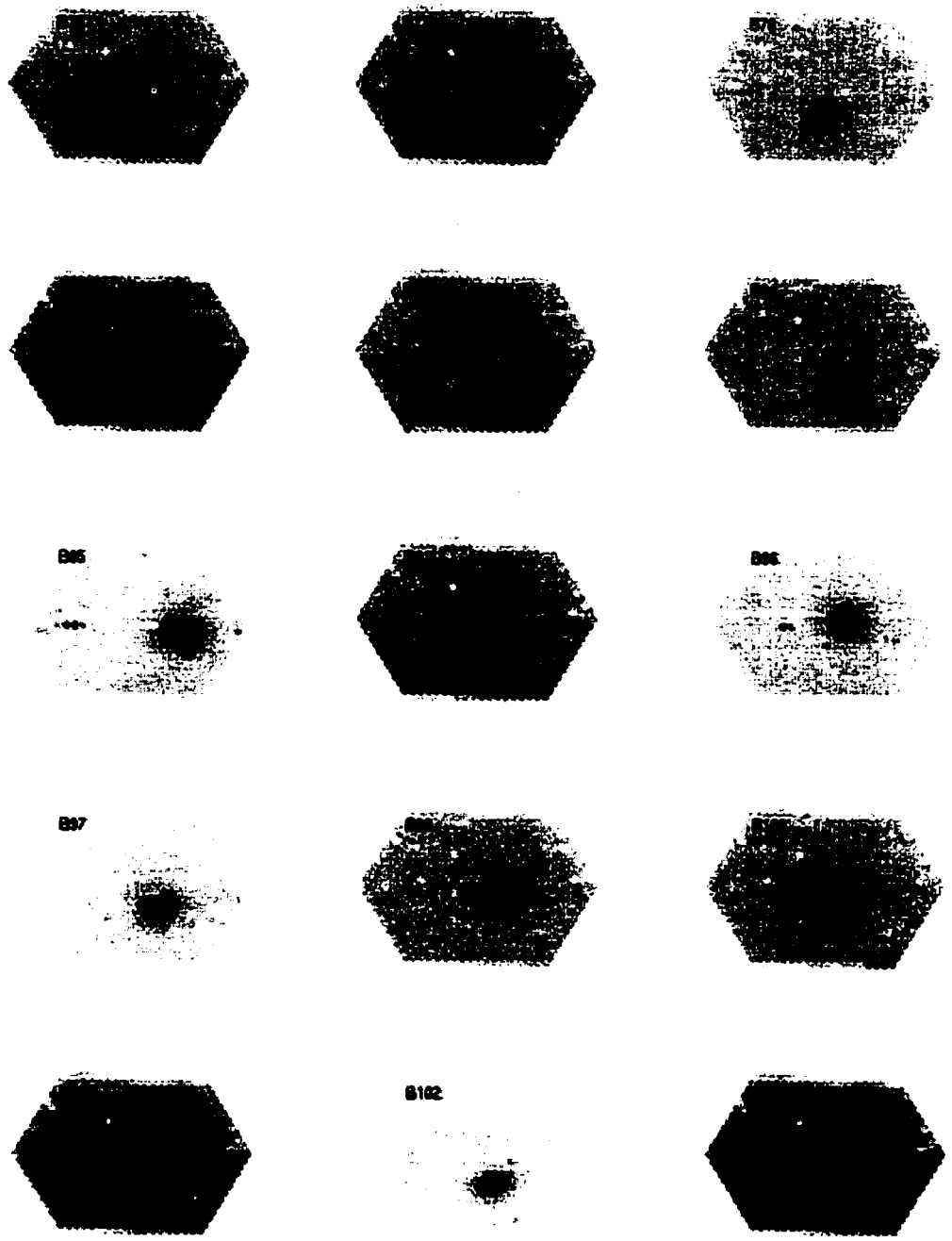
B85
B97
B102

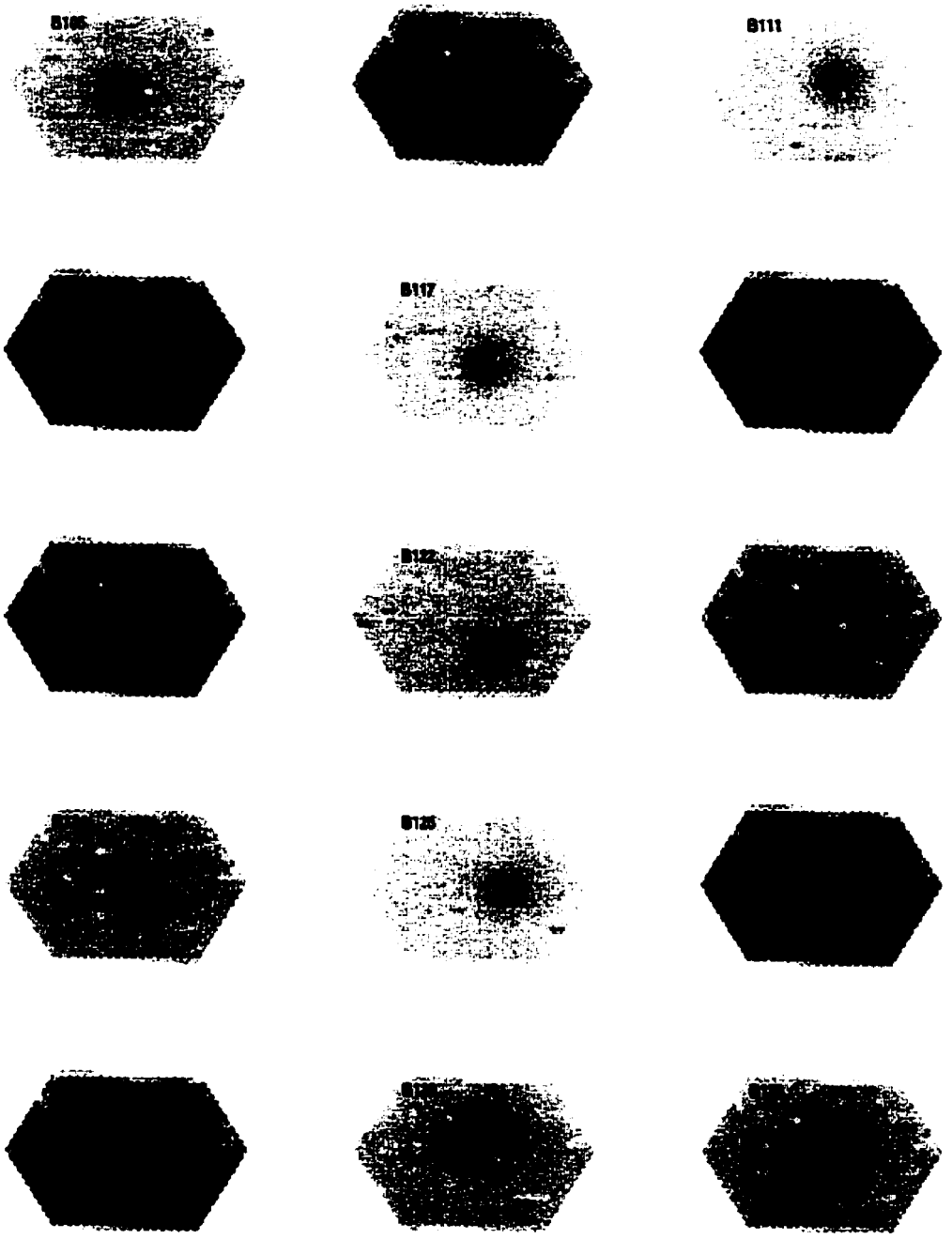
B111

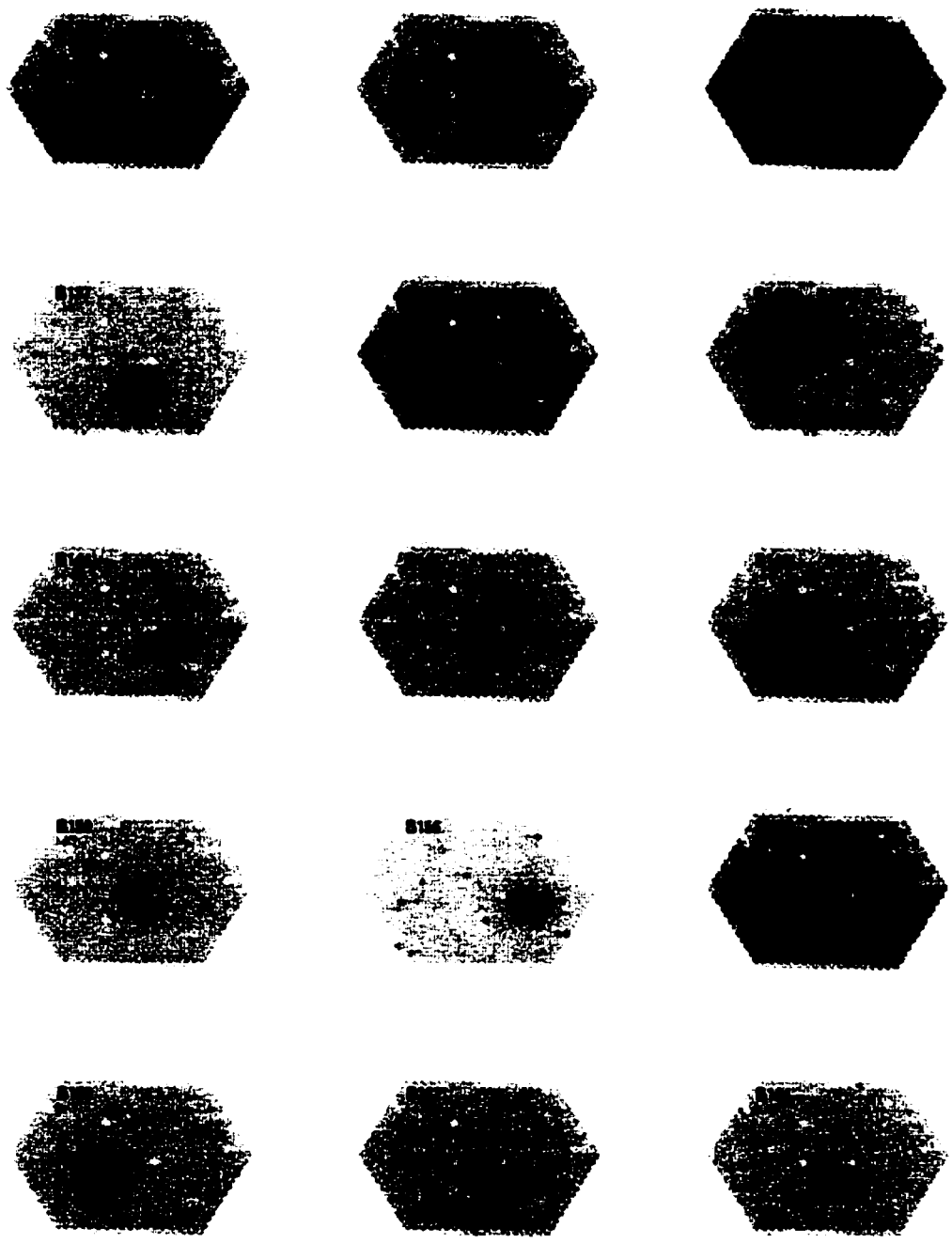

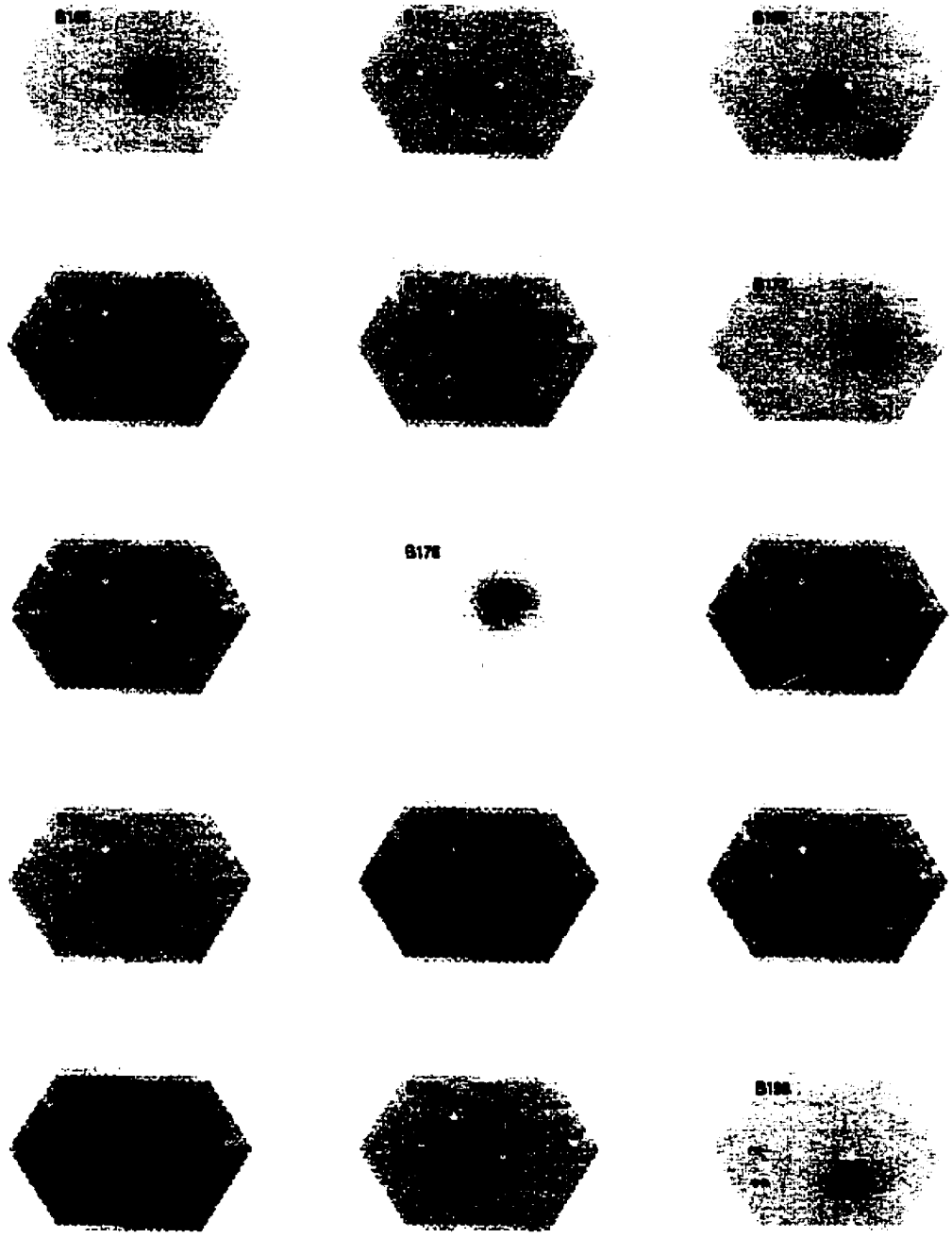
B178

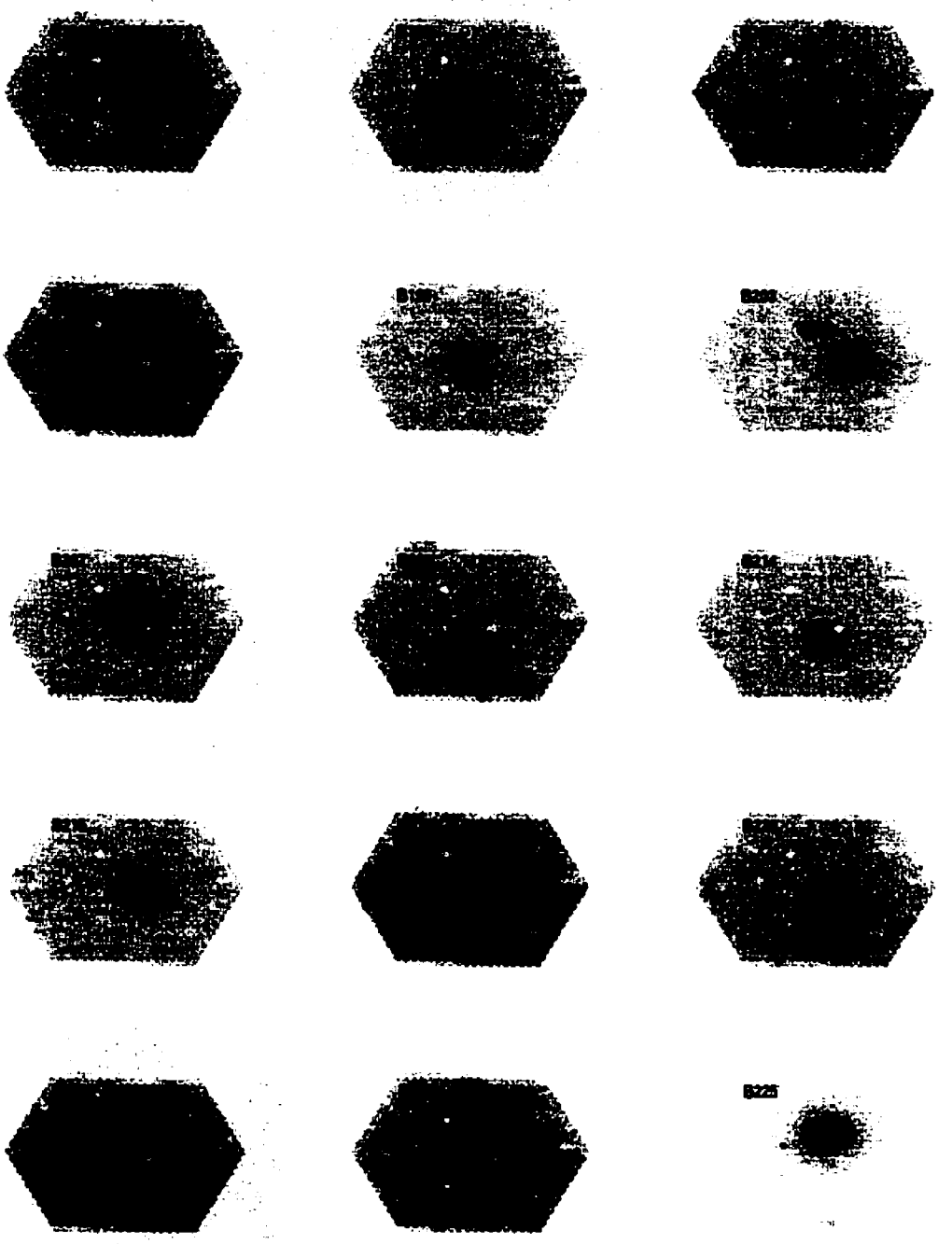

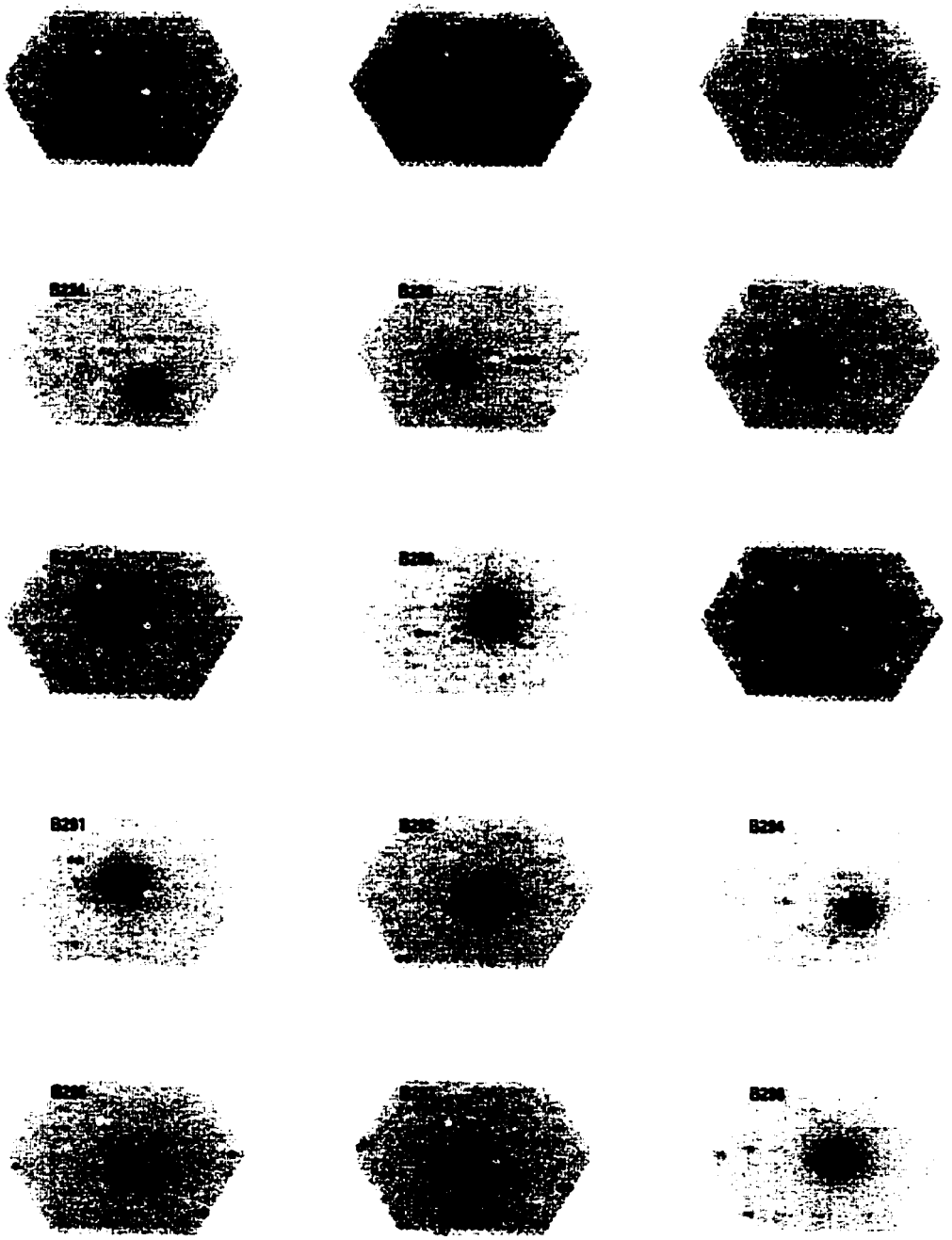

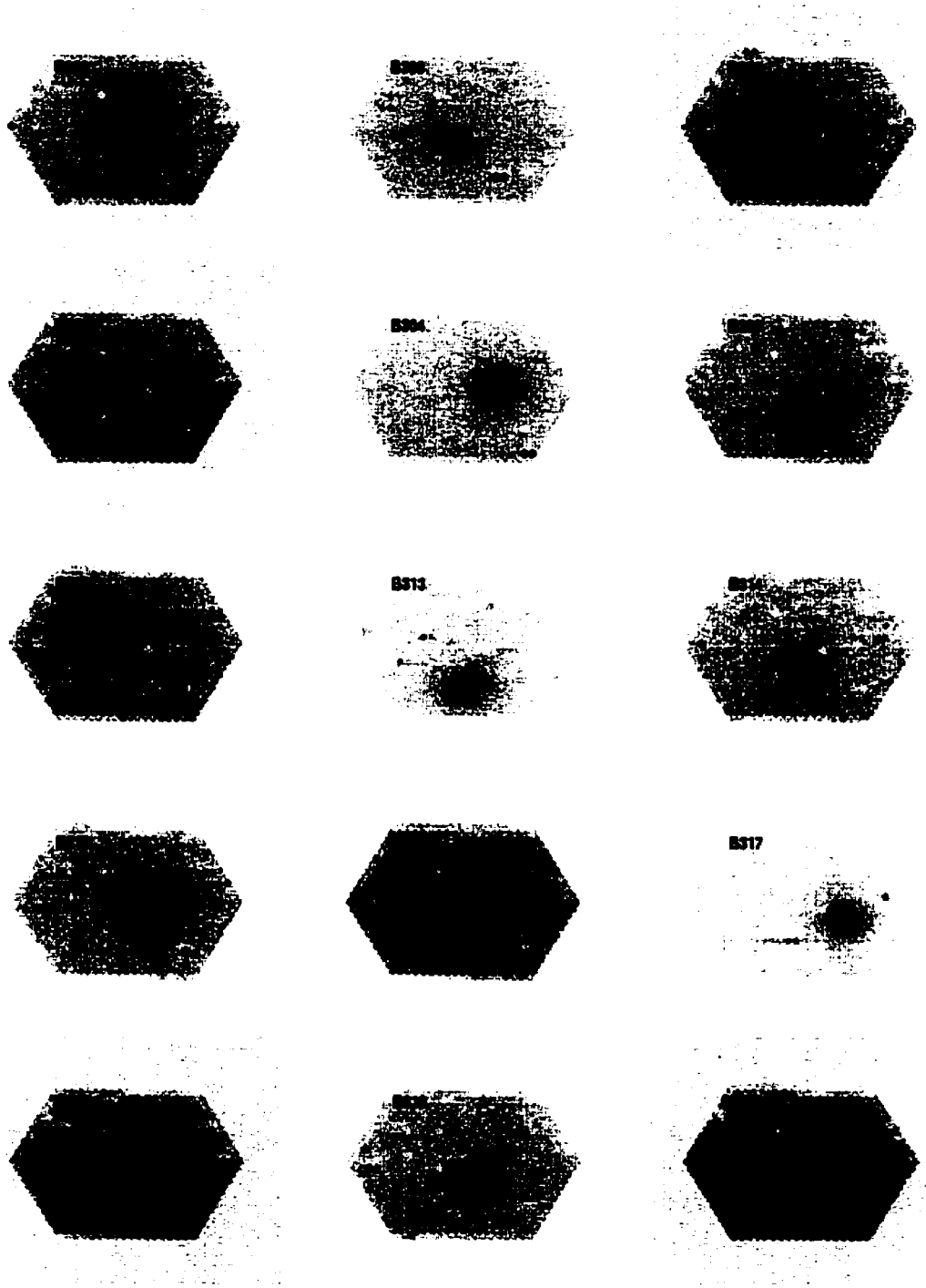
BS13
BS17

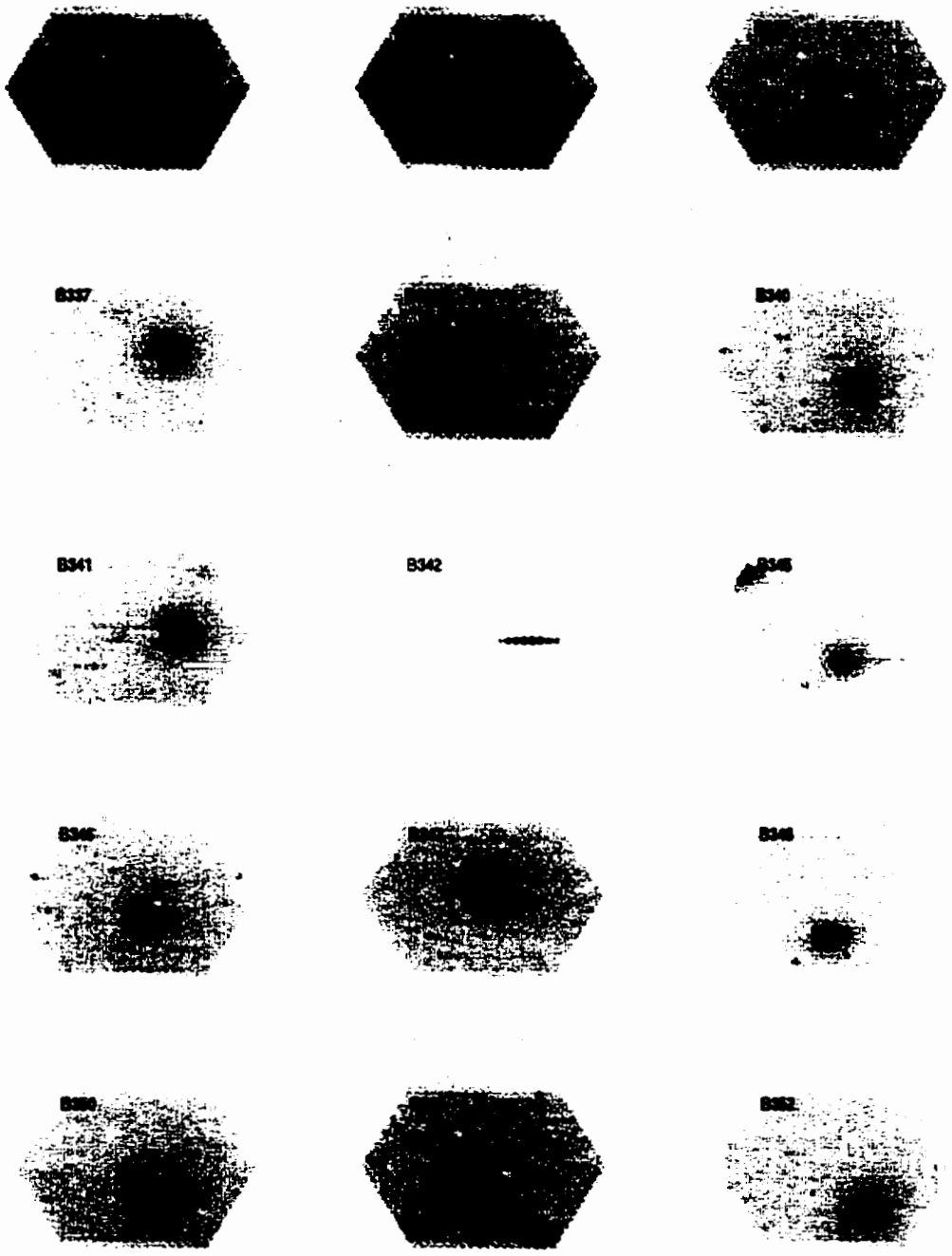
B337
B340
B341
B342
B345
B346
B348

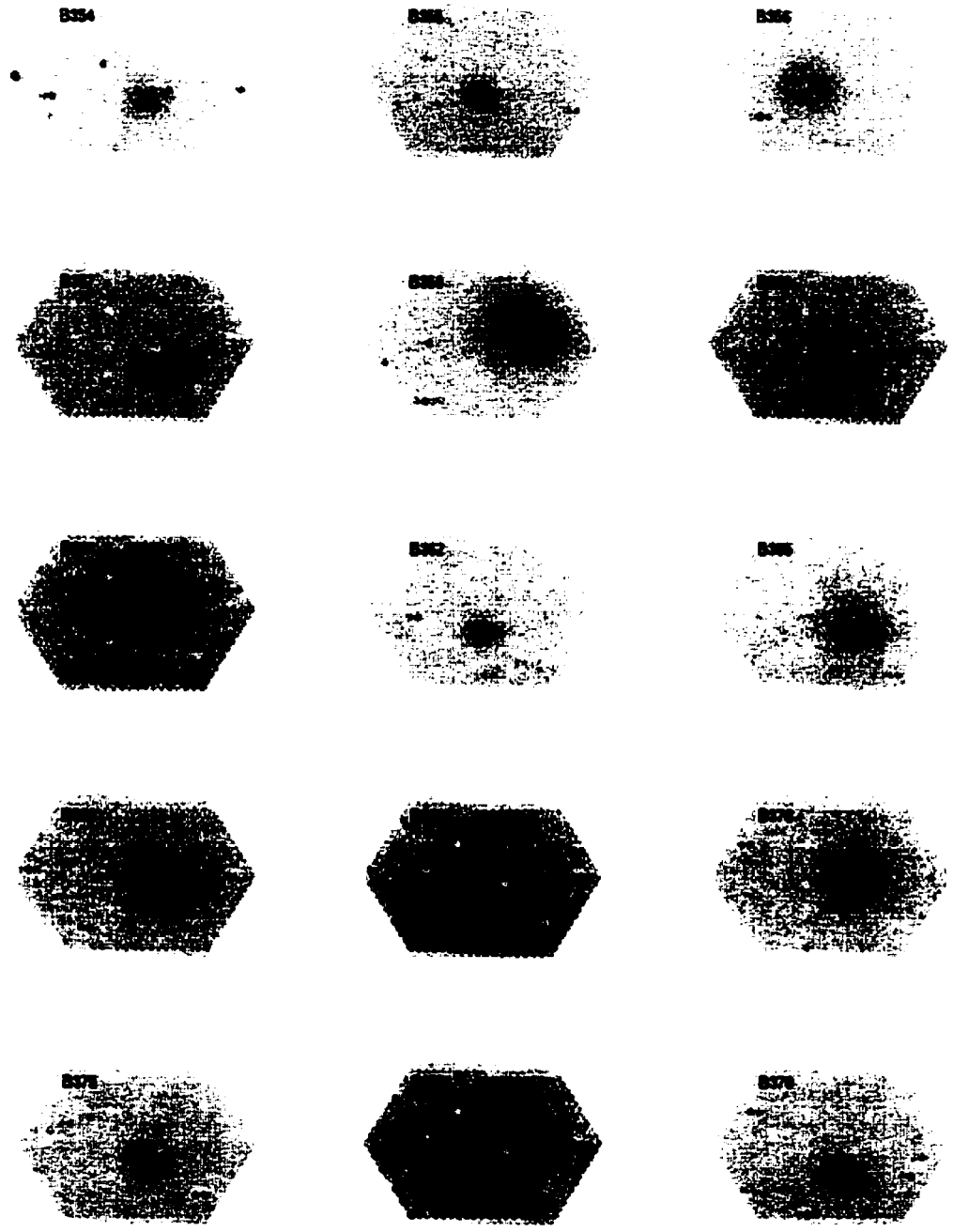

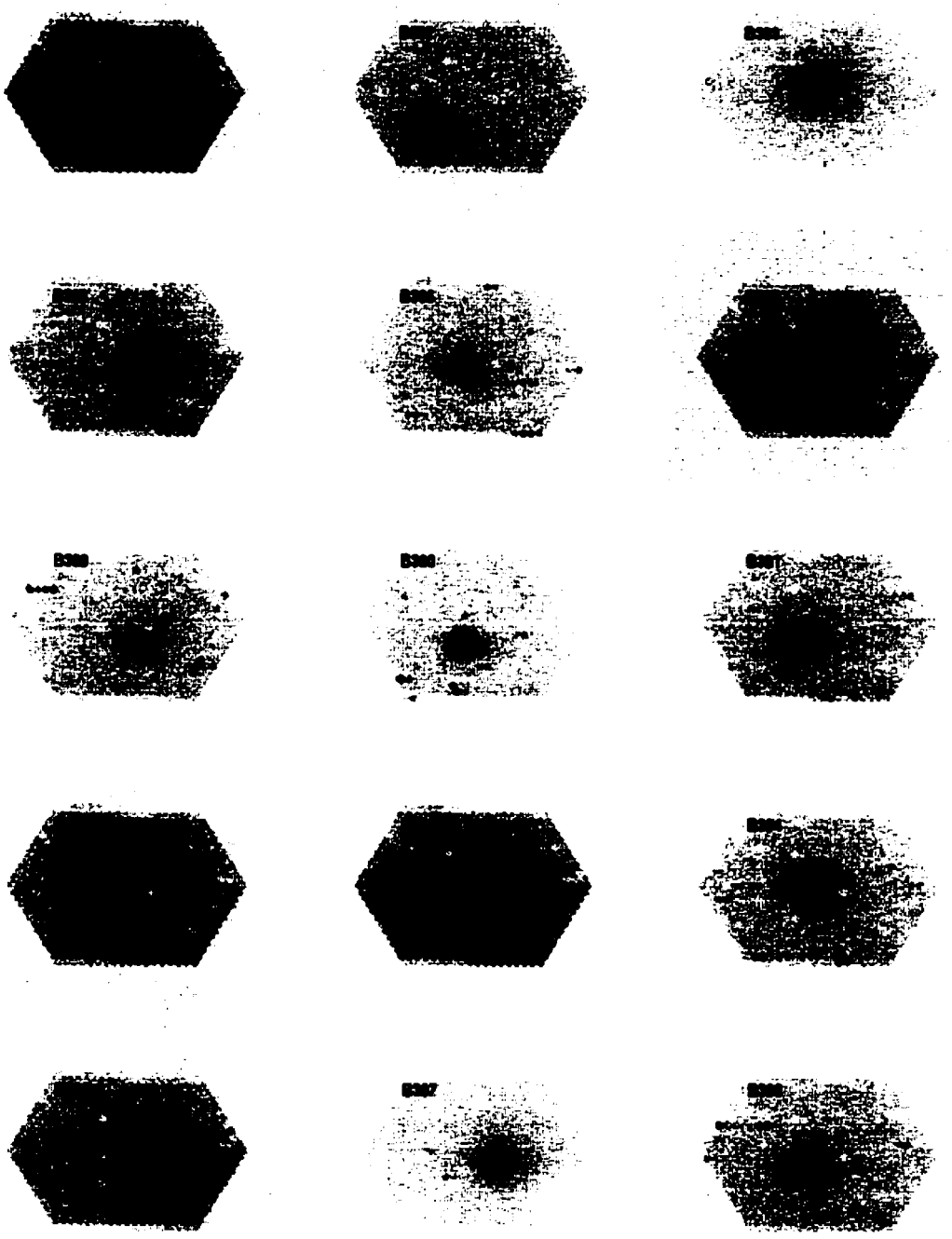

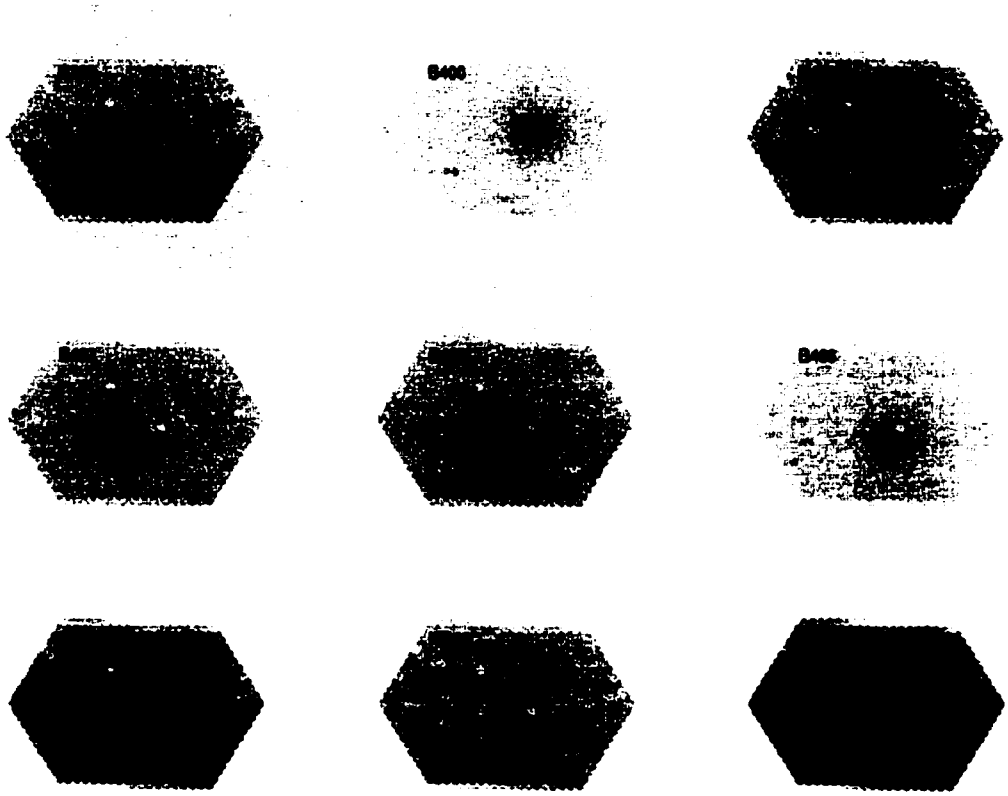

GLOSSARY OF TERMS AND UNITS

$'$: Minutes of arc or arcminutes (1/60 of a degree).

$''$: Seconds of arc or arcseconds (1/3600 of degree).

$\alpha_{(B1950)}$: Right ascension in reference to a standard epoch (Besselian year 1950).

Å: Angstrom (10^{-10} m).

Abundance: Term used to refer to the metal abundance of a target (e.g. star, globular cluster or galaxy), as determined from the strength of its spectral features. In astronomy, a metal can be any element heavier than helium.

ADU: Analog-to-Digital Unit.

Airmass: ($\mathcal{X}$) The length of the light path through the atmosphere in the direction of the target, compared to the width of the atmosphere overhead. By definition, $\mathcal{X} \equiv 1$ for objects directly overhead.

APM: Automatic Plate-Measuring machine, a National Astronomy Facility run by the Institute of Astronomy in Cambridge.

ARGUS: Fibre bundle spectrograph formerly used at CFHT in combination with the MOS instrument to perform integral field spectroscopy. This instrument is described in Chapter 5.

Bias Image: A zero duration exposure used to read the bias level of the detector. See description in Section 3.2.1.

CC: Cross-correlation coefficient, the peak value of the normalized correlation function.

CCD: (Charge-Coupled Device) Light-sensitive detector widely used in optical and infrared astronomy. Astronomical CCDs consist of a two-dimensional array of pixels on a thin wafer of semiconductor; electric charge is produced in response to incident photons.

CFHT: (Canada-France Hawaii Telescope) A 3.6 m diameter optical/infrared telescope atop Mauna Kea, a dormant volcano on the island of Hawaii which is (arguably) the best observing site in the world.

CMD: (colour-magnitude diagram) A plot of the magnitude or luminosity of stars versus colour, spectral type or temperature. Stars form well-defined sequences in the CMD. See §3.5 of Binney and Merrifield (1998) for more information.

COBE: (COsmic Background Explorer) An orbiting satellite mission launched by NASA in 1989 to study the cosmic microwave background radiation.

Cosmic Rays: Highly energetic particles (e.g. hydrogen nuclei, electrons, positrons, neutrinos) which are continuously bombarding the Earth's atmosphere.

$\delta_{(B1950)}$: Declination in reference to a standard epoch (Besselian year 1950).

Declination: (δ, Dec) The angular distance to a celestial body measured north (0° to $+90^\circ$) or south (0° to -90°) of the Celestial Equator (the projection of the Earth's equator into space). Typically expressed in degrees, arcminutes and arcseconds.

dex: An increment in $\log_{10}$, used here as a unit of [Fe/H].

DIRBE: (Diffuse InfraRed Background Experiment) An experiment conducted to search for the cosmic infrared background. Maps were made of the sky brightness at infrared wavelengths of 1.25 to 240 μm.

Dynamical Friction: Transfer of energy from an object to the surrounding medium due to interaction.

Elliptical Galaxies: Galaxies with no disk component. Most are triaxial ellipsoids with no obvious internal structure.

Ellipticity: (ϵ) A parameter which specifies the flattening of an orbit: $\epsilon = (1 - \frac{a}{b})$, where a and b are the lengths of the semi-major-axis and semi-minor-axis, respectively.

[Fe/H]: The heavy-element abundance or metallicity of an object relative to solar (see Equation 2.1).

Flatfield Image: An image of a uniformly illuminated source used to measure the pixel-to-pixel differences in the sensitivity of the CCD. See description in Section 3.2.1.

FWHM: The Full Width at Half-Maximum.

G: The gravitational constant: 6.672×10^{-11} $m^3\,kg^{-1}\,sec^{-2}$.

Gain: The number of ADU counts per electron (i.e. per photon) in the output signal.

GC: (Globular Cluster) Gravitationally-bound agglomerations of several tens of thousands to a few million stars. See Section 1.3 for more information.

GCS: (Globular Cluster System) The collection of all **globular clusters** belonging to a particular galaxy, typically described as a component of its stellar population.

Grism: A transmission diffraction grating + prism combination, used to deflect the light to remain on the optical axis, and to centre a particular wavelength on the detector.

Gyr: (Giga-year) Unit representing 1 billion years.

HI : Neutral hydrogen.

HII : Singly-ionized hydrogen.

Heteroscedastic: (In reference to the KMM mixture modeling test of Section 6.2.1) A fit in which the populations are not constrained to have a common covariance. The opposite of **homoscedastic**.

HST: (Hubble Space Telescope) NASA's orbiting 2.4 m diameter telescope, launched in 1990. Its instrumentation includes WFPC2, a wide-field planetary camera.

IFS: (Integral Field Spectroscopy) Spectroscopy of a two-dimensional area on the sky, resulting in three dimensions of output: α, β and λ (e.g. see Vanderriest 1993).

Irregular Galaxies: Galaxies of irregular shape and structure, with large amounts of interstellar matter.

kpc: (kiloparsec) One thousand parsecs (pc).

λ: The wavelength of light.

Lenticular Galaxies: Galaxies with a large bulge and small disk. The disk in a lenticular (S0) galaxy shows no evidence of spiral arms.

Linear Correlation Coefficient: (r) A statistic used to test the quality of a linear fit $y = a + bx$ to a set of N data points (x_i, y_i):

$$r \equiv \frac{N\sum x_i y_i - \sum x_i \sum y_i}{\sqrt{N\sum x_i^2 - (\sum x_i)^2}\sqrt{N\sum y_i^2 - (\sum y_i)^2}} \qquad \text{(C.1)}$$

LMC: (Large Magellanic Cloud) See **Magellanic Clouds**.

LSR: The local standard of rest is the frame of reference centred on the Sun in which all of the nearby stars are at rest. The rotational velocity of the local standard of rest is ~ 220 km/s.

$M_\odot$: Mass of the Sun (2×10^{30} kg).

M/L: Mass-to-Light ratio, generally measured in solar units.

Magellanic Clouds: Two relatively small irregular galaxies which are nearby neighbours of the Milky Way. The Large and Small Magellanic Clouds can be seen with the naked eye in the Southern Hemisphere.

Magnitude: A measure of brightness. A difference in the apparent magnitude of two objects (e.g. stars) is proportional to the differences in the log of their brightness:

$$m_1 - m_2 = 2.5 \log_{10} \left(\frac{f_2}{f_1} \right), \tag{C.2}$$

where m_1 and m_2 are the apparent magnitudes of objects 1 and 2, and f_1 and f_2 represent the energy fluxes from the objects. Therefore, a magnitude difference of 5 corresponds to a factor of 100 in the ratio of the radiation fluxes. Brighter objects have lower magnitudes.

Metal: In an astronomical context, a metal refers to any element heavier than helium. This includes light elements such as oxygen and nitrogen.

Metallicity: The logarithmic abundance of iron relative to hydrogen, as expressed in term of solar abundance (see Equation 2.1).

MOS: (Multi-Object Spectrograph) Instrument which permits the spectroscopic study of multiple objects at once.

Myr: (Mega-year) Unit representing 1 million years.

Order-sorting filter: A blocking filter used to prevent higher-order spectral light beyond a certain wavelength from falling on the detector. This light results from the fact that for any given angle of diffraction, the grating equation $m\lambda = d(sin\, i + sin\, \theta)$ is satisfied for several values of m and λ (m is the grating order, d is the spacing of the grating etches, i is the angle of incidence of the light and θ is the angle of diffraction measured from the normal). See Walker (1987) for more details.

Overscan/overclock strip: Region of an output CCD image which reflects the bias level of the chip.

PA: (Position Angle) Typically, position angle refers to the angle from north to the object (or axis), measured eastward.

pc: (parsec) Unit of distance (3.26 light years or 3×10^{13} km).

pix: (pixel) Picture element (see **CCD**).

Photometry: The measurement of the brightness of a source within specific wavelength ranges.

Proper motion: The apparent angular motion of an object per year in a direction perpendicular to the line of sight.

r: See Linear Correlation Coefficient.

$R_{\odot}$: Galactocentric radius of the Sun ($\sim$ 8.5 kpc).

Readnoise: (Readout noise) The number of electrons per pixel introduced upon readout of the device, caused by the electronics of the CCD and noise introduced by the conversion of an analog signal to a digital number.

Right ascension: (α, RA) The angular distance to a celestial body, measured eastwards along the Celestial Equator (the projection of the Earth's equator into space). Typically expressed in hours, minutes and seconds.

S/N: Signal-to-Noise ratio.

SGMC: (SuperGiant Molecular Cloud) Large ($10^9 M_\odot$, 1 kpc diameter) versions of giant molecular clouds (see Section 1.3.1).

SMC: (Small Magellanic Cloud) See **Magellanic Clouds**.

Solar: Of the Sun.

Solar circle: A circle of radius $R_\odot$ about the centre of the Galaxy.

UT: (Universal Time) Equivalent to Greenwich mean time.

V: Apparent magnitude of an object in the visual photometric wave-band (centred on ~ 5500 Å).

Vignetting: Restriction of the field of view due to incomplete illumination of the detector, generally resulting from the internal optics of the system.

WHT: (William Herschel Telescope) A 4.2 m telescope in La Palma, Canary Islands.

WYFFOS: Wide-Field Fibre Optic Spectrograph at the WHT.